Rigorous Analysis of Dielectric Resonator Antenna Using the Method of Moments

A Dissertation

Presented in Partial Fulfillment of the Requirements for

the Degree Doctor of Philosophy in the

Graduate School of the Chinese University of Hong Kong

by

LEUNG, Kwok-wa, B.Sc.

Department of Electronic Engineering

The Chinese University of Hong Kong

May, 1993

Abstract

In this dissertation, the hemispherical DR antenna is investigated theoretically and experimentally. The hemispherical DR is chosen because its interface between dielectric and air requires no magnetic wall assumption so that during the formulation of the problem a more accurate solution can be obtained.

Both coaxial probe-fed and aperture-coupled DR antennas are studied. In the former, the exact electric field Green's function with separate particular and homogeneous parts is derived rigorously in a form which can be evaluated very efficiently. Both TE to r and TM to r modes of the hemispherical DR are discussed. The probe current and hence the input impedance are obtained by using the method of moments with the Galerkin's procedure. Convergence checks of the numerical solutions for the present problem are discussed for different excitation models and dipole kernels.

The effects of the probe length and the probe position on the input impedance are also studied. It is found that there are two degrees of freedom for the impedance matching of the DR antenna, namely the probe length and the probe position. Although the antenna size can be reduced if a higher dielectric constant is used, the dielectric constant cannot be increased indefinitely otherwise radiation will be severely suppressed and very narrow bandwidth will result. Moreover, by exciting different resonant modes, either a broadside or an end-fire radiation pattern can be obtained.

In the case of aperture-coupled excitation, the reciprocity method is used to formulate the problem. The analysis consists of two parts: the DR antenna above the ground plane and the microstrip feed line below the ground plane. In the former, the exact magnetic field Green's function of the magnetic field inside the DR

antenna due to an equivalent magnetic current of the slot (aperture) is derived. The technique similar to that employed in the probe-fed case is used to avoid numerical difficulties in evaluating the Green's function. For the analysis of the microstrip part, the expressions are evaluated in the spectral domain. Such calculations are well developed and computationally efficient.

The broadside TE_{111} mode and the end-fire TE_{221} mode are studied, and verified by measurements. The effects of the slot length, the slot position and the slot width on the input impedance are studied. By varying these parameters, impedance matching can be achieved .

Dedication

To Jesus Christ my Lord,

who loves me completely and unconditionally

Acknowledgments

I would like to show my deep gratitude towards my supervisors, Dr. Albert Lai and Dr. K. M. Luk, for their kind guidance and encouragement throughout the course of the study.

I would like to express my appreciation to Prof. D. Lin, who has given me support and encouragement during the study.

Sincere thanks are due to Mr. Douglas Chun and Mr. K. T. Cheng, who have changed my way of thinking when I was a trainee student in Motorola.

Special thanks are also due to K. W. Wong, W. P. Tan, Terry Lo, S. C. Lee and W. C. Chan, who have brought me unforgettable days in my graduate study.

Also I would like to thank K. T. Ng, Cathay Leung and Bonnie Lo for their cares during my graduate study.

Finally, I would like to thank Mr. S. H. Zhao, Mr. Dickson Poon, and Mrs. L. Y. Yam Pi for their invaluable help in the measurement process.

Last and least, I would like to thank Pui-nan for supporting not only my study but also my future.

CONTENTS

CHAPTER 1

INTRODUCTION

Today the frequency range of modern communication systems has gradually progressed upward into the millimeter wave region. Although microstrip antennas were studied and used extensively during the last decade, they cannot be simply scaled up in frequency. Ohmic power loss in the imperfectly conducting portion is increased at higher frequencies, and the efficiency of the antenna may be reduced significantly. While dielectric resonator (DR) is traditionally used in filter and oscillator applications [1], Long and his collaborators [2]-[4] showed that DRs of different shapes (cylindrical [2], rectangular [3] and hemispherical [4]) can also be used as effective radiators. The various shapes of DR antennas are shown in Fig. 1-1. With the use of DRs, small size and low cost antennas can be frabricated while maintaining efficient radiation. Without the metal portion, loss of the DR antenna is mainly caused by dielectric loss, which is very small in practice.

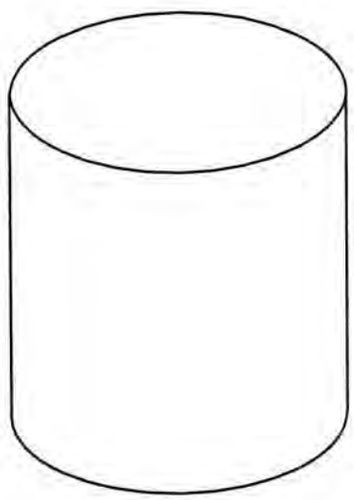

Fig. 1-1(a)

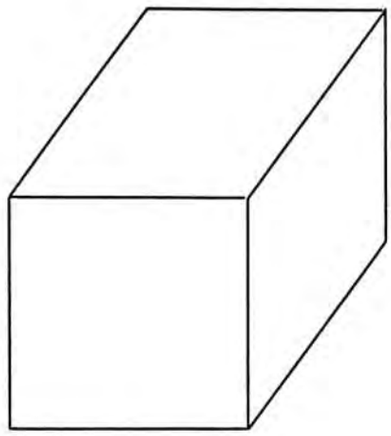

Fig. 1-1(b)

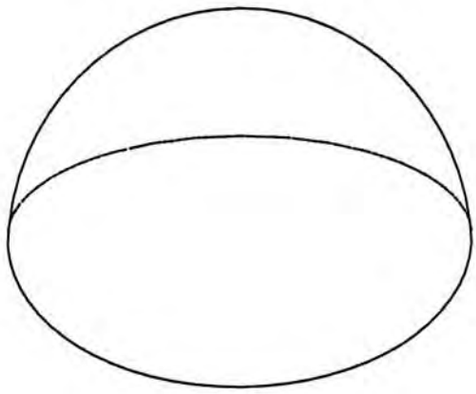

Fig. 1-1(c)

Fig. 1-1 Various shapes for DR antennas (a) Cylindrical (b) Rectangular (c) Hemispherical

Although DR antennas are so promising for high frequency applications, limited information about the antenna characteristics is available in the literature. Apart from experimental studies [2]-[7], most of the analysis concentrate only on radiation patterns [8]. In this dissertation, the input impedance of a DR antenna is analyzed. Experiment is carried out to verify the theory.

Cylindrical DRs are easy to frabricate, but have edge-shaped boundaries which make the analytical solution difficult to find explicitly. In analyzing cylindrical DRs, the perfect magnetic wall approximation is usually used to estimate the resonant frequencies of the structure. This model simply covers the surface of the DR with a perfect magnetic conductor, and the analysis procedure is similar to that of a metallic hollow resonator. However, the results given by this method are not satisfactory with discrepancies of 20% or more between theory and measured values [1]. Furthermore, since the fields outside the DR are neglected in using the magnetic wall approximation, this method is not feasible in evaluating the input impedance with which the present work is concerned. To account for the fields outside an open DR, J Van Bladel [9]-[11] used perturbational method which is based on the asymptotic expansion of the fields in terms of the inverse powers of $\sqrt{\varepsilon_r}$. Using this method, the explicit dependence of various parameters on ε_r can be obtained, but the results are only accurate in the limit as $\varepsilon_r \to \infty$. This is unsuitable for practical antenna designs as DRs of high ε_r will severely suppress the radiated fields. Although this method can derive more accurate results by considering higher order correction terms in $1/\sqrt{\varepsilon_r}$, the treatment becomes very complicated.

Surface integral equation technique, which is formulated in a rigorous fashion, can accurately computed not only the resonant frequencies and Q factors [12], but also the electromagnetic field distributions in the vicinity of the DR [13]. This method is based on the equivalence principle [14] from which the equivalent surface electric current $\vec{J}_s$ and the equivalent surface magnetic current $\vec{M}_s$ on the DR surface are derived. The currents $\vec{J}_s$ and $\vec{M}_s$ are then solved numerically through two coupled

equations. From the surface currents, all field components inside and outside the DR can be computed. Ghods and Rahmat-Sammi [15] used this method to obtain the input impedance of a dielectric coated monopole antenna. However, solving the coupled equations is computationally expensive and, therefore, time inefficient.

A DR antenna of the rectangular shape is also easy to fabricate. However, due to the fact that it has even more boundaries, the analysis of this geometry is most difficult and complicated. Moreover, it was found that the estimated resonant frequency obtained by using the perfect magnetic wall approximation has a larger discrepancy between theory and measured value than that in the cylindrical case [3]. Nevertheless, other methods as discussed before are basically applicable to this geometry. Again, the solution relies heavily on intensive numerical computations, and usually it takes a long time to obtain the results.

This dissertation will concentrate on hemispherical DR antennas [4]. The hemispherical shape is chosen because of the simple interface between itself and free space. In the spherical coordinate system, the variables of the wave functions are separable, which simplifies the analysis a lot. For example, the orthogonality of the modes can now be utilized to determine the modal coefficients. Due to the simple structure, no magnetic wall assumption is required in the problem formulation, and hence a more accurate solution can be obtained. In fact, exact solutions of DRs are derivable only for spheres and doughnuts [16].

The resonance behaviour and the field configurations of a dielectric sphere were investigated systematically by M. Gastine *et al.* [17] in 1967. In their work, the characteristic equations for the TE to r modes (TE_{nmp} modes with n=1,2,..., m=0,1,... and p=1,2,...) and TM to r modes (TM_{nmp} modes with n=1,2,..., m=0,1,... and p=1,2,...) were given. By solving the characteristic equations, one can obtain the resonant frequencies as well as the Q factors for various TE and TM modes. The theory was shown to agree well with measured data. Later in 1984, the use of hemispherical DR as an antenna was demonstrated experimentally by M. W. Mark

et al. [4]. In the demonstration, a coaxial probe penetrating into a DR was used as the excitation source. The measured input impedance of the lowest order TE_{111} to *r* mode that radiates efficiently in the broadside direction was shown. It was found that the measured resonant frequency agreed well with that predicted by solving the TE_{111} mode characteristic equation. Using this antenna, one can achieve impedance matching in antenna designs by simply varying the probe length as well as the feed position.

Several excitation methods for DR antennas were investigated, such as using the coaxial probe feed [4], microstripline feed [5] and the aperture coupling [6]. The DR antenna using the microstripline feed is shown in Fig. 1-2, where the antenna is placed on the top of a common microstrip substrate for its excitation. However, the analysis of this structure is difficult due to the presence of the dielectric substrate which separates the DR antenna from the ground plane. Because of the separation, the application of image theory will result in a configuration in which the dielectric substrate lies between two DR antennas. Matching the boundary conditions for such configuration is complicated. In contrast, when image theory is applied to the case of coaxial probe feed (Fig.1-3) or aperture coupling (Fig.1-4), a single DR antenna with excitation source inside itself is obtained. The analysis of this configuration is relatively simple. In this dissertation, the coaxial probe fed as well as the aperture coupled DR antennas are investigated both theoretically and experimentally.

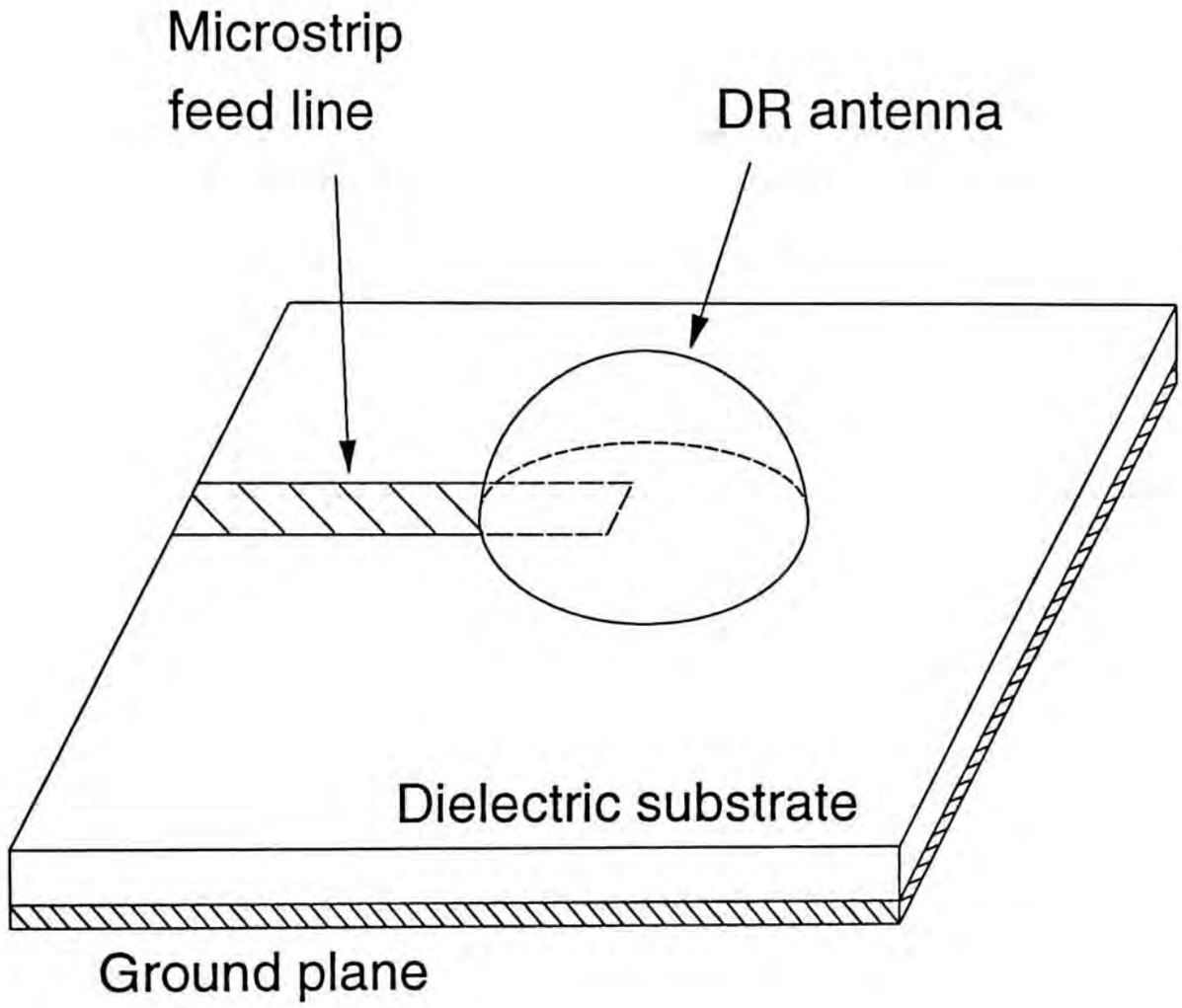

Fig. 1-2 Geometry of DR antenna fed by microstripline

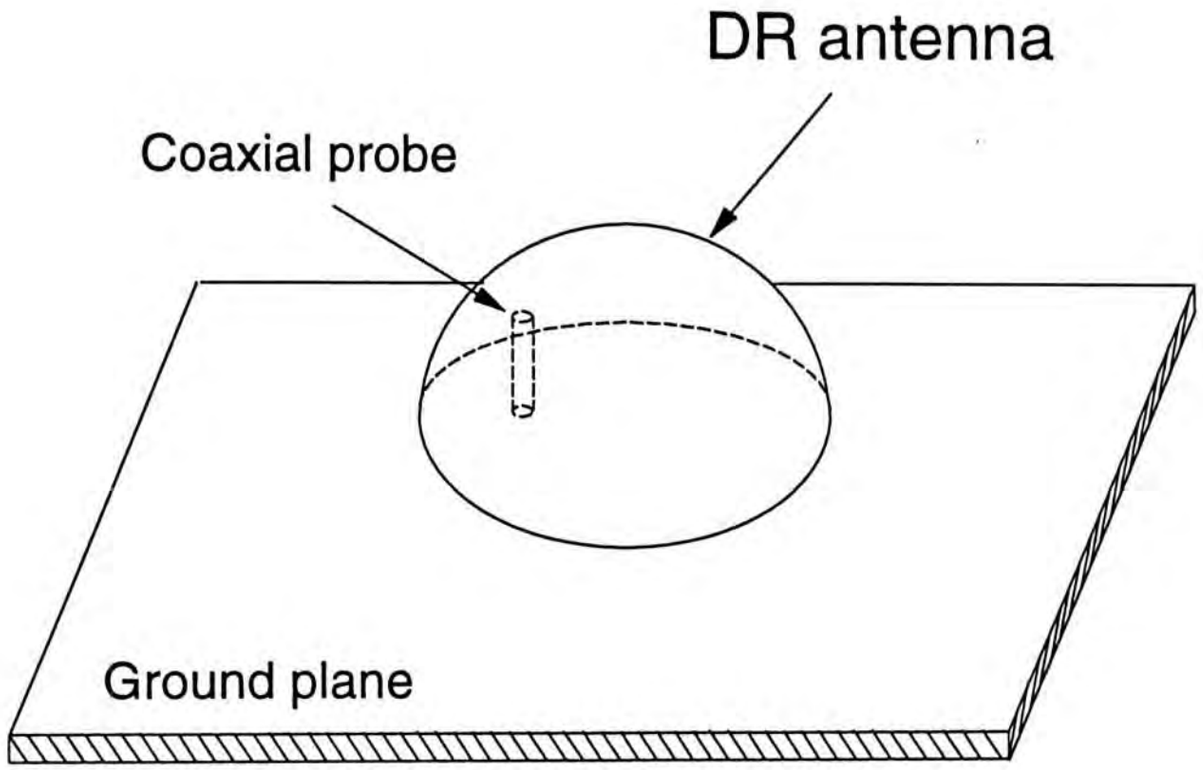

Fig. 1-3 Geometry of DR antenna fed by a coaxial probe

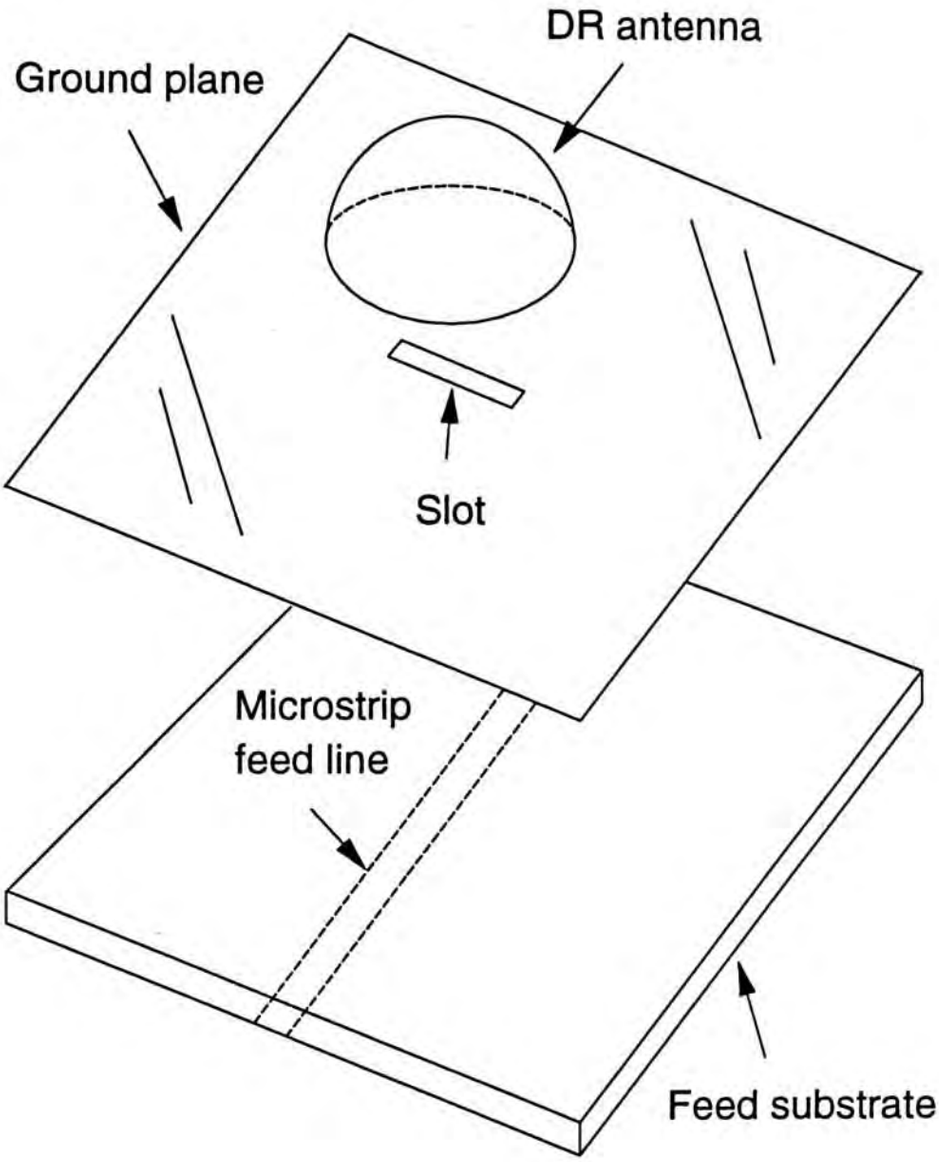

Fig. 1-4 Geometry of DR antenna fed by an aperture

In the analysis of the input impedance of a probe fed hemispherical DR antenna, the mode matching method [18] is used. In this method, the fields are first expressed as summations of spherical harmonics in spherical coordinates. Boundary conditions are then enforced at the source point and the surface of the DR antenna. An integral equation for the probe current is formulated and is solved by the method of moments [19] with the Galerkin's procedure. Once the probe current is found, the input impedance can be obtained readily. The theory is then verified by the experimental data available in the literature as well as additional measurements.

To find the input impedance using the method of moments (MM), the probe current is first expanded by a set of basis functions. In this dissertation, both entire domain sinusoidal basis (EB) functions and piecewise sinusoidal (PWS) basis functions are used. Although the use of PWS modes introduce singularities at certain points along the probe due to the discontinuous derivatives, the series does converge faster than the case of EB modes when only little information is known about the true current. However, because EB modes have continuous derivatives, the results produced by this method are generally closer to the expected values [20]. A comparison between EB functions and PWS functions will be shown. Moreover, convergency checks for the MM solutions are also performed.

The radiation machanisim of the probe fed DR antenna in fact consists of two parts. The energy first radiates from the coaxial probe to the DR, this energy then radiates from the DR to the air. In the first part, the problem of a cylindrical monopole antenna is encountered. Traditionally, two excitation models are used for the cylindrical monopole antenna : delta gap and magnetic frill source models. Although the delta gap source model allows a simpler problem formulation, it usually leads to a divergent solution as the model does not represent any realistic source. For example, the current near the driving point is found to be logarithmically singular [21]. Moreover, a divergent series of the loop current is obtained when it is applied to a loop antenna [22]. On the other hand, although the use of a magnetic

frill source model requires more computational effort, it does represent a realistic source and hence a convergent result can be obtained. The difference between using a delta gap source model and a magnetic frill source model is also studied in this dissertation.

In analyzing the cylindrical monopole (which is presently a part of the probe fed DR antenna), the reduced kernel [23]-[24] is usually used to approximate the exact kernel. In using the reduced kernel, the axial current is assumed to concentrate on the axis of the cylindrical antenna. This approximation avoids the singularity which occurs when the field point coincides with the source point, and hence the problem can be implemented numerically without difficulty. Moreover, a circumferential integration, which is required for the exact kernel, is avoided in the reduced kernel, resulting in a substantial reduction in computation time. The reduced kernel, however, is valid only for thin wires. Imbriale and Ingerson [25] derived a correction term for the wire radius so that the reduced kernel remains accurate even for moderately thick wire antennas. However, for thick wire antennas, the exact kernel should be used. The results of using the traditional reduced kernel, the reduced kernel with effective radius and the exact kernel will be presented in this dissertation.

The excitation of a DR antenna using aperture coupling is first suggested by J.T.H.ST. Martin *et. al.* [6] in 1990. This new feed mechanism was originally proposed by Pozar [26] for the excitation of microstrip antennas. Such feeding method offers several advantages for DR antennas :

(1) active devices can be integrated on a dielectric substrate with the feed network, and the DR antenna is located on the adjacent side. This allows the usage of DR antennas in MMIC applications ;

(2) the problem of large probe self reactances, which is critical at millimeter-wave frequencies, is avoided because the connection made to the DR antenna is now indirect ;

(3) Drilling holes in DR antennas for probe penetrations is no longer necessary.

Although this excitation method is somewhat better than the probe-fed one from the practical point of view, the analysis of the aperture-coupled version is more complicated than that of the probe-fed version. Sullivan and Schaubert [27] presented a rigorous treatment for an aperture coupled microstrip antenna using the method of moments. In their analysis, the current on the feed line is expanded in a combination of subsectional and entire domain basis functions, whereas the incident and reflected currents are represented by travelling wave modes corresponding to the fundamental microstrip mode. By enforcing appropriate boundary conditions, three matrix equations are derived. Solving the matrix equations yields the current reflection coefficient at the center of the aperture. The input impedance at the aperture position is then computed from the current reflection coefficient. Since the non-uniform currents on the feed line are modelled rigorously to account for higher order modes on the microstrip line, it requires tedious formulation and is computationally inefficient.

A simpler method which combines the reciprocity analysis and a moment method solution was presented by Pozar [28], who used the method to solve the problems of a printed slot and an aperture coupled microstrip antenna. It applies the reciprocity theorem to the total fields and the transmitted as well as the reflected propagating microstripline fields. This leads to two equations for three unknowns, namely the reflection coefficient, the transmission coefficient and the aperture field at the aperture position. The third equation comes from enforcing the boundary condition on the aperture. The equivalent series impedance of the slot is then derived from the reflection coefficient. Using the concept of the equivalent series impedance, the input impedance of the slot terminated by an open circuited stub is easily obtained. In this dissertation, the microstripline excitation is analyzed based on the Pozar's method while the antenna part is analyzed using the mode matching method similar to the probe fed case.

The organization of this dissertation is as follows. Chapter 2 deals with the analysis of a probe fed hemispherical DR antenna. Both the broadside TE_{111} mode and the end-fire TM_{101} mode are considered. By using the mode matching method, the exact Green's function of the $\hat{z}$-directed electric field due to a $\hat{z}$-directed point current is derived. The single cavity mode approximation as well as the exact modal solution on the input impedance are studied. Measurements are carried out to verify the theory. The effects of the probe length, probe position and the dielectric constant on the input impedance are studied. In addition, the theoretical single mode radiation patterns are also shown.

The theoretical and experimental studies of the aperture coupled hemispherical DR antenna are presented in Chapter 3. The analysis of the microstripline excitation is carried out in spectral domain while the modal (spatial) technique is used to study the DR antenna. In the latter, the exact Green's function of the $\hat{y}$-directed magnetic field due to a $\hat{y}$-directed magnetic point current is derived. The input impedance at the aperture position is evaluated using the single mode approximation as well as the exact modal solution. The results are verified by measurements. The effects of the slot length, the slot width and the slot position on the input impedance are studied.

Chapter 4 concludes the research and points to future development directions.

CHAPTER 2

ANALYSIS OF A PROBE FED HEMISPHERICAL DR ANTENNA

2.1 Introduction

This chapter deals with a rigorous analysis of a probe-fed hemispherical DR antenna. The mode matching method [18] is used to derive the exact Green's function of a $\hat{z}$-directed electric field due to a $\hat{z}$-directed point current. This method enables one to understand the property of an individual resonant mode easily. However, the traditional problem associated with the method is the convergence of the modal solution. When a source free problem is encountered, the modal solution usually converges very quickly and therefore the problem is not obvious. However, when the excitation source is also considered, the modal solution near the source region converges very slowly and numerical problems will arise. The main problem is the numerical difficulties encountered in evaluating higher-order wave functions, which are needed for a slowly convergent modal solution. For example, Hankel functions of high order have such a large amplitude that they are difficult to handle numerically, and very often the technique of pre-scaling is required. To avoid this difficulty, Nevels and his collaborators [29]-[31] have presented the modal Green's function as the sum of a slowly converging particular solution portion and a rapidly converging homogeneous portion. This allows a special treatment to the slowly converging portion and thus alleviates the numerical problems of the overall modal solution. This technique is used in this formulation.

2.2 Problem Formulation

The antenna configuration is shown in Fig.2-1. The DR of radius a is fed with a probe of length l and radius r_1, located at a displacement b from the center. The outer radius of the coaxial aperture is r_2.

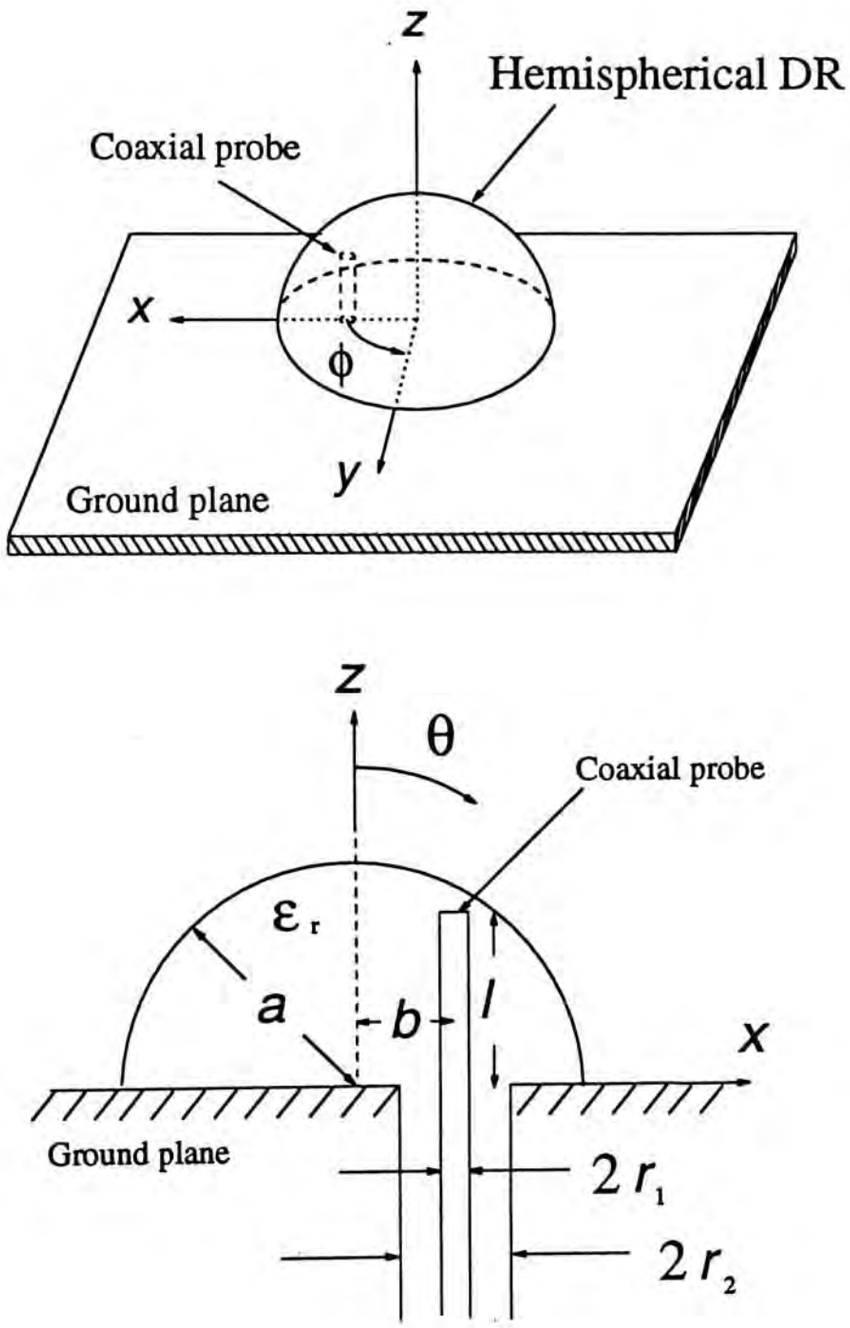

Fig. 2-1 Configuration of a probe fed DR antenna

Using the equivalence principle and image theory, the equivalent geometry of Fig.2-1 is obtained and it is shown in Fig.2-2(a) (delta gap source) and Fig.2-2(b) (magnetic frill source).

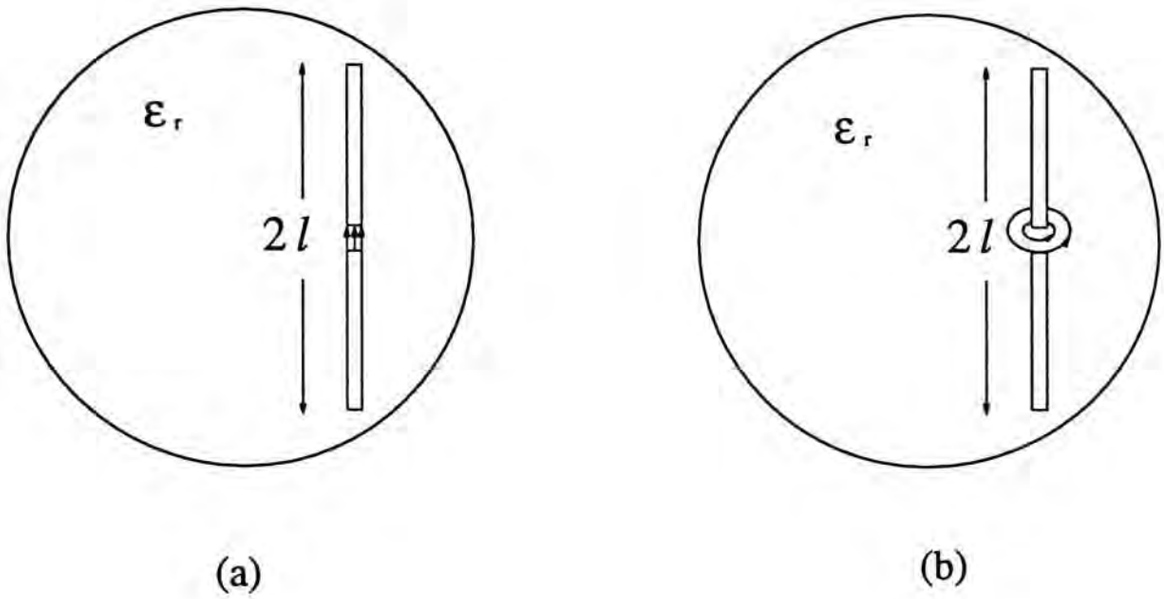

(a) (b)

Fig. 2-2 Equivalent geometry by using equivalence principle and image theory
(a) Delta gap source model (b) magnetic frill source model

The input impedance of the original problem is then equal to one half of that of the new problem [22]. In the magnetic frill source model, the electric field on the coaxial aperture is assumed to be a TEM mode, with the equivalent magnetic frill current given by :

$$\overrightarrow{M_s}(\rho) = -\frac{V}{\rho \ln(r_2/r_1)}\,\hat{\phi} \qquad r_1 \le \rho \le r_2 \qquad (2-1)$$

where V is the aperture voltage.

In the following formulation, $\vec{r}(r, \theta, \phi)$ refers to the field point and $\vec{r}'(r', \theta', \phi')$ refers to the source point, and an $e^{j\omega t}$ dependence is assumed for the fields and therefore suppressed throughout. The $\hat{z}$-directed current is first resolved into $\hat{\theta}$- and $\hat{r}$-directed components as shown in Fig.2-3 :

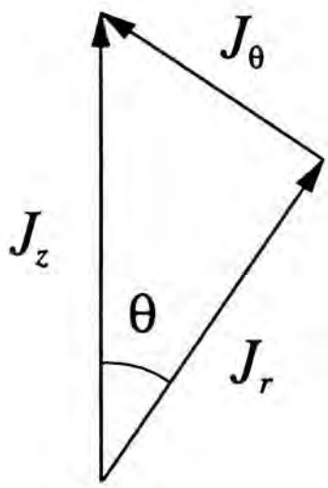

Fig. 2-3 The $\hat{z}$-directed current resolved into $\hat{\theta}$- and $\hat{r}$-directed components

Mathematically, we have :

$$J_z(\vec{r}')\hat{z} = J_r(\vec{r}')\hat{r} + J_\theta(\vec{r}')\hat{\theta} \tag{2-2}$$

where

$$J_r(\vec{r}') = J_z(\vec{r}')\cos\theta' \tag{2-3a}$$

$$J_\theta(\vec{r}') = -J_z(\vec{r}')\sin\theta' \tag{2-3b}$$

The electric potential F_r and magnetic potential A_r of the resolved point currents J_r and J_θ can be found easily. Once the potentials are obtained, the various field components due to the $\hat{z}$-directed current are evaluated using the following equations [32]:

$$E_r = \frac{1}{j\omega\varepsilon\mu_o}\left(\frac{\partial^2}{\partial r^2}+k^2\right)A_r \tag{2-4a}$$

$$E_\theta = \frac{-1}{\varepsilon r\sin\theta}\cdot\frac{\partial F_r}{\partial\phi}+\frac{1}{j\omega\varepsilon\mu_o r}\cdot\frac{\partial^2 A_r}{\partial r\partial\theta} \tag{2-4b}$$

$$E_\phi = \frac{1}{\varepsilon r}\cdot\frac{\partial F_r}{\partial\theta}+\frac{1}{j\omega\varepsilon\mu_o r\sin\theta}\cdot\frac{\partial^2 A_r}{\partial r\partial\phi} \tag{2-4c}$$

$$H_r = \frac{1}{j\omega\varepsilon\mu_o}\left(\frac{\partial^2}{\partial r^2}+k^2\right)F_r \tag{2-4d}$$

$$H_\theta = \frac{1}{\mu_o r\sin\theta}\cdot\frac{\partial A_r}{\partial\phi}+\frac{1}{j\omega\varepsilon\mu_o r}\cdot\frac{\partial^2 F_r}{\partial r\partial\theta} \tag{2-4e}$$

$$H_\phi = \frac{-1}{\mu_o r}\cdot\frac{\partial A_r}{\partial\theta}+\frac{1}{j\omega\varepsilon\mu_o r\sin\theta}\cdot\frac{\partial^2 F_r}{\partial r\partial\phi} \tag{2-4f}$$

Note that when A_r=0 (i.e. only F_r exists), equation (2-4) gives the fields of TE to r mode. Similarly, when F_r=0, fields of TM to r mode will result. It should be mentioned that a $\hat{\theta}$-directed current will excite both TE and TM to r modes of the spherical dielectric resonator while an $\hat{r}$-directed current can excite only TM to r modes. Therefore two potential functions, $G_{J_\theta}^{A_r}$ and $G_{J_\theta}^{F_r}$, are required to represent all the possible fields excited by a $\hat{\theta}$-directed current, but one potential function $G_{J_r}^{A_r}$ alone is sufficient for an $\hat{r}$-directed one. The Green's functions $G_{J_\theta}^{A_r}$ and $G_{J_\theta}^{F_r}$ denote, respectively, the electric potential and the magnetic potential due to a $\hat{\theta}$-directed point current, while the Green's function $G_{J_r}^{A_r}$ denotes the electric potential due to

an $\hat{r}$-directed one. To begin with, the potentials are represented as sums of particular and homogeneous solutions as discussed in Section 2.1. In the following presentation, subscripts p and h are used to denote, respectively, the particular solution and the homogeneous solution.

(A) Derivation of $G_{J_\theta}^{F_r}$ and $G_{J_\theta}^{A_r}$

For $G_{J_\theta}^{F_r}$, we write :

Particular solution

$$G_{J_\theta}^{F_{rp}} = \sum_{n=0}^{\infty} \sum_{m=-n}^{n} A_{nm} P_n^m(\cos\theta) e^{jm\phi} \cdot \begin{cases} \hat{J}_n(kr') \hat{H}_n^{(2)}(kr) & r > r' \\ \hat{H}_n^{(2)}(kr') \hat{J}_n(kr) & r < r' \end{cases} \tag{2-5a}$$

Homogeneous solution

$$G_{J_\theta}^{F_{rh}} = \sum_{n=0}^{\infty} \sum_{m=-n}^{n} P_n^m(\cos\theta) e^{jm\phi} \cdot \begin{cases} B_{nm} \hat{J}_n(kr) & r \le a \\ C_{nm} \hat{H}_n^{(2)}(k_o r) & r \ge a \end{cases} \tag{2-5b}$$

For $G_{J_\theta}^{A_r}$, we write :

Particular solution

$$G_{J_\theta}^{A_{rp}} = \sum_{n=0}^{\infty} \sum_{m=-n}^{n} D_{nm} P_n^m(\cos\theta) e^{jm\phi} \cdot \begin{cases} \hat{J}_n'(kr') \hat{H}_n^{(2)}(kr) & r > r' \\ \hat{H}_n^{(2)\prime}(kr') \hat{J}_n(kr) & r < r' \end{cases} \tag{2-5c}$$

Homogeneous solution

$$G_{J_\theta}^{A_{rh}} = \sum_{n=0}^{\infty} \sum_{m=-n}^{n} P_n^m(\cos\theta) e^{jm\phi} \cdot \begin{cases} E_{nm} \hat{J}_n(kr) & r \le a \\ F_{nm} \hat{H}_n^{(2)}(k_o r) & r \ge a \end{cases} \tag{2-5d}$$

where

$$k_o = \omega\sqrt{\varepsilon_o \mu_o} \tag{2-5e}$$

$$k = \omega\sqrt{\varepsilon\mu_o} \tag{2-5f}$$

$$\varepsilon = \varepsilon_r\varepsilon_o \tag{2-5g}$$

and the coefficients A_{nm} , B_{nm} , C_{nm} , D_{nm} , E_{nm} and F_{nm} are constants to be determined. $P_n^m(x)$ is the associated Legendre function of the first kind with order m and degree n, and $\hat{J}_n(x)$ and $\hat{H}_n^{(2)}(x)$ are, respectively, spherical Bessel function of the first kind (Schelkunoff type [32, pp.268]) and spherical Hankel function (Schelkunoff type) of the second kind, both of order n. All other symbols have the usual meanings.

(a) Particular Solutions

The particular solutions are considered first. The coefficients A_{nm} and D_{nm} are solved by matching the boundary conditions at the source point (i.e. E_θ, E_ϕ, and H_θ are continuous at $\vec{r} = \vec{r}'$ where H_ϕ is discontinuous by a surface electric current $J_{\theta s}$). It is easy to verify that (2-5a)-(2-5d) have already satisfied the boundary conditions for both E_θ and E_ϕ. The boundary conditions for H_θ and H_ϕ are now enforced.

(i) Boundary Condition for H_ϕ at $\vec{r} = \vec{r}'$

Using the fact that H_ϕ is discontinuous by a surface current $J_{\theta s}$ at $\vec{r} = \vec{r}'$, we have:

$$H_\phi^+ - H_\phi^- = -J_{\theta s} \tag{2-6}$$

where the superscripts '+' and '–' correspond to, respectively, the fields at $r = r' + \delta$ and $r = r' - \delta$, and δ is positive and vanishingly small. Starting from (2-5) and using (2-4), we get the following equation after simplification:

$$\frac{-j}{\mu_o r'}\sum_{n=1}^{\infty}\sum_{m=-n}^{n} D_{nm}\frac{d}{d\theta}P_n^m(\cos\theta)\,e^{jm\phi}+\frac{k}{j\omega\mu_o\varepsilon r'\sin\theta}\sum_{n=1}^{\infty}\sum_{m=-n}^{n} m\,A_{nm}\,P_n^m(\cos\theta)\,e^{jm\phi}=-J_{\theta s}$$

(2-7)

In deriving (2-7), we have used the Wronskian of the spherical Bessel's equation:

$$\hat{J}_n'(kr')\,\hat{H}_n^{(2)}(kr')-\hat{J}_n(kr')\,\hat{H}_n^{(2)\prime}(kr')=j \tag{2-8}$$

Summation over the index m is first eliminated by using the orthogonal relationship for the trigonometric functions :

$$\int_0^{2\pi} e^{jp\phi}\cdot e^{jm\phi}d\phi=\begin{cases}2\pi & p=-m\\ 0 & p\neq -m\end{cases} \tag{2-9}$$

Equation (2-7) then becomes :

$$\sum_{n=1}^{\infty} D_{nm}\frac{d}{d\theta}P_n^m(\cos\theta)+\frac{k}{\omega\varepsilon}\cdot\frac{m}{\sin\theta}\sum_{n=1}^{\infty} A_{nm}\,P_n^m(\cos\theta)=\frac{-j\mu_o r'}{2\pi}\int_0^{2\pi} J_{\theta s}\,e^{-jm\phi}d\phi \tag{2-10}$$

(ii) Boundary Condition for H_θ at $\vec{r}=\vec{r}'$

Since H_θ is continuous at $\vec{r}=\vec{r}'$, we have:

$$H_\theta^+-H_\theta^-=0 \tag{2-11}$$

Starting from (2-5) and using (2-4), the following equation is obtained after simplification :

$$\frac{1}{\mu_o r'\sin\theta}\sum_{n=1}^{\infty}\sum_{m=-n}^{n} m\,D_{nm}P_n^m(\cos\theta)\,e^{jm\phi}+\frac{k}{\omega\mu_o\varepsilon r'}\sum_{n=1}^{\infty}\sum_{m=-n}^{n} A_{nm}\frac{d}{d\theta}P_n^m(\cos\theta)\,e^{jm\phi}=0$$

(2-12)

Eliminating the summation over the index m (using (2-9)), we obtain :

$$\frac{m}{\sin\theta}\sum_{n=1}^{\infty} D_{nm}P_n^m(\cos\theta)+\frac{k}{\omega\varepsilon}\sum_{n=1}^{\infty} A_{nm}\frac{d}{d\theta}P_n^m(\cos\theta)=0 \tag{2-13}$$

The coefficients A_{nm} and D_{nm} are solved from the two coupled equations (2-10) and (2-13). To solve for the unknown coefficient A_{nm}, we first multiply (2-10) by $(mP_r^m(\cos\theta)/\sin\theta)$ and (2-13) by $(dP_r^m(\cos\theta)/d\theta)$ and then add the two equations together. This gives the following equation:

$$\frac{m}{\sin\theta}\sum_{n=1}^{\infty} D_{nm}\left[P_r^m\frac{d}{d\theta}P_n^m+P_n^m\frac{d}{d\theta}P_r^m\right]+\frac{k}{\omega\varepsilon}\sum_{n=1}^{\infty} A_{nm}\left[\frac{d}{d\theta}P_n^m\frac{d}{d\theta}P_r^m+\frac{m^2}{\sin^2\theta}P_n^m P_r^m\right]$$

$$=\frac{-j\mu_o r'}{2\pi}\cdot\frac{m}{\sin\theta}\cdot P_r^m\int_0^{2\pi} J_{\theta s}e^{-jm\phi}d\phi \qquad (2\text{-}14)$$

where $P_n^m = P_n^m(\cos\theta)$.

Finally by using the orthogonal relationship for the associated Legendre functions [33, pp. 417]

$$\int_o^{\pi}\left(\frac{d}{d\theta}P_n^m\frac{d}{d\theta}P_r^m+\frac{m^2}{\sin^2\theta}P_n^m P_r^m\right)\sin\theta\ d\theta=\begin{cases}\dfrac{2}{2n+1}\cdot\dfrac{(n+m)!}{(n-m)!}\cdot n(n+1) & n=r\\ 0 & n\neq r\end{cases} \qquad (2\text{-}15)$$

and the following mathematical identity (Appendix A)

$$m\int_0^{\pi}\left[P_n^m\frac{d}{d\theta}P_r^m+\frac{d}{d\theta}P_n^m\ P_r^m\right]d\theta=0 \quad \forall \text{ integers } m,\ n \text{ and } r. \qquad (2\text{-}16)$$

the coefficient A_{nm} can be found:

$$A_{nm}=\frac{-jkr'}{4\pi\omega}\cdot\frac{2n+1}{n(n+1)}\cdot\frac{(n-m)!}{(n+m)!}\cdot m\int_{\theta=0}^{\pi}\int_{\phi=0}^{2\pi} J_{\theta s}\,P_n^m(\cos\theta)e^{-jm\phi}\ d\phi d\theta \qquad (2\text{-}17)$$

The coefficient D_{nm} is solved similarly by first multiply (2-10) by $(dP_r^m(\cos\theta)/d\theta)$ and (2-13) by $(mP_r^m(\cos\theta)/\sin\theta)$ and then add the results together. The result is shown as follows:

$$\frac{k}{\omega\varepsilon\sin\theta}\sum_{n=1}^{\infty}A_{nm}\left[P_r^m\frac{d}{d\theta}P_n^m+P_n^m\frac{d}{d\theta}P_r^m\right]+\sum_{n=1}^{\infty}D_{nm}\left[\frac{d}{d\theta}P_n^m\frac{d}{d\theta}P_r^m+\frac{m^2}{\sin^2\theta}P_n^m P_r^m\right]$$

$$=\frac{-j\mu_o r'}{2\pi}\cdot\frac{d}{d\theta}P_r^m\int_0^{2\pi}J_{\theta s}e^{-jm\phi}d\phi \qquad (2\text{-}18)$$

Using the orthogonal relationship for the associated Legendre functions (2-15) and the mathematical identity (2-16), we obtain D_{nm} as follows:

$$D_{nm}=\frac{-j\mu_o r'}{4\pi}\cdot\frac{2n+1}{n(n+1)}\cdot\frac{(n-m)!}{(n+m)!}\int_{\theta=0}^{\pi}\int_{\phi=0}^{2\pi}J_{\theta s}\sin\theta\frac{d}{d\theta}P_n^m(\cos\theta)e^{-jm\phi}\,d\phi d\theta \qquad (2\text{-}19)$$

For a (surface) point current $J_{\theta s}$ located at (r', θ', ϕ'), we write :

$$J_{\theta s}=\frac{\delta(\theta-\theta')\,\delta(\phi-\phi')}{r'^2\sin\theta} \qquad (2\text{-}20)$$

Substituting (2-17), (2-19) and (2-20) into (2-5), we have the following particular solutions for the potential Green's functions:

$$G_{J_\theta}^{F_{rp}}=\frac{1}{r'\sin\theta'}\sum_{n=1}^{\infty}\sum_{m=1}^{n}a_{nm}P_n^m(\cos\theta')P_n^m(\cos\theta)\sin m(\phi-\phi')\cdot\begin{cases}\hat{J}_n(kr')\hat{H}_n^{(2)}(kr) & r>r'\\ \hat{H}_n^{(2)}(kr')\hat{J}_n(kr) & r<r'\end{cases} \qquad (2\text{-}21a)$$

$$G_{J_\theta}^{A_{rp}}=\frac{1}{r'}\sum_{n=1}^{\infty}\sum_{m=0}^{n}d_{nm}\frac{d}{d\theta'}P_n^m(\cos\theta')P_n^m(\cos\theta)\cos m(\phi-\phi')\cdot\begin{cases}\hat{J}_n'(kr')\hat{H}_n^{(2)}(kr) & r>r'\\ \hat{H}_n^{(2)\prime}(kr')\hat{J}_n(kr) & r<r'\end{cases} \qquad (2\text{-}21b)$$

where
$$a_{nm}=\frac{k}{2\pi\omega}\cdot\frac{2n+1}{n(n+1)}\cdot\frac{(n-m)!}{(n+m)!}\cdot m \qquad (2\text{-}21c)$$

$$d_{nm}=\frac{-j\mu_o}{\Delta_m 2\pi}\cdot\frac{2n+1}{n(n+1)}\cdot\frac{(n-m)!}{(n+m)!} \qquad (2\text{-}21d)$$

$$\Delta_m=\begin{cases}1 & \text{for } m>0\\ 2 & \text{for } m=0\end{cases} \qquad (2\text{-}21e)$$

(b) Homogeneous Solutions

The homogeneous solutions for the potential Green's functions are obtained in a similar fashion, only that the boundary conditions are matched at the spherical surface of the DR (i.e. E_θ, E_ϕ, H_θ and H_ϕ are continuous at $r = a$).

(i) Boundary Condition for E_θ at $r = a$

E_θ is continuous on the surface $r = a$, and therefore

$$E_\theta^+ = E_\theta^- \tag{2-22}$$

where the superscripts '+' and '–' now correspond to, respectively, the fields at $r = a + \delta$ and $r = a - \delta$, and δ is positive and vanishingly small.

Starting from (2-5) and using (2-4), we have:

$$\frac{-1}{\varepsilon \sin\theta} \sum_{n=1}^{\infty} \sum_{m=-n}^{n} m \left[A_{nm} \hat{J}_n(kr') \hat{H}_n(ka) + B_{nm} \hat{J}_n(ka)\right] P_n^m(\cos\theta)\, e^{jm\phi}$$

$$+ \frac{\omega}{jk} \sum_{n=1}^{\infty} \sum_{m=-n}^{n} \left[D_{nm} \hat{J}_n'(kr') \hat{H}_n'(ka) + E_{nm} \hat{J}_n'(ka)\right] \frac{d}{d\theta} P_n^m(\cos\theta)\, e^{jm\phi}$$

$$= \frac{-1}{\varepsilon_o \sin\theta} \sum_{n=1}^{\infty} \sum_{m=-n}^{n} m\, C_{nm} \hat{H}_n(k_o a) P_n^m(\cos\theta)\, e^{jm\phi}$$

$$+ \frac{\omega}{jk_o} \sum_{n=1}^{\infty} \sum_{m=-n}^{n} F_{nm} \hat{H}_n'(k_o a) \frac{d}{d\theta} P_n^m(\cos\theta)\, e^{jm\phi} \tag{2-23}$$

After eliminating the summation over the index m (using (2-9)), we get

$$\frac{-m}{\sin\theta} \sum_{n=1}^{\infty} \Lambda_{nm} P_n^m(\cos\theta) - j\omega \sum_{n=1}^{\infty} \Omega_{nm} \frac{d}{d\theta} P_n^m(\cos\theta) = 0 \tag{2-24}$$

where

$$\Lambda_{nm} = \frac{A_{nm}}{\varepsilon} \hat{J}_n(kr') \hat{H}_n(ka) + \frac{B_{nm}}{\varepsilon} \hat{J}_n(ka) - \frac{C_{nm}}{\varepsilon_o} \hat{H}_n(k_o a) \tag{2-25a}$$

$$\Omega_{nm} = \frac{D_{nm}}{k} \hat{J}_n'(kr') \hat{H}_n'(ka) + \frac{E_{nm}}{k} \hat{J}_n'(ka) - \frac{F_{nm}}{k_o} \hat{H}_n'(k_o a) \tag{2-25b}$$

(ii) Boundary Condition for E_ϕ at $r = a$

E_ϕ continuous on the surface $r = a$, and therefore

$$E_\phi^+ = E_\phi^- \tag{2-26}$$

Starting from (2-5) and using (2-4), we have:

$$\frac{1}{\varepsilon}\sum_{n=1}^{\infty}\sum_{m=-n}^{n}[A_{nm}\hat{J}_n(kr')\hat{H}_n(ka)+B_{nm}\hat{J}_n(ka)]\frac{d}{d\theta}P_n^m(\cos\theta)\,e^{jm\phi}$$

$$-\frac{\omega}{jk\sin\theta}\sum_{n=1}^{\infty}\sum_{m=-n}^{n}m\,[D_{nm}\hat{J}_n'(kr')\hat{H}_n'(ka)+E_{nm}\hat{J}_n'(ka)]\,P_n^m(\cos\theta)\,e^{jm\phi}$$

$$=\frac{1}{\varepsilon_o}\sum_{n=1}^{\infty}\sum_{m=-n}^{n}C_{nm}\hat{H}_n(k_oa)\frac{d}{d\theta}P_n^m(\cos\theta)\,e^{jm\phi}$$

$$-\frac{\omega}{jk_o\sin\theta}\sum_{n=1}^{\infty}\sum_{m=-n}^{n}m\,F_{nm}\hat{H}_n'(k_oa)P_n^m(\cos\theta)\,e^{jm\phi} \tag{2-27}$$

The summation over the index m is eliminated using (2-9) and the above equation is simplified to

$$\sum_{n=1}^{\infty}\Lambda_{nm}\frac{d}{d\theta}P_n^m(\cos\theta)-\frac{\omega m}{j\sin\theta}\sum_{n=1}^{\infty}\Omega_{nm}\,P_n^m(\cos\theta)=0 \tag{2-28}$$

where Λ_{nm} and Ω_{nm} are give by (2-25a) and (2-25b), respectively. Now the unknowns Λ_{nm} and Ω_{nm} are solved through the coupled equations (2-24) and (2-28). The procedure is similar to that used in solving the particular solutions, and therefore it is not repeated. After solving the equations (2-24) and (2-28), we obtain Λ_{nm} = 0 and Ω_{nm} = 0, or equivalently,

$$\frac{A_{nm}}{\varepsilon}\hat{J}_n(kr')\hat{H}_n(ka)+\frac{B_{nm}}{\varepsilon}\hat{J}_n(ka)-\frac{C_{nm}}{\varepsilon_o}\hat{H}_n(k_oa)=0 \tag{2-29}$$

$$\frac{D_{nm}}{k}\hat{J}_n'(kr')\hat{H}_n'(ka)+\frac{E_{nm}}{k}\hat{J}_n'(ka)-\frac{F_{nm}}{k_o}\hat{H}_n'(k_oa)=0 \tag{2-30}$$

(iii) Boundary Conditions for H_θ at $r = a$

H_θ is continuous on the surface $r = a$, and therefore

$$H_\theta^+ = H_\theta^- \tag{2-31}$$

Starting from (2-5) and using (2-4), we have:

$$\frac{-1}{\mu_o \sin\theta} \sum_{n=1}^{\infty} \sum_{m=-n}^{n} m \left[D_{nm} \hat{J}_n'(kr') \hat{H}_n(ka) + E_{nm} \hat{J}_n(ka)\right] P_n^m(\cos\theta)\, e^{jm\phi}$$

$$-\frac{j\omega}{k} \sum_{n=1}^{\infty} \sum_{m=-n}^{n} \left[A_{nm} \hat{J}_n(kr') \hat{H}_n'(ka) + B_{nm} \hat{J}_n'(ka)\right] \frac{d}{d\theta} P_n^m(\cos\theta)\, e^{jm\phi}$$

$$= \frac{-1}{\mu_o \sin\theta} \sum_{n=1}^{\infty} \sum_{m=-n}^{n} m\, F_{nm} \hat{H}_n(k_o a)\, P_n^m(\cos\theta)\, e^{jm\phi}$$

$$-\frac{j\omega}{k_o} \sum_{n=1}^{\infty} \sum_{m=-n}^{n} C_{nm} \hat{H}_n'(k_o a) \frac{d}{d\theta} P_n^m(\cos\theta)\, e^{jm\phi} \tag{2-32}$$

Eliminating the summation over the index m (using (2-9)), we have, after simplification,

$$\frac{m}{\mu_o \sin\theta} \sum_{n=1}^{\infty} \Gamma_{nm} P_n^m(\cos\theta) + j\omega \sum_{n=1}^{\infty} Z_{nm} \frac{d}{d\theta} P_n^m(\cos\theta) = 0 \tag{2-33}$$

where

$$\Gamma_{nm} = D_{nm} \hat{J}_n'(kr') \hat{H}_n(ka) + E_{nm} \hat{J}_n(ka) - F_{nm} \hat{H}_n(k_o a) \tag{2-34a}$$

$$Z_{nm} = \frac{A_{nm}}{k} \hat{J}_n(kr') \hat{H}_n'(ka) + \frac{B_{nm}}{k} \hat{J}_n'(ka) - \frac{C_{nm}}{k_o} \hat{H}_n'(k_o a) \tag{2-34b}$$

(iv) Boundary Condition for H_ϕ at $r = a$

H_ϕ is continuous on the surface $r = a$, and therefore

$$H_\phi^+ = H_\phi^- \tag{2-35}$$

Starting from (2-5) and using (2-4), we have:

$$\frac{1}{\mu_o}\sum_{n=1}^{\infty}\sum_{m=-n}^{n}\left[D_{nm}\hat{J}_n'(kr')\hat{H}_n(ka)+E_{nm}\hat{J}_n(ka)\right]\frac{d}{d\theta}P_n^m(\cos\theta)\,e^{jm\phi}$$

$$+\frac{j\omega}{k\sin\theta}\sum_{n=1}^{\infty}\sum_{m=-n}^{n} m\left[A_{nm}\hat{J}_n(kr')\hat{H}_n'(ka)+B_{nm}\hat{J}_n'(ka)\right]P_n^m(\cos\theta)\,e^{jm\phi}$$

$$=\frac{1}{\mu_o}\sum_{n=1}^{\infty}\sum_{m=-n}^{n}F_{nm}\hat{H}_n(k_o a)\frac{d}{d\theta}P_n^m(\cos\theta)\,e^{jm\phi}$$

$$+\frac{j\omega}{k_o\sin\theta}\sum_{n=1}^{\infty}\sum_{m=-n}^{n} m\,C_{nm}\hat{H}_n'(k_o a)\,P_n^m(\cos\theta)\,e^{jm\phi} \tag{2-36}$$

Eliminating the summation over the index m (using (2-9)), the above equation is simplified to

$$\frac{1}{\mu_o}\sum_{n=1}^{n}\Gamma_{nm}\frac{d}{d\theta}P_n^m(\cos\theta)+\frac{j\omega m}{\sin\theta}\sum_{n=1}^{n}Z_{nm}P_n^m(\cos\theta)=0 \tag{2-37}$$

where Γ_{nm} and Z_{nm} are given in (2-34a) and (2-34b), respectively. The unknowns Γ_{nm} and Z_{nm} are solved from the coupled equations (2-33) and (2-37), and the results are $\Gamma_{nm} = 0$ and $Z_{nm} = 0$, or equivalently,

$$D_{nm}\hat{J}_n'(kr')\hat{H}_n(ka)+E_{nm}\hat{J}_n(ka)-F_{nm}\hat{H}_n(k_o a)=0 \tag{2-38}$$

$$\frac{A_{nm}}{k}\hat{J}_n(kr')\hat{H}_n'(ka)+\frac{B_{nm}}{k}\hat{J}_n'(ka)-\frac{C_{nm}}{k_o}\hat{H}_n'(k_o a)=0 \tag{2-39}$$

Note that A_{nm} and D_{nm} have already been obtained in (2-17) and (2-19), respectively. The unknowns B_{nm} and C_{nm} are solved from the equations (2-29) and (2-39), whereas the unknowns E_{nm} and F_{nm} are solved from the equations (2-30) and (2-38). The results are as follows:

$$B_{nm} = \frac{-A_{nm}}{\Delta_n^{TE}} \left[\hat{H}_n^{(2)}(ka)\hat{H}_n^{(2)\prime}(k_o a) - \frac{k}{k_o}\hat{H}_n^{(2)\prime}(ka)\hat{H}_n^{(2)}(k_o a) \right] \tag{2-40a}$$

$$C_{nm} = -j\frac{k_o}{k} \cdot \frac{A_{nm}}{\Delta_n^{TE}} \tag{2-40b}$$

$$E_{nm} = \frac{-D_{nm}}{\Delta_n^{TM}} \left[\hat{H}_n^{(2)\prime}(ka)\hat{H}_n^{(2)}(k_o a) - \frac{k}{k_o}\hat{H}_n^{(2)}(ka)\hat{H}_n^{(2)\prime}(k_o a) \right] \tag{2-40c}$$

$$F_{nm} = j\frac{D_{nm}}{\Delta_n^{TM}} \tag{2-40d}$$

where

$$\Delta_n^{TE} = \hat{J}_n(ka)\hat{H}_n^{(2)\prime}(k_o a) - \frac{k}{k_o}\hat{J}_n{}'(ka)\hat{H}_n^{(2)}(k_o a) \tag{2-40e}$$

$$\Delta_n^{TM} = \hat{J}_n{}'(ka)\hat{H}_n^{(2)}(k_o a) - \frac{k}{k_o}\hat{J}_n(ka)\hat{H}_n^{(2)\prime}(k_o a) \tag{2-40f}$$

Substituting (2-40) into (2-5), we obtain the homogeneous solutions for the potential Green's functions:

$$G_{J_\theta}^{F_{rh}} = \frac{1}{r'\sin\theta'} \sum_{n=1}^{\infty} \sum_{m=1}^{n} P_n^m(\cos\theta')P_n^m(\cos\theta)\sin m(\phi-\phi')\hat{J}_n(kr') \cdot \begin{cases} b_{nm}\hat{J}_n(kr) & r \le a \\ c_{nm}\hat{H}_n^{(2)}(k_o r) & r \ge a \end{cases} \tag{2-41a}$$

$$G_{J_\theta}^{A_{rh}} = \frac{1}{r'} \sum_{n=1}^{\infty} \sum_{m=0}^{n} \frac{d}{d\theta'} P_n^m(\cos\theta')P_n^m(\cos\theta)\cos m(\phi-\phi')\hat{J}_n{}'(kr') \cdot \begin{cases} e_{nm}\hat{J}_n(kr) & r \le a \\ f_{nm}\hat{H}_n^{(2)}(k_o r) & r \ge a \end{cases} \tag{2-41b}$$

where

$$b_{nm} = \frac{-a_{nm}}{\Delta_n^{TE}} \left[\hat{H}_n^{(2)}(ka)\hat{H}_n^{(2)\prime}(k_o a) - \frac{k}{k_o}\hat{H}_n^{(2)\prime}(ka)\hat{H}_n^{(2)}(k_o a) \right] \tag{2-41c}$$

$$c_{nm} = -j\frac{k_o}{k} \cdot \frac{a_{nm}}{\Delta_n^{TE}} \tag{2-41d}$$

$$e_{nm} = \frac{-d_{nm}}{\Delta_n^{TM}} \left[\hat{H}_n^{(2)\prime}(ka)\hat{H}_n^{(2)}(k_o a) - \frac{k}{k_o}\hat{H}_n^{(2)}(ka)\hat{H}_n^{(2)\prime}(k_o a) \right] \tag{2-41e}$$

$$f_{nm} = j\frac{d_{nm}}{\Delta_n^{TM}} \tag{2-41f}$$

and a_{nm} and d_{nm} are given in (2-21c) and (2-21d), respectively. In (2-40e) and (2-40f), it is worth noting that $\Delta_n^{TE} = 0$ and $\Delta_n^{TM} = 0$ are, respectively, the characteristic equations for TE and TM modes as given in [17]. By solving the characteristic equations, one can predict the resonant frequencies and the Q factors for various TE and TM modes [4].

Finally, the Green's functions $G_{J_\theta}^{F_r}$ and $G_{J_\theta}^{A_r}$ are given by :

$$G_{J_\theta}^{F_r} = G_{J_\theta}^{F_{rp}} + G_{J_\theta}^{F_{rh}} \tag{2-42a}$$

$$G_{J_\theta}^{A_r} = G_{J_\theta}^{A_{rp}} + G_{J_\theta}^{A_{rh}} \tag{2-42b}$$

(B) Derivation of $G_{J_r}^{A_r}$

Following the procedure given in [32, pp. 267-269], the following differential equation for the Green's function $G_{J_r}^{A_{rp}}$ can be derived (Appendix B) :

$$(\nabla^2 + k^2)\frac{G_{J_r}^{A_{rp}}}{r} = -\frac{\mu_o}{r}\cdot\frac{\delta(r-r')\delta(\theta-\theta')\delta(\phi-\phi')}{r^2\sin\theta} \tag{2-43}$$

Equation (2-43) is solved (Appendix C) and the result for the particular solution $G_{J_r}^{A_{rp}}$ is given by:

$$G_{J_r}^{A_{rp}} = \frac{1}{r'^2}\sum_{n=0}^{\infty}\sum_{m=0}^{n} g_{nm}P_n^m(\cos\theta')P_n^m(\cos\theta)\cos m(\phi-\phi')\cdot\begin{cases}\hat{J}_n(kr')\hat{H}_n^{(2)}(kr) & r>r'\\ \hat{H}_n^{(2)}(kr')\hat{J}_n(kr) & r<r'\end{cases} \tag{2-44a}$$

where

$$g_{nm} = \frac{1}{k}n(n+1)d_{nm} \tag{2-44b}$$

and the coefficient d_{nm} is given in (2-21d).

By matching the boundary conditions at the spherical surface of the DR, the homogeneous solution is obtained as follows :

$$G_{J_r}^{A_{rh}} = \frac{1}{r'^2}\sum_{n=0}^{\infty}\sum_{m=0}^{n} P_n^m(\cos\theta')P_n^m(\cos\theta)\cos m(\phi-\phi')\hat{J}_n(kr')\cdot\begin{cases}h_{nm}\hat{J}_n(kr) & r\le a\\ i_{nm}\hat{H}_n^{(2)}(k_o r) & r\ge a\end{cases} \tag{2-45a}$$

where

$$h_{nm} = \frac{1}{k}n(n+1)e_{nm} \tag{2-45b}$$

$$i_{nm} = \frac{1}{k}n(n+1)f_{nm} \tag{2-45c}$$

and e_{nm} and f_{nm} are given in (2-41e) and (2-41f), respectively. The Green's function $G_{J_r}^{A_r}$ is then given by :

$$G_{J_r}^{A_r} = G_{J_r}^{A_{rp}} + G_{J_r}^{A_{rh}} \tag{2-46}$$

(C) Derivation of $G_{J_z}^{E_z}$

Define two dyadic Green's functions :

$$\overline{\overline{G}}_{J_r}^{\vec{E}} = G_{J_r}^{E_r}\,\hat{r}\hat{r} + G_{J_r}^{E_\theta}\,\hat{\theta}\hat{r} + G_{J_r}^{E_\phi}\,\hat{\phi}\hat{r} \tag{2-47a}$$

$$\overline{\overline{G}}_{J_\theta}^{\vec{E}} = G_{J_\theta}^{E_r}\,\hat{r}\hat{\theta} + G_{J_\theta}^{E_\theta}\,\hat{\theta}\hat{\theta} + G_{J_\theta}^{E_\phi}\,\hat{\phi}\hat{\theta} \tag{2-47b}$$

where $G_{J_\alpha}^{E_\beta}$ ($\alpha = r, \theta$ and $\beta = r, \theta, \phi$) is the electric field Green's function derived from $G_{J_r}^{A_r}$, $G_{J_\theta}^{F_r}$ and $G_{J_\theta}^{A_r}$ using (2-4). The total electric field excited by the $\hat{z}$-directed current is then given by :

$$\vec{E} = \int_{S_o}\int \left[\overline{\overline{G}}_{J_r}^{\vec{E}} \cdot (J_r'\hat{r}) + \overline{\overline{G}}_{J_\theta}^{\vec{E}} \cdot (J_\theta'\hat{\theta})\right] dS' \tag{2-48}$$

where S_o is the surface on which the $\hat{z}$-directed current is flowing.

Substitute (2-47) into (2-48), we have :

$$\begin{aligned}\vec{E} &= \int_{S_o}\int \left(G_{J_r}^{E_r} J_r'\,\hat{r} + G_{J_r}^{E_\theta} J_r'\,\hat{\theta} + G_{J_r}^{E_\phi} J_r'\,\hat{\phi}\right) + \left(G_{J_\theta}^{E_r} J_\theta'\,\hat{r} + G_{J_\theta}^{E_\theta} J_\theta'\,\hat{\theta} + G_{J_\theta}^{E_\phi} J_\theta'\,\hat{\phi}\right) dS' \\ &= \int_{S_o}\int \left(G_{J_r}^{E_r} J_r' + G_{J_\theta}^{E_r} J_\theta'\right)\hat{r} + \left(G_{J_r}^{E_\theta} J_r' + G_{J_\theta}^{E_\theta} J_\theta'\right)\hat{\theta} + \left(G_{J_r}^{E_\phi} J_r' + G_{J_\theta}^{E_\phi} J_\theta'\right)\hat{\phi}\; dS'\end{aligned} \tag{2-49}$$

Using the fact that :

$$E_z = E_r \cos\theta - E_\theta \sin\theta \tag{2-50}$$

$$J_r' = J_z' \cos\theta' \tag{2-51a}$$

and

$$J_\theta' = -J_z' \sin\theta' \tag{2-51b}$$

we have :

$$E_z = \int_{S_o}\int \left[\left(G_{J_r}^{E_r} \cos\theta' - G_{J_\theta}^{E_r} \sin\theta' \right) \cos\theta - \left(G_{J_r}^{E_\theta} \cos\theta' - G_{J_\theta}^{E_\theta} \sin\theta' \right) \sin\theta \right] J_z' \, dS'$$

$$= \int_{S_o}\int G_{J_z}^{E_z} J_z' dS' \tag{2-52}$$

where

$$G_{J_z}^{E_z} = \left(G_{J_r}^{E_r} \cos\theta' - G_{J_\theta}^{E_r} \sin\theta' \right) \cos\theta - \left(G_{J_r}^{E_\theta} \cos\theta' - G_{J_\theta}^{E_\theta} \sin\theta' \right) \sin\theta \tag{2-53}$$

is the desired Green's function for the evaluation of the input impedance. After simplification, we get ($r \le a$) :

$$G_{J_z}^{E_z} = G_P + G_H \tag{2-54a}$$

where

$$G_P = \frac{\omega}{jk^2} \frac{\cos\theta \cos\theta'}{r^2 r'^2} \sum_{n=1}^{\infty} \sum_{m=0}^{n} n(n+1) g_{nm} P_n^m(\cos\theta') P_n^m(\cos\theta) \cos m(\phi - \phi') \Phi_n(kr') \Psi_n(kr)$$

$$- \frac{\omega}{jk} \frac{\sin\theta' \cos\theta}{r^2 r'} \sum_{n=1}^{\infty} \sum_{m=0}^{n} g_{nm} \frac{d}{d\theta'} P_n^m(\cos\theta') P_n^m(\cos\theta) \cos m(\phi - \phi') \Phi_n'(kr') \Psi_n(kr)$$

$$- \frac{\omega}{jk} \frac{\cos\theta' \sin\theta}{r r'^2} \sum_{n=1}^{\infty} \sum_{m=0}^{n} g_{nm} P_n^m(\cos\theta') \frac{d}{d\theta} P_n^m(\cos\theta) \cos m(\phi - \phi') \Phi_n(kr') \Psi_n'(kr)$$

$$- \frac{1}{\varepsilon} \frac{1}{r r'} \sum_{n=1}^{\infty} \sum_{m=1}^{n} m a_{nm} P_n^m(\cos\theta') P_n^m(\cos\theta) \cos m(\phi - \phi') \Phi_n(kr') \Psi_n(kr)$$

$$+ \frac{\omega}{jk} \frac{\sin\theta' \sin\theta}{r r'} \sum_{n=1}^{\infty} \sum_{m=0}^{n} d_{nm} \frac{d}{d\theta'} P_n^m(\cos\theta') \frac{d}{d\theta} P_n^m(\cos\theta) \cos m(\phi - \phi') \Phi_n'(kr') \Psi_n'(kr)$$

(2-54b)

$$G_H = \frac{\omega}{jk^2}\frac{\cos\theta\cos\theta'}{r^2 r'^2}\sum_{n=1}^{\infty}\sum_{m=0}^{n} n(n+1)h_{nm}P_n^m(\cos\theta')P_n^m(\cos\theta)\cos m(\phi-\phi')\hat{J}_n(kr')\hat{J}_n(kr)$$

$$-\frac{\omega}{jk}\frac{\sin\theta'\cos\theta}{r^2 r'}\sum_{n=1}^{\infty}\sum_{m=0}^{n} h_{nm}\frac{d}{d\theta'}P_n^m(\cos\theta')P_n^m(\cos\theta)\cos m(\phi-\phi')\hat{J}_n'(kr')\hat{J}_n(kr)$$

$$-\frac{\omega}{jk}\frac{\cos\theta'\sin\theta}{rr'^2}\sum_{n=1}^{\infty}\sum_{m=0}^{n} h_{nm}P_n^m(\cos\theta')\frac{d}{d\theta}P_n^m(\cos\theta)\cos m(\phi-\phi')\hat{J}_n(kr')\hat{J}_n'(kr)$$

$$-\frac{1}{\varepsilon}\frac{1}{rr'}\sum_{n=1}^{\infty}\sum_{m=1}^{n} mb_{nm}P_n^m(\cos\theta')P_n^m(\cos\theta)\cos m(\phi-\phi')\hat{J}_n(kr')\hat{J}_n(kr)$$

$$+\frac{\omega}{jk}\frac{\sin\theta'\sin\theta}{rr'}\sum_{n=1}^{\infty}\sum_{m=0}^{n} e_{nm}\frac{d}{d\theta'}P_n^m(\cos\theta')\frac{d}{d\theta}P_n^m(\cos\theta)\cos m(\phi-\phi')\hat{J}_n'(kr')\hat{J}_n'(kr) \tag{2-54c}$$

$$\Phi_n(kr') = \begin{cases} \hat{J}_n(kr') & r > r' \\ \hat{H}_n^{(2)}(kr') & r < r' \end{cases} \tag{2-54d}$$

$$\Psi_n(kr) = \begin{cases} \hat{H}_n^{(2)}(kr) & r > r' \\ \hat{J}_n(kr) & r < r' \end{cases} \tag{2-54e}$$

and a_{nm}, b_{nm}, d_{nm}, e_{nm}, g_{nm} and h_{nm} are given in (2-21), (2-41), (2-44) and (2-45). It should be noted that $G_{J_z}^{E_z}$ is reciprocal in $\vec{r}$ and $\vec{r}'$ as expected.

2.3 Single Cavity Mode Approximation

In the previous section, the exact Green's function of the $\hat{z}$-directed electric field due to the $\hat{z}$-directed point current was derived. However, the modal solution involves infinite summations which converge very slowly for G_P (equation (2-54b)). Therefore special technique must be used to avoid the convergence problem. The technique will be discussed in Section 2.4 in detail. In this section, the single mode approximation is taken to simplify the problem. Both the lowest order TE mode (the TE_{111} mode) and the lowest order TM mode (the TM_{101} mode) are considered in this section. It is interesting to note that the radiation patterns of these two modes are basically complementary to each other : the TE_{111} mode is a broadside mode whereas the TM_{101} mode is an end-fire one.

2.3.1 Evaluation of Input Impedance

Using the single mode approximation, the broadside TE_{111} mode Green's function and the end-fire TM_{101} mode Green's function are approximated by G_{111}^{TE} and G_{101}^{TM}, respectively. The single mode Green's functions are given by :

$$G_{111}^{TE} = \frac{-1}{\varepsilon r r'} \sin\theta \sin\theta' \cos(\phi-\phi') \left[a_{11}\Phi_1(kr')\Psi_1(kr) + b_{11}\hat{J}_1(kr')\hat{J}_1(kr) \right] \tag{2-55}$$

$$\begin{aligned} G_{101}^{TM} = {} & \frac{-j2\omega}{k^2 r^2 r'^2} \cos^2\theta \cos^2\theta' \left[g_{10}\Phi_1(kr')\Psi_1(kr) + h_{10}\hat{J}_1(kr')\hat{J}_1(kr) \right] \\ & - \frac{j\omega}{kr^2 r'} \cos^2\theta \sin^2\theta' \left[g_{10}\Phi_1'(kr')\Psi_1(kr) + h_{10}\hat{J}_1'(kr')\hat{J}_1(kr) \right] \\ & - \frac{j\omega}{krr'^2} \sin^2\theta \cos^2\theta' \left[g_{10}\Phi_1(kr')\Psi_1'(kr) + h_{10}\hat{J}_1(kr')\hat{J}_1'(kr) \right] \\ & - \frac{j\omega}{2rr'} \sin^2\theta \sin^2\theta' \left[g_{10}\Phi_1'(kr')\Psi_1'(kr) + h_{10}\hat{J}_1'(kr')\hat{J}_1'(kr) \right] \end{aligned} \tag{2-56}$$

where

$$\Phi_1(kr') = \begin{cases} \hat{J}_1(kr') & r > r' \\ \hat{H}_1^{(2)}(kr') & r < r' \end{cases} \tag{2-57c}$$

$$\Psi_1(kr) = \begin{cases} \hat{H}_1^{(2)}(kr) & r > r' \\ \hat{J}_1(kr) & r < r' \end{cases} \tag{2-57d}$$

$$a_{11} = \frac{3k}{8\pi\omega} \tag{2-57e}$$

$$b_{11} = \frac{-a_{11}}{\Delta_1^{TE}} \left[\hat{H}_1^{(2)}(ka)\hat{H}_1^{(2)\prime}(k_o a) - \frac{k}{k_o}\hat{H}_1^{(2)\prime}(ka)\hat{H}_1^{(2)}(k_o a) \right] \tag{2-67f}$$

$$g_{10} = \frac{-3j\mu}{4\pi k} \tag{2-57g}$$

$$h_{10} = \frac{-g_{10}}{\Delta_1^{TM}} \left[\hat{H}_1^{(2)\prime}(ka)\hat{H}_1^{(2)}(k_o a) - \frac{k}{k_o}\hat{H}_1^{(2)}(ka)\hat{H}_1^{(2)\prime}(k_o a) \right] \tag{2-57h}$$

$$\Delta_1^{TE} = \hat{J}_1(ka)\hat{H}_1^{(2)\prime}(k_o a) - \frac{k}{k_o}\hat{J}_1{}'(ka)\hat{H}_1^{(2)}(k_o a) \tag{2-57i}$$

$$\Delta_1^{TM} = \hat{J}_1{}'(ka)\hat{H}_1^{(2)}(k_o a) - \frac{k}{k_o}\hat{J}_1(ka)\hat{H}_1^{(2)\prime}(k_o a) \tag{2-57j}$$

Note that only one electric potential Green's function $G_{J_\theta}^{F_r}$ contributes to the Green's function G_{111}^{TE}, whereas two magnetic potential Green's functions $G_{J_\theta}^{A_r}$ and $G_{J_r}^{A_r}$ contribute to the Green's function G_{101}^{TM}. Given the Green's function G (G=G_{111}^{TE} or G_{101}^{TM}), we can evaluate the $\hat{z}$-directed electric field E_z due to the $\hat{z}$-directed current J_z as follows:

$$E_z(\vec{r}) = \iint_{S_o} G(\vec{r},\vec{r}')\, J_z(z')\, dS' \tag{2-58}$$

where

$$J_z(z) = J_o \sin k(l - |z|) \qquad -l \le z \le l \tag{2-59}$$

is the assumed surface current [34, pp. 264] flowing on the dipole surface S_o.

The input impedance is then determined using the variational formula :

$$Z_{in} = \frac{-1}{I_z^2(0)} \iint_{S_o} E_z(\vec{r})\, J_z(z)\, dS$$

$$= \frac{-1}{I_z^2(0)} \iint_{S_o} \iint_{S_o} J_z(z)\, G(\vec{r},\vec{r}')\, J_z(z')\, dS'\, dS \tag{2-60}$$

where

$$I_z(z) = 2\pi r_1\, J_z(z) \tag{2-61}$$

is a valid assumption for the small probe radius r_1. It should be mentioned that the input impedance obtained by (2-60) is correct to the second order for an assumed current distribution J_z correct to the first order [34, pp. 260-261]. Note that Z_{in} obtained from (2-60) is the input impedance of a dipole embedded in the spherical DR antenna. To obtain the input impedance of the original configuration of a probe-fed hemispherical DR antenna, one has to divide Z_{in} by two.

2.3.2 Measured and Computed Results

(A) Experimental Set-up

The calculated TE_{111} mode input impedance using the present theory is conveniently compared with a previous measurement made by McAllister and Long [4]. The DR used had a radius of 2.54 cm, with ε_r=8.9, and the probe of length 1.52 cm penetrated the DR with an offset 1.74 cm. For the TM_{101} mode, an experiment has been carried out with the experimental set-up shown in Appendix F. In the experiment, a DR with ε_r = 9.8 and radius 11.5 mm is used. The DR is mounted on a 60 cm by 60 cm copper ground plane and probed by a Radiall coaxial launcher with diameter 1.25 mm, penetrating 4.5 mm into the dielectric. Measurements are taken with an HP8510C network analyzer. Port extension was used to set the reference plane at the point of penetration into the DR.

(B) The Broadside TE_{111} Mode

The calculated TE_{111} mode input impedance and the measurement made by McAllister and Long are shown in Fig.2-4. From the theory, the resonance frequency is 1.88 GHz, which is very close to the theoretical value of 1.89 GHz as obtained by solving the TE mode characteristic equation Δ_1^{TE}=0. Moreover, it agrees with the measured value of 1.90 GHz. Measured and predicted bandwidths also match reasonably well at 10.3 % and 13.1 % respectively.

Fig.2-5 shows the variation of the input impedance with frequency for different probe lengths. It is observed that while the input impedance increases significantly with the probe length, the resonant frequency shifts only slightly. This is in contrast to a bare monopole of which the resonant frequency varies significantly with the probe length. This shows that performing impedance matching at a given (resonant) frequency is possible for a DR antenna.

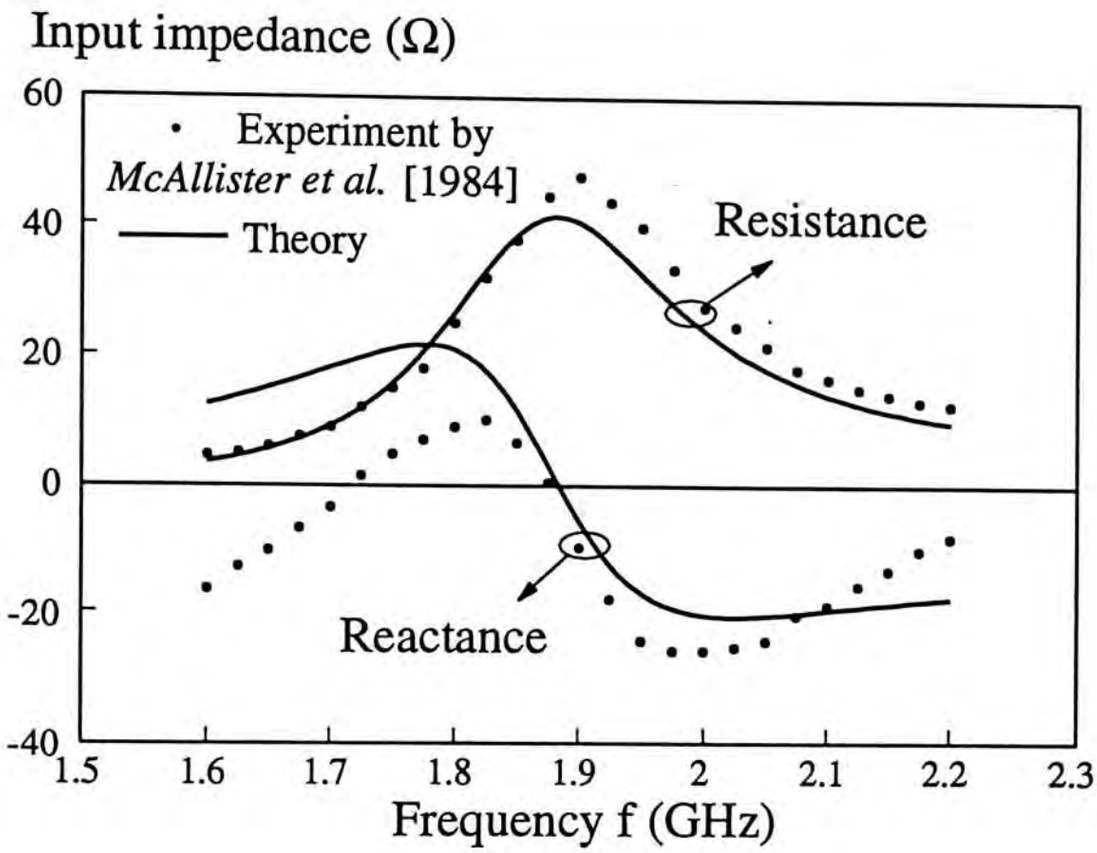

Fig. 2-4 Input impedance of the TE_{111} mode against frequency:

a = 2.54 mm, b = 1.74 mm, l = 1.52 mm,

ε_r = 9.8, r_1 = 0.075 mm

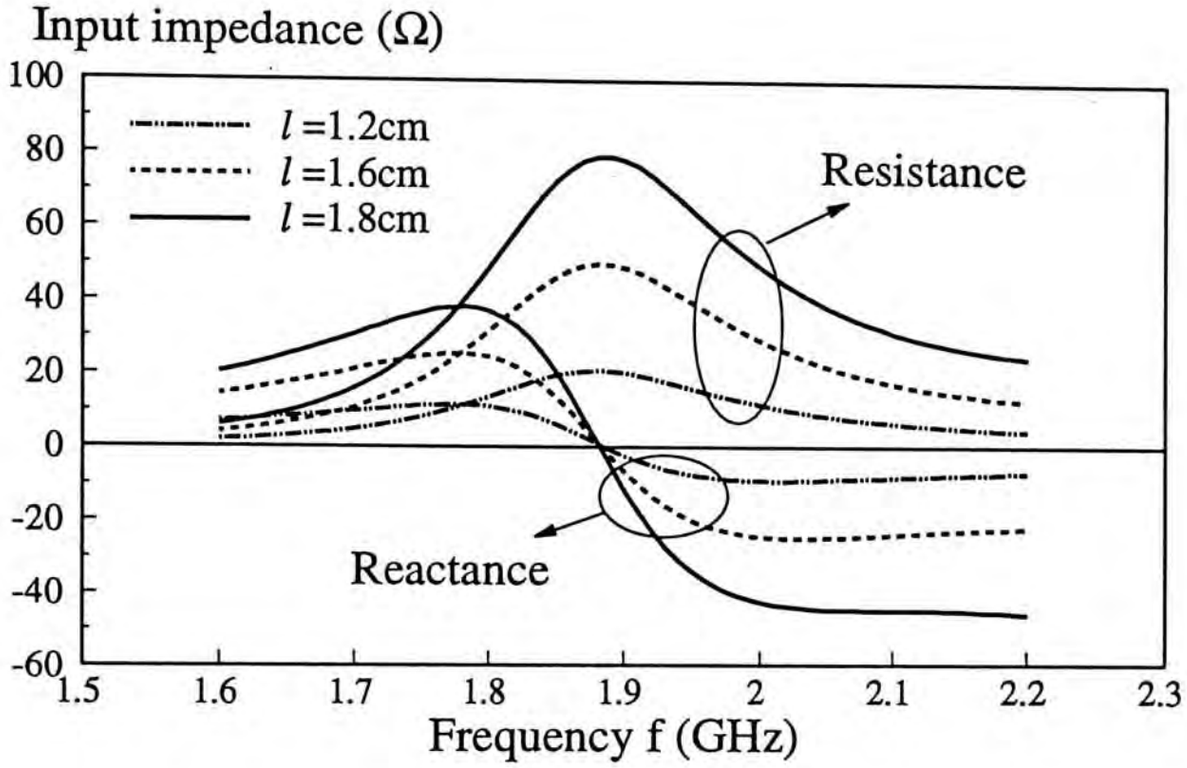

Fig. 2-5 Input impedance of the TE_{111} mode against frequency for different probe lengths: a = 2.54 mm, b = 1.74 mm, l = 1.52 mm, ε_r = 8.9, r_1 = 0.075 mm

The variation of input resistance with the feed position for different probe lengths is shown in Fig.2-6. The input resistance increases as the probe is displaced away from the center of the DR until a maximum point is reached. It then decreases slightly as the displacement is increased further. Therefore, although the probe has small input resistance near the center, it should not be placed too close to the edge for good matching. Furthermore, the input resistance increases with the probe length. From the figure, it is also seen that the TE_{111} mode cannot be excited properly when the feed position is near the center. This is expected because in this case the probe current is dominant by the $\hat{r}$-directed component, which can excite only TM modes.

Fig.2-7(a) shows the resonant input resistance of the TE_{111} mode as a function of ε_r for different probe lengths, whereas Fig.2-7(b) shows the TE_{111} mode resonant frequency $f_{TE_{111}}$ as a function of ε_r. The resonant frequency $f_{TE_{111}}$ is obtained by solving the characteristic equation $\Delta_1^{TE} = 0$. With reference to Fig.2-7(a), the input resistance increases with the dielectric constant. At high ε_r, the input resistance is very high and a lot of energy will be reflected back. This is consistent with the well-known fact that for high dielectric constants, the magnetic wall effect on the dielectric boundary will greatly reduce radiated power from DR antennas. Again, the longer the probe length, the larger the input resistance.

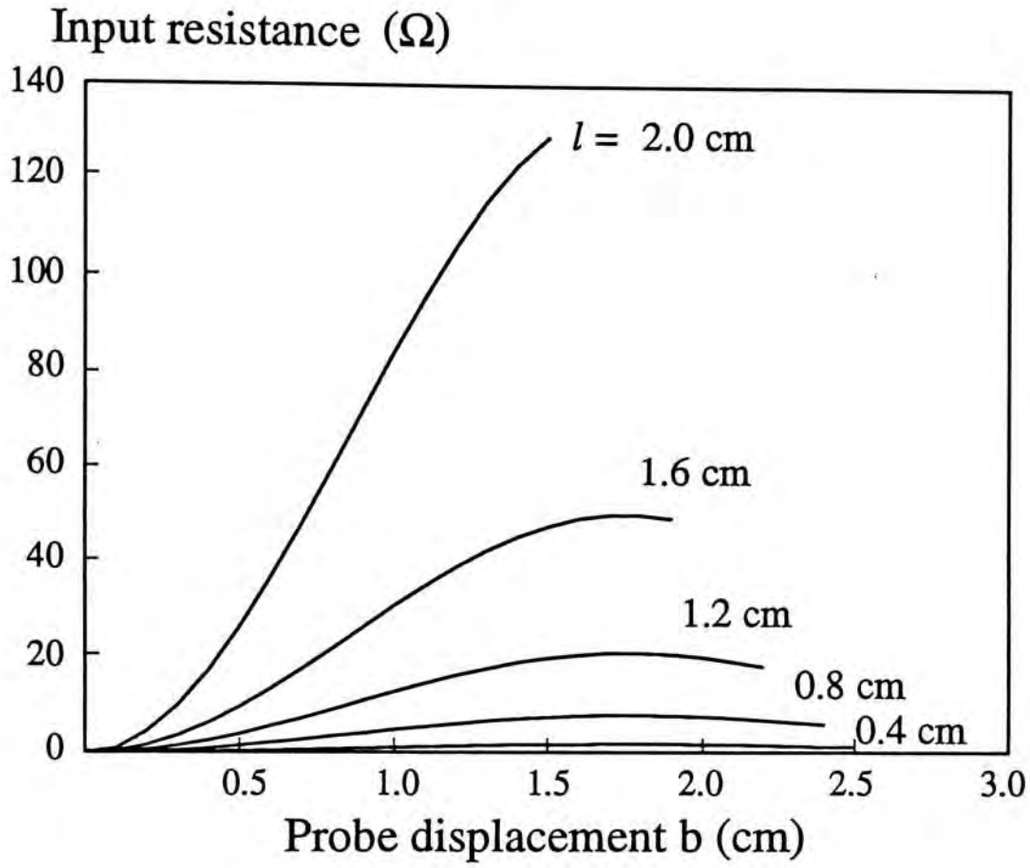

Fig. 2-6 Input impedance of the TE_{111} mode against probe displacement b :

a = 2.54 mm, f = 1.88 GHz, ε_r = 9.8, and r_1 = 0.075 mm

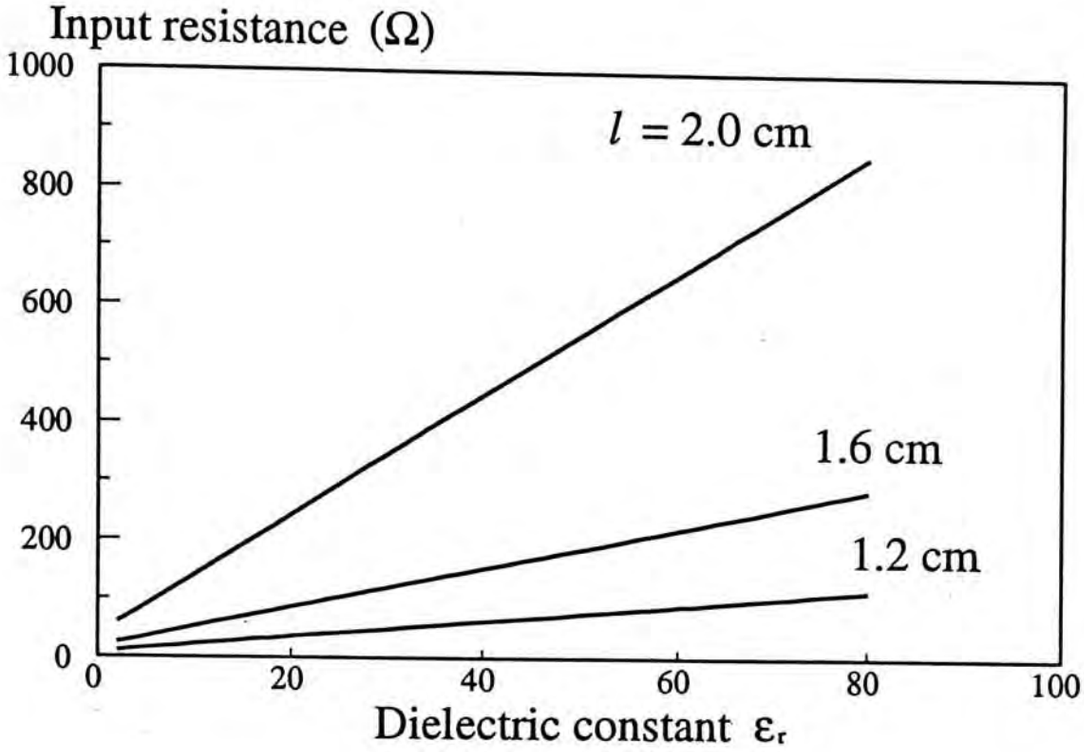

Fig. 2-7(a) Input resistance of the TE_{111} mode at resonance against dielectric constant ε_r for different probe length l : a = 2.54 mm, b = 1.74 mm, $f = f_{TE_{111}}$, r_1 = 0.075 mm

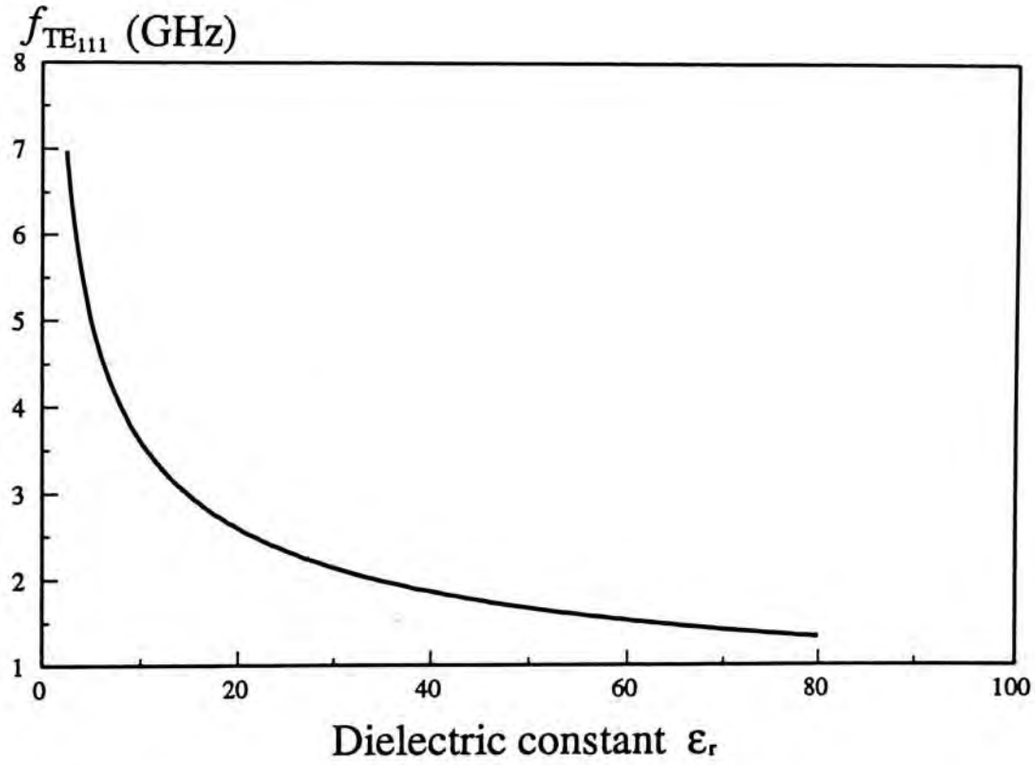

Fig. 2-7(b) TE_{111} mode resonant frequency $f_{TE_{111}}$ against ε_r for a = 12.5 mm

(C) The End-fire TM_{101} Mode

The input impedance as a function of frequency is shown in Fig.2-8. From the theory, the resonant frequency is 5.85 GHz, which is very close to the measured value of 5.95 GHz. In view of the predicted resonant frequency of 5.70 GHz obtained by solving the characteristic equation $\Delta_1^{TM}=0$, the results are quite consistent. A reasonably good match is also observed for the bandwidth (20.4 % measured versus 23.5 % calculated).

Fig.2-9 shows the TM_{101} mode input impedance as a function of frequency for different probe lengths. The input impedance increases for increasing probe length, and the results are similar to the case of the TE_{111} mode.

The effect of the dielectric constant on the input impedance is shown in Fig.2-10(a), while the TM_{101} mode resonant frequency $f_{TM_{101}}$ as a function of dielectric constant ε_r is shown in Fig.2-10(b). The TM_{101} mode resonant frequency $f_{TM_{101}}$ is obtained by solving the characteristic equation $\Delta_1^{TM} = 0$. From Fig.2-10(a), it can be seen that the input resistance increases with the dielectric constant ε_r. Although the size of the antenna can be reduced by using material of high dielectric constant, poor radiation may result if ε_r is too high. Again, the longer the probe length, the larger the input resistance.

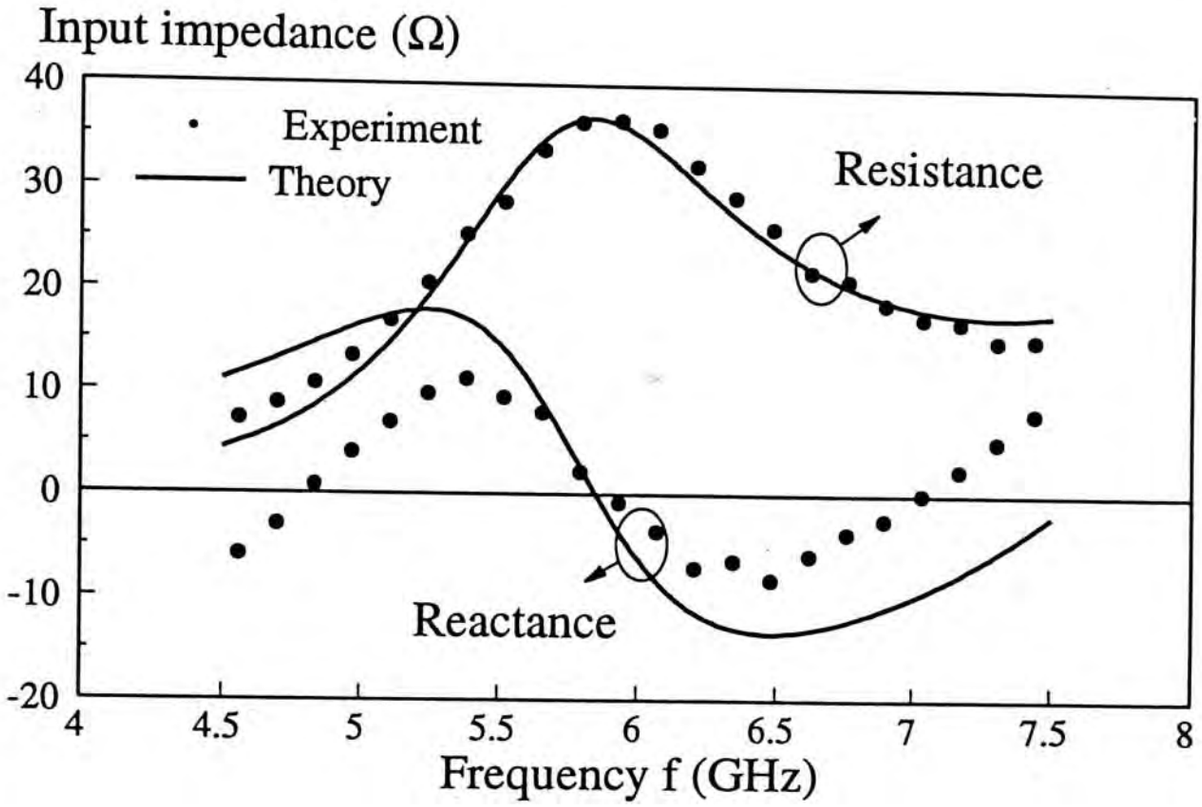

Fig. 2-8 Input impedance of the TM_{101} mode against frequency:

a = 11.5 mm, b = 0.0 mm, l = 4.5 mm,

ε_r = 9.8, r_1 = 0.63 mm, r_2 = 2.0 mm

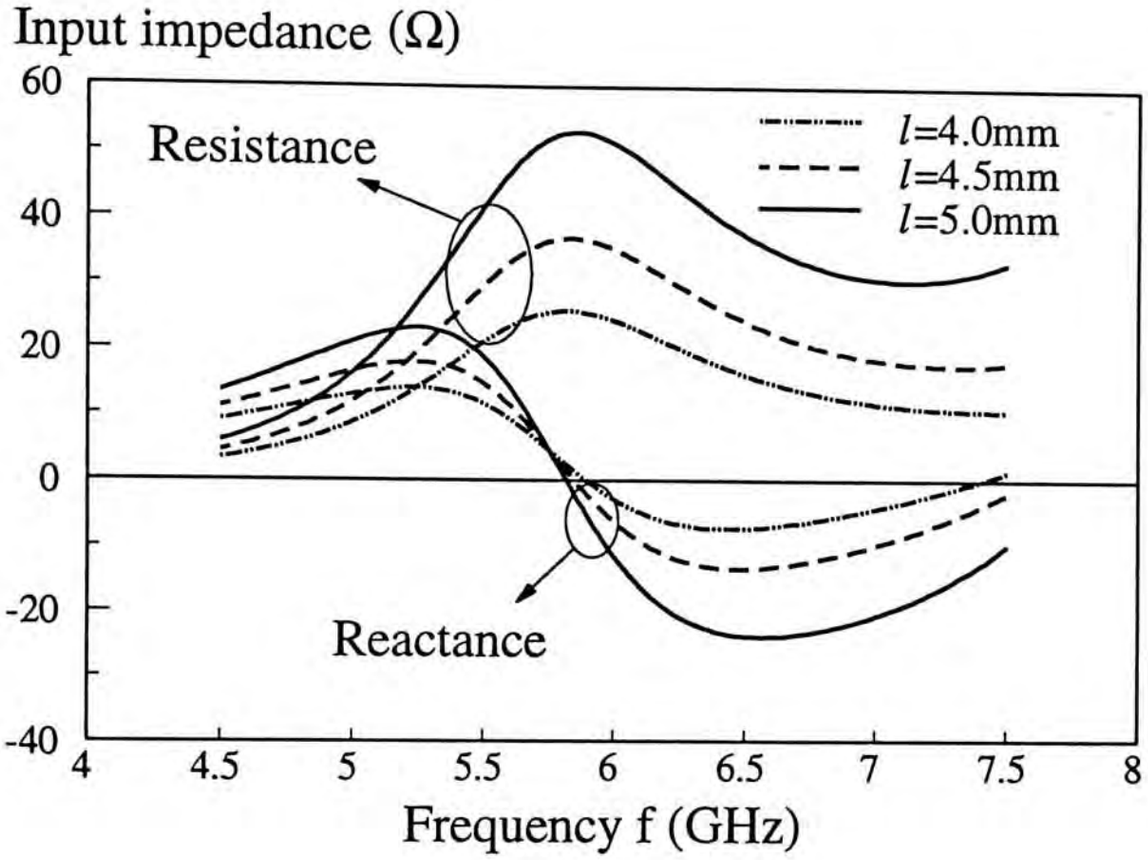

Fig. 2-9 Input impedance of the TM_{101} mode against frequency for different probe lengths:

a = 11.5 mm, b = 0.0 mm, ε_r = 9.8,

r_1 = 0.63 mm, r_2 = 2.0 mm

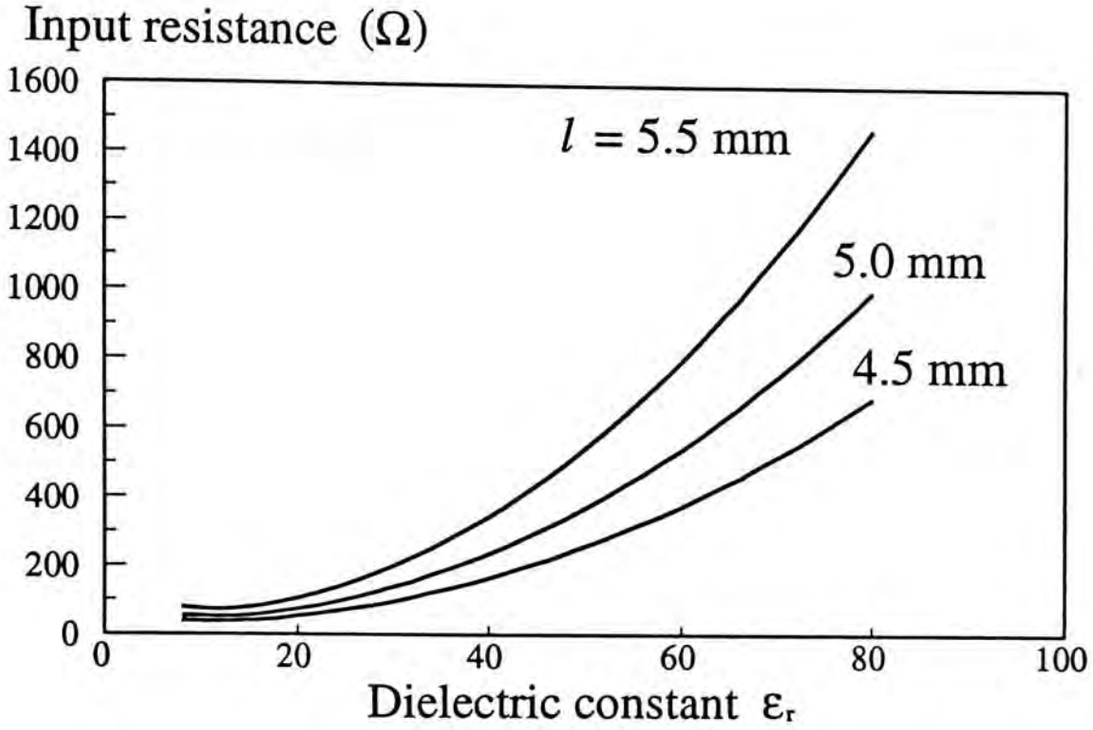

Fig. 2-10(a) Input resistance of the TM_{101} mode at resonance against dielectric constant ε_r for different probe length l : a = 11.5 mm, b = 0.0 mm, $f = f_{TM_{101}}$, r_1 = 0.63 mm.

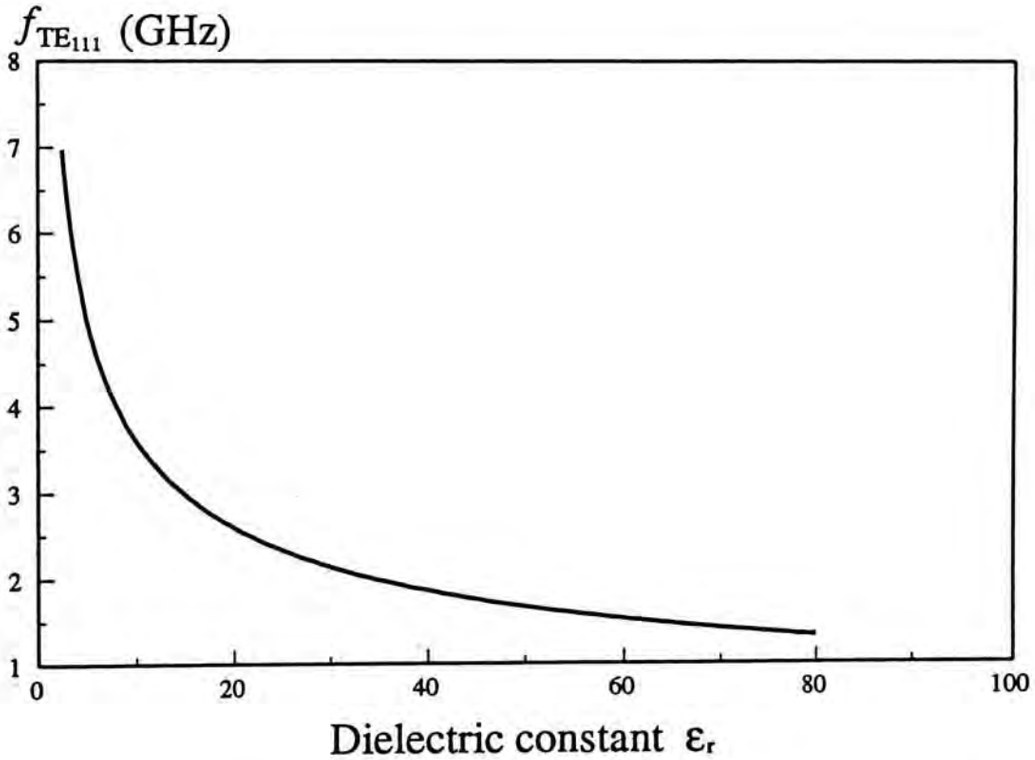

Fig.2-10(b) TM_{101} mode resonant frequency $f_{TM_{101}}$ against ε_r for a = 11.5 mm

2.3.3 Conclusion

The single mode approximation is used to obtain a simplified Green's function for the broadside TE_{111} mode and the end-fire TM_{101} mode. The input impedance is evaluated using the variational formula. Reasonable agreement between theory and experiment is obtained. The discrepancy is mainly caused by the unfitted hole where the coaxial probe is placed for measurements.

The input resistance value at resonance can be adjusted by changing probe lengths or feed positions, and hence one can achieve impedance matching in circuit designs.

In the next section, a rigorous treatment of the exact modal solution is presented.

2.4 Rigorous Moment Method Solution

Although the single mode approximation presented in the previous section gives reasonable agreement between the simplified theory and the measurements, the solution so obtained is not general. For example, in the evaluation of the TE_{111} mode input impedance, the simplified theory can only predict the input resistance when the probe approaches the center at which the probe fails to excite the TE_{111} mode. This is because other resonant modes will have stronger influence in the input reactance when a particular mode cannot be excited properly. For the TM_{101} mode, the simplified theory is valid only when the probe is fed near the center. This is due to the fact that for a displaced probe, the TE_{221} mode, whose resonant frequency is very close to that of the TM_{101} mode, will also be excited. In this case, the simplified theory cannot give accurate results, as the effect of the TE_{221} mode is also significant.

In this section, a rigorous treatment of the exact modal solution is considered. Furthermore, moment method is used to solve for the unknown probe current from which the input impedance is evaluated.

2.4.1 Efficient Evaluation of $G_{J_z}^{E_z}$

The Green's function $G_{J_z}^{E_z}$ as given by (2-54) involves infinite series of the double-summation. To reduce the computational effort, the double-summation is reduced to the single-summation using the addition theorem for Legendre polynomials [32, pp. 292]:

$$P_n(\cos\xi) = \sum_{m=0}^{n} \frac{2}{\Delta_m} \cdot \frac{(n-m)!}{(n+m)!} P_n^m(\cos\theta)\, P_n^m(\cos\theta')\cos m(\phi-\phi') \qquad (2\text{-}62)$$

where

$$\cos\xi = \cos\theta\cos\theta' + \sin\theta\sin\theta'\cos(\phi - \phi') \tag{2-63}$$

and Δ_m is given in (2-21e). The resulting equations are shown as belows :

$$G_{J_z}^{E_z} = G_P + G_H \tag{2-64a}$$

where

$$\begin{aligned} G_P = & -\frac{1}{4\pi\omega\varepsilon k}\cdot\frac{\cos\theta\cos\theta'}{r^2 r'^2}\sum_{n=1}^{\infty} n(n+1)(2n+1)P_n(\cos\xi)\Phi_n(kr')\Psi_n(kr) \\ & +\frac{1}{4\pi\omega\varepsilon}\cdot\frac{\sin\theta'\cos\theta}{r^2 r'}\sum_{n=1}^{\infty}(2n+1)\frac{\partial}{\partial\theta'}P_n(\cos\xi)\Phi_n'(kr')\Psi_n(kr) \\ & +\frac{1}{4\pi\omega\varepsilon}\cdot\frac{\cos\theta'\sin\theta}{r r'^2}\sum_{n=1}^{\infty}(2n+1)\frac{\partial}{\partial\theta}P_n(\cos\xi)\Phi_n(kr')\Psi_n'(kr) \\ & -\frac{k}{4\pi\omega\varepsilon}\cdot\frac{1}{r r'}\sum_{n=1}^{\infty}\frac{(2n+1)}{n(n+1)}\frac{\partial}{\partial\phi}\frac{\partial}{\partial\phi'}P_n(\cos\xi)\Phi_n(kr')\Psi_n(kr) \\ & -\frac{k}{4\pi\omega\varepsilon}\cdot\frac{\sin\theta'\sin\theta}{r r'}\sum_{n=1}^{\infty}\frac{(2n+1)}{n(n+1)}\frac{\partial}{\partial\theta}\frac{\partial}{\partial\theta'}P_n(\cos\xi)\Phi_n'(kr')\Psi_n'(kr) \end{aligned} \tag{2-64b}$$

$$\begin{aligned} G_H = & -\frac{1}{4\pi\omega\varepsilon k}\cdot\frac{\cos\theta\cos\theta'}{r^2 r'^2}\sum_{n=1}^{\infty} n(n+1)h_n P_n(\cos\xi)\hat{J}_n(kr')\hat{J}_n(kr) \\ & +\frac{1}{4\pi\omega\varepsilon}\cdot\frac{\sin\theta'\cos\theta}{r^2 r'}\sum_{n=1}^{\infty} h_n\frac{\partial}{\partial\theta'}P_n(\cos\xi)\hat{J}_n'(kr')\hat{J}_n(kr) \\ & +\frac{1}{4\pi\omega\varepsilon}\cdot\frac{\cos\theta'\sin\theta}{r r'^2}\sum_{n=1}^{\infty} h_n\frac{\partial}{\partial\theta}P_n(\cos\xi)\hat{J}_n(kr')\hat{J}_n'(kr) \\ & -\frac{k}{4\pi\omega\varepsilon}\cdot\frac{1}{r r'}\sum_{n=1}^{\infty} b_n\frac{\partial}{\partial\phi}\frac{\partial}{\partial\phi'}P_n(\cos\xi)\hat{J}_n(kr')\hat{J}_n(kr) \\ & -\frac{k}{4\pi\omega\varepsilon}\cdot\frac{\sin\theta'\sin\theta}{r r'}\sum_{n=1}^{\infty}\frac{h_n}{n(n+1)}\frac{\partial}{\partial\theta}\frac{\partial}{\partial\theta'}P_n(\cos\xi)\hat{J}_n'(kr')\hat{J}_n'(kr) \end{aligned} \tag{2-64c}$$

$$h_n = \frac{-(2n+1)}{\Delta_n^{TM}}\left[\hat{H}_n^{(2)\prime}(ka)\hat{H}_n^{(2)}(k_o a) - \frac{k}{k_o}\hat{H}_n^{(2)}(ka)\hat{H}_n^{(2)\prime}(k_o a)\right] \tag{2-64d}$$

$$b_n = \frac{-(2n+1)}{n(n+1)} \cdot \frac{1}{\Delta_n^{TE}} \left[\hat{H}_n^{(2)}(ka) \hat{H}_n^{(2)\prime}(k_o a) - \frac{k}{k_o} \hat{H}_n^{(2)\prime}(ka) \hat{H}_n^{(2)}(k_o a) \right] \qquad \text{(2-64e)}$$

and $\Phi_n(kr')$ and $\Psi_n(kr)$ are defined in (2-54d) and (2-54e).

The particular solution G_P in (2-64b) is a slowly convergent series, and hence, an excessive number of terms for accurate summation is required. However, Hankel functions of high order have such a large amplitude that they are difficult to handle numerically. To avoid these difficulties, recall that the particular solution G_P simply represents a $\hat{z}$-directed electric field excited by a $\hat{z}$-directed point current in an unbounded medium of permittivity ε. This has been well-studied by many researchers in analyzing the cylindrical dipole with the Green's function given by :

$$G_P = -\frac{j}{\omega\varepsilon}\left(\frac{\partial^2}{\partial z^2} + k^2\right)\frac{e^{-jkR}}{4\pi R} \qquad \text{(2-65)}$$

where $R = |\vec{r} - \vec{r}'|$ is the distance between the field point and the source point. Realizing this fact, a mathematical identity can be established :

$$\begin{aligned}
&\left[-\frac{j}{\omega\varepsilon}\left(\frac{\partial^2}{\partial z^2} + k^2\right)\frac{e^{-jkR}}{4\pi R}\right]_{z=r\cos\theta} \\
&= -\frac{1}{4\pi\omega\varepsilon k} \cdot \frac{\cos\theta\cos\theta'}{r^2 r'^2} \sum_{n=1}^{\infty} n(n+1)(2n+1) P_n(\cos\xi)\Phi_n(kr')\Psi_n(kr) \\
&+ \frac{1}{4\pi\omega\varepsilon} \cdot \frac{\sin\theta'\cos\theta}{r^2 r'} \sum_{n=1}^{\infty} (2n+1)\frac{\partial}{\partial\theta'} P_n(\cos\xi)\Phi_n'(kr')\Psi_n(kr) \\
&+ \frac{1}{4\pi\omega\varepsilon} \cdot \frac{\cos\theta'\sin\theta}{r r'^2} \sum_{n=1}^{\infty} (2n+1)\frac{\partial}{\partial\theta} P_n(\cos\xi)\Phi_n(kr')\Psi_n'(kr) \\
&- \frac{k}{4\pi\omega\varepsilon} \cdot \frac{1}{r r'} \sum_{n=1}^{\infty} \frac{(2n+1)}{n(n+1)} \frac{\partial}{\partial\phi}\frac{\partial}{\partial\phi'} P_n(\cos\xi)\Phi_n(kr')\Psi_n(kr) \\
&- \frac{k}{4\pi\omega\varepsilon} \cdot \frac{\sin\theta'\sin\theta}{r r'} \sum_{n=1}^{\infty} \frac{(2n+1)}{n(n+1)} \frac{\partial}{\partial\theta}\frac{\partial}{\partial\theta'} P_n(\cos\xi)\Phi_n'(kr')\Psi_n'(kr)
\end{aligned} \qquad \text{(2-66a)}$$

where

$$R = [(z - r'\cos\theta')^2 + r^2\sin^2\theta + r'^2\sin^2\theta' - 2rr'\sin\theta\sin\theta'\cos(\phi - \phi')]^{\frac{1}{2}} \qquad (2\text{-}66b)$$

Finally the Green's function $G_{J_z}^{E_z}$ can be written as :

$$\begin{aligned} G_{J_z}^{E_z} = & -\frac{j}{\omega\varepsilon}\left(\frac{\partial^2}{\partial z^2} + k^2\right)\frac{e^{-jkR}}{4\pi R} \\ & -\frac{1}{4\pi\omega\varepsilon k}\cdot\frac{\cos\theta\cos\theta'}{r^2r'^2}\sum_{n=1}^{\infty} n(n+1)h_n P_n(\cos\xi)\hat{J}_n(kr')\hat{J}_n(kr) \\ & +\frac{1}{4\pi\omega\varepsilon}\cdot\frac{\sin\theta'\cos\theta}{r^2r'}\sum_{n=1}^{\infty} h_n\frac{\partial}{\partial\theta'}P_n(\cos\xi)\hat{J}_n'(kr')\hat{J}_n(kr) \\ & +\frac{1}{4\pi\omega\varepsilon}\cdot\frac{\cos\theta'\sin\theta}{rr'^2}\sum_{n=1}^{\infty} h_n\frac{\partial}{\partial\theta}P_n(\cos\xi)\hat{J}_n(kr')\hat{J}_n'(kr) \\ & -\frac{k}{4\pi\omega\varepsilon}\cdot\frac{1}{rr'}\sum_{n=1}^{\infty} b_n\frac{\partial}{\partial\phi}\frac{\partial}{\partial\phi'}P_n(\cos\xi)\hat{J}_n(kr')\hat{J}_n(kr) \\ & -\frac{k}{4\pi\omega\varepsilon}\cdot\frac{\sin\theta'\sin\theta}{rr'}\sum_{n=1}^{\infty}\frac{h_n}{n(n+1)}\frac{\partial}{\partial\theta}\frac{\partial}{\partial\theta'}P_n(\cos\xi)\hat{J}_n'(kr')\hat{J}_n'(kr) \end{aligned} \qquad (2\text{-}67)$$

where h_n and b_n are given in (2-64d) and (2-64e), respectively.

It was found that the homogeneous solution converges very quickly. In conjunction with the simple form for the particular solution, the Green's function $G_{J_z}^{E_z}$ can be evaluated very efficiently.

2.4.2 Moment Method Formulation for Input Impedance

(A) Formulation of Moment Method Solution

The method of moments [19] with the Galerkin's procedure is used to solve for the probe current from which the input impedance is obtained. To begin with, the scattered field E_z^s due to a $\hat{z}$-directed current J_z inside the DR is written as:

$$E_z^s(\vec{r}) = \int\int_{S_o} G_{J_z}^{E_z}(\vec{r},\vec{r}')\, J_z(z')\, dS' \tag{2-68}$$

Define $E_z^i(\vec{r})$ as the impressed field due to the excitation source. Then by enforcing the boundary condition that the total tangential electric field is zero on the dipole surface, the following equation results:

$$E_z^s(\vec{r}) + E_z^i(\vec{r}) = 0 \tag{2-69}$$

or

$$E_z^s(\vec{r}) = -E_z^i(\vec{r}) \tag{2-70}$$

Equation (2-68) then becomes :

$$E_z^i(\vec{r}) = -\int\int_{S_o} G_{J_z}^{E_z}(\vec{r},\vec{r}')\, J_z(z')\, dS' \tag{2-71}$$

Assume that the dipole current has only a longitudinal part and it is circumferentially independent. With this assumption, the current density $J_z(z')$ is expressed as follows:

$$J(z') = \frac{I(z')}{2\pi r_1} \tag{2-72}$$

and therefore (2-71) becomes :

$$E_z^i(\vec{r}) = \frac{-1}{2\pi r_1} \iint_{S_o} G_{J_z}^{E_z}(\vec{r},\vec{r}')\, I_z(z')\, dS' \tag{2-73}$$

Using the moment method, we expand $I(z)$ by a set of basis function $f_n(z)$ as follows:

$$I(z) = \sum_{n=1}^{N} I_n f_n(z) \tag{2-74}$$

where I_n's are unknowns to be determined.

Substituting (2-74) into (2-73), one obtains:

$$E_z^i(\vec{r}) = \sum_{n=1}^{N} I_n \cdot \frac{-1}{2\pi r_1} \iint_{S_o} G_{J_z}^{E_z}(\vec{r},\vec{r}')\, f_n(z')\, dS' \tag{2-75}$$

Equation (2-75) is then weighted by a set of weighting function $w_m(z)$ on both sides. In the Galerkin's procedure, the weighting function $w_m(z)$ is chosen as the same set of the basis function $f_m(z)$, i.e. $w_m(z) = f_m(z)$. This leads to the following equation :

$$\iint_{S_o} E_z^i(\vec{r})\, f_m(z)\, dS = \sum_{n=1}^{N} I_n \cdot \frac{-1}{2\pi r_1} \iint_{S_o} \iint_{S_o} f_m(z)\, G_{J_z}^{E_z}(\vec{r},\vec{r}')\, f_n(z')\, dS\, dS' \tag{2-76}$$

where m=1,2,...,N.

For either magnetic frill source excitation or delta gap source excitation, the impressed field has no circumferential variation on the dipole surface and therefore:

$$\int\int_{S_o} E_z^i(\vec{r})\, f_m(z)\, dS = \int\int_{S_o} E_z^i(z)\, f_m(z)\, dS$$

$$= 2\pi r_1 \int_{-l}^{l} E_z^i(z)\, f_m(z)\, dz$$

$$= 2\pi r_1 \int_{-l}^{l} V\, e_a(z)\, f_m(z)\, dz \qquad (2\text{-}77)$$

where V is the voltage associated with the excitation and $e_a(z)$ is a normalized electric field along the dipole. In the following derivation, V=1 is assumed for convenience.

Substitution of (2-77) and (2-76) gives

$$\frac{-1}{(2\pi r_1)^2} \sum_{n=1}^{N} I_n \int\int_{S_o} \int\int_{S_o} f_m(z)\, G_{J_z}^{E_z}(\vec{r},\vec{r}')\, f_n(z')\, dS' dS = \int_{-l}^{l} e_a(z)\, f_m(z)\, dz \qquad (2\text{-}78)$$

Since n=1,2,...,N and m=1,2,...,N, a matrix equation is obtained:

$$[Z_{mn}^P + Z_{mn}^H]\,[I_n] = [V_m] \qquad (2\text{-}79a)$$

where

$$Z_{mn}^P = \frac{-1}{(2\pi r_1)^2} \int\int_{S_o} \int\int_{S_o} f_m(z)\, G_P\, f_n(z')\, dS'\, dS \qquad (2\text{-}79b)$$

$$Z_{mn}^H = \frac{-1}{(2\pi r_1)^2} \int\int_{S_o} \int\int_{S_o} f_m(z)\, G_H\, f_n(z')\, dS'\, dS \qquad (2\text{-}79c)$$

$$V_m = \int_{-l}^{l} e_a(z)\, f_m(z)\, dz \qquad (2\text{-}79d)$$

and G_P and G_H are given in (2-64b) and (2-64c), respectively.

The normalized electric field $e_a(z)$ in (2-79d) is given by :

$$e_a(z)=\begin{cases}\delta(z) & \text{for delta gap source}\\ \dfrac{-1}{4\pi\ln\left(\frac{r_2}{r_1}\right)}\displaystyle\int_{r_1}^{r_2}\int_0^{2\pi}\frac{\partial}{\partial\rho}\frac{e^{-jkR}}{R}\,d\phi d\rho & \text{for magnetic frill source}\end{cases} \tag{2-80a}$$

where

$$R=\sqrt{z^2+\rho^2+r_1^2-2\rho r_1\cos(\phi-\phi')} \tag{2-80b}$$

(B) Choices of Basis Function

Both entire basis (EB) and piecewise sinusoidal (PWS) expansion modes are used. For EB expansion modes, $f_n(z)$ is chosen as [35] :

$$f_n(z)=\frac{\sqrt{l^2-z^2}}{l}\cos\left(\frac{(2n-1)\pi z}{4l}\right) \qquad -l\le z\le l \tag{2-81}$$

in which the factor $\sqrt{l^2-z^2}/l$ accounts for the edge condition and $n=1,2,..,N$.

For PWS expansion modes,

$$f_n(z)=\begin{cases}\dfrac{\sin k(d-|z-z_{n+1}|)}{\sin kd} & z_n\le z\le z_{n+2}\\ 0 & \text{elsewhere}\end{cases} \tag{2-82a}$$

where

$$z_n=-l+(n-1)d \tag{2-82b}$$

$$d=\frac{2l}{N+1} \tag{2-82c}$$

and $n=1,2,..,N$..

Although the use of PWS modes introduces singularities at certain points along the probe due to the discontinuous derivatives, the series does converge faster than

the case of using EB modes when only little information is known about the true current. Moreover, integration involving PWS modes requires less computation time for $N > 1$ [20]. However, because EB modes have continuous derivatives, the results produced by this choice are generally closer to the expected values. Hence, the use of PWS is admissible if one is interested only in finding an approximate solution [35]. This is in fact the trade-off between using PWS and EB modes.

Finally, the input impedance of the dipole embedded inside the spherical DR is given by :

$$Z_{in} = \frac{1}{I(0)} \tag{2-83}$$

or

$$Z_{in} = \frac{1}{\sum_{n=1}^{N} I_n f_n(0)} \tag{2-84}$$

Dividing Z_{in} by two will give the input impedance of the probe fed hemispherical DR antenna. Note that the evaluations of Z-matrix and V-matrix need special technique to simplify computations. These will be discussed in the following two sections in detail.

2.4.3 Evaluation of Z-matrix

The Z-matrix element as given by (2-79a) consists of two sub-elements, namely Z_{mn}^{P} and Z_{mn}^{H}. The evaluation of Z_{mn}^{H} can be performed easily as G_H is a smooth and slowly varying function. However, special attention must be paid to Z_{mn}^{P} because G_P is singular as $\vec{r} \to \vec{r}'$. First of all, Z_{mn}^{P} involves the integration over the probe surface on which the current $I(z)$ is not a function of the transverse coordinates (x, y). Second, Z_{mn}^{P} represents the self- and mutual-impedances of a free space dipole and such quantities are not affected by the position of the dipole. Therefore, the integration of the surface S_o can be performed as if the probe was centered along the $\hat{z}$-axis ($b = 0$ in Fig. 2-1). Then the crucial step is to evaluate the kernel :

$$K(z,z') = \frac{1}{2\pi}\int_{-\pi}^{\pi} \frac{e^{-jkR}}{R} d\phi \tag{2-85a}$$

where

$$R = \sqrt{(z-z')^2 + 4r_1^2 \sin^2\left(\frac{\phi-\phi'}{2}\right)} \tag{2-85b}$$

Note that $K(z,z')$ is singular as $z \to z'$.

A well-known approximation, the so called 'reduced kernel' [36]-[37] is widely used to simplify the computations. The reduced kernel is given by :

$$K_r(z,z') = \frac{e^{-jk\zeta}}{\zeta} \tag{2-86a}$$

where

$$\zeta = \sqrt{(z-z')^2 + r_1^2} \tag{2-86b}$$

With this approximation, the integration for ϕ and the singularity at $z = z'$ are avoided. In the Richmond form [36, pp. 391-392], Z_{mn}^{P} is given by :

$$Z_{mn}^{P} = -\frac{j\eta}{4\pi k}\int_{-l}^{l}\int_{-l}^{l} f_m(z)\frac{e^{-jk\zeta}}{\zeta^5}[(1+jk\zeta)(2\zeta^2-3r_1^2)+r_1^2k^2\zeta^2]\, f_n(z')\, dz'dz \qquad (2\text{-}87a)$$

where

$$\eta = \sqrt{\frac{\mu_o}{\varepsilon}} \qquad (2\text{-}87b)$$

The evaluation of (2-87) has been well-developed for PWS modes [38], and some formulae and routines are documented by Pozar [39]. The results are:

$$Z_{mn}^{P} = \frac{1}{\sqrt{\varepsilon_r}}\cdot\frac{15}{\sin^2 kd}\sum_{p=-2}^{2}\sum_{\substack{q=-1\\(\text{step }2)}}^{1} A(p+3)\, e^{-jkq(x_o+pd)}\, E(k\beta) \qquad (2\text{-}88a)$$

where

$$\beta = \sqrt{r_1^2+(x_o+pd)^2}-q(x_o+pd) \qquad (2\text{-}88b)$$

$$x_o = |m-n|\,d \qquad (2\text{-}88c)$$

$$A(1) = A(5) = 1 \qquad (2\text{-}88d)$$

$$A(2) = A(4) = -4\cos kd \qquad (2\text{-}88e)$$

$$A(3) = 2+4\cos^2 kd \qquad (2\text{-}88f)$$

$$E(k\beta) = Ci(k\beta) - jSi(k\beta) \qquad (2\text{-}88g)$$

In (88), $Ci(x)$ and $Si(x)$ are Cosine integral and Sine integral, respectively and their values can be easily computed by using simple formulae [40, pp.231-233]. Note that the factor of $1/\sqrt{\varepsilon_r}$ is added to Z_{mn}^{P} so that the surrounding of the dipole is a dielectric medium of permittivity ε_r instead of air as considered in [39]. It should be mentioned that if N expansion modes are used, only N of the N^2 Z_{mn}^{P}'s need to be computed. This results in substantial savings in time.

If the EB expansion modes are used instead of PWS modes, the numerical integration to evaluate Z_{mn}^{P} (equation (2-87a)) must be performed directly. So for the present problem, using PWS modes is much more computationally efficient than using EB modes.

The reduced kernel offers the merit that it avoids the singularity at $z = z'$ as well as the integration for ϕ, and therefore it greatly saves the programming effort and computation time. However, the reduced kernel is valid only for thin dipoles which have a large length to radius ratio. For thick or moderately thick dipoles, the reduced kernel is no longer valid. In order to utilize the reduced kernel even for moderately thick dipoles, Imbriale and Ingerson [25] have derived a two term equivalent radius r_e which is given by:

$$r_e = r_1\left[1 - 0.40976\frac{r_1}{d}\right] \tag{2-89}$$

where d is the half-width of the PWS modes (equation (2-82c)). The reduced kernel is now given by:

$$K_t(z,z') = \frac{e^{-jk\zeta'}}{\zeta'} \tag{2-90a}$$

where

$$\zeta' = \sqrt{(z-z')^2 + r_e^2} \tag{2-90b}$$

Note that when the dipoles is thin (i.e., $r_1 << d$), we have $r_e \approx r_1$ as expected. It should be mentioned that by using the two term equivalent radius, the accuracy as well as the convergence of Z_{mn}^{P} are improved for a moderately thick dipole [25].

For thick dipoles, the two term equivalent radius will also fail to give accurate results. In this case, the exact kernel as given by (2-85a) should be used. The exact kernel has been analyzed by a number of researchers [41]-[46]. It is found that the

exact kernel has a logarithmic singularity which is integrable. Schelkunoff [41] gives a partition of the exact kernel into a complete elliptic integral of the first kind and an integral of a regular integrand. The partition procedure is shown as follows. From (2-85a), we have:

$$\begin{aligned} K(z,z') &= \frac{1}{2\pi}\int_{-\pi}^{\pi}\frac{e^{-jkR}}{R}d\phi \\ &= \frac{1}{2\pi}\int_{-\pi}^{\pi}\frac{1}{R}d\phi + \frac{1}{2\pi}\int_{-\pi}^{\pi}\frac{e^{-jkR}-1}{R}d\phi \\ &= \frac{\beta F(\beta)}{\pi r_1} + K_R(z,z') \end{aligned} \tag{2-91a}$$

where

$$F(\beta) = \int_0^{\frac{\pi}{2}} \frac{1}{\sqrt{1-\beta^2\sin^2\phi}}d\phi \tag{2-91b}$$

$$K_R(z,z') = \frac{1}{2\pi}\int_{-\pi}^{\pi}\frac{e^{-jkR}-1}{R}d\phi \tag{2-91c}$$

$$\beta = \frac{2r_1}{\sqrt{(z-z')^2+4r_1^2}} \tag{2-91d}$$

In (91), $F(\beta)$ is the complete elliptic integral of the first kind. Note that $K_R(z,z')$ in (2-91c) has a regular integral and therefore the integration can be performed numerically in a straightforward manner. The singularity of the exact kernel $K(z,z')$ is now absorbed in $F(\beta)$, whose behaviour is well studied. The elliptic integral $F(\beta)$ can be expanded into a series [47] as given by:

$$\begin{aligned} F(\beta) = \frac{\beta}{\pi r_1}\{ &\ln\frac{4}{\beta'} + \left(\frac{1}{2}\right)^2\left[\ln\frac{4}{\beta'} - \frac{2}{1\cdot 2}\right]\beta'^2 + \left(\frac{1\cdot 3}{2\cdot 4}\right)^2\left[\ln\frac{4}{\beta'} - \frac{2}{1\cdot 2} - \frac{2}{3\cdot 4}\right]\beta'^4 \\ &+ \left(\frac{1\cdot 3\cdot 5}{2\cdot 4\cdot 6}\right)\left[\ln\frac{4}{\beta'} - \frac{2}{1\cdot 2} - \frac{2}{3\cdot 4} - \frac{2}{5\cdot 6}\right]\beta'^6 + \cdots\} \end{aligned} \tag{2-92a}$$

where

$$\beta' = \sqrt{1-\beta^2} \tag{2-92b}$$

Although (2-92) gives an exact mathematical identity, it involves an infinite summation which converges slowly for large $|z-z'|$ ($|z-z'| >> 4r_1$). A more convenient method is to use the polynomial approximation [40, p. 591] as given by:

$$F(\beta) = (a_0 + a_1\beta'^2 + \cdots + a_4\beta'^8) + (b_0 + b_1\beta'^2 + \cdots + b_4\beta'^8)\ln\left(\frac{1}{\beta'^2}\right) + \varepsilon(\beta) \tag{2-93}$$

where

$$\begin{aligned} a_0 &= 1.38629436112 & b_0 &= 0.5 \\ a_1 &= 0.09666344259 & b_1 &= 0.12498593597 \\ a_2 &= 0.03590092383 & b_2 &= 0.06880248576 \\ a_3 &= 0.03742563713 & b_3 &= 0.03328355346 \\ a_4 &= 0.01451196212 & b_4 &= 0.00441787012 \end{aligned}$$

in which $|\varepsilon(\beta)| \le 2\times 10^{-8}$ is the tolerance of the polynomial approximation and β' is given in (2-92b). Note that the singularity is due to the term $\ln(1/\beta'^2)$, which can be simplified to

$$\ln\frac{1}{\beta'^2} = -2\left[\ln|z-z'| + \frac{1}{2}\ln|4r_1^2 + (z-z')^2|\right] \tag{2-94}$$

in which the singularity is explicitly given by the term $\ln|z-z'|$, which is integrable. By using this technique, one can obtain the electric field along the probe surface:

$$E_{zn}(z) = \frac{-j}{\omega\varepsilon}\left(\frac{\partial^2}{\partial z^2} + k^2\right)A_{zn}(z) \tag{2-95a}$$

where

$$A_{zn}(z) = \int_{-l}^{l} K(z,z') f_n(z') dz' \tag{2-95b}$$

The differential operator $\partial^2/\partial z^2$ in (2-95a) is implemented using the five point formula:

$$\frac{\partial^2}{\partial z^2} f(z) = \frac{-f(z-2h) + 16f(z-h) - 30f(z) + 16f(z+h) - f(z+2h)}{12h^2} + O(h^4) \tag{2-96}$$

Finally Z_{nm}^P using the exact kernel is given by:

$$Z_{mn}^P = \frac{-1}{(2\pi r_1)^2} \int_{-l}^{l} f_m(z) E_{zn}(z) dz \tag{2-97}$$

When the PWS modes expansion are used with the exact kernel, the numerical differentiation is very unstable due to the discontinuous derivatives of the PWS modes. Therefore only EB modes are employed in this case.

2.4.4 Evaluation of V-matrix

When the delta gap source model is used, the expression of the voltage element V_m is very simple, and it is given by:

$$\begin{aligned} V_m &= \int_{-l}^{l} e_a(z) f_m(z) dz \\ &= \int_{-l}^{l} \delta(z) f_m(z) dz \\ &= f_m(0) \end{aligned} \tag{2-98}$$

However, if the magnetic frill source model is used instead, special numerical consideration is required because now the field $e_a(z)$ has a logarithmic singularity as z approaches to zero. To tackle the singularity, Collin [48] has derived an expression for V_m so that it can be implemented in a straightforward manner. To begin with, the field $e_a(z)$ is approximated by a quasi-static solution. This approximation is based on the fact that $e_a(z)$ is strongly localized near the probe input at z=0. The normalized electric field $e_a(z)$ is then given by:

$$\begin{aligned} e_a(z) &\approx \frac{-1}{4\pi \ln\left(\frac{r_2}{r_1}\right)} \int_{r_1}^{r_2} \int_0^{2\pi} \frac{\partial}{\partial \rho} \frac{1}{R} d\phi d\rho \\ &= \frac{-1}{4\pi \ln\left(\frac{r_2}{r_1}\right)} \int_0^{\frac{\pi}{2}} \left[\frac{1}{\sqrt{z^2 + (r_1 + r_2)^2 - 4 r_1 r_2 \cos^2 u}} - \frac{1}{\sqrt{z^2 + 4 r_1^2 - 4 r_1^2 \cos^2 u}} \right] du \end{aligned} \tag{2-99}$$

where $u = (\phi - \phi')/2$ and $R = \sqrt{z^2 + \rho^2 + r_1^2 - 2\rho r_1 \cos(\phi - \phi')}$.

Expressing $e_a(z)$ in terms of elliptic integrals, we have

$$e_a(z) = \frac{-2}{\pi \ln\left(\frac{r_2}{r_1}\right)} \left[\frac{k_1 F(k_1)}{2\sqrt{r_1 r_2}} - \frac{k_2 F(k_2)}{2 r_1} \right] \tag{2-100a}$$

where

$$k_1^2 = \frac{4r_1 r_2}{z^2 + (r_1 + r_2)^2} \tag{2-100b}$$

$$k_2^2 = \frac{4r_1^2}{z^2 + 4r_1^2} \tag{2-100c}$$

and $F(x)$ is the complete elliptic integral of the first kind. Note that as z approaches to zero, the field $e_a(z)$ takes on the limiting value

$$e_a(z) \sim \frac{-1}{2r_1 \pi \ln(r_2/r_1)} \ln\left(\frac{z}{8r_1}\right) \tag{2-101}$$

which gives the singular behaviour.

The numerical difficulty of the singularity can be alleviated by writing

$$\int_{-l}^{l} e_a(z) f_m(z) dz = \int_{-l}^{l} e_a(z) [f_m(z) - 1] dz + \int_{-l}^{l} e_a(z) dz \tag{2-102}$$

Since we have chosen $f_m(z)$ such that $f_m(0)=1$, the first integral can be evaluated very easily. The second integral involves the direct integration of the field $e_a(z)$ which has integrable singularity. It is shown by Collin [48] that the second integral is given by

$$\int_{-l}^{l} e_a(z) dz = 1 - \frac{2}{\pi \ln(r_2/r_1)} \int_0^{\frac{\pi}{2}} \ln \frac{l + \sqrt{l^2 + (r_1 + r_2)^2 - 4r_1 r_2 \cos^2 u}}{l + \sqrt{l^2 + 4r_1^2 - 4r_1^2 \cos^2 u}} du \tag{2-103}$$

which can also be evaluated in a straightforward manner.

The frequency dependent contribution to the applied electric field is easily included to give a more accurate solution. Denote V_m' and $\Delta V_m'$ as, respectively, the static field approximation and the correction term for dispersion, then the more accurate expression of V_m is given by:

$$V_m = V_m' + \Delta V_m' \tag{2-104a}$$

where

$$V_m' = \int_{-l}^{l} [f_m(z) - 1] e_a(z) dz$$

$$+1 - \frac{2}{\pi \ln\left(\frac{r_2}{r_1}\right)} \int_0^{\frac{\pi}{2}} \ln\left[\frac{l + \sqrt{l^2 + (r_1 + r_2)^2 - 4r_1 r_2 \cos^2 u}}{l + \sqrt{l^2 + 4r_1^2 - 4r_1^2 \cos^2 u}}\right] du \qquad \text{(2-104b)}$$

$$\Delta V_m' = \frac{jk}{\pi \ln\left(\frac{r_2}{r_1}\right)} \int_{z=-l}^{l} \int_{u=0}^{\frac{\pi}{2}} f_m(z) \left[\frac{-jkR}{2!} + \frac{(-jkR)^2}{3!} + \frac{(-jkR)^3}{4!} + \cdots\right]_{\rho=r_1}^{r_2} du\, dz \qquad \text{(2-104c)}$$

It was found that the infinite series in $\Delta V_m'$ converges very quickly especially for the first few DR's resonant modes.

Before comparing the results between theory and experiment, convergence tests for the MM solution using different excitation models (delta gap source and magnetic frill source) are studied in the next section. Moreover, a comparison between EB modes and PWS modes in terms of the convergence behaviour will also be given. Finally the convergence tests using the traditional reduced kernel, the reduced kernel with the effective probe radius and the exact kernel are shown in the next section.

2.4.5 Convergence Checks

In this section, the convergence tests of the MM solution using different basis functions as well as different dipole kernels are presented. Since we will consider two feeding positions for the coaxial probe (fed with displacement from the center, $b>0$ in Fig. 2-1, and fed axisymmetrically without displacement, $b=0$), the convergence tests for the two cases are also shown. It should be mentioned that for the case of a displaced probe, there are two resonance peaks in the graphs. The first one corresponds to the fundamental TE_{111} mode whereas the second one is mixed by the TE_{221} mode and the TM_{101} mode. The mixed resonance of the second peak can be seen from the fact that, with the current antenna settings, the predicted resonant frequency for the TM_{101} mode is 5.245 GHz (obtained by solving the characteristic equation $\Delta_1^{TM} = 0$, see (2-40f)) and it is 5.267 GHz (by solving the characteristic equation $\Delta_2^{TE} = 0$, see (2-40e)) for the TE_{221} mode. For the case of a center fed probe, however, there is only one resonance peak, which is the TM_{101} mode, in the graphs. Note that all TE modes are now eliminated. This is expected because at this feed position, the probe current is mainly $\hat{r}$-directed, and such component can excite only TM modes as discussed in Section 2.2.

Figs. 2-11 to 2-14 (Figs 2-11 to 2-12 for the displaced probe, and Figs. 2-13 to 2-14 for the centered probe) compare the convergence behaviour between the magnetic frill source and delta gap source models for the EB expansion modes using the traditional reduced kernel. Another set of convergence tests is shown in Figs. 2-15 to 2-18 (Figs 2-15 to 2-16 for the displaced probe, and Figs. 2-17 to 2-18 for the centered probe) to compare the convergence behaviour between the two different excitation models for the PWS expansion modes using also the traditional reduced kernel. From either set of the graphs (EB modes or PWS modes), one can see that the convergence behaviour using the magnetic frill source model is always better than that using the delta gap one as expected. In fact, if N is

increased further, a divergent result will be obtained for the delta gap source model [49]. Now consider the magnetic frill source model only. From the two sets of graphs, one can also compare the convergence behaviour between EB modes and PWS modes. Basically, the EB results and the PWS results are similar to each other. However, it is noted that EB results converge in a more uniform fashion than the PWS does. This is probably due to the fact that the PWS modes have discontinuous derivatives which make the convergence less uniform. On the other hand, however, the PWS results have higher convergence rate than that of the EB results. This is expected because when there is no prior information about the true current, the PWS results usually converge faster than the EB results as discussed in Section 2.4.2.

The convergence checks using the reduced kernel with effective radius (which is applicable only to PWS modes) are shown in Fig. 2-19 (displaced probe) and Fig. 2-20 (centered probe). As compared to the results using the traditional reduced kernel (with PWS modes), the convergence of the results is improved by using the effective radius.

Fig. 2-21 (displaced probe) and Fig. 2-22 (centered probe) show the convergence of the MM solution using the exact kernel together with EB modes. It is seen that the convergence so obtained give the best satisfactory behaviour among that using the other dipole kernels.

In the next section, a comparison between theory and experiment is presented.

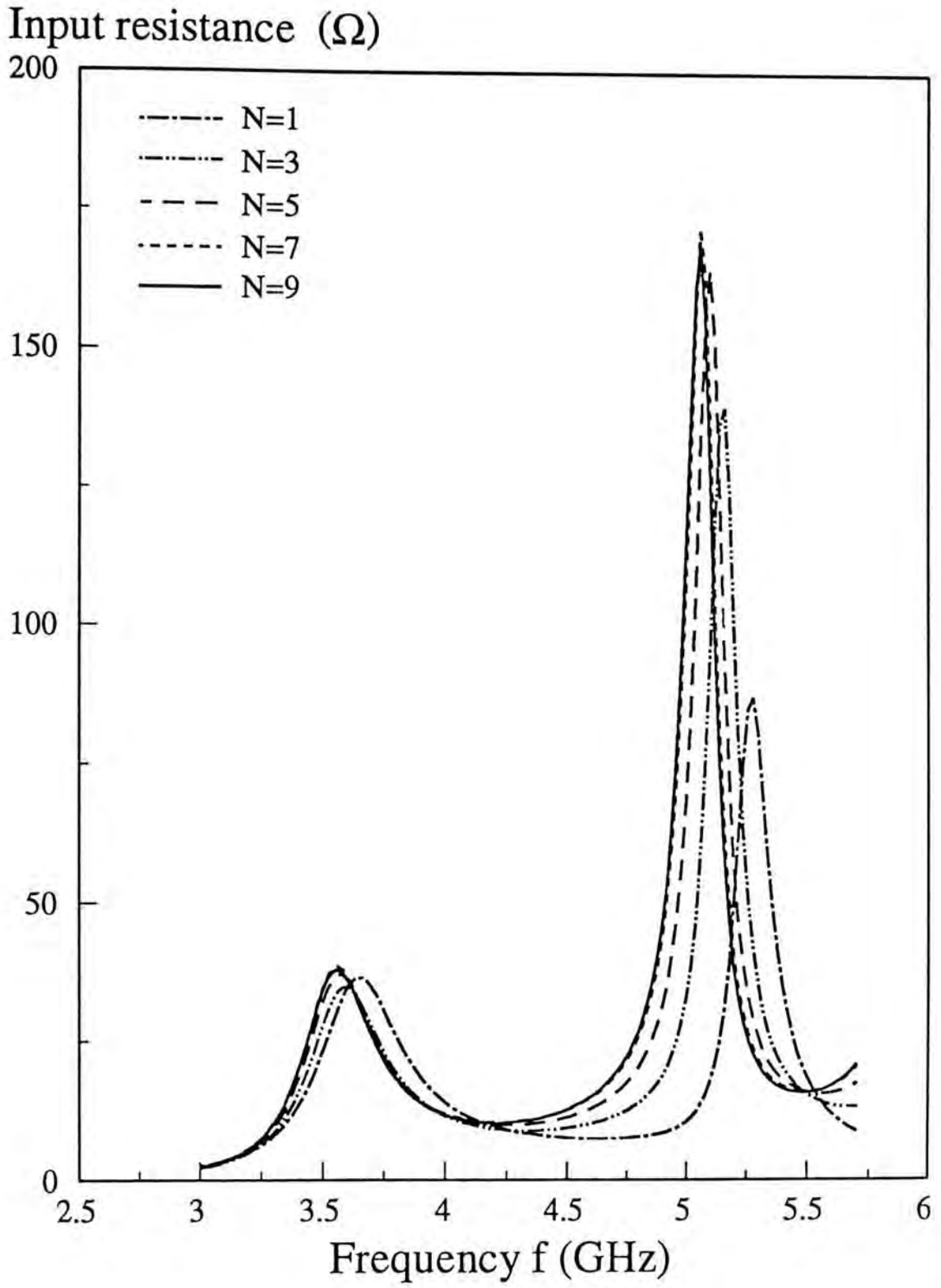

Fig. 2-11(a): Convergence check for the input resistance against frequency using magnetic frill source model and EB functions: a=12.5 mm, b=6.4 mm, l=6.5 mm, ε_r=9.8, r_1=0.63 mm, r_2=2.0 mm.

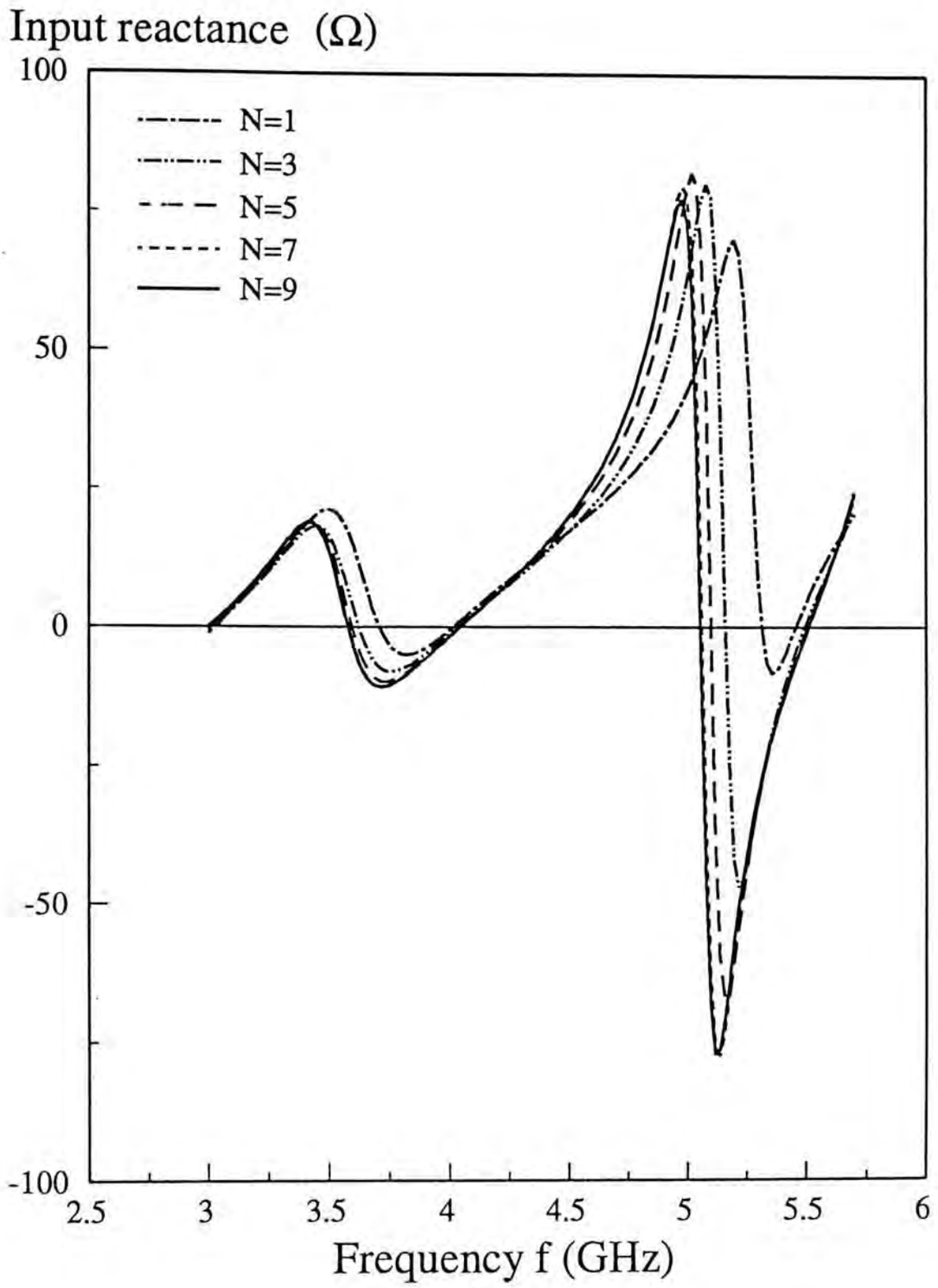

Fig. 2-11(b): Convergence check for the input reactance against frequency using magnetic frill source model and EB functions: a=12.5 mm, b=6.4 mm, l=6.5 mm, ε_r=9.8, r_1=0.63 mm, r_2=2.0 mm.

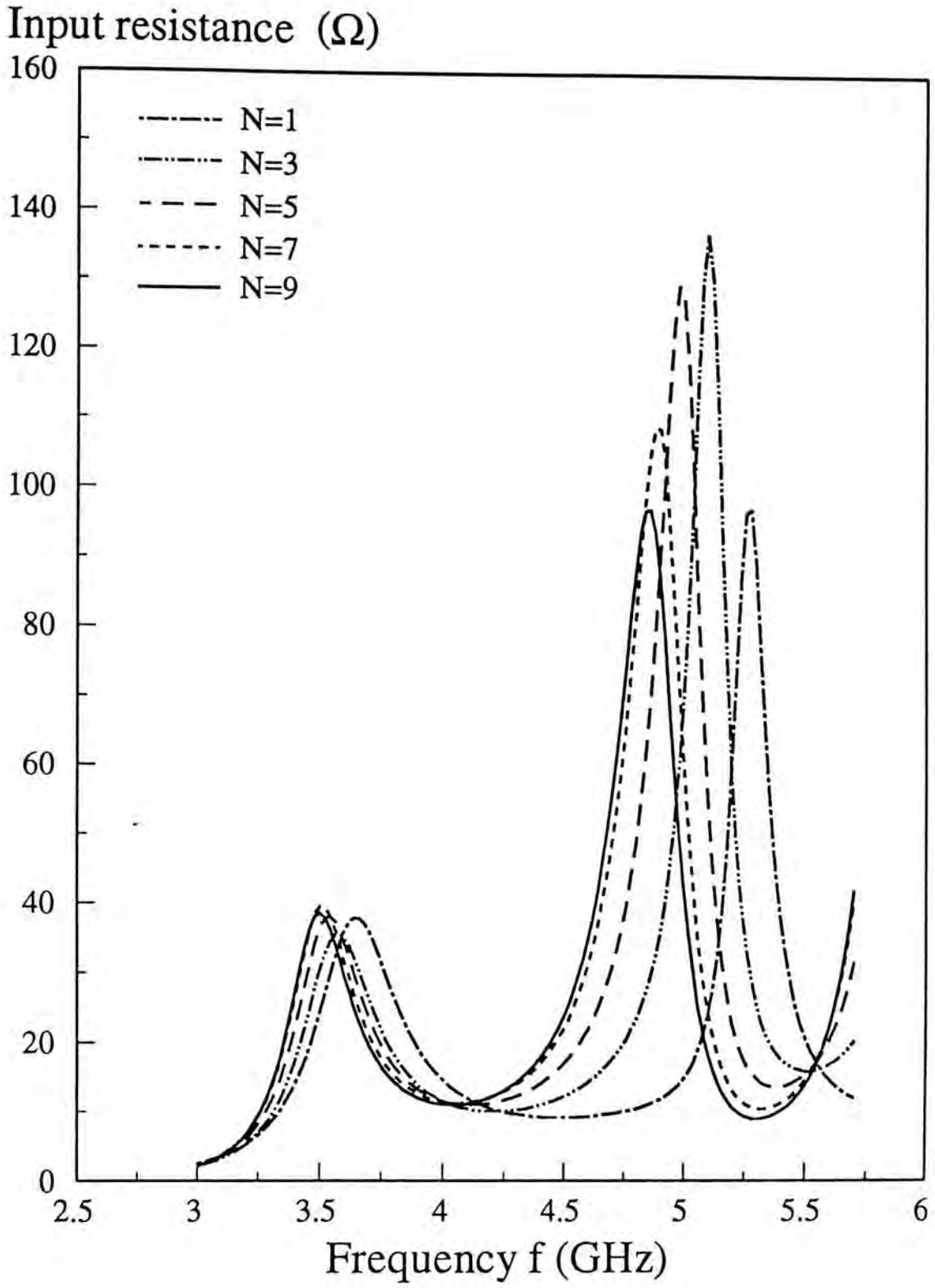

Fig. 2-12(a): Convergence check for the input resistance against frequency using delta gap source model and EB functions: a=12.5 mm, b=6.4 mm, l=6.5 mm, ε_r=9.8, r_1=0.63 mm, r_2=2.0 mm.

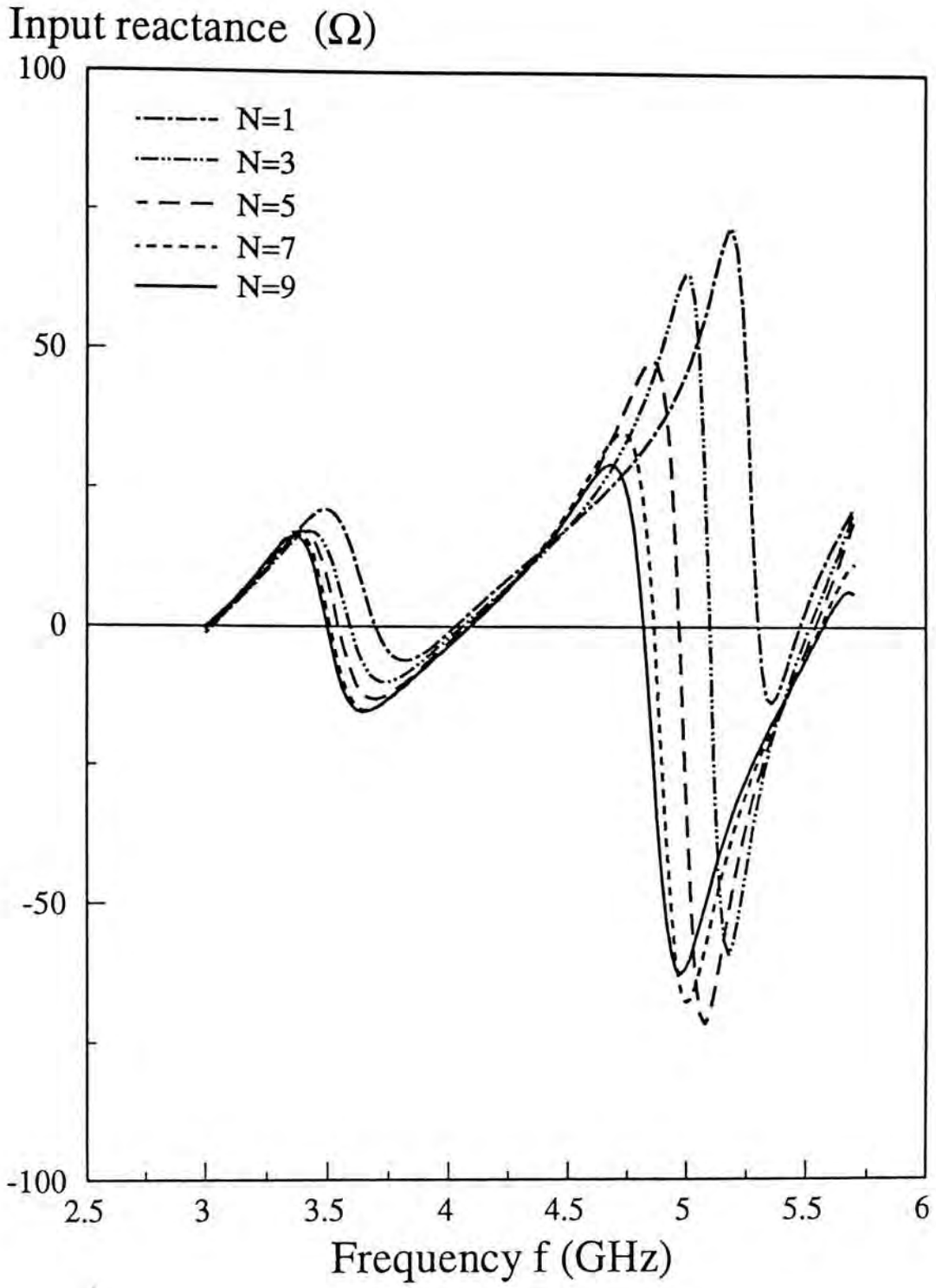

Fig. 2-12(b): Convergence check for the input reactance against frequency using delta gap source model and EB functions: a=12.5 mm, b=6.4 mm, l=6.5 mm, ε_r=9.8, r_1=0.63 mm, r_2=2.0 mm.

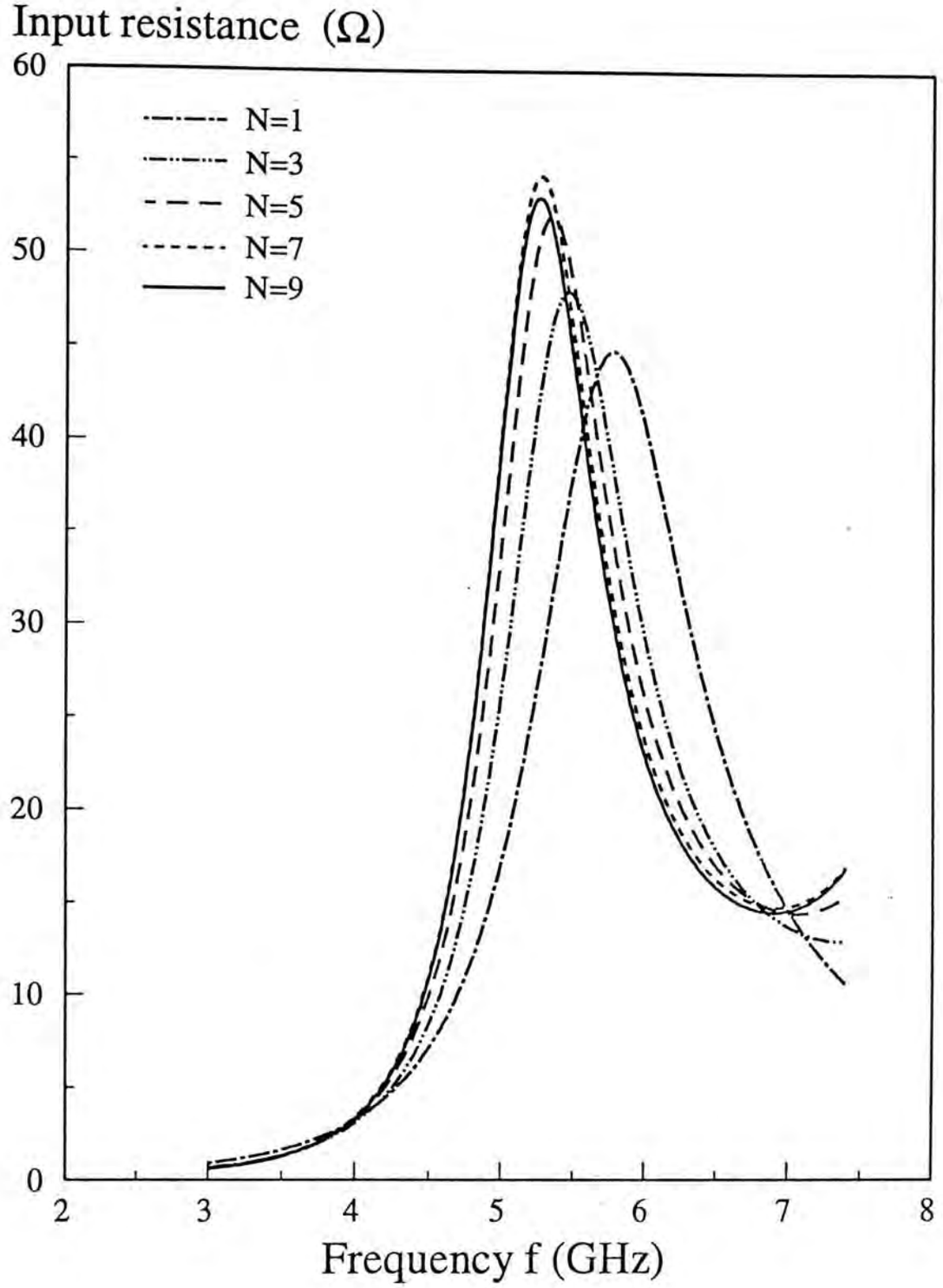

Fig. 2-13(a): Convergence check for the input resistance against frequency using magnetic frill source model and EB functions: a=11.5 mm, b=0.0 mm, l=4.5 mm, ε_r=9.8, r_1=0.63 mm, r_2=2.0 mm.

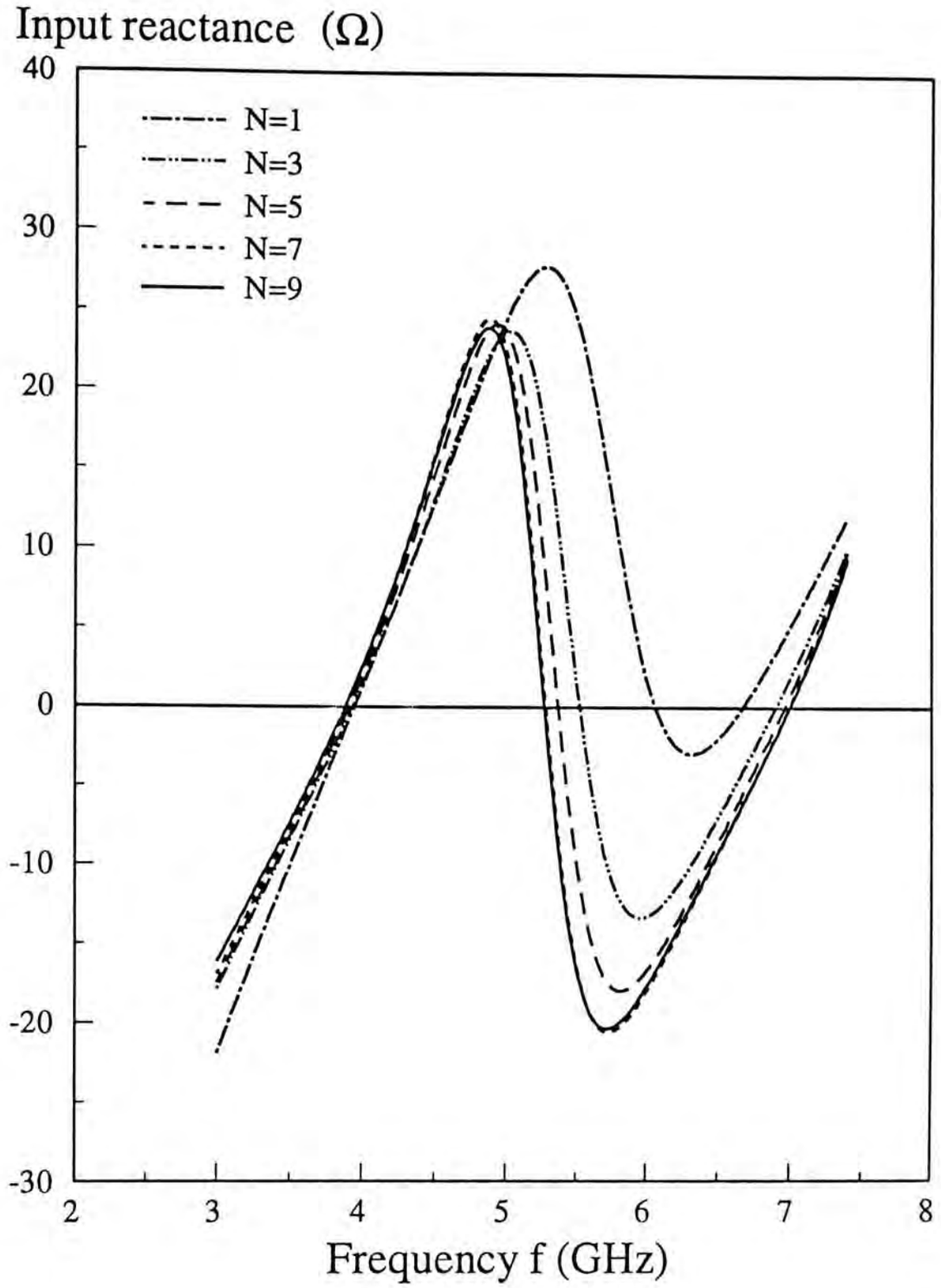

Fig. 2-13(b): Convergence check for the input reactance against frequency using magnetic frill source model and EB functions: a=11.5 mm, b=0.0 mm, l=4.5 mm, ε_r=9.8, r_1=0.63 mm, r_2=2.0 mm.

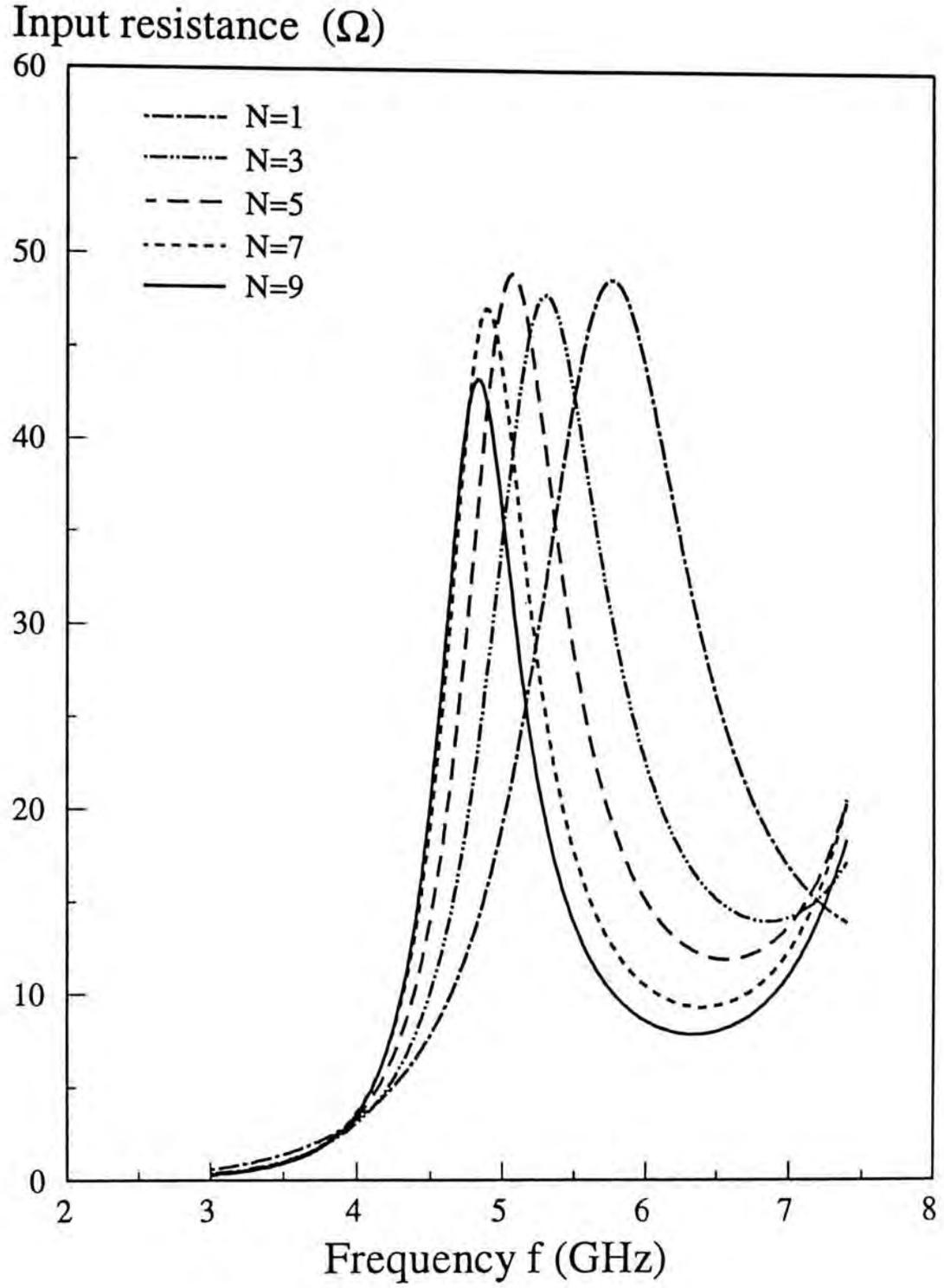

Fig. 2-14(a): Convergence check for the input resistance against frequency using delta gap source model and EB functions: a=11.5 mm, b=0.0 mm, l=4.5 mm, ε_r=9.8, r_1=0.63 mm, r_2=2.0 mm.

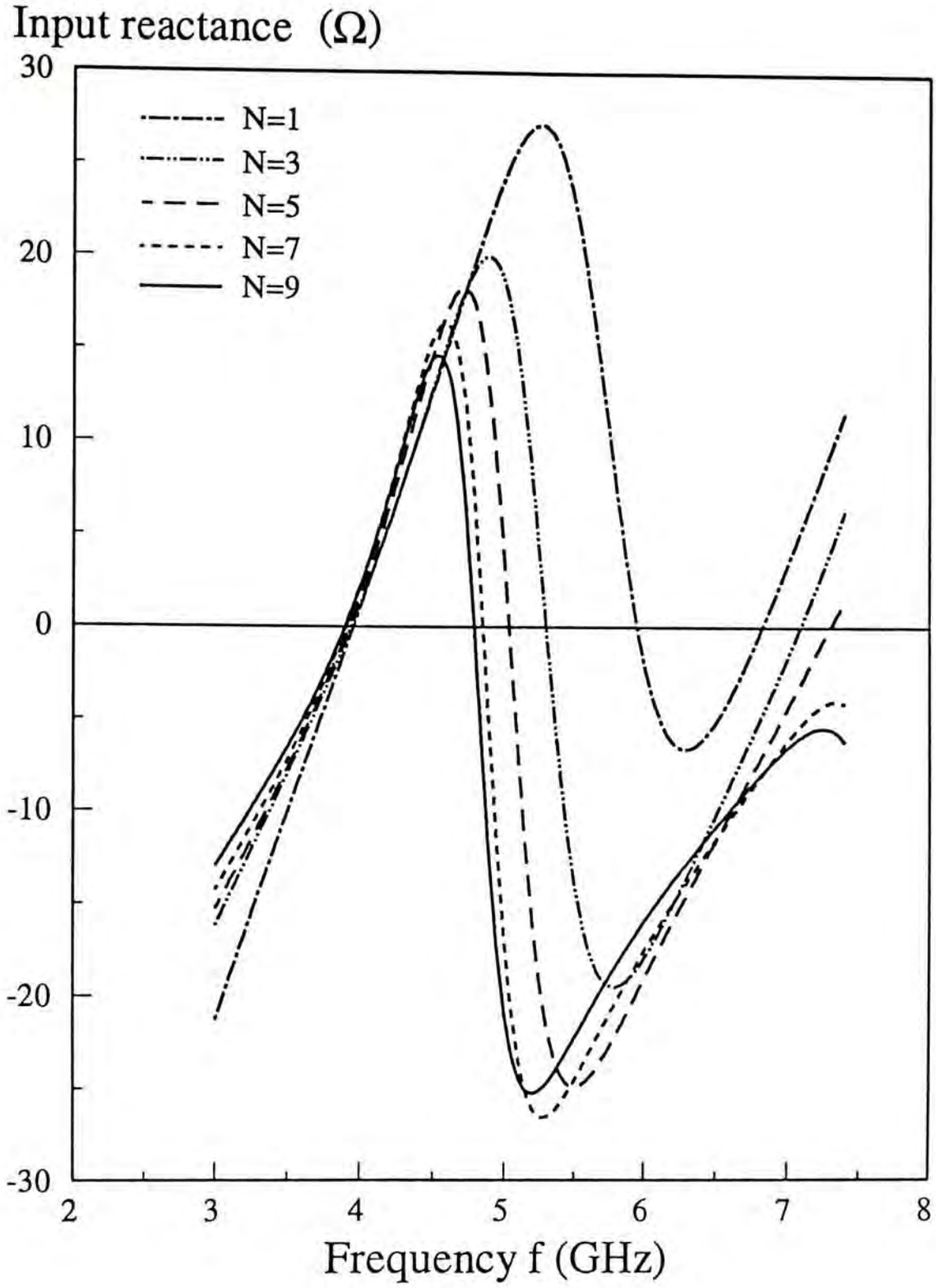

Fig. 2-14(b): Convergence check for the input reactance against frequency using delta gap source model and EB functions: a=11.5 mm, b=0.0 mm, l=4.5 mm, ε_r=9.8, r_1=0.63 mm, r_2=2.0 mm.

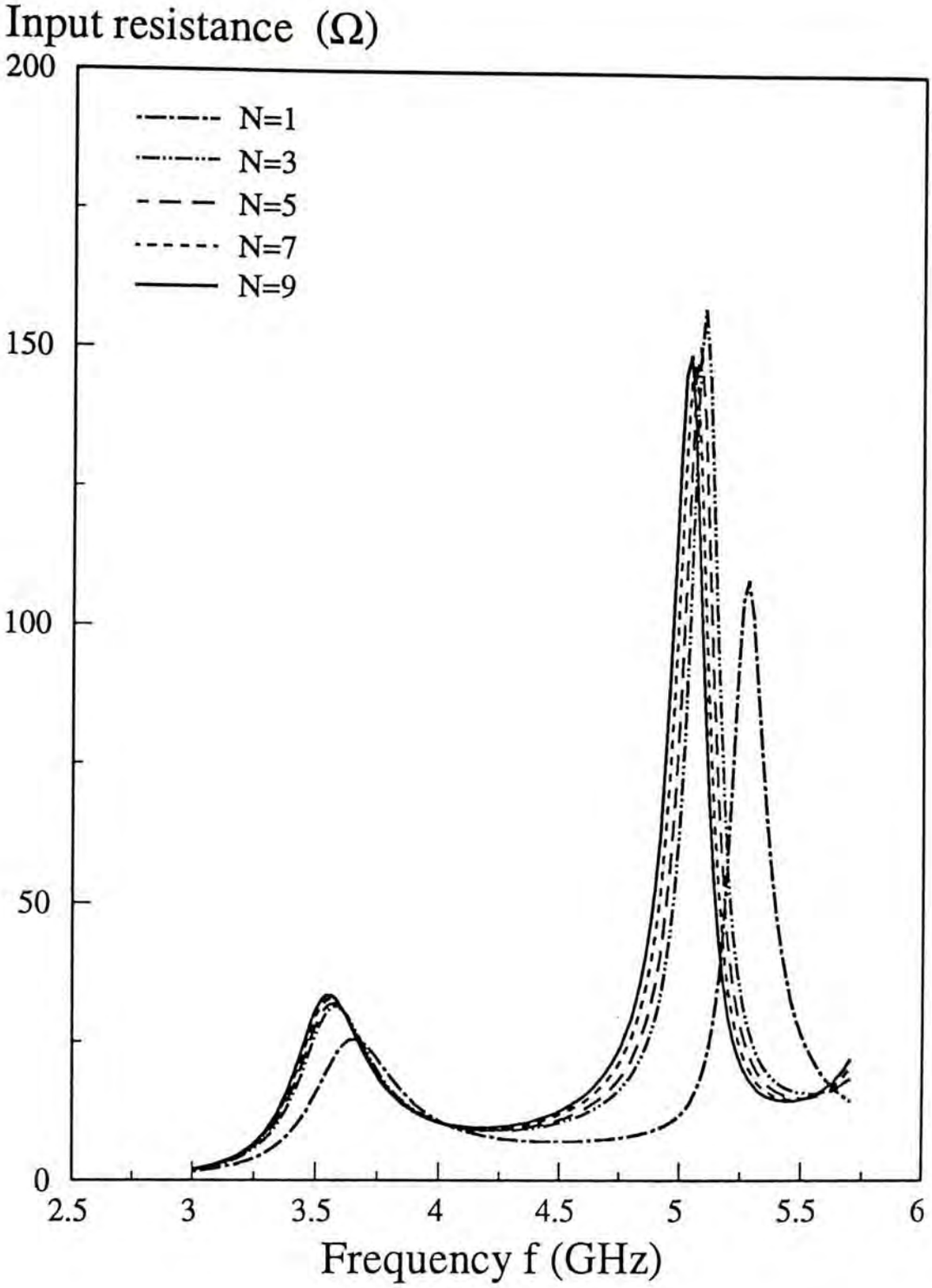

Fig. 2-15(a): Convergence check for the input resistance against frequency using magnetic frill source model and PWS functions: a=12.5 mm, b=6.4 mm, l=6.5 mm, ε_r=9.8, r_1=0.63 mm, r_2=2.0 mm.

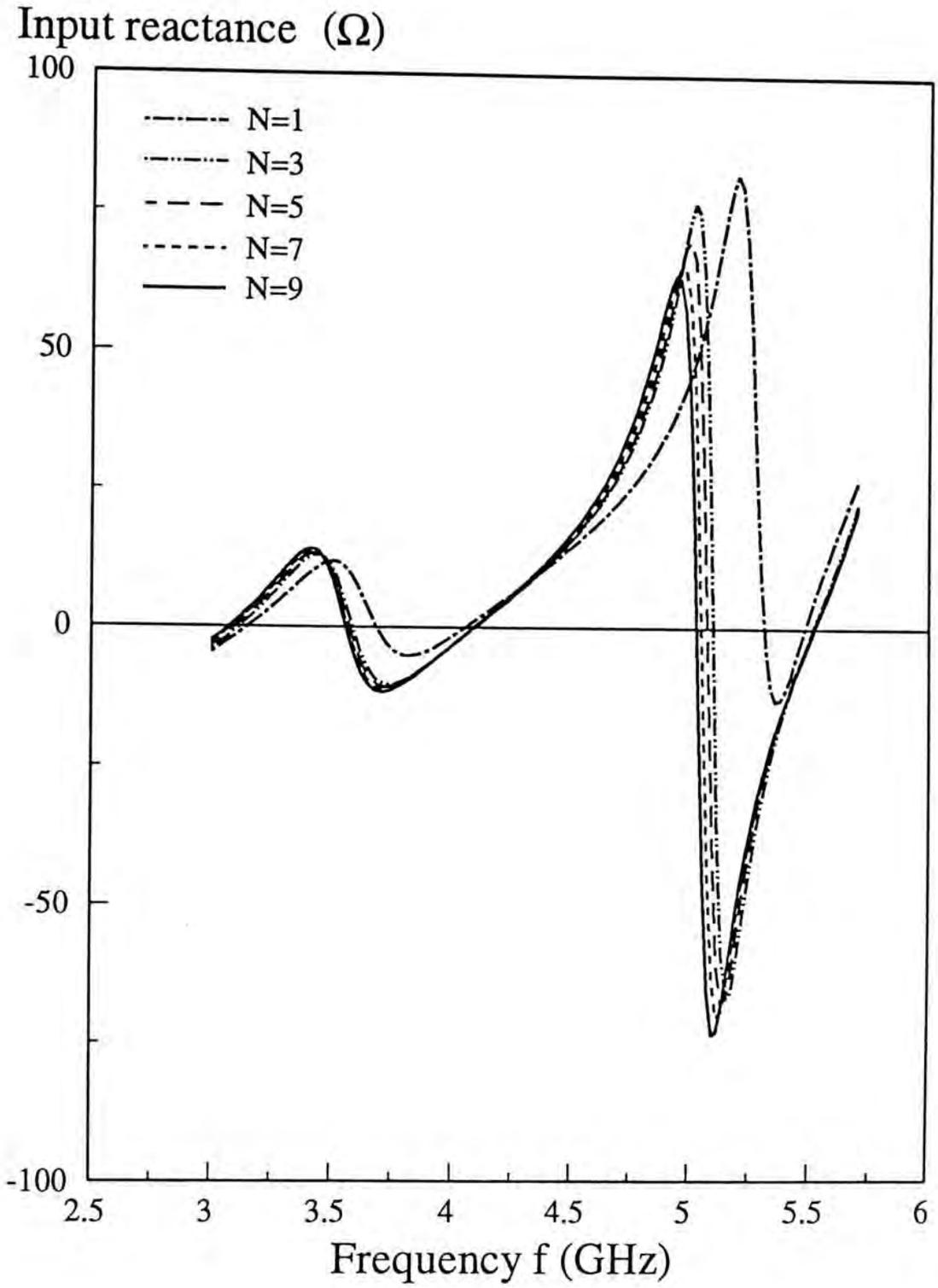

Fig. 2-15(b): Convergence check for the input reactance against frequency using magnetic frill source model and PWS functions: a=12.5 mm, b=6.4 mm, l=6.5 mm, ε_r=9.8, r_1=0.63 mm, r_2=2.0 mm.

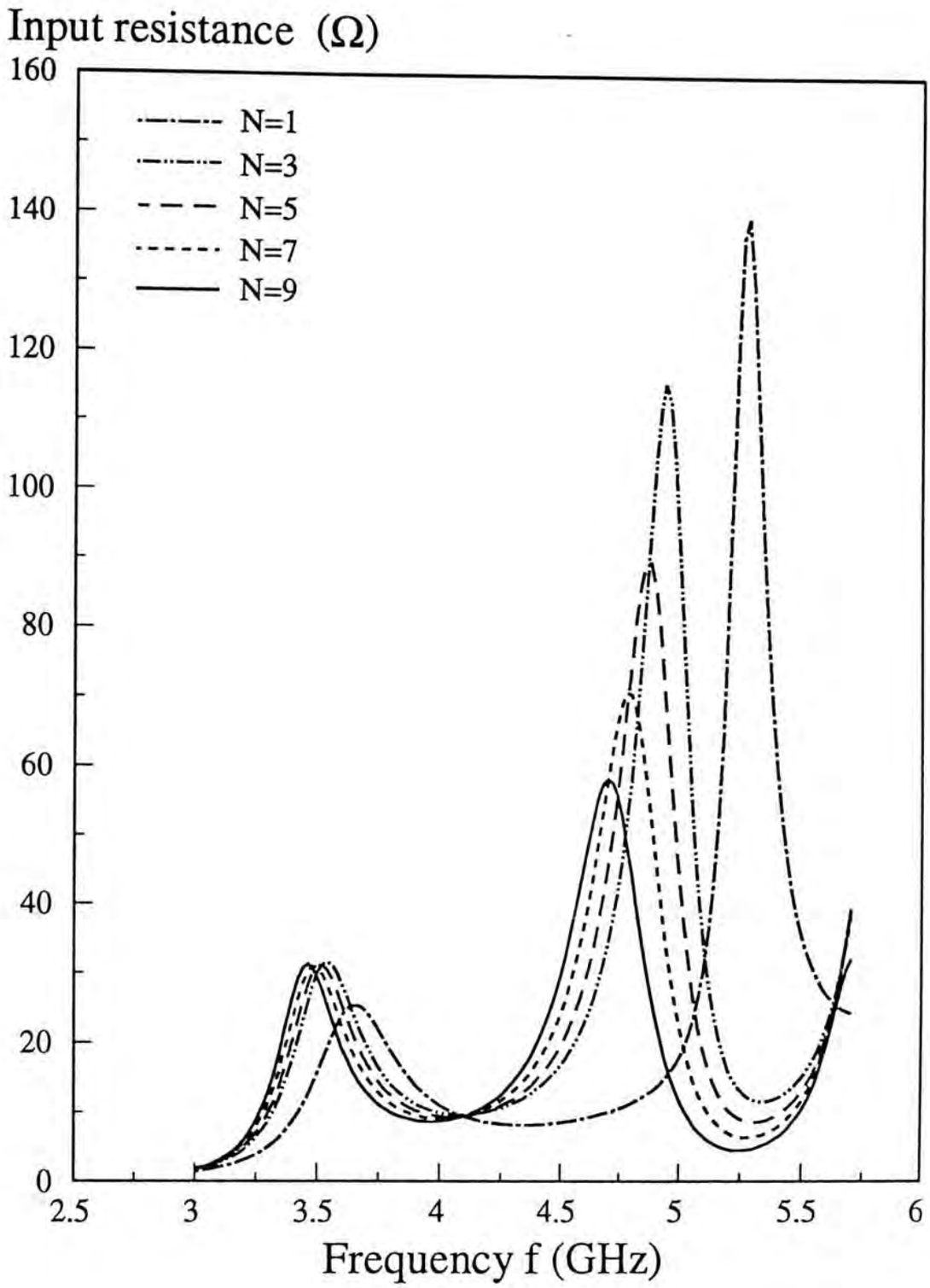

Fig. 2-16(a): Convergence check for the input resistance against frequency using delta gap source model and PWS functions: a=12.5 mm, b=6.4 mm, l=6.5 mm, ε_r=9.8, r_1=0.63 mm, r_2=2.0 mm.

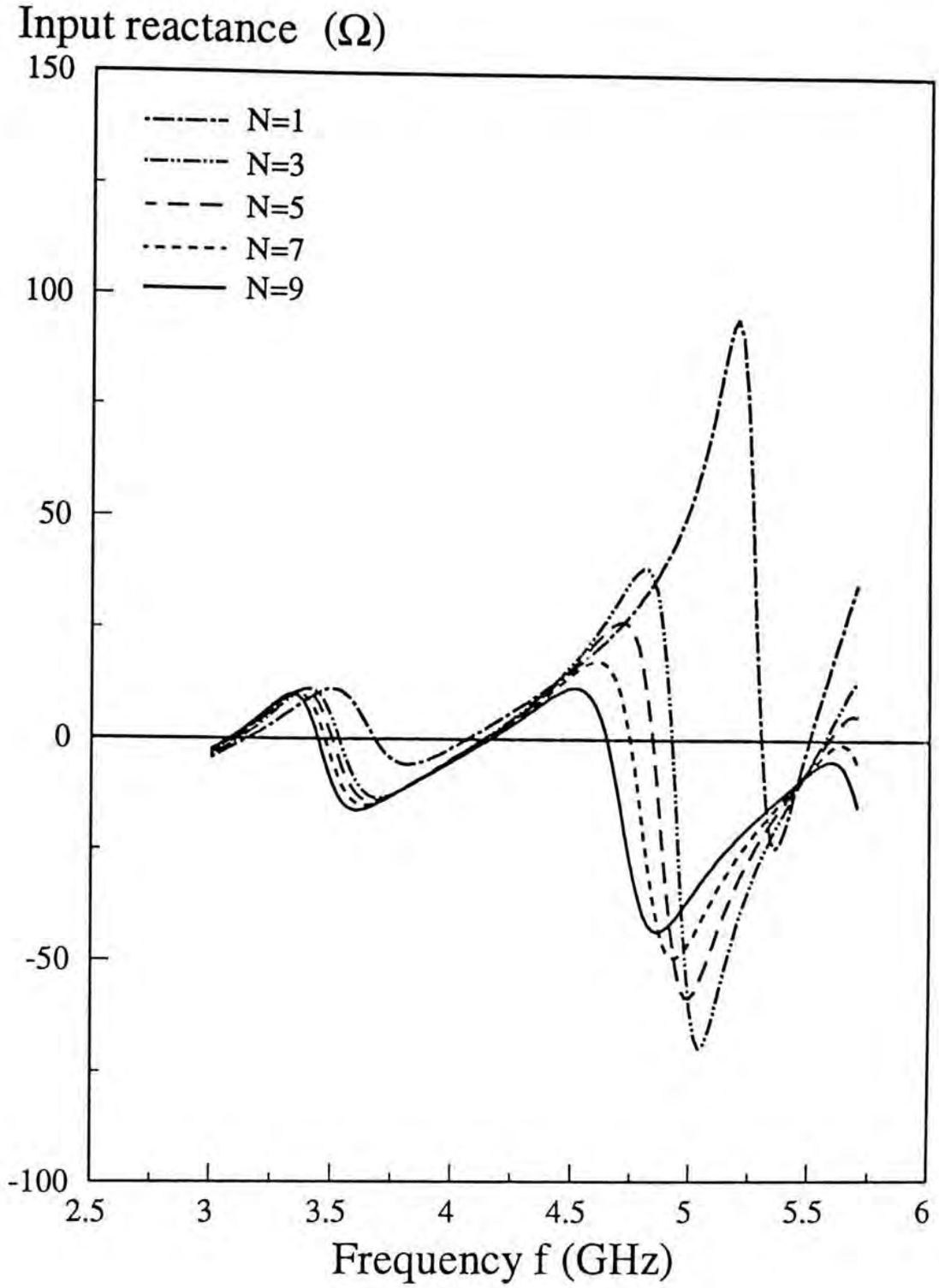

Fig. 2-16(b): Convergence check for the input reactance against frequency using delta gap source model and PWS functions: a=12.5 mm, b=6.4 mm, l=6.5 mm, ε_r=9.8, r_1=0.63 mm, r_2=2.0 mm.

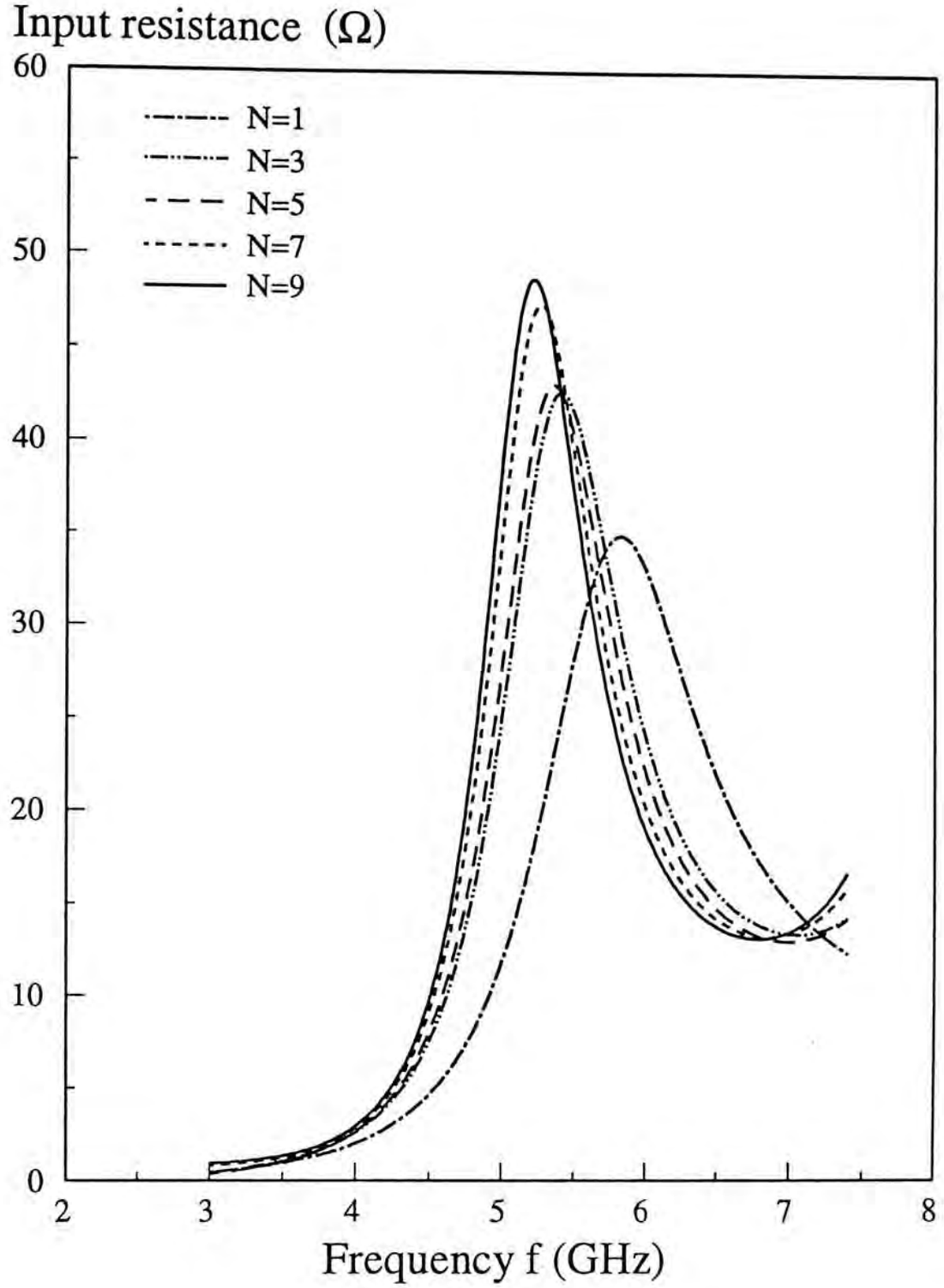

Fig. 2-17(a): Convergence check for the input resistance against frequency using magnetic frill source model and PWS functions: a=11.5 mm, b=0.0 mm, l=4.5 mm, ε_r=9.8, r_1=0.63 mm, r_2=2.0 mm.

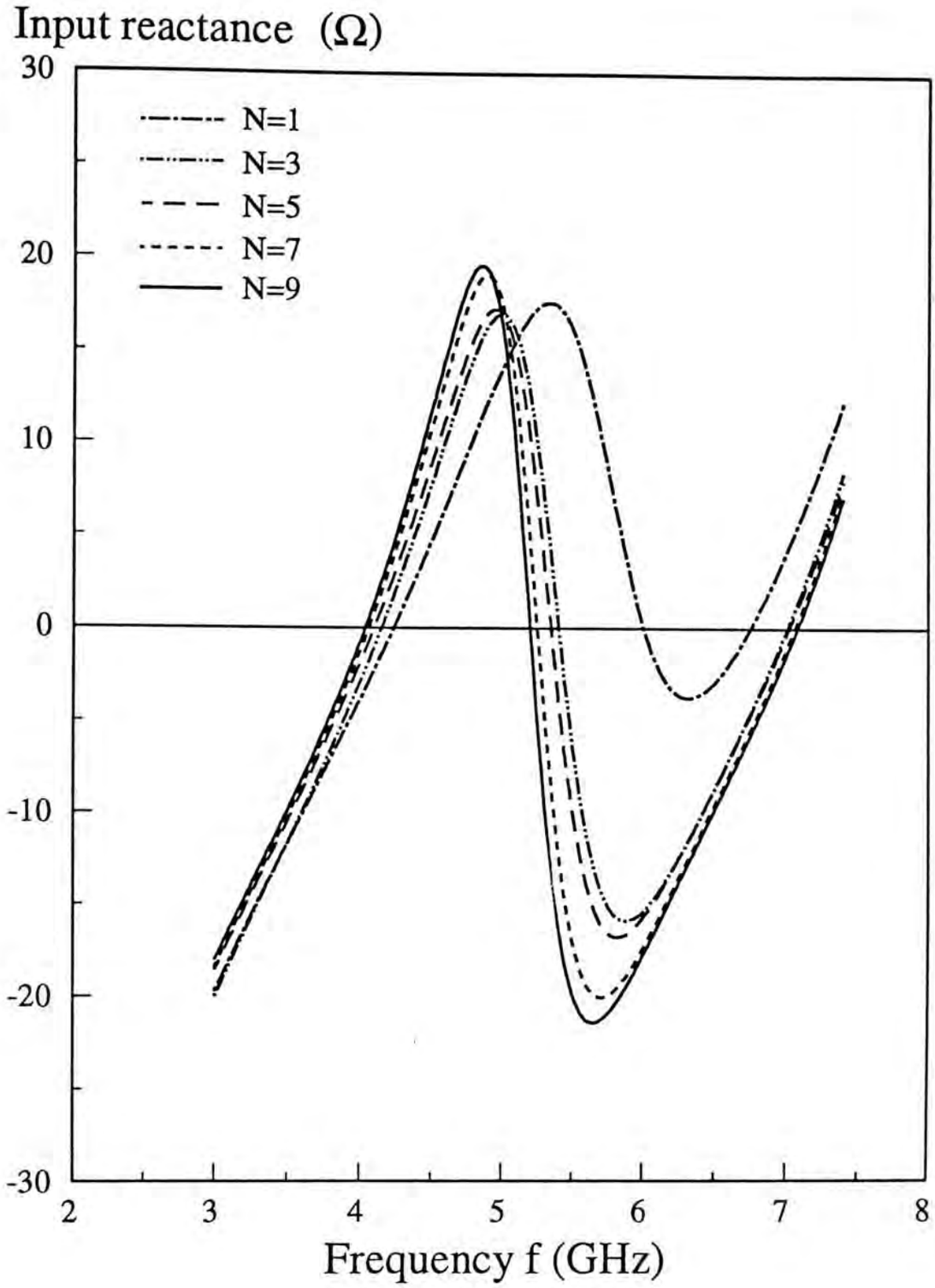

Fig. 2-17(b): Convergence check for the input reactance against frequency using magnetic frill source model and PWS functions: a=11.5 mm, b=0.0 mm, l=4.5 mm, ε_r=9.8, r_1=0.63 mm, r_2=2.0 mm.

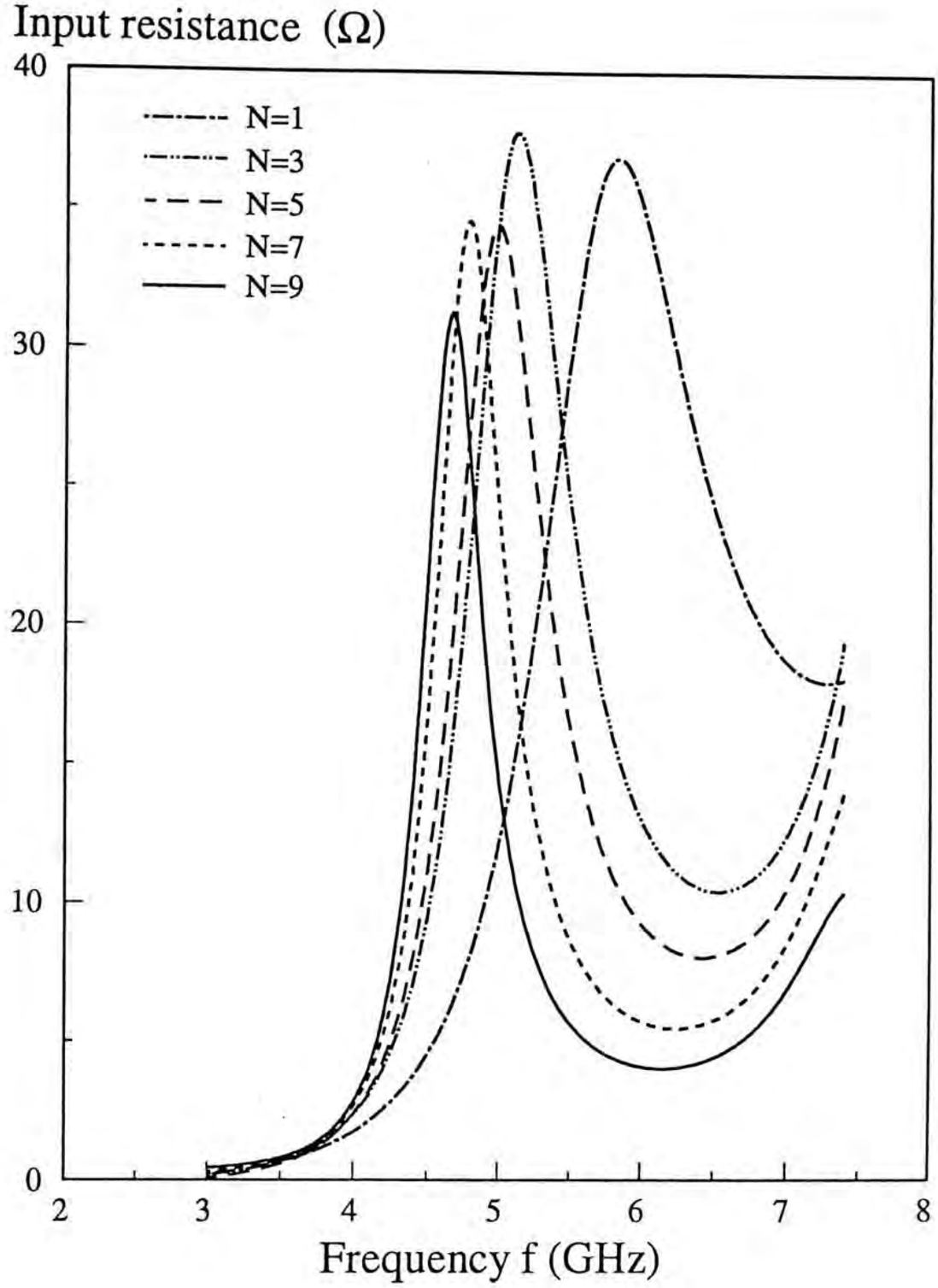

Fig. 2-18(a): Convergence check for the input resistance against frequency using delta gap source model and PWS functions: a=11.5 mm, b=0.0 mm, l=4.5 mm, ε_r=9.8, r_1=0.63 mm, r_2=2.0 mm.

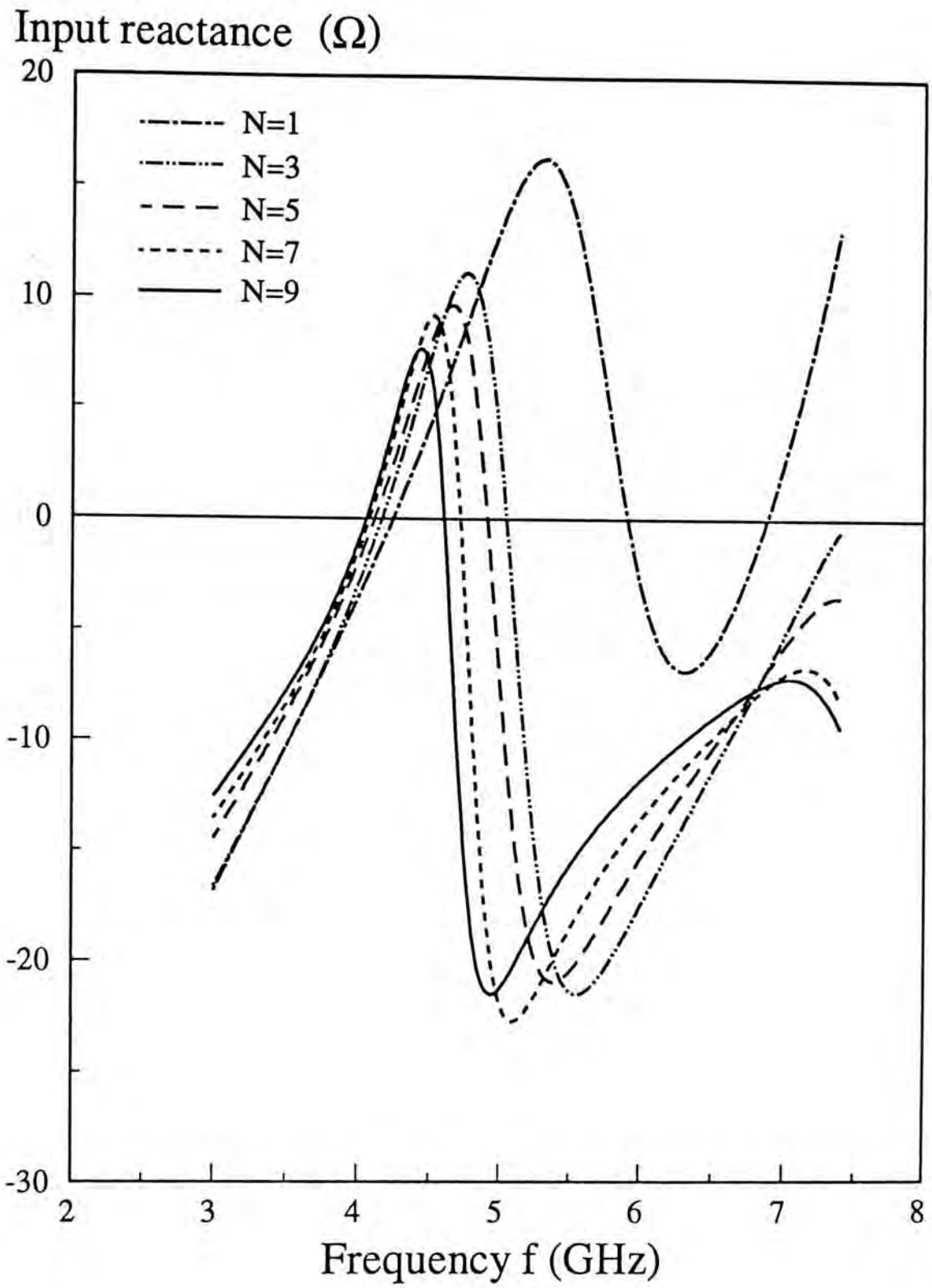

Fig. 2-18(b): Convergence check for the input reactance against frequency using delta gap source model and PWS functions: a=11.5 mm, b=0.0 mm, l=4.5 mm, ε_r=9.8, r_1=0.63 mm, r_2=2.0 mm.

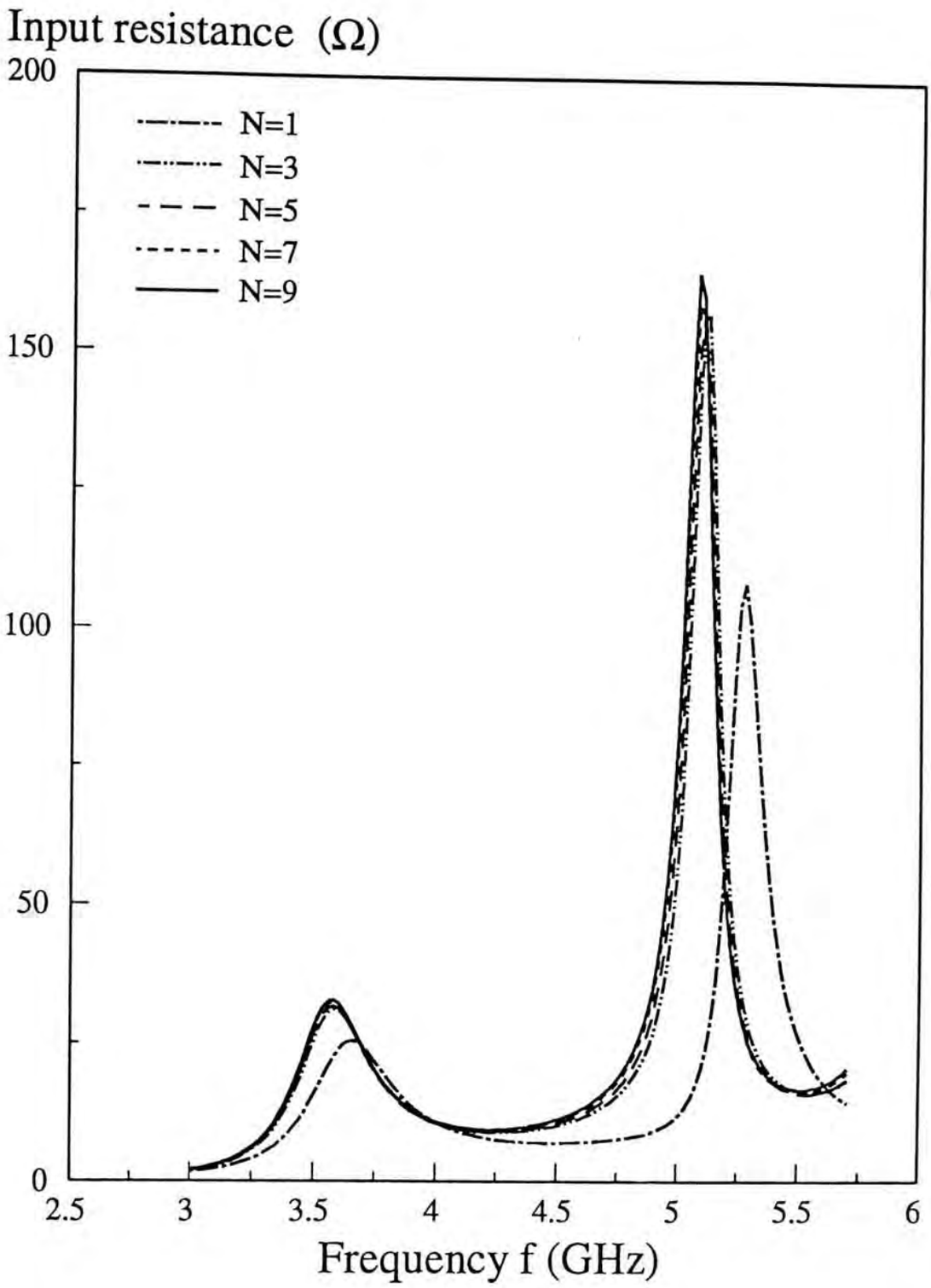

Fig. 2-19(a): Convergence check for the input resistance against frequency using reduced kernel with effective radius (with magnetic frill source and PWS functions): a=12.5 mm, b=6.4 mm, l=6.5 mm, ε_r=9.8, r_1=0.63 mm, r_2=2.0 mm.

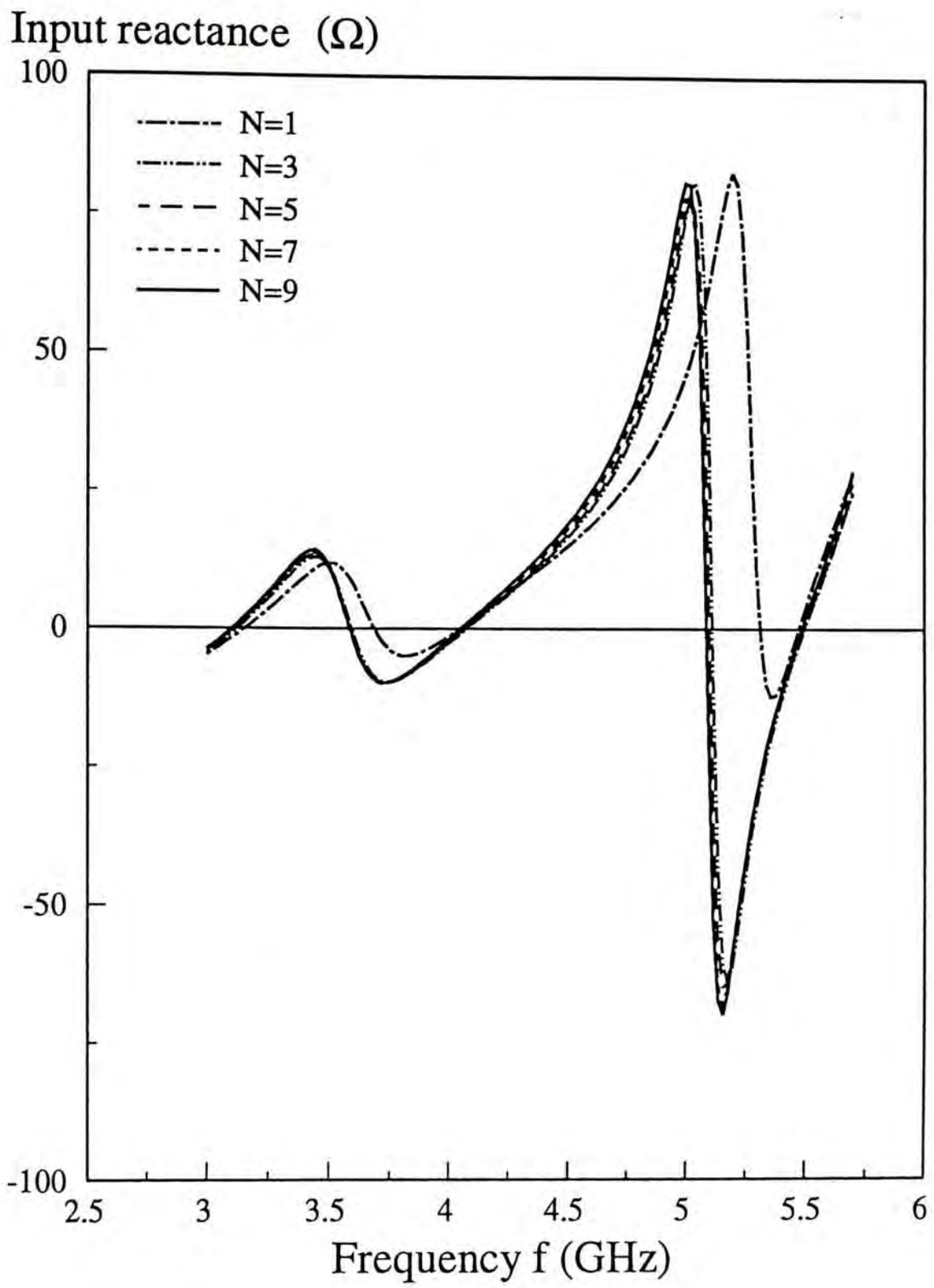

Fig. 2-19(b): Convergence check for the input reactance against frequency using reduced kernel with effective radius (with magnetic frill source and PWS functions): a=12.5 mm, b=6.4 mm, l=6.5 mm, ε_r=9.8, r_1=0.63 mm, r_2=2.0 mm.

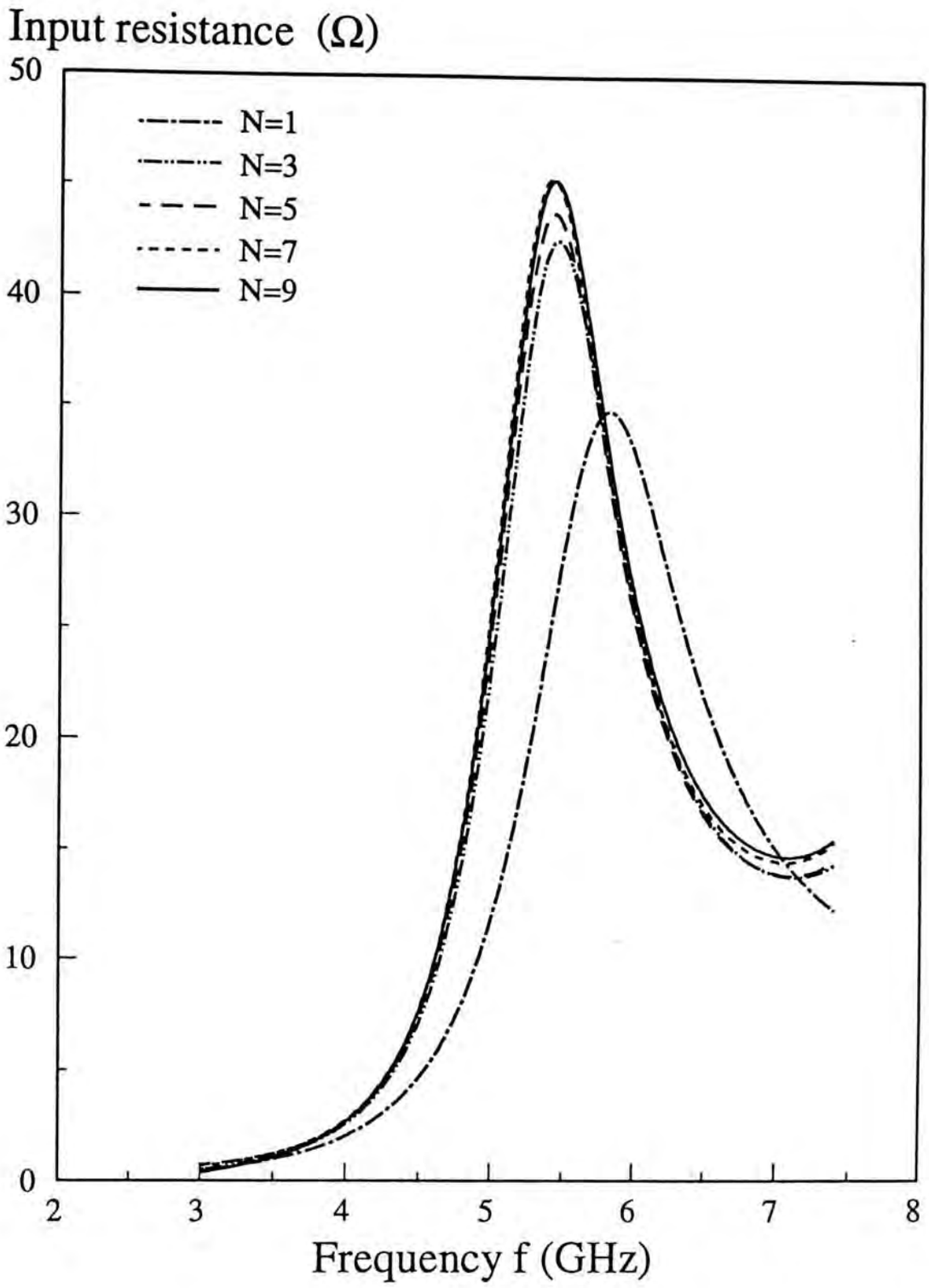

Fig. 2-20(a): Convergence check for the input resistance against frequency using reduced kernel with effective radius (with magnetic frill source and PWS functions): a=11.5 mm, b=0.0 mm, l=4.5 mm, ε_r=9.8, r_1=0.63 mm, r_2=2.0 mm.

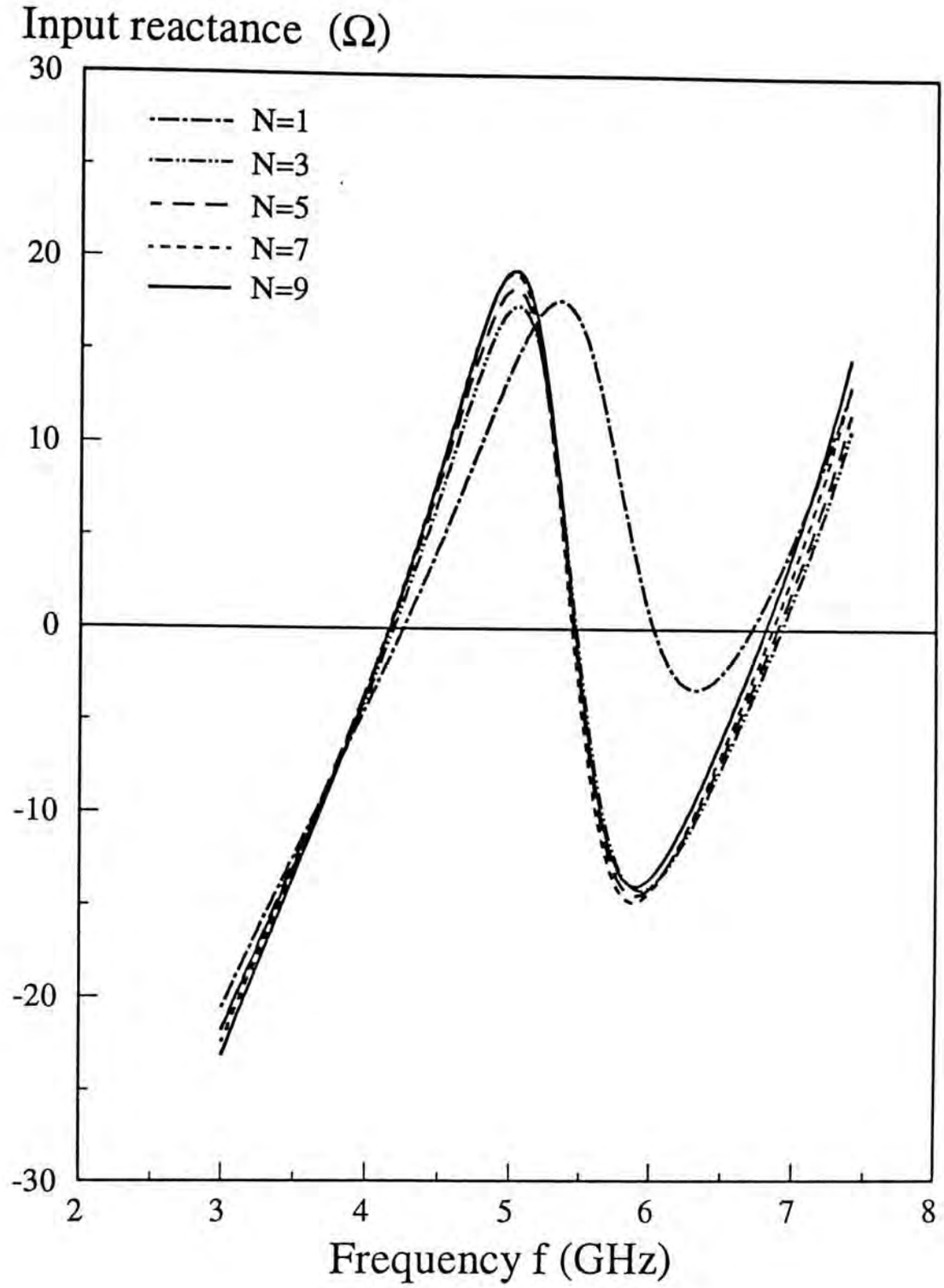

Fig. 2-20(b): Convergence check for the input reactance against frequency using reduced kernel with effective radius (with magnetic frill source and PWS functions): a=11.5 mm, b=0.0 mm, l=4.5 mm, ε_r=9.8, r_1=0.63 mm, r_2=2.0 mm.

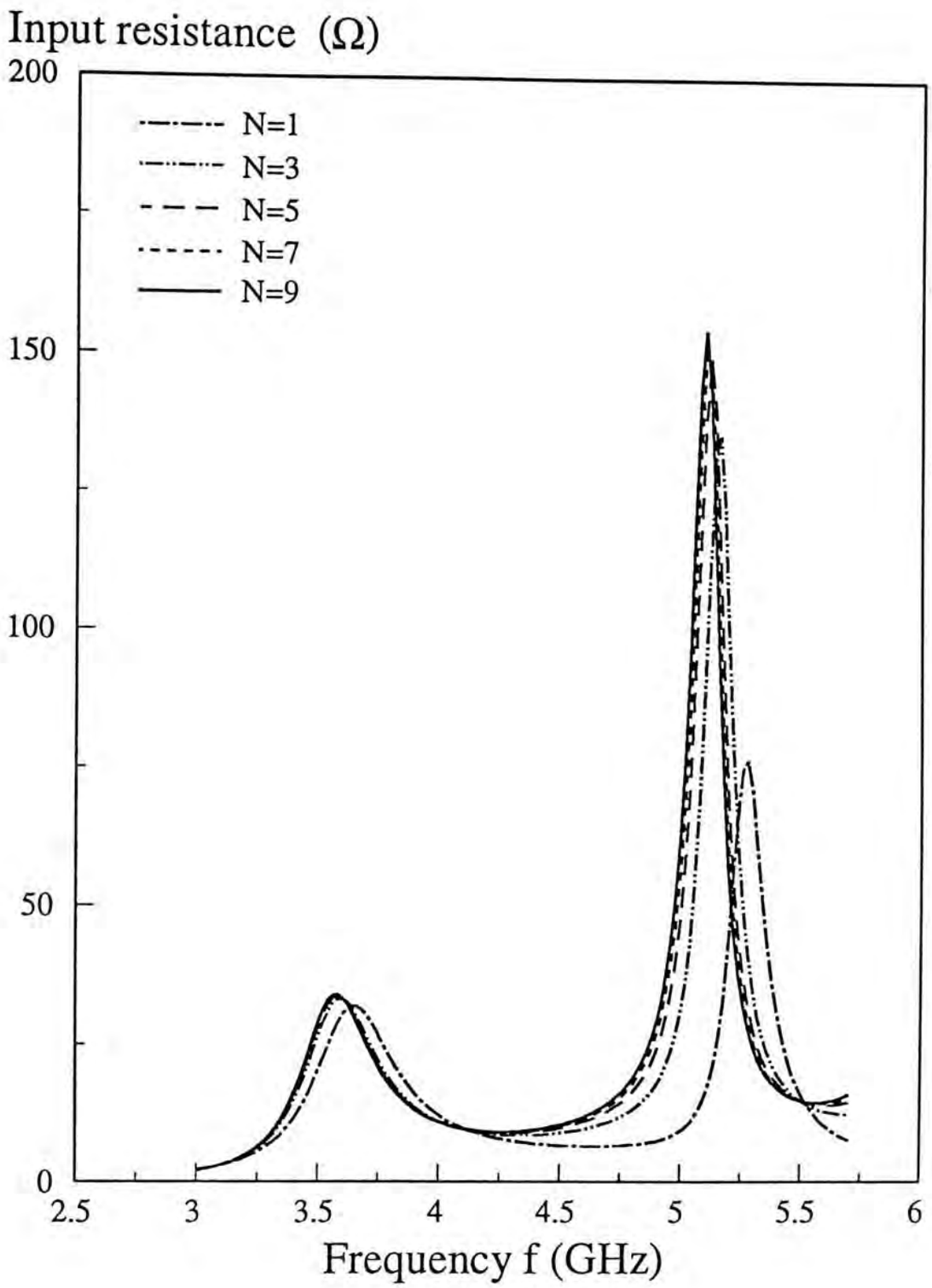

Fig. 2-21(a): Convergence check for the input resistance against frequency using the exact kernel (with magnetic frill source and EB functions):
a=12.5 mm, b=6.4 mm, l=6.5 mm, ε_r=9.8, r_1=0.63 mm, r_2=2.0 mm.

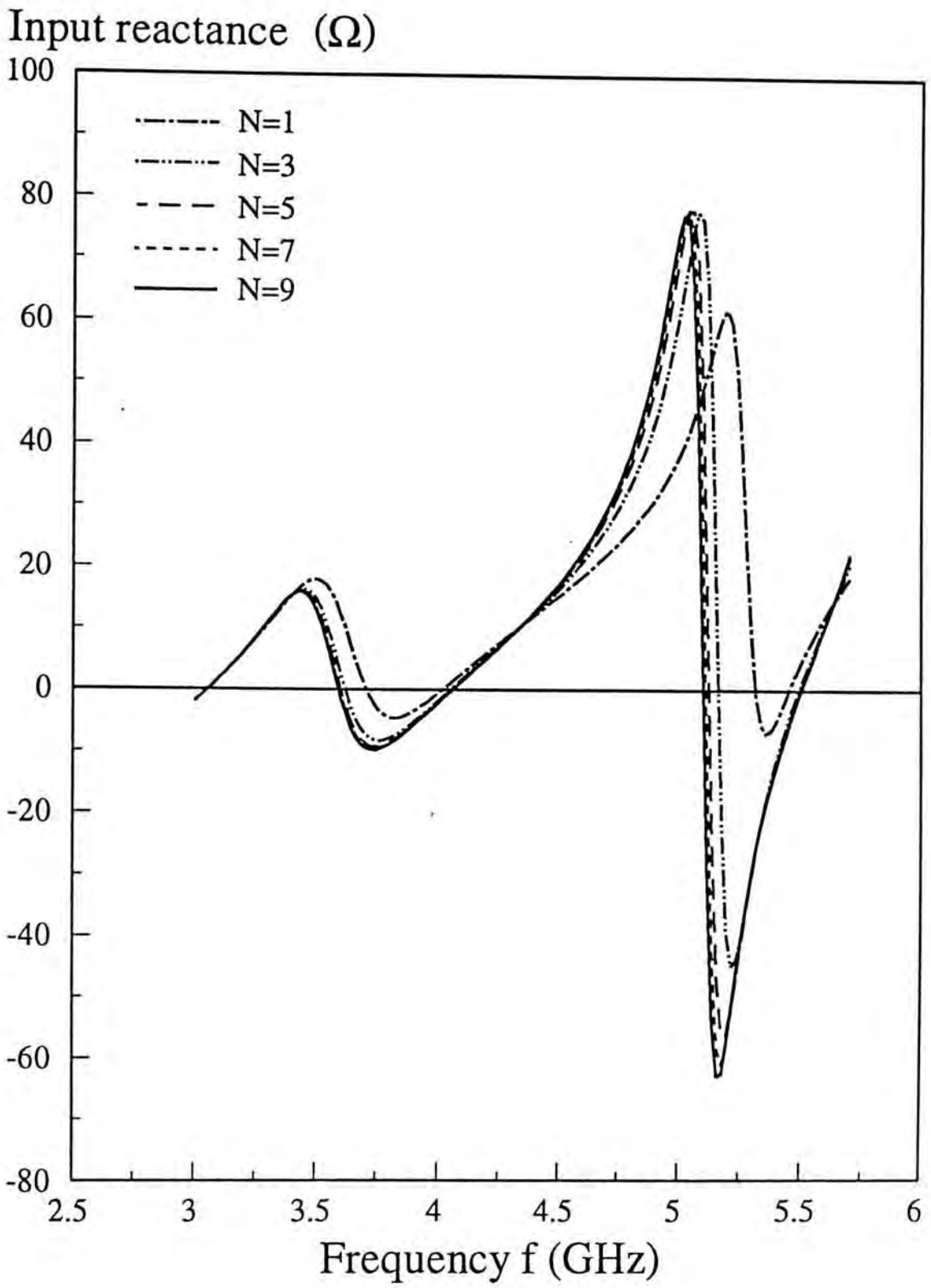

Fig. 2-21(b): Convergence check for the input reactance against frequency using the exact kernel (with magnetic frill source and EB functions):

a=12.5 mm, b=6.4 mm, l=6.5 mm, ε_r=9.8, r_1=0.63 mm, r_2=2.0 mm.

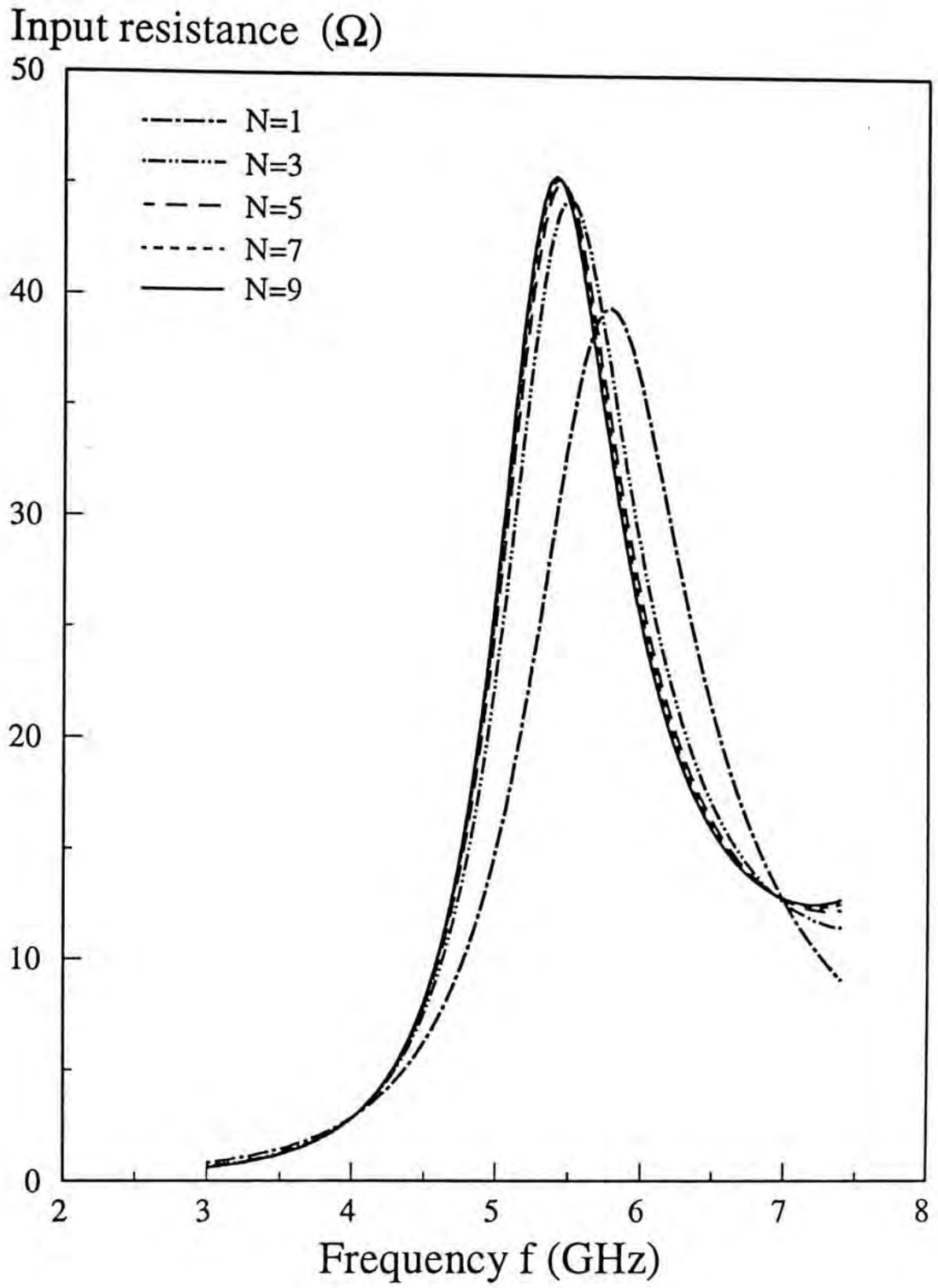

Fig. 2-22(a): Convergence check for the input resistance against frequency using the exact kernel (with magnetic frill source and EB functions):
a=11.5 mm, b=0.0 mm, l=4.5 mm, ε_r=9.8, r_1=0.63 mm, r_2=2.0 mm.

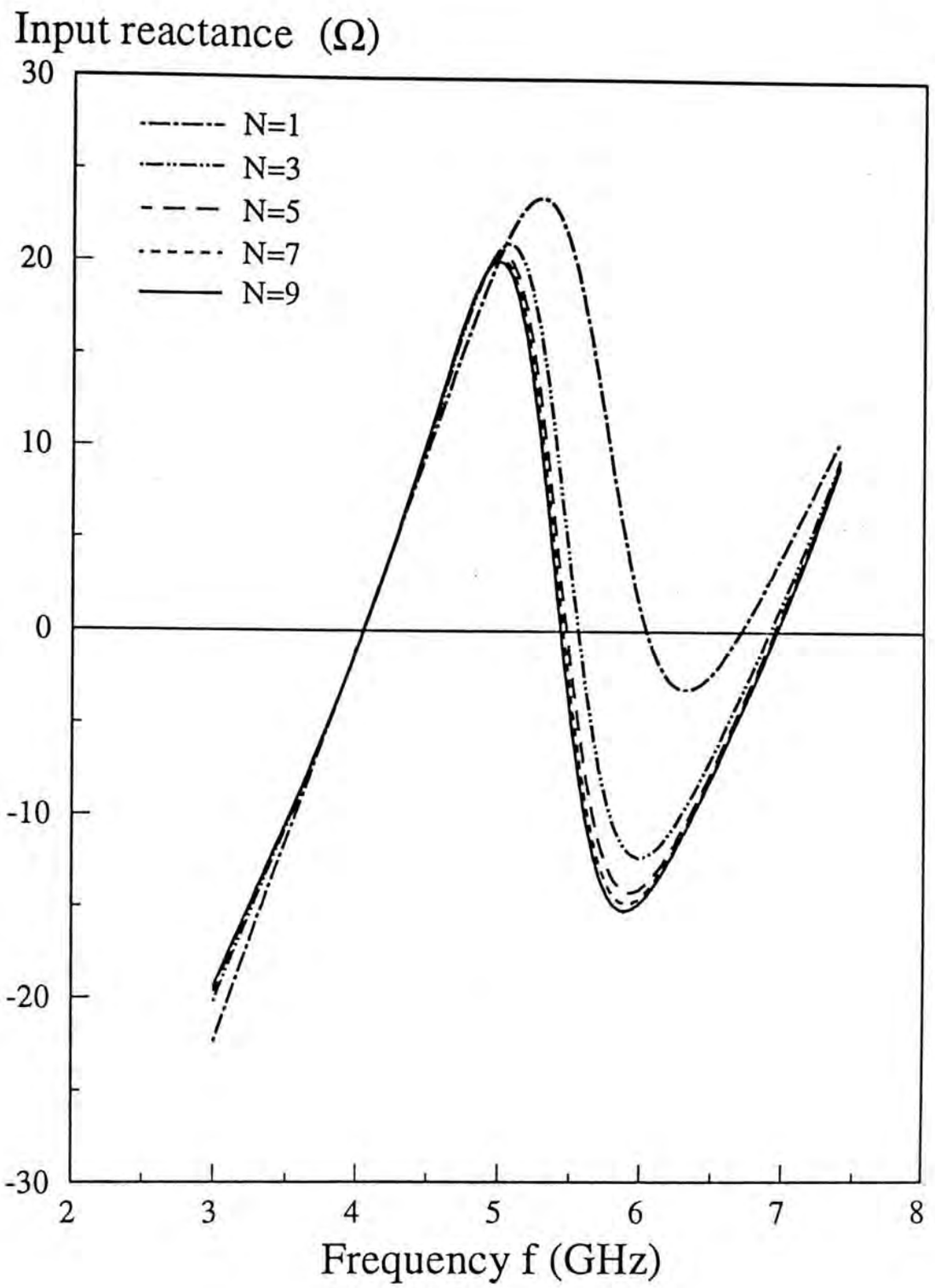

Fig. 2-22(b): Convergence check for the input reactance against frequency using the exact kernel (with magnetic frill source and EB functions):
a=11.5 mm, b=0.0 mm, l=4.5 mm, ε_r=9.8, r_1=0.63 mm, r_2=2.0 mm.

2.4.6 Measured and Computed Results

(A) Experimental Set-up

To verify the theoretical model, the input impedance of a coaxial probe-fed hemispherical DR antenna is measured with the experimental set-up shown in Appendix F. In the displaced probe case (b >0 in Fig. 2-1), a dielectric hemisphere of effective radius 12.5 mm (height 12.3 mm and base radius 12.8 mm) and dielectric constant ε_r=9.8 was used. A Radiall coaxial probe of diameter 1.25 mm and length 6.5 mm penetrated the DR with displacement b=6.4 mm. For the case of a center fed probe, a dielectric hemisphere of effective radius 11.5 mm (height 11.2 mm and base radius 11.9 mm) and dielectric constant ε_r=9.8 was measured. A Radiall coaxial probe of diameter 1.25 mm and length 4.5 mm penetrated the center of the dielectric hemisphere (b=0). In both cases, the ground plane was a 60 cm square copper plate. Since a diamond drill bit of 1.25 mm diameter was unavailable, a slightly larger bit of diameter 1.45 mm was used. In the measurements, the reference plane was chosen at the junction between coaxial aperture and DR antenna. It is established by shorting the probe to the ground plane at the aperture position. Measurements were taken using an HP8510C network analyzer. Port extension, which affects only the phase of the reflection coefficient, is used to set the reference plane for the input impedance measurements.

(B) Displaced Probe-fed (b>0)

Fig2-23 shows the theoretical results using the EB modes as well as the PWS modes. Experimental result is also shown in the same figure for comparison. It is seen that the EB result and the PWS result are close to each other. Moreover, they agree reasonably well with the measured result. Note that the second resonance is mixed by the TE_{221} mode and the TM_{101} mode as discussed in Section 2.4.5.

The comparison between the traditional reduced kernel result (with PWS modes) and the effective result is shown in Fig. 2-24. Again, the results are close to each other. This shows that the length to radius ratio of the probe ($l/r_1 = 10.4$) is large enough to use the reduced kernel.

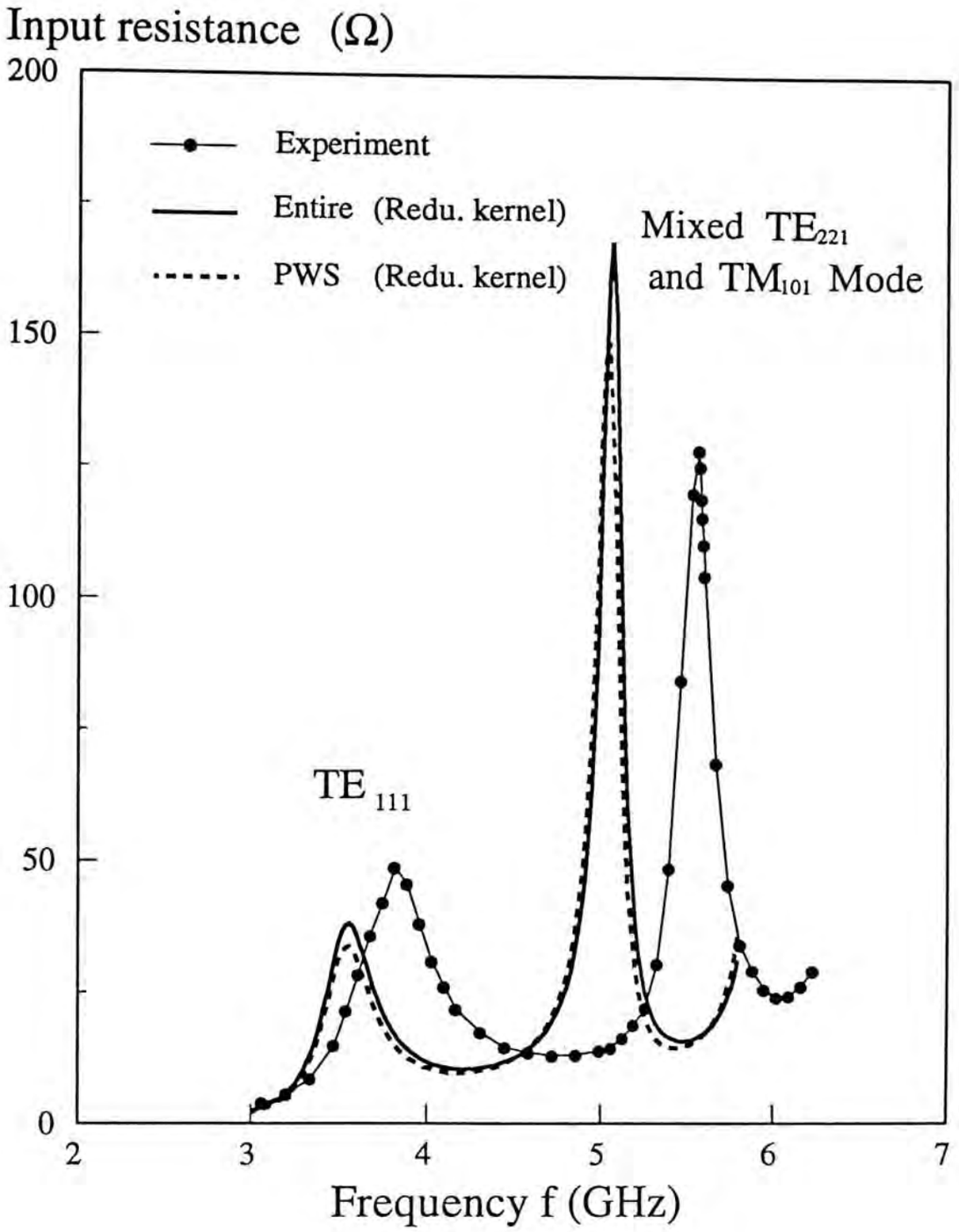

Fig. 2-23(a): Computed and measured input resistance against frequency (using magnetic frill source model): a=12.5 mm, b=6.4 mm, l=6.5 mm, ε_r=9.8, r_1=0.63 mm, r_2=2.0 mm.

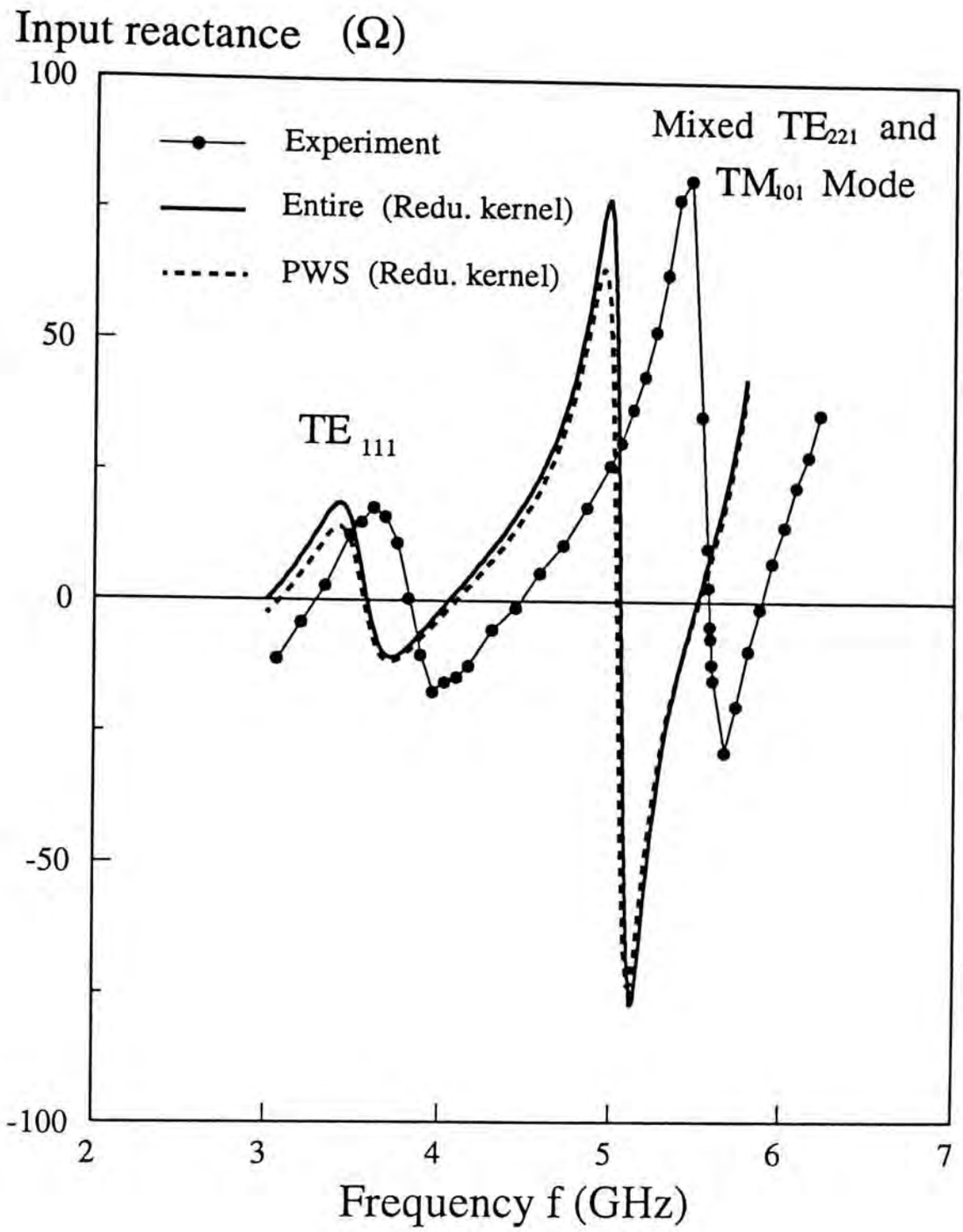

Fig. 2-23(b): Computed and measured input reactance against frequency (using magnetic frill source model): a=12.5 mm, b=6.4 mm, l=6.5 mm, ε_r=9.8, r_1=0.63 mm, r_2=2.0 mm.

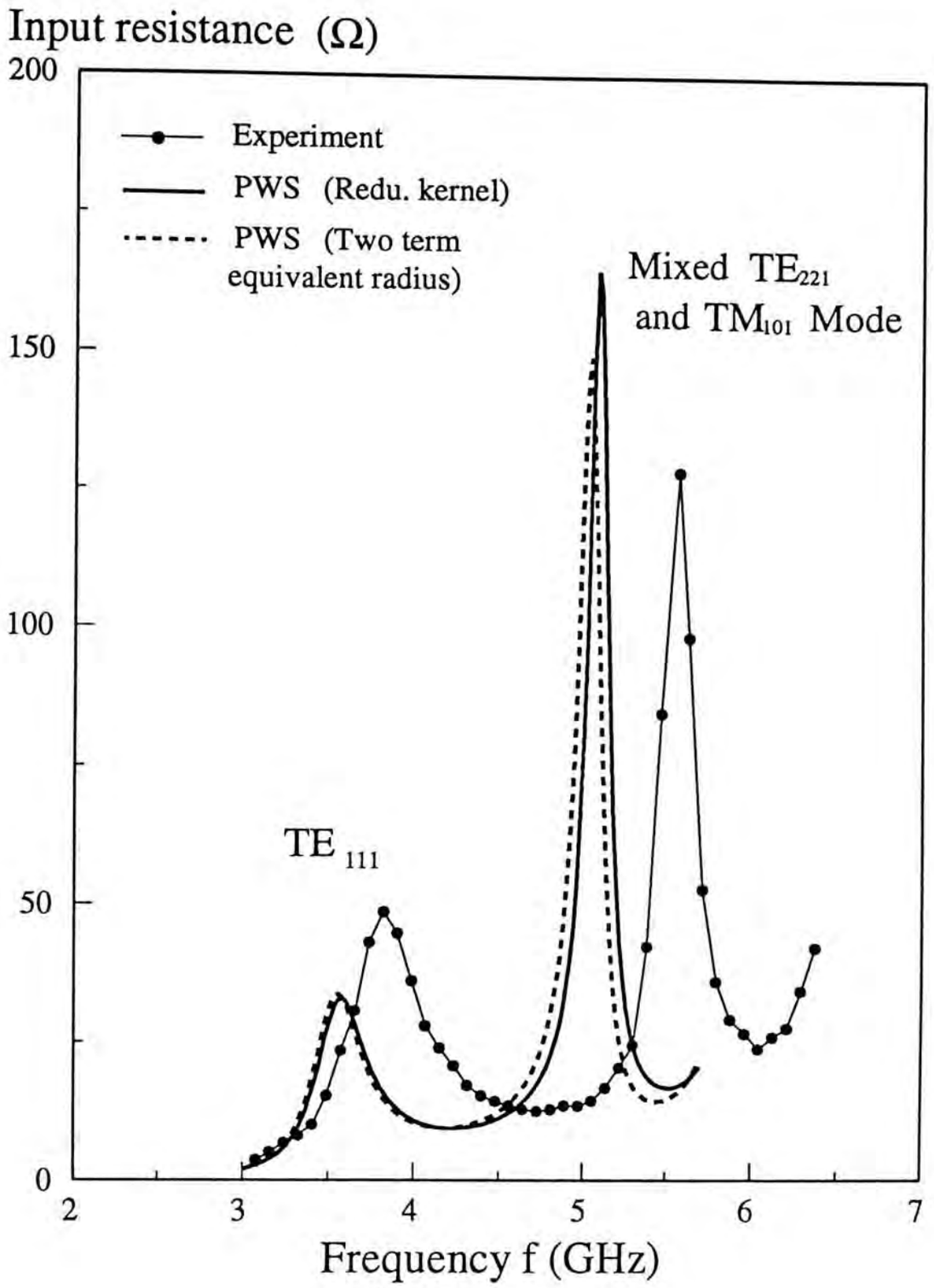

Fig. 2-24(a): Computed and measured input resistance against frequency (using magnetic frill source model): a=12.5 mm, b=6.4 mm, l=6.5 mm, ε_r=9.8, r_1=0.63 mm, r_2=2.0 mm.

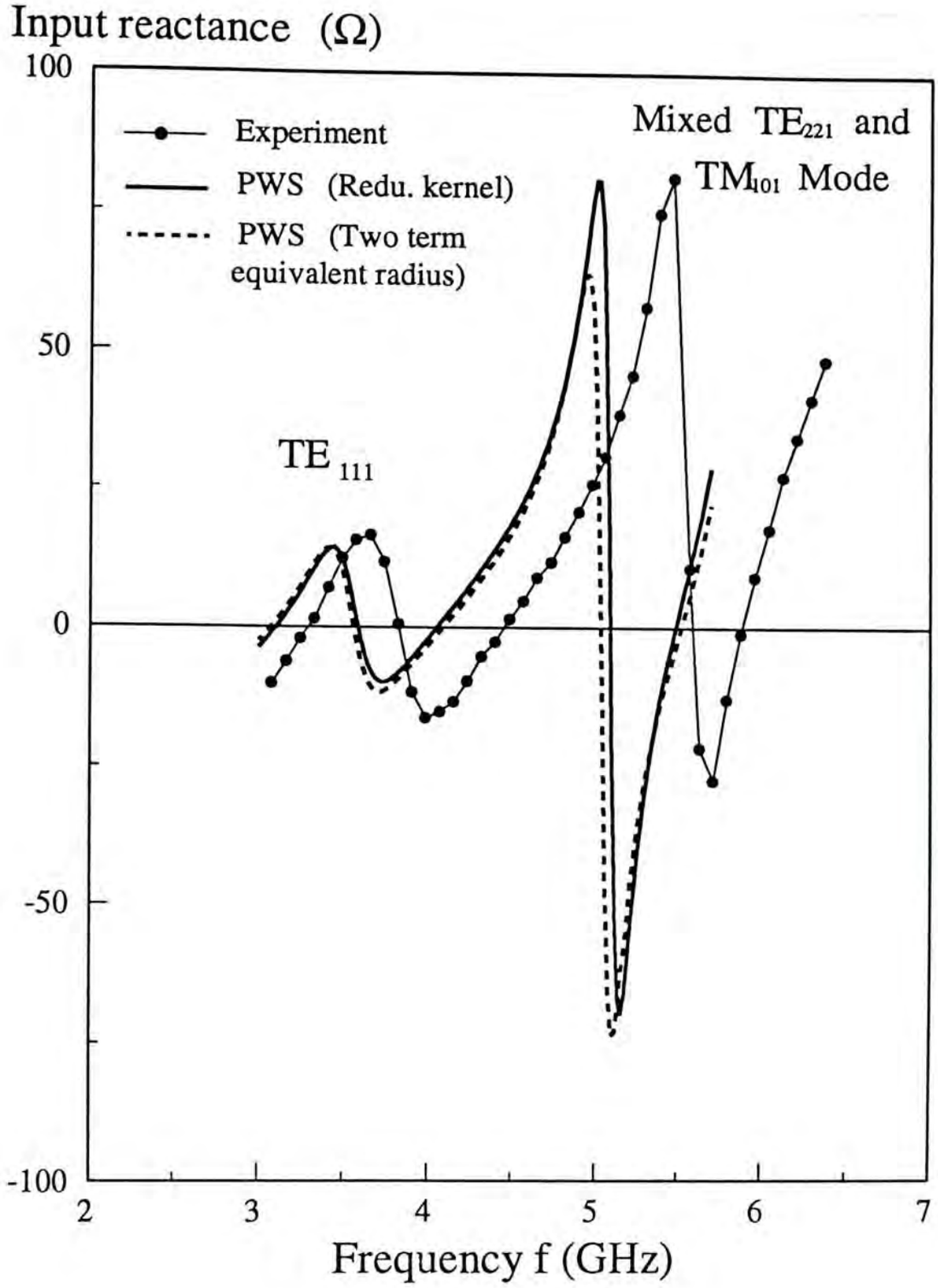

Fig. 2-24(b): Computed and measured input reactance against frequency (using magnetic frill source model): a=12.5 mm, b=6.4 mm, l=6.5 mm, ε_r=9.8, r_1=0.63 mm, r_2=2.0 mm.

Fig. 2-25 compares the effective radius result to the exact kernel one. Reasonable agreement between the results are obtained, showing again that the use of the reduced kernel is justified in this antenna setting.

Fig. 2-26 shows the input impedance of the DR antenna fed by a displaced probe as a function of frequency for different probe lengths. It is seen that the longer the probe length, the larger the input impedance. This suggests that performing impedance matching is possible by varying the probe length.

The TE_{111} mode input impedance of the DR antenna as a function of the probe displacement b is shown in Fig. 2-27. It can be seen that the TE_{111} mode cannot be excited as discussed before when the probe is near the center of the DR. However, the probe also cannot be moved too far from the center if one wants to have a pure resistance for impedance matching, the reason being that there is significant capacitive reactance as the probe approaches the edge of the DR. Again, the longer the probe, the larger the input impedance.

The effect of the dielectric constant ε_r on the input impedance for the TE_{111} mode is shown in Fig. 2-28. The figure shows that the resonant frequency decreases with ε_r. It is also seen that the input impedance increases with, and hence the radiated power decreases with, increasing ε_r. Moreover, the higher the ε_r, the narrower the bandwidth and hence the higher the Q factor. This is consistent with the fact that material of high ε_r is a poor radiator and has a high Q factor.

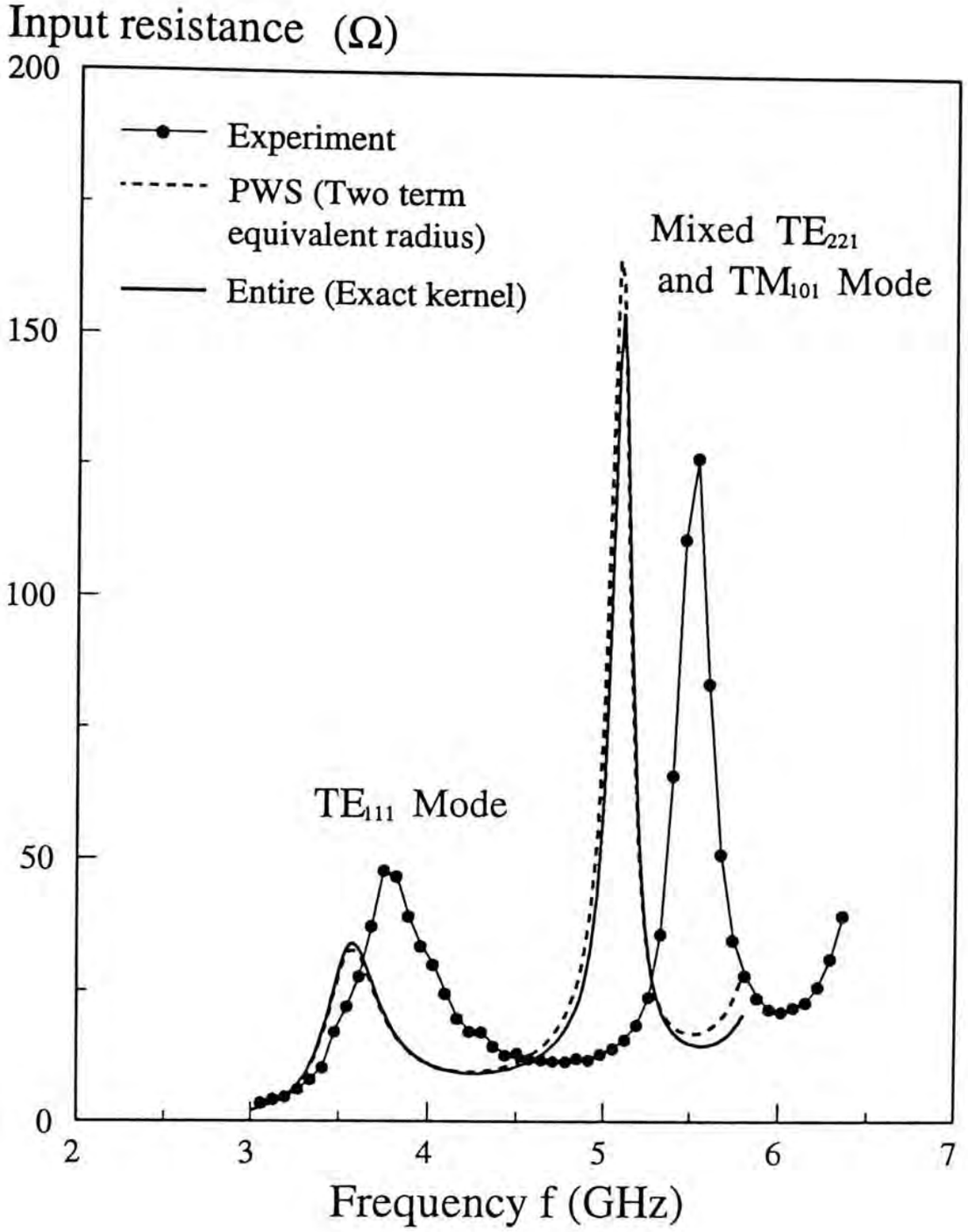

Fig. 2-25(a): Computed and measured input resistance against frequency (using magnetic frill source model): a=12.5 mm, b=6.4 mm, l=6.5 mm, ε_r=9.8, r_1=0.63 mm, r_2=2.0 mm.

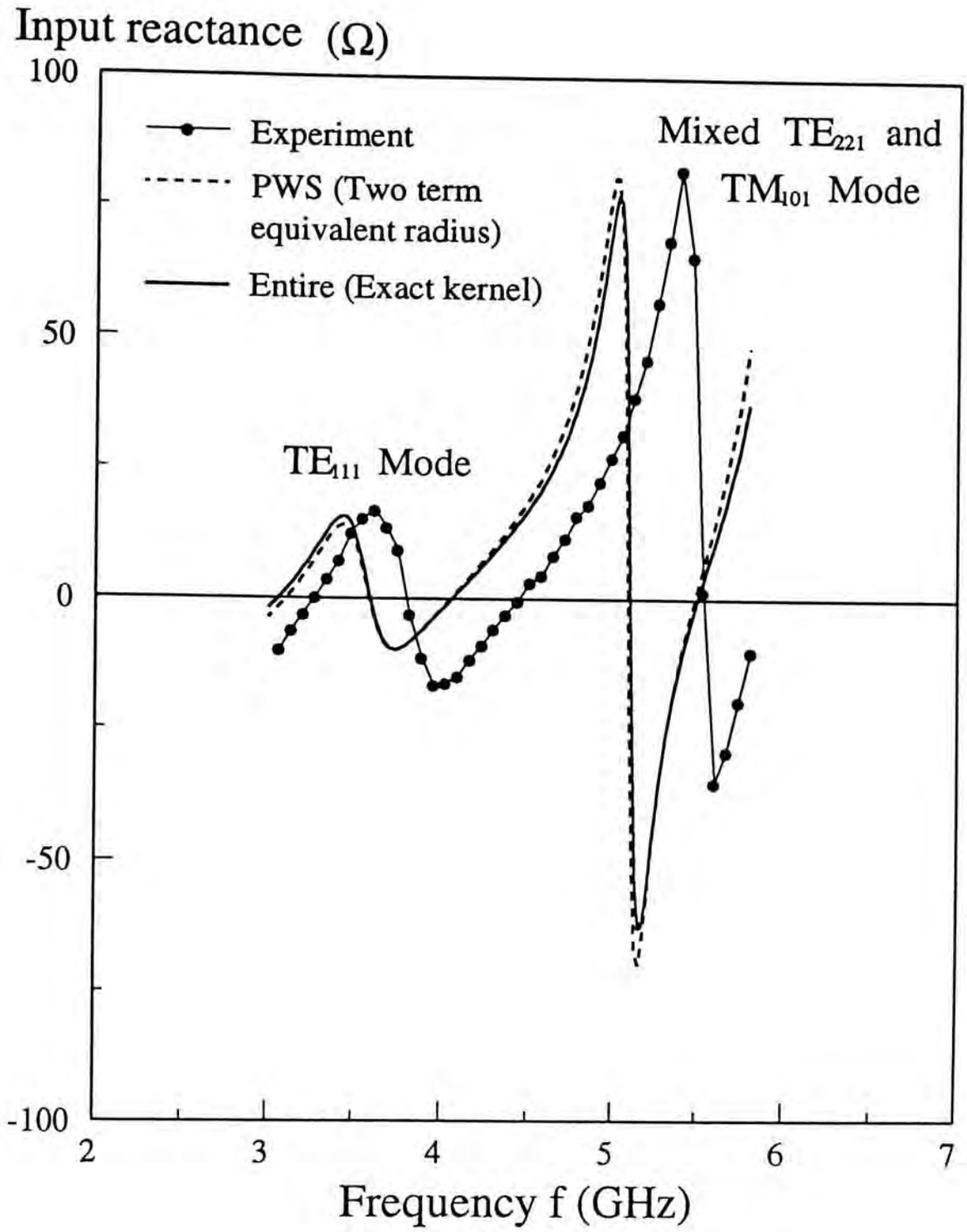

Fig. 2-25(b): Computed and measured input reactance against frequency (using magnetic frill source model): a=12.5 mm, b=6.4 mm, l=6.5 mm, ε_r=9.8, r_1=0.63 mm, r_2=2.0 mm.

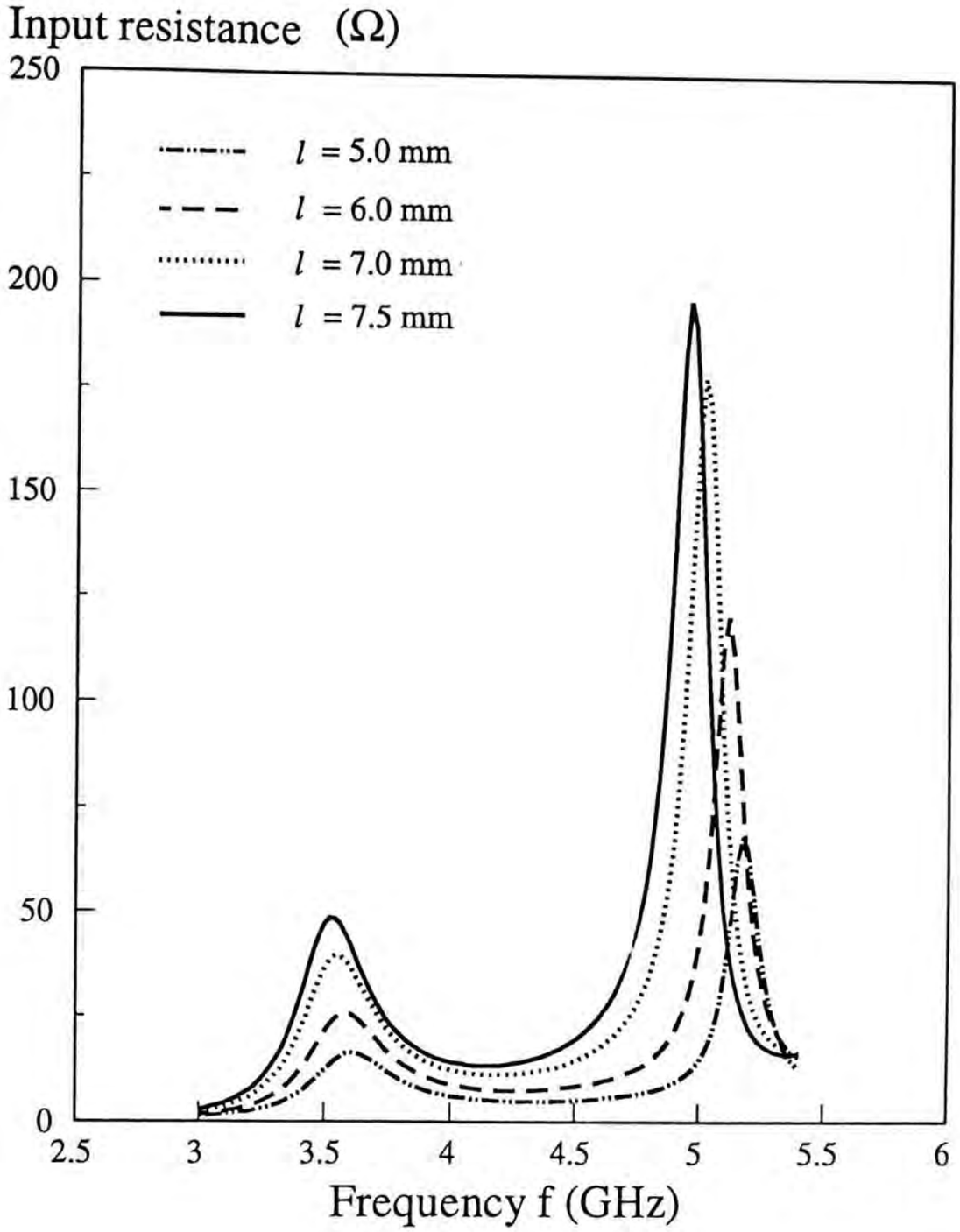

Fig. 2-26(a): Computed input resistance against frequency for different probe lengths using traditional reduced kernel with PWS modes and magnetic frill source model: a=12.5 mm, b=6.4 mm, ε_r=9.8, r_1=0.63 mm, r_2=2.0 mm.

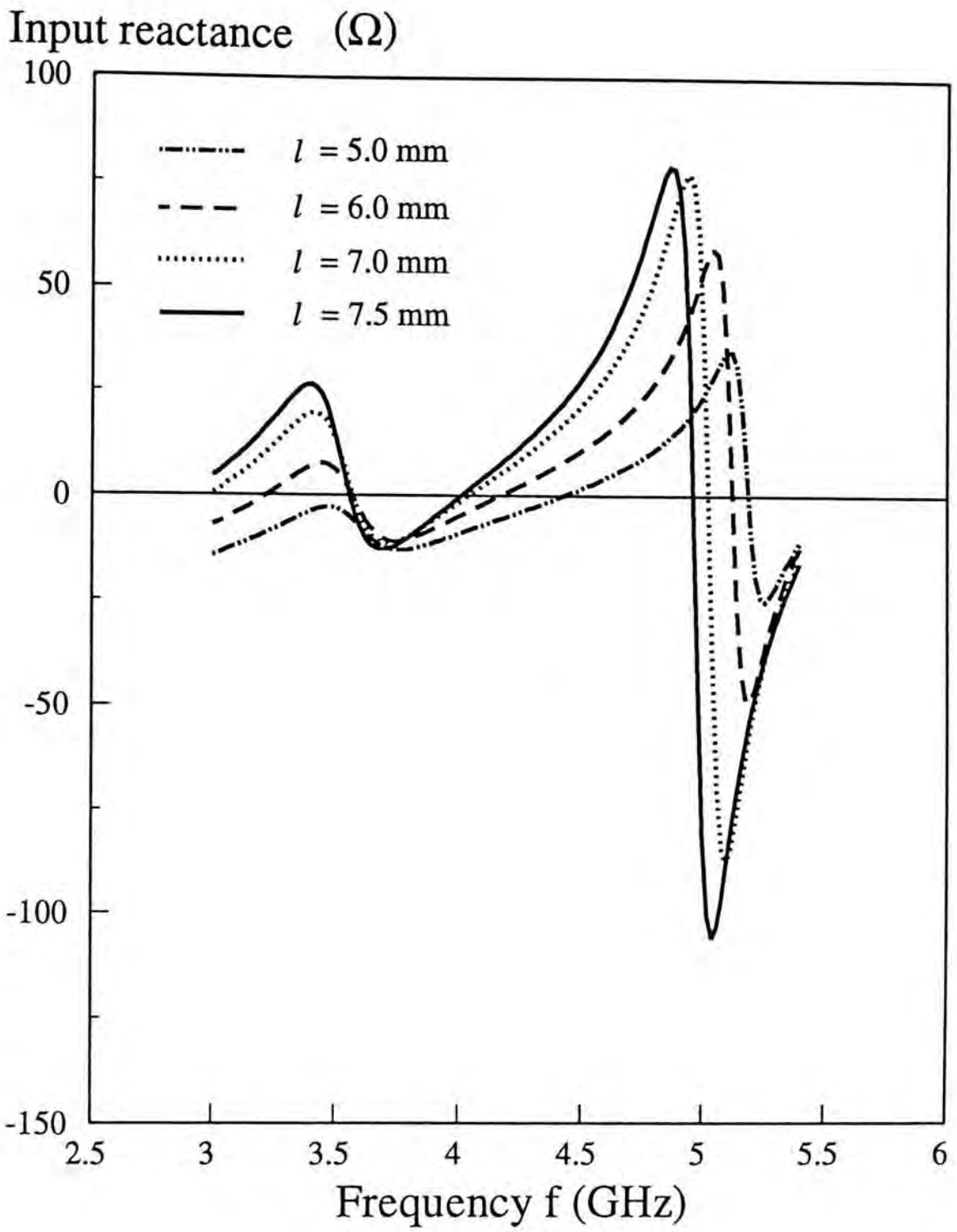

Fig. 2-26(b): Computed input reactance against frequency for different probe lengths using traditional reduced kernel with PWS modes and magnetic frill source model: a=12.5 mm, b=6.4 mm, ε_r=9.8, r_1=0.63 mm, r_2=2.0 mm.

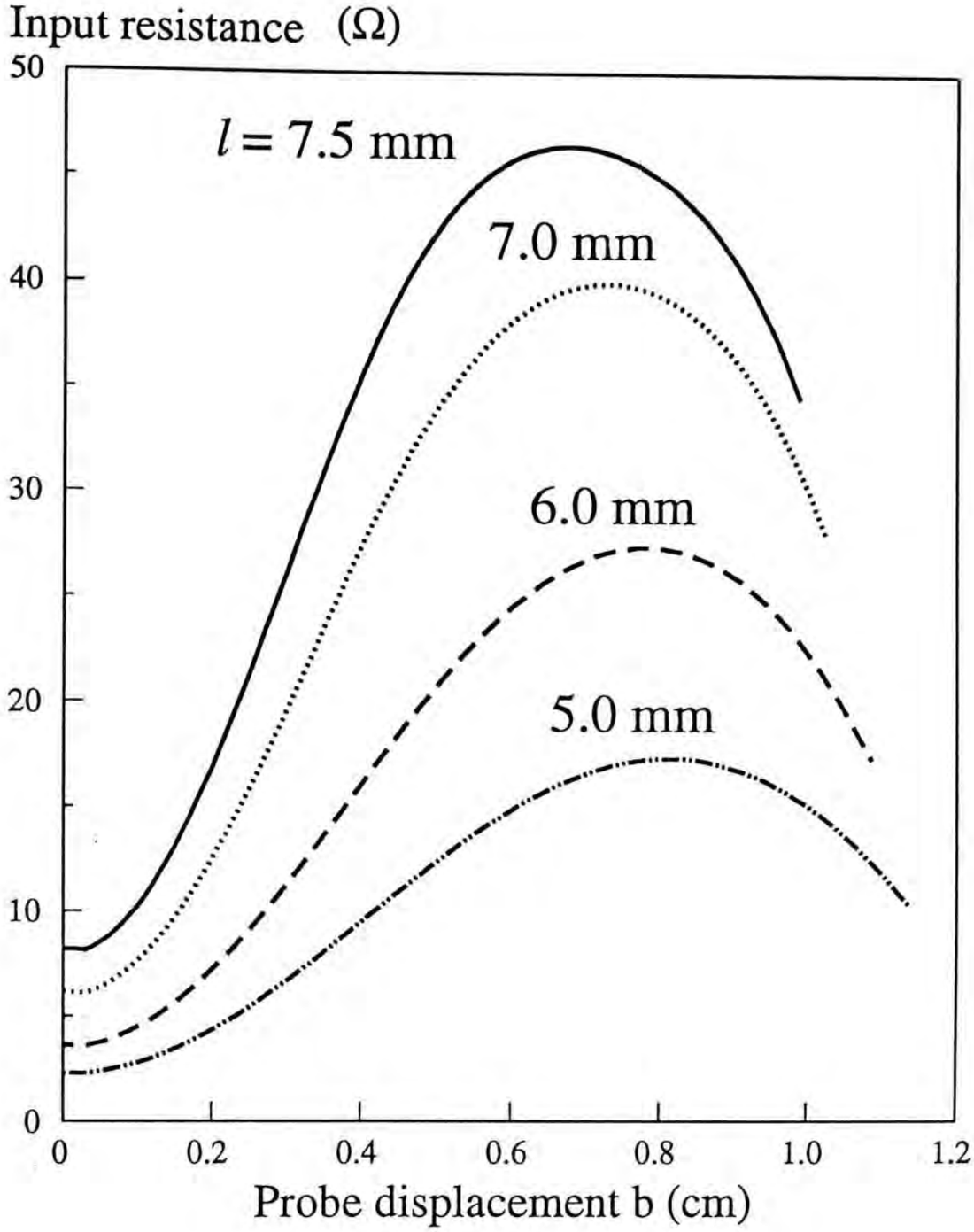

Fig. 2-27(a): Computed input resistance against displacement for different probe lengths using traditional reduced kernel with PWS modes and magnetic frill source model: a=12.5 mm, f=3.57 GHz, ε_r=9.8, r_1=0.63 mm, r_2=2.0 mm.

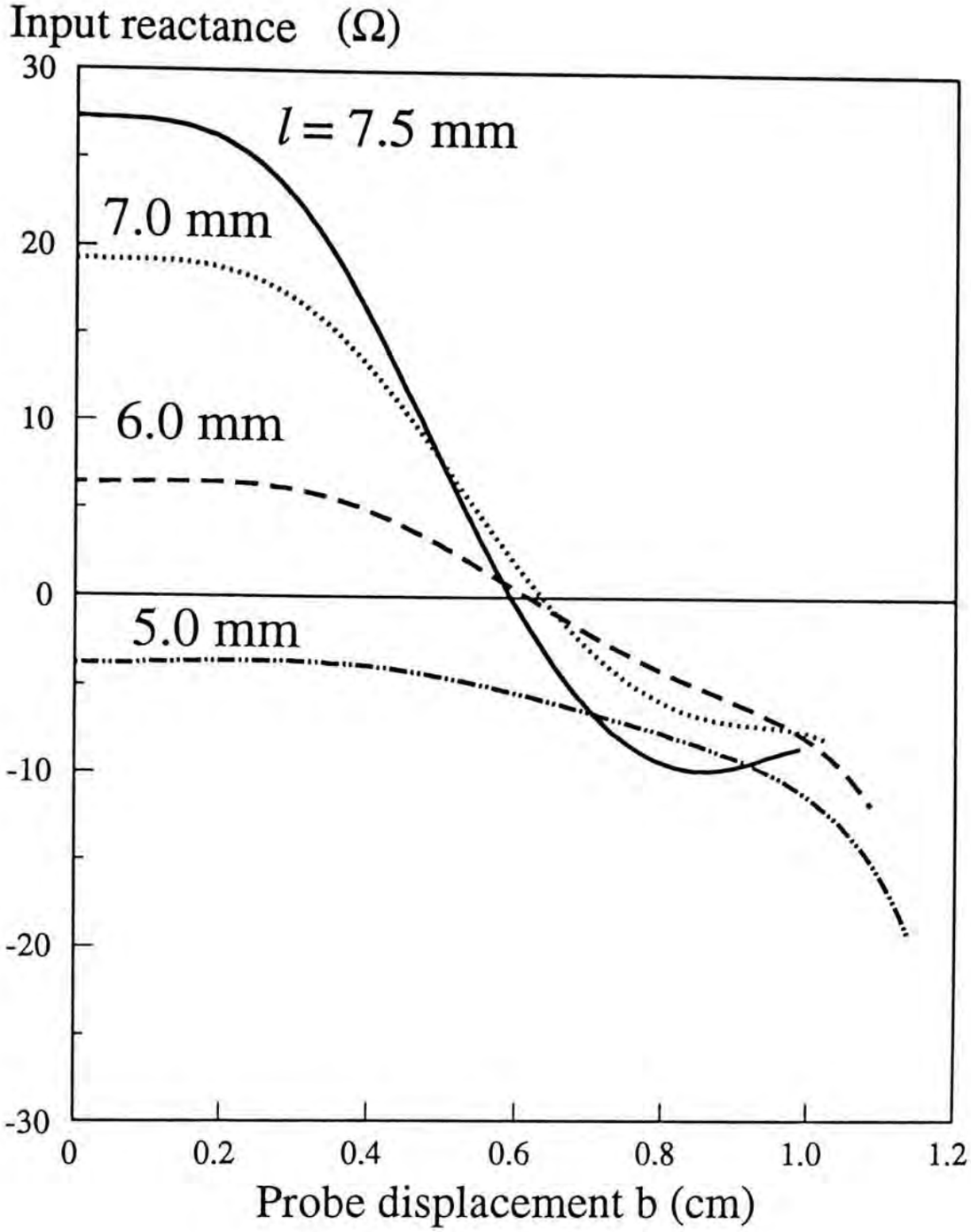

Fig. 2-27(b): Computed input reactance against displacement for different probe lengths using traditional reduced kernel with PWS modes and magnetic frill source model: a=12.5 mm, f=3.57 GHz, ε_r=9.8, r_1=0.63 mm, r_2=2.0 mm.

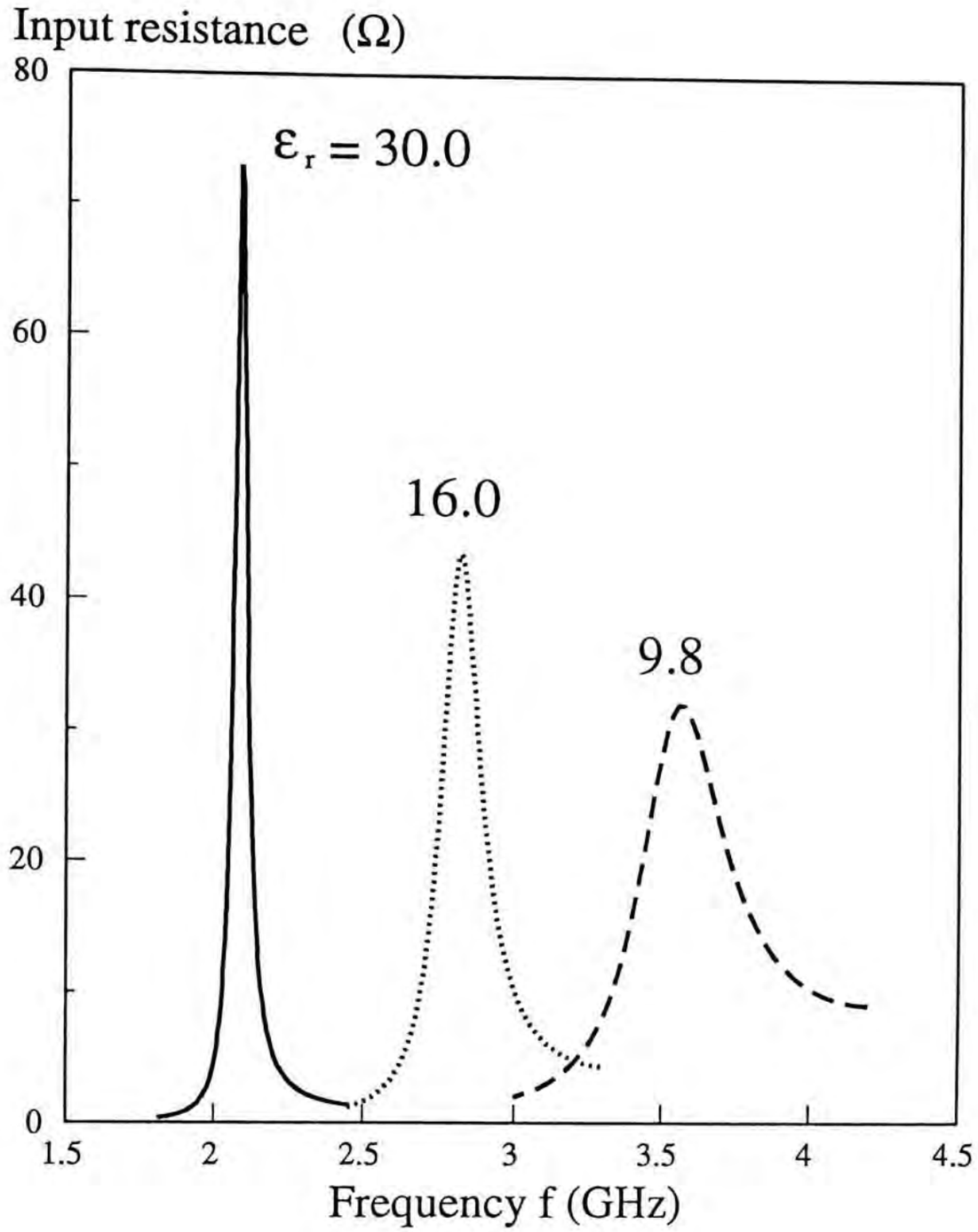

Fig. 2-28(a): Computed input resistance against frequency for different dielectric constant using traditional reduced kernel with PWS modes and magnetic frill source model: a=12.5 mm, b=6.4 mm, l=6.5 mm, r_1=0.63 mm, r_2=2.0 mm.

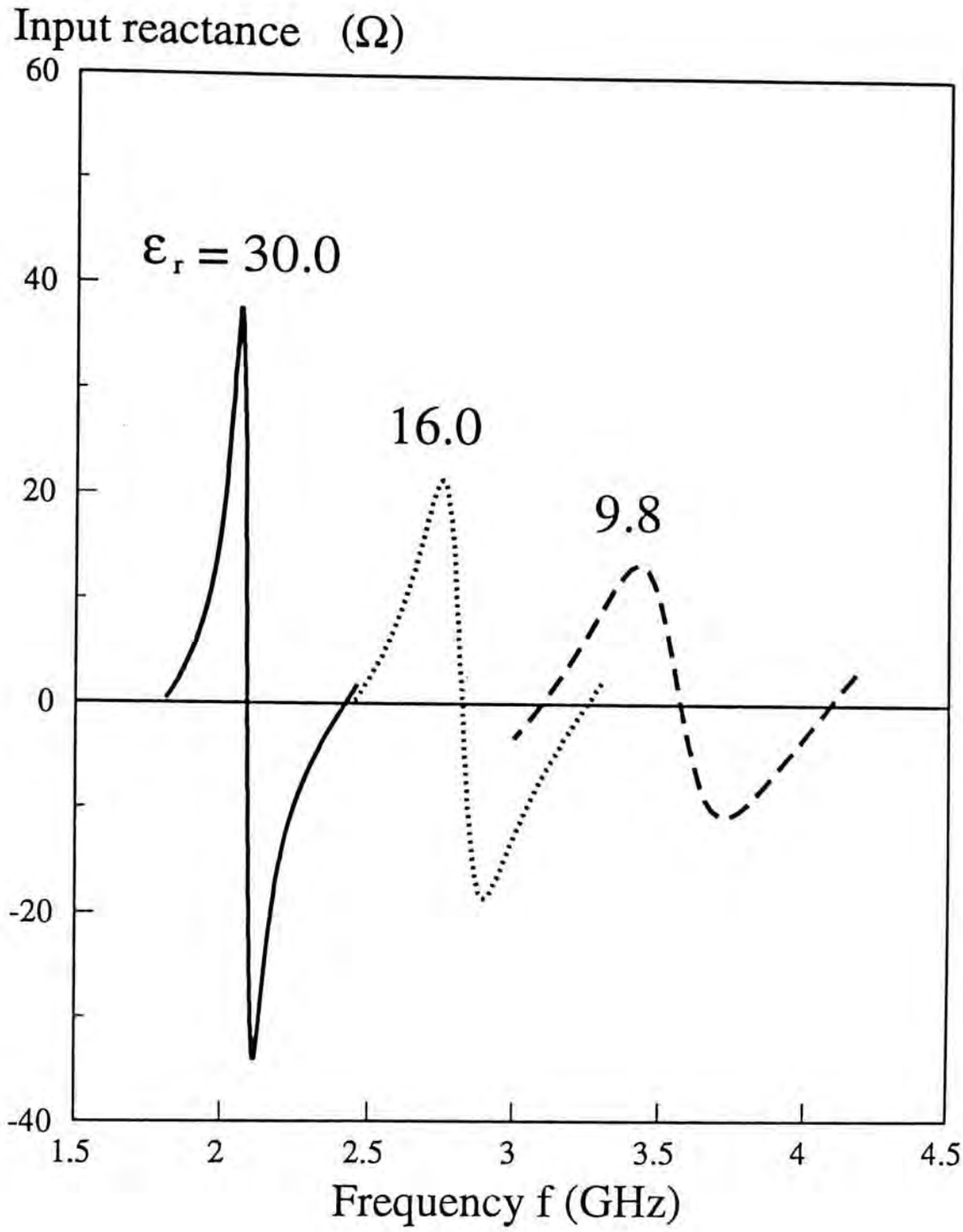

Fig. 2-28(b): Computed input reactance against frequency for different dielectric constant using traditional reduced kernel with PWS modes and magnetic frill source model: a=12.5 mm, b=6.4 mm, l=6.5 mm, r_1=0.63 mm, r_2=2.0 mm.

(C) Center Probe-fed (b=0)

Fig. 2-29 shows the comparison between theory and experiment for the input impedance of the center probe-fed DR antenna as a function of frequency. The traditional reduced kernel results (both EB and PWS modes), the two term equivalent radius result and the exact kernel result are all shown in the same figure for comparison. It is seen that the exact kernel as well as the two term equivalent radius give better results than that given by the traditional reduced kernel. This is expected as the probe length to radius ratio (l/r_1) is now only 7.36, which is not large enough to justify using the reduced kernel. Again the result using the exact kernel is very close to that using the two term equivalent radius. Note that no TE mode can be excited in this case because the current on the probe is now mainly $\hat{r}$-directed. This is different from the case of the displaced probe in which both TE and TM modes are excited as discussed in Section 2.2.

Fig. 2-30 shows the input impedance of the DR antenna fed by a centered probe as a function of frequency for different probe lengths. Like the displaced probe case, the input impedance increases with the probe length, and therefore impedance matching is also possible for the center probe-fed DR antenna.

The effect of the dielectric constant ε_r on the input impedance for the TM_{101} mode is shown in Fig. 2-31. The results are similar to the displaced probe case as shown in Fig. 2-28, only that the impedance level increases very fast with ε_r in the present case. This is expected as one can see from Figs. 2-7 and 2-10 in Section 2.3.2 that the dependence of the input resistance on ε_r appears to be almost exactly linear for the TE_{111} mode, whereas the curves appear to be almost exponential for the TM_{101} mode.

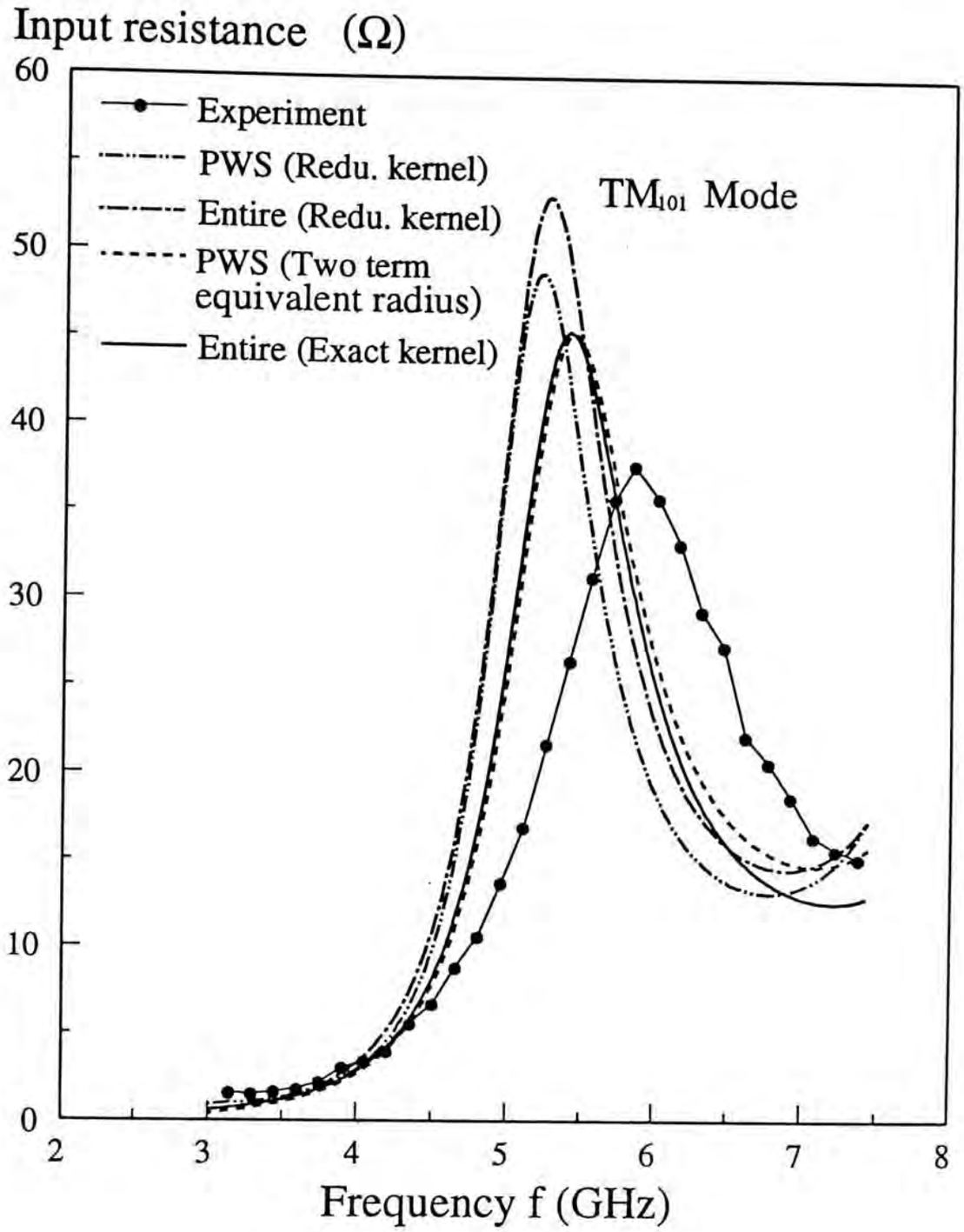

Fig. 2-29(a): Computed and measured input resistance against frequency using magnetic frill source model: a=11.5 mm, b=0.0 mm, l=4.5 mm, ε_r=9.8, r_1=0.63 mm, r_2=2.0 mm.

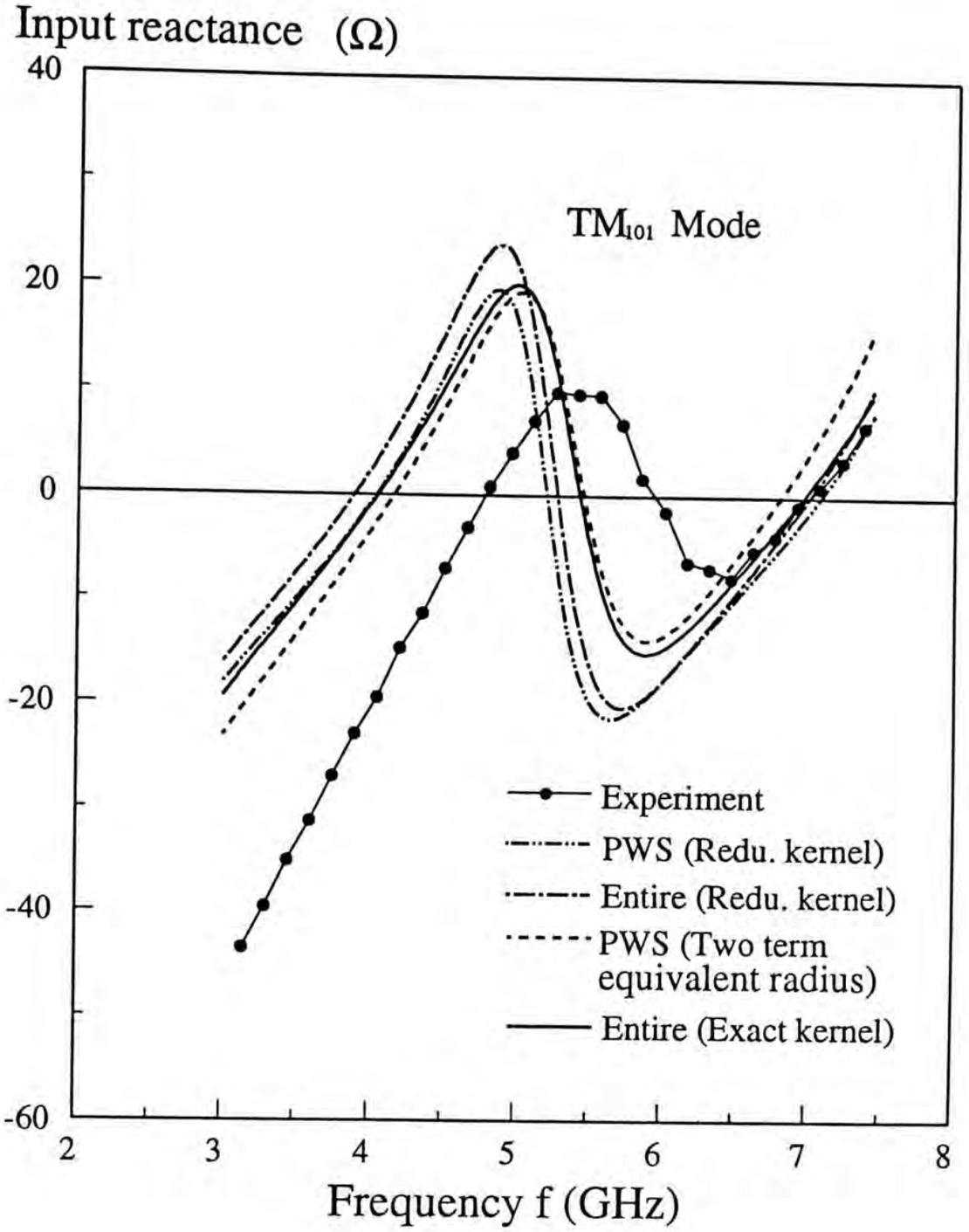

Fig. 2-29(b): Computed and measured input reactance against frequency using magnetic frill source model: a=11.5 mm, b=0.0 mm, l=4.5 mm, ε_r=9.8, r_1=0.63 mm, r_2=2.0 mm.

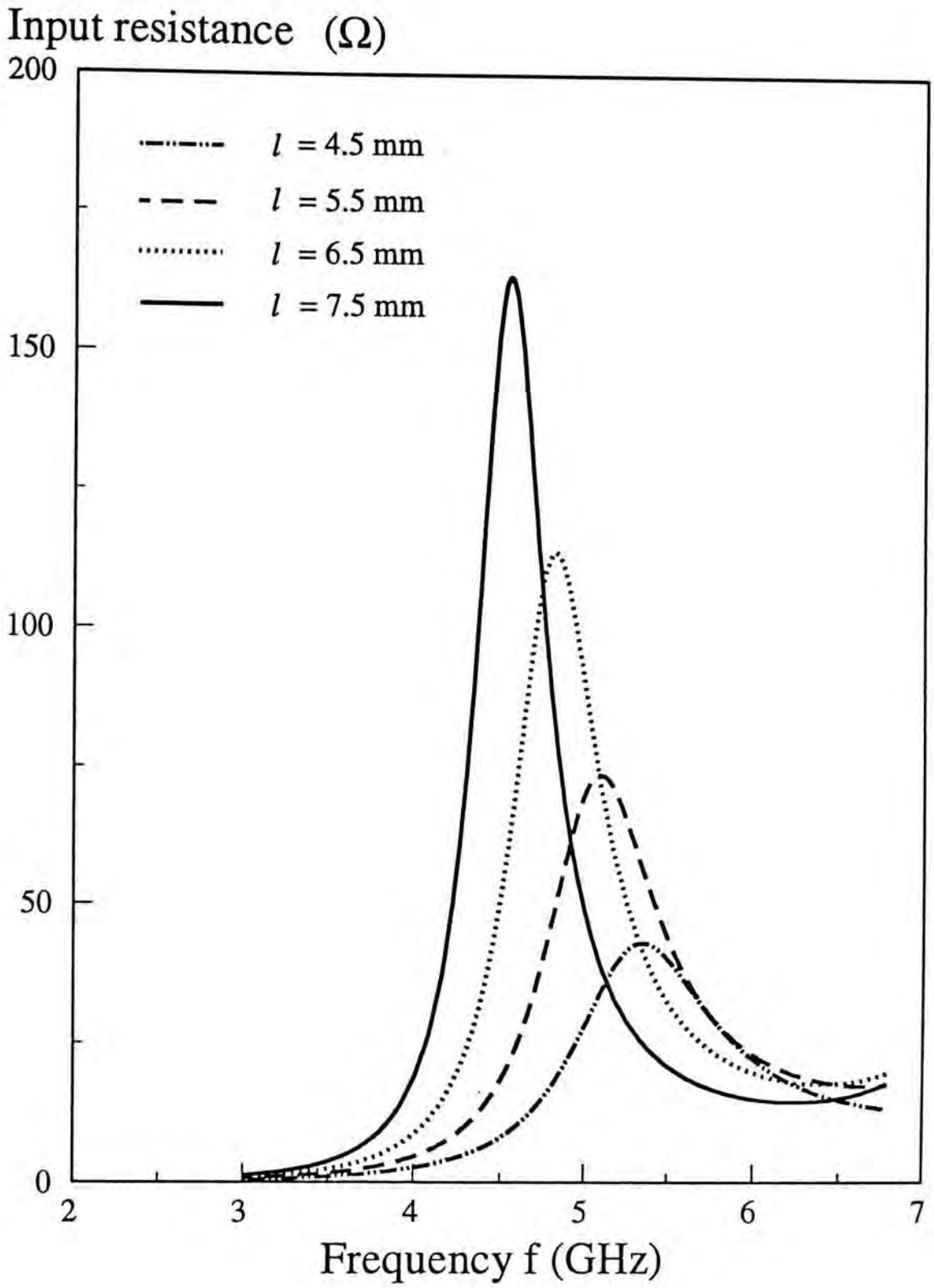

Fig. 2-30(a): Computed input resistance against frequency for different probe lengths using traditional reduced kernel with PWS modes and magnetic frill source model: a=11.5 mm, b=0.0 mm, ε_r=9.8, r_1=0.63 mm, r_2=2.0 mm.

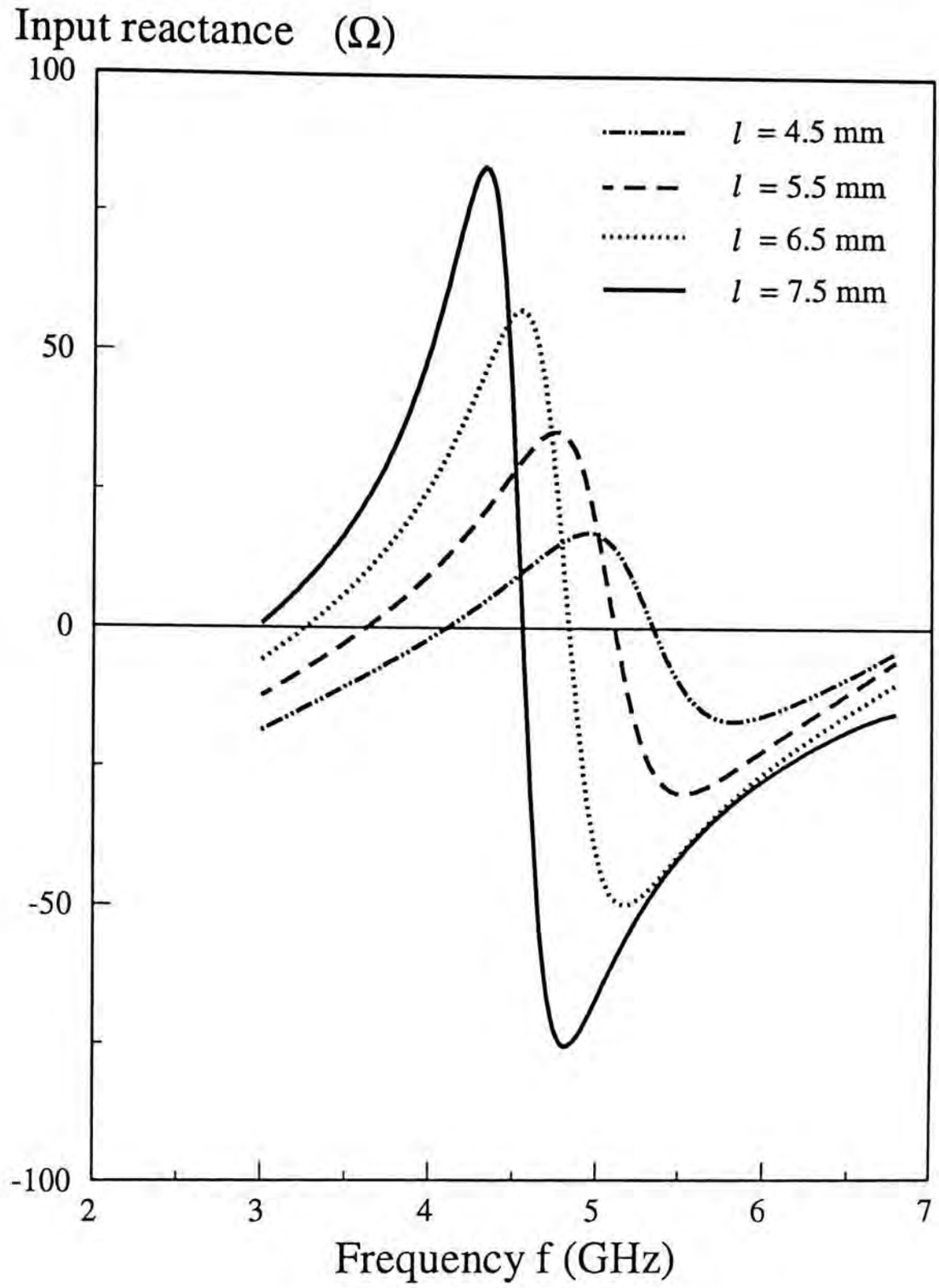

Fig. 2-30(b): Computed input reactance against frequency for different probe lengths using traditional reduced kernel with PWS modes and magnetic frill source model: a=11.5 mm, b=0.0 mm, ε_r=9.8, r_1=0.63 mm, r_2=2.0 mm.

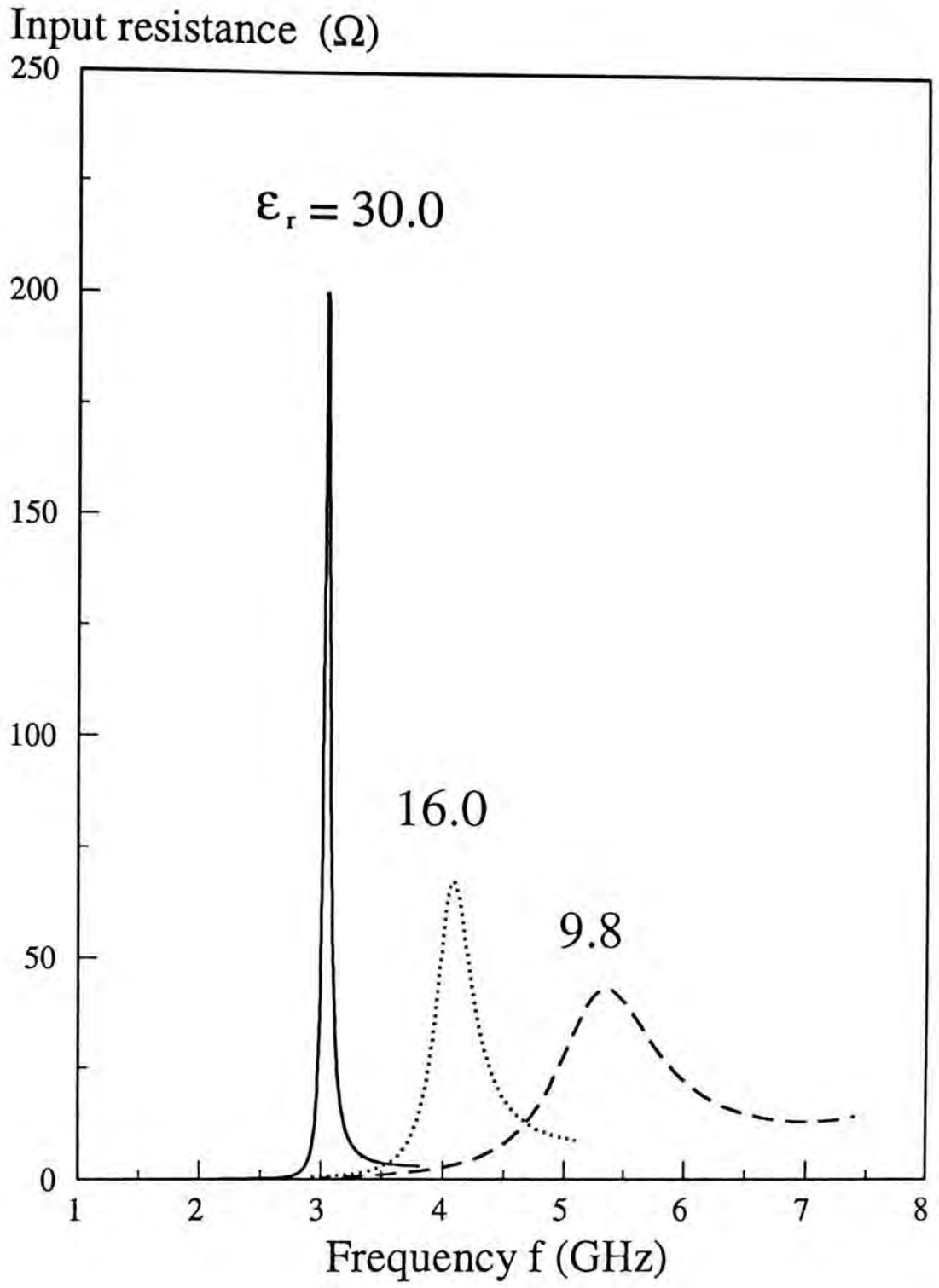

Fig. 2-31(a): Computed input resistance against frequency for different dielectric constant using traditional reduced kernel with PWS modes and magnetic frill source model: a=11.5 mm, b=0.0 mm, l=4.5 mm, r_1=0.63 mm, r_2=2.0 mm.

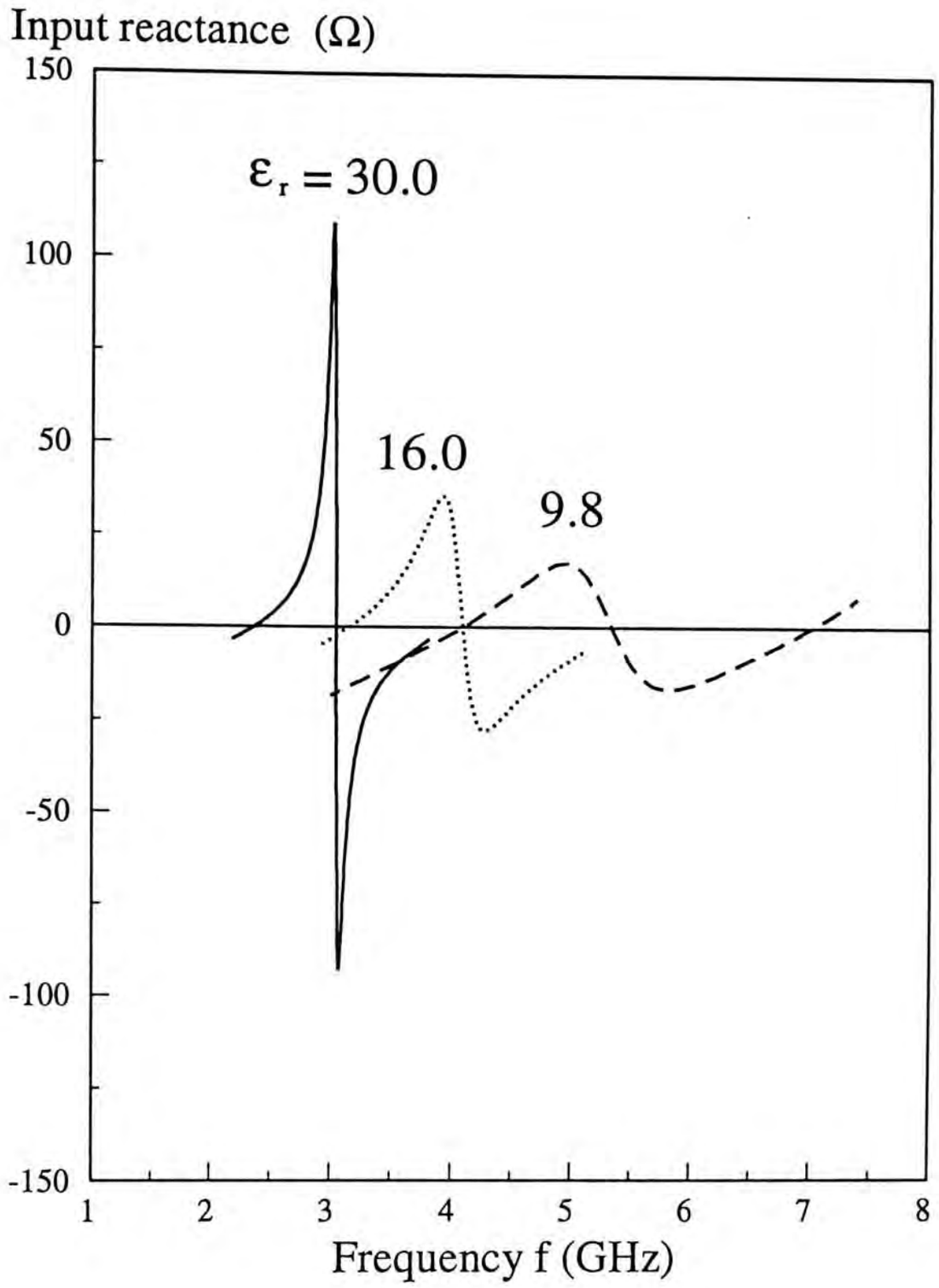

Fig. 2-31(b): Computed input reactance against frequency for different dielectric constant using traditional reduced kernel with PWS modes and magnetic frill source model: a=11.5 mm, b=0.0 mm, l=4.5mm, r_1=0.63 mm, r_2=2.0 mm.

(D) Error Discussion

The discrepancy between theory and experiment is mainly caused by the oversized hollow cavity into which the coaxial probe is placed for measurements. As the air trapped inside the cavity will reduce the effective ε_r of the DR, the measured resonant frequencies are expected to be higher than the calculated values. Furthermore, the DRs used are not perfectly hemispherical and the effective radius is taken as the mean value of the height and the base radius of the DR. The imperfection of the hemispherical shape also gives rise to the mismatch between theory and experiment. In addition, the tolerance of ε_r is not given for the DRs and the uncertainty of the true ε_r has introduced a source of error. Finally, by neglecting the higher order modes of the aperture field, the accuracy of the solution is decreased, although this effect is relatively small compared to the others for the modes presently under consideration.

2.4.7 Conclusion

The exact Green's function of the DR antenna is used to evaluate the input impedance of the probe-fed DR antenna. The probe current is solved rigorously by moment method, and from the current the input impedance is evaluated. The results using different excitation models, different basis functions and different dipole kernels are compared. Experiment is carried out to verify the theory, and reasonable agreement between them is obtained.

In the next section, we will study the radiation patterns of the first three resonant modes, namely the TE_{111} mode, the TE_{221} mode and the TM_{101} mode.

2.5 Theoretical Single Cavity Mode Radiation Patterns

The theoretical single mode radiation patterns for the TE_{111} mode, the TE_{221} mode and the TM_{101} mode are shown in Figs. 2-32, 2-33 and 2-34, respectively. Basically, the TE_{111} mode is a broadside mode while the TE_{221} mode as well as the TM_{101} mode are end-fire modes. Note that the H-plane for the TM_{101} mode is on the ground plane and is omitted from the figure. By exciting different resonant modes, different radiation patterns can be obtained.

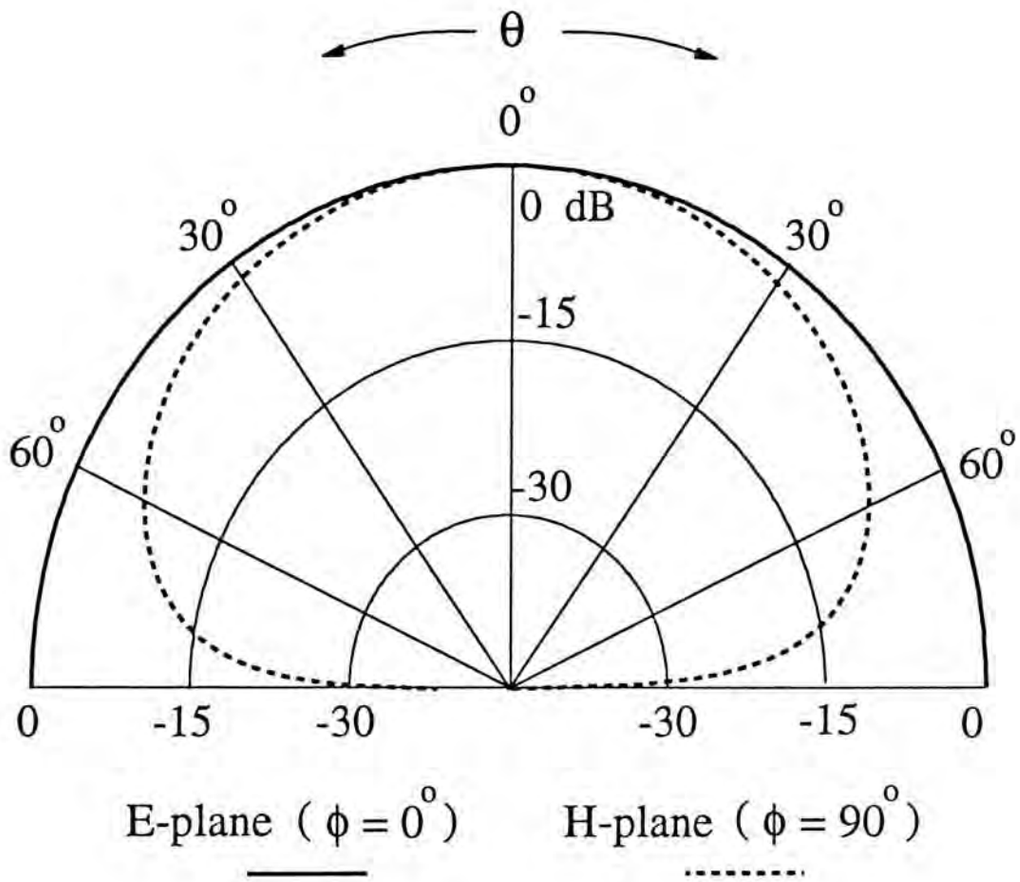

Fig. 2-32: Computed TE_{111} mode radiation pattern

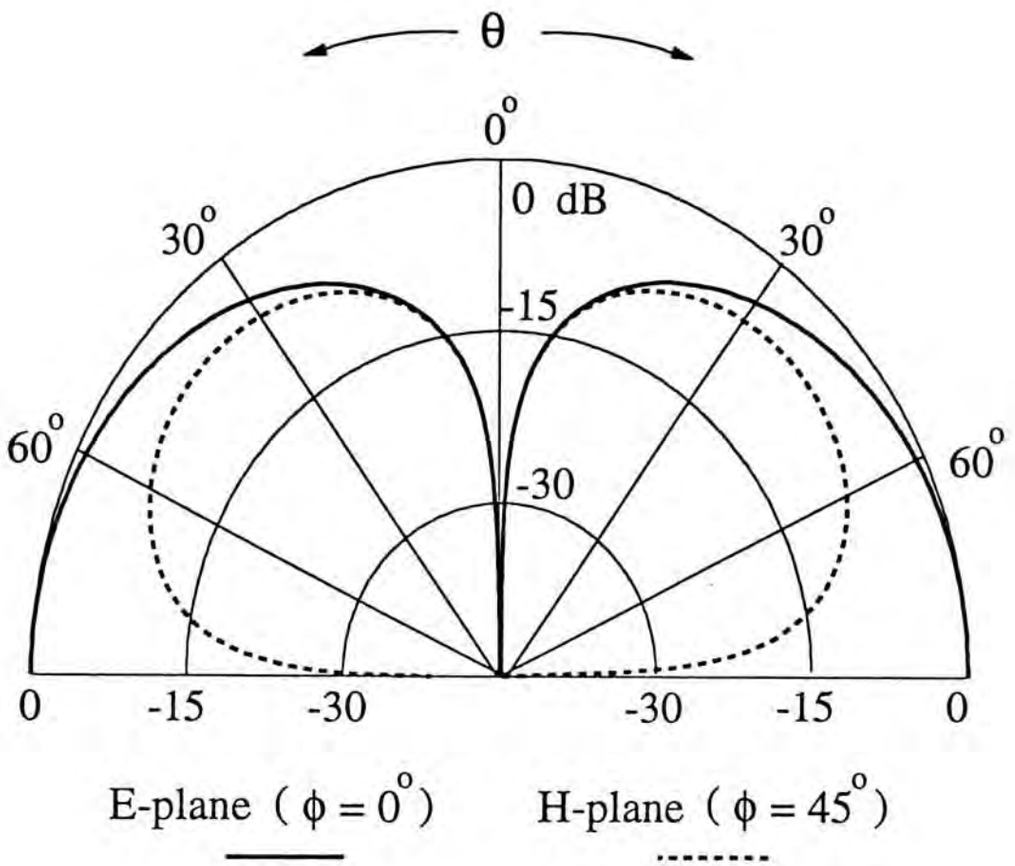

Fig. 2-33: Computed TE_{221} mode radiation pattern

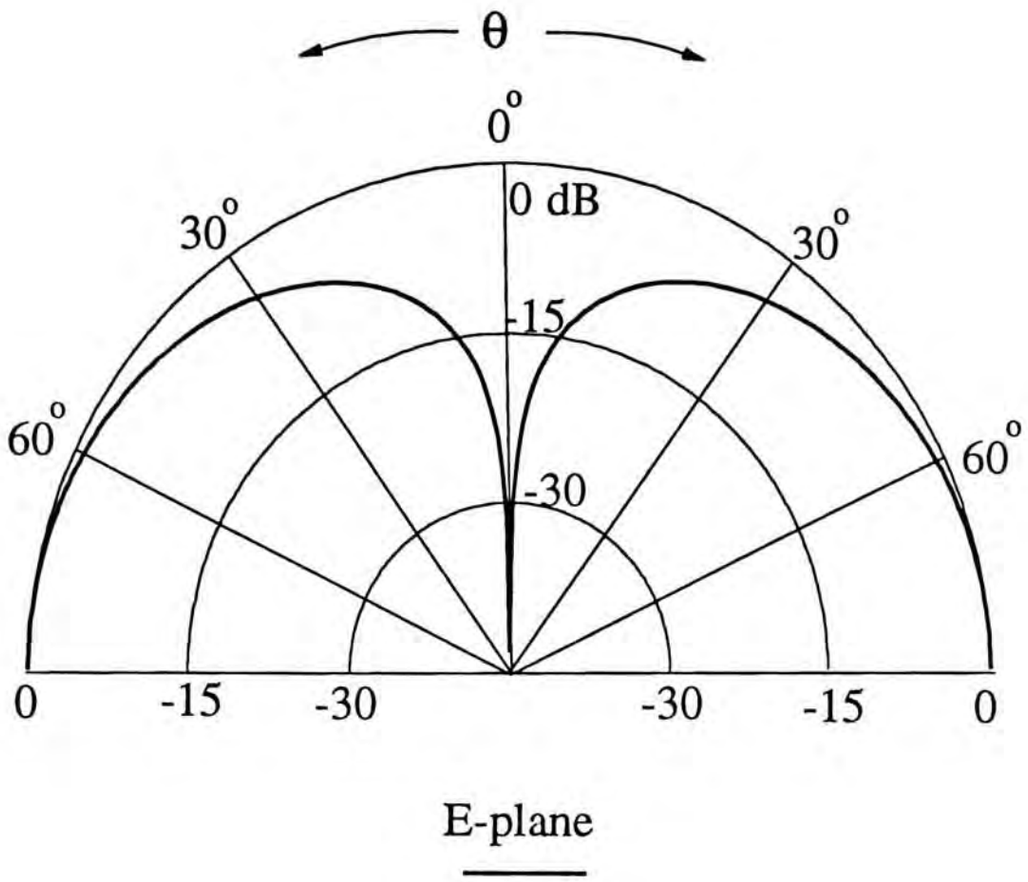

Fig. 2-34: Computed TM_{101} mode radiation pattern

2.6 Conclusion

The input impedance of a hemispherical DR antenna fed by a coaxial probe has been studied both theoretically and experimentally. Both simple cavity mode results and the exact Green's function results are presented. In the latter, the Green's function with separate particular and homogeneous parts is derived rigorously in a form which can be evaluated very efficiently. Both TE to r and TM to r modes of the hemispherical DR are discussed. The probe current and hence the input impedance are obtained by using the method of moments with the Galerkin's procedure. Convergence checks of the numerical solutions for the present problem have been discussed for different excitation models and kernels.

The effects of the probe length and the probe position on the input impedance are also studied. It is found that there are two degrees of freedom for the impedance matching of the DR antenna, namely the probe length and the probe position. In the next chapter, we will investigate another DR antenna configuration, the aperture coupled DR antenna, both theoretically and experimentally.

CHAPTER 3

ANALYSIS OF APERTURE COUPLED HEMISPHERICAL DR ANTENNA

3.1 Introduction

In this chapter, the aperture-coupled DR antenna is analyzed. This new excitation method has several advantages over the probe fed one such as the feasibility of integration with MMIC's and the avoidance of large probe self reactances at millimeter wave frequencies. While the probe-fed DR antenna uses electric source excitation, the aperture-coupled DR antenna utilizes magnetic source excitation. Due to the duality of the sources, the position of the source to excite a particular mode is different in the two configurations. For example, in the aperture-coupled case, the excitation of the TE_{111} mode is strongest when the slot is fed at the center of the DR. This is in contrast to the probe-fed case where the TE_{111} mode is excited by a probe with a displacement from the center. Moreover, while a center-fed probe can only excite TM modes, a slot aligned with a diameter of the DR can only excite TE modes. In this chapter, both the broadside TE_{111} mode and the end-fire TE_{221} mode of the DR antenna are investigated.

The analysis consists of two parts: the DR antenna above the ground plane and the microstripline below the ground plane. In the former, mode matching method [18] is employed to determine the exact magnetic field Green's function inside the DR due to an equivalent magnetic current in the slot. Analysis of the latter is based on the reciprocity method by Pozar [28].

The modal solution of the DR antenna involves an infinite summation which is usually difficult to compute directly as discussed in Section 2.1. The numerical technique presented in the previous chapter is employed again to solve the numerical problems. Moreover, the concept of the equivalent radius [50] is used so that the planar slot can be treated as a (magnetic) cylindrical dipole which has been well studied by many researchers. The reduced kernel of the cylindrical dipole is used to artificially avoid the singularity of the magnetic field Green's function, and therefore the numerical integration can be carried out without difficulties.

The microstrip feed line excitation is analyzed in the spectral domain. In the evaluation of an integral involving a surface wave pole which gives rise to the integrable singularity, we will follow Pozar's method [20] in which the vicinity of the pole is integrated analytically. Using this method, the numerical difficulties are avoided, and therefore the integral can be evaluated in a straightforward manner.

3.2 Problem Formulation

The geometry of the DR antenna is shown in Fig.3-1, where the slot of length L and width W couples the energy from the microstrip line to the hemispherical DR of radius a and dielectric constant ε_{ra}. The grounded dielectric slab has dielectric constant ε_{rs} and height d, whereas the microstrip feed line has width W_f. To begin with, the microstripline is assumed to be infinitely long, and propagating a quasi-transverse electromagnetic (TEM) mode. The TEM modal fields are given by

$$\vec{e}(y,z) = e_y\hat{y} + e_z\hat{z} \tag{3-1a}$$

$$\vec{h}(y,z) = h_y\hat{y} + h_z\hat{z} \tag{3-1b}$$

and normalized as follows:

$$\int_{y=-\infty}^{\infty}\int_{z=0}^{\infty} \vec{e}\times\vec{h}\cdot\hat{x}\,dy\,dz = 1 \tag{3-2}$$

Using the $e^{j\omega t}$ time dependence, the propagating microstripline fields are given by

$$\vec{E}^{\pm} = \vec{e}\,e^{\mp j\beta x} \tag{3-3a}$$

$$\vec{H}^{\pm} = \pm\vec{h}\,e^{\mp j\beta x} \tag{3-3b}$$

where β is the propagating constant of the fields. The evaluation of β is discussed in Appendix D. In (3-3), $\vec{E}^{+}$ represents the electric field propagating in the $+\hat{x}$-direction, whereas $\vec{E}^{-}$ represents that propagating in the $-\hat{x}$-direction.

Due to the presence of the slot at x=0, there are reflected as well as transmitted fields at the discontinuity, and therefore the total microstripline fields can be written as

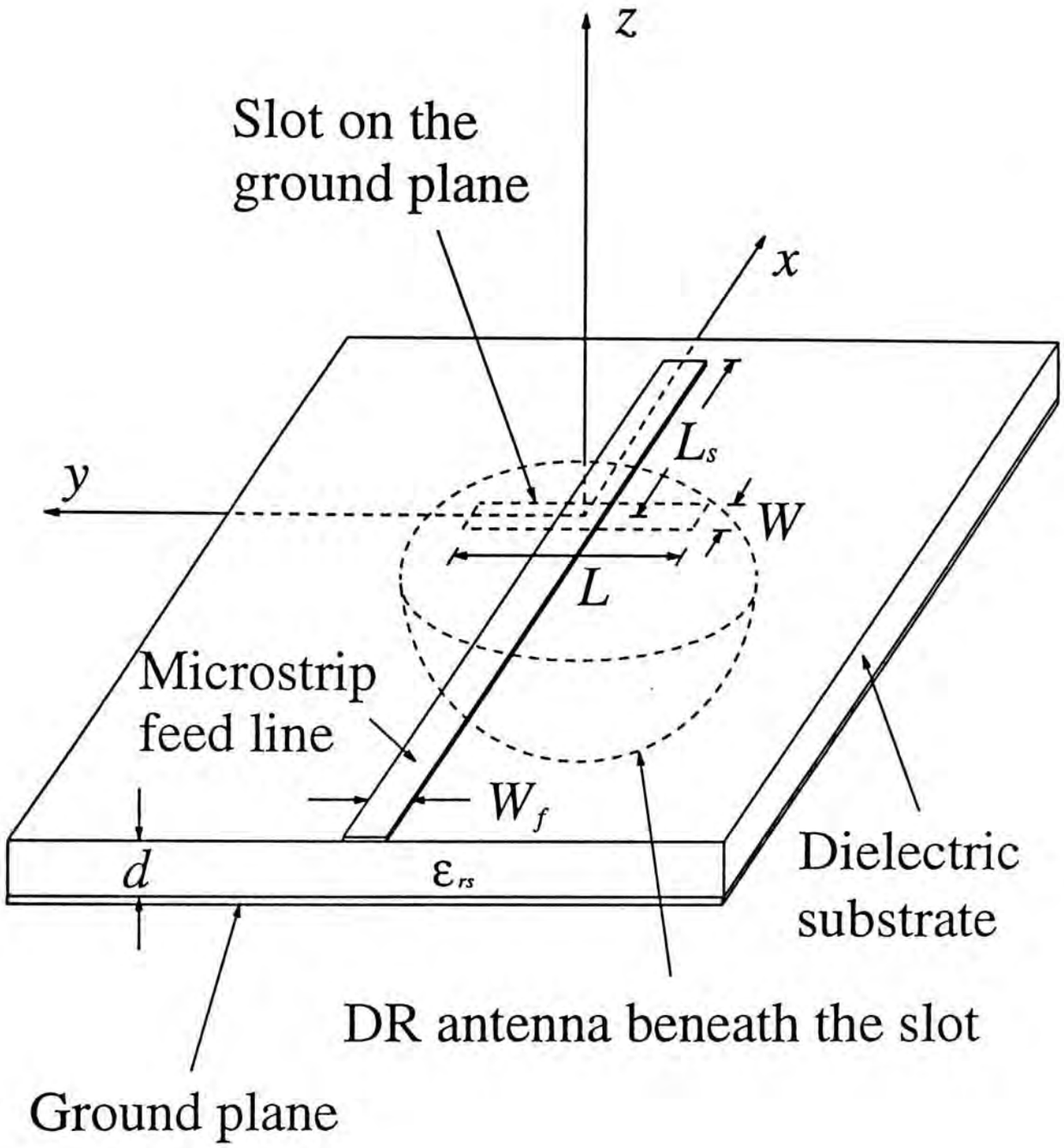

Fig. 3-1 Geometry of an aperture coupled hemispherical DR antenna

$$\vec{E} = \begin{cases} \vec{E}^{+} + R\,\vec{E}^{-} & x < 0 \\ T\,\vec{E}^{+} & x > 0 \end{cases} \tag{3-4a}$$

$$\vec{H} = \begin{cases} \vec{H}^{+} + R\,\vec{H}^{-} & x < 0 \\ T\,\vec{H}^{+} & x > 0 \end{cases} \tag{3-4b}$$

where R and T are the voltage reflection coefficient and the transmission coefficient on the line, respectively. Define a closed surface S consisting of three pieces as shown in Fig. 3-2.

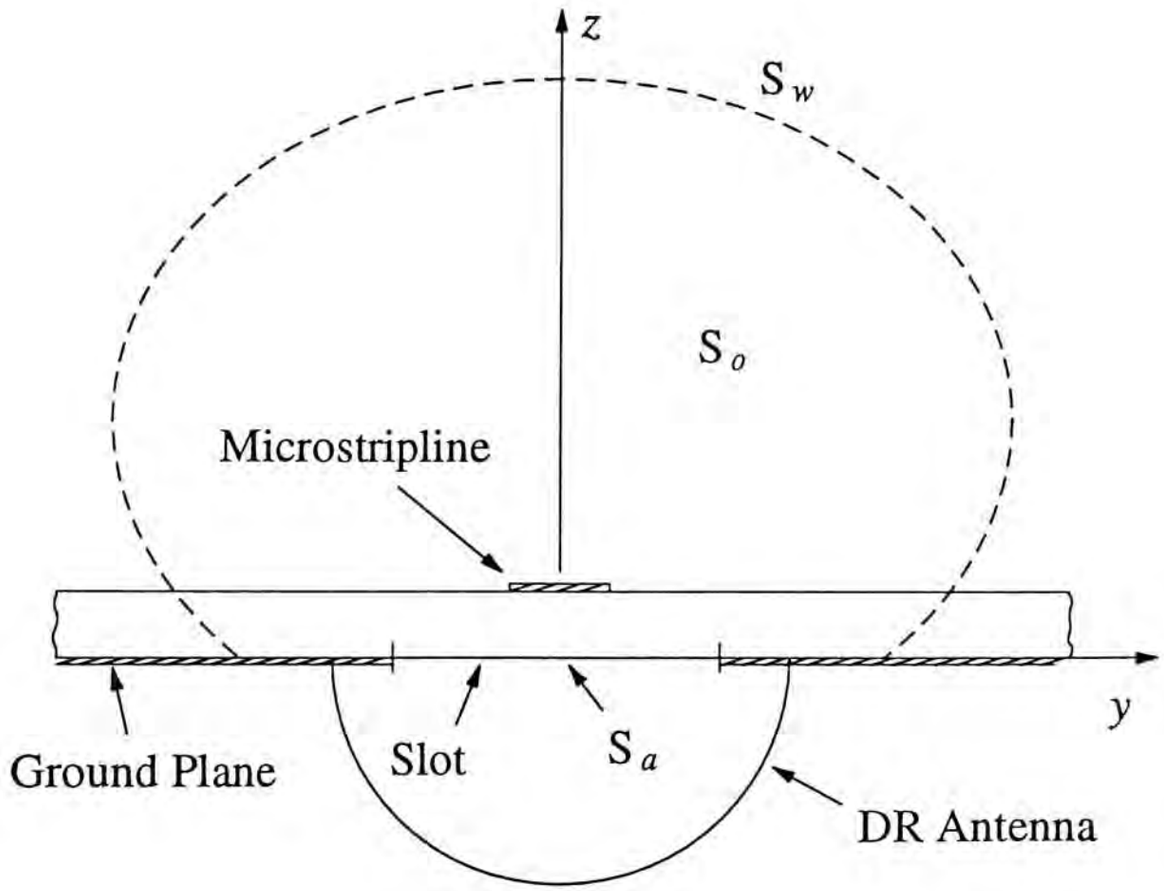

Fig. 3-2 The closed surface used in the reciprocity analysis

or mathematically

$$S = S_o + S_a + S_w \tag{3-5}$$

where S_o, S_a and S_w are, respectively, the effective cross section of the microstrip ($-\infty < y < \infty$; $0 < z < \infty$), the aperture surface, and the "wall" of the microstripline ($y \to \pm\infty$; $z \to \infty$; z=0). Applying the reciprocity theorem to the total fields $\vec{E}$, $\vec{H}$ and the positive travelling fields $\vec{E}^+$, $\vec{H}^+$ on the closed surface S, one obtains:

$$\iint_S \vec{E} \times \vec{H}^+ \cdot d\vec{S} = \iint_S \vec{E}^+ \times \vec{H} \cdot d\vec{S} \tag{3-6}$$

or equivalently,

$$\iint_{S_w} \vec{E} \times \vec{H}^+ \cdot d\vec{S} + \iint_{S_o} \vec{E} \times \vec{H}^+ \cdot d\vec{S} + \iint_{S_a} \vec{E} \times \vec{H}^+ \cdot d\vec{S}$$

$$= \iint_{S_w} \vec{E}^+ \times \vec{H} \cdot d\vec{S} + \iint_{S_o} \vec{E}^+ \times \vec{H} \cdot d\vec{S} + \iint_{S_a} \vec{E}^+ \times \vec{H} \cdot d\vec{S} \tag{3-7}$$

But on S_w, we have $r \to \infty$ and the (far) fields $\vec{E}$ and $\vec{H}$ are now related as in a spherical TEM wave [51] given by:

$$\vec{E} = -\eta \hat{r} \times \vec{H} \tag{3-8}$$

where η is the wave impedance. Using (3-8), one obtains:

$$\vec{E} = E_\theta \hat{\theta} + E_\phi \hat{\phi} \tag{3-9a}$$

$$\vec{H} = H_\theta \hat{\theta} + H_\phi \hat{\phi} = \frac{-1}{\eta} E_\phi \hat{\theta} + \frac{1}{\eta} E_\theta \hat{\phi} \tag{3-9b}$$

$$\vec{E}^+ = E_\theta^+ \hat{\theta} + E_\phi^+ \hat{\phi} \tag{3-9c}$$

and

$$\vec{H}^+ = H_\theta^+ \hat{\theta} + H_\phi^+ \hat{\phi} = \frac{-1}{\eta} E_\phi^+ \hat{\theta} + \frac{1}{\eta} E_\theta^+ \hat{\phi} \tag{3-9d}$$

Therefore on S_w

$$\vec{E}\times\vec{H}^{+}-\vec{E}^{+}\times\vec{H}=(E_\theta\hat{\theta}+E_\phi\hat{\phi})\times\frac{1}{\eta}(-E_\phi^{+}\hat{\theta}+E_\theta^{+}\hat{\phi})-(E_\theta^{+}\hat{\theta}+E_\phi^{+}\hat{\phi})\times\frac{1}{\eta}(-E_\phi\hat{\theta}+E_\theta\hat{\phi})$$

$$=\frac{1}{\eta}(E_\theta E_\theta^{+}\hat{r}+E_\phi E_\phi^{+}\hat{r})-\frac{1}{\eta}(E_\theta^{+}E_\theta\hat{r}+E_\phi^{+}E_\phi\hat{r})$$

$$=0 \tag{3-10}$$

which gives

$$\iint_{S_w}\vec{E}\times\vec{H}^{+}dS-\iint_{S_w}\vec{E}^{+}\times\vec{H}dS=0 \tag{3-11}$$

Next we consider the fields on the surface S_a. As $\vec{E}^{+}$ is the travelling wave of a completely grounded dielectric slab, its tangential components are zero on $z = 0$, and therefore $\hat{n}\times\vec{E}^{+} = 0$. But since there is aperture field $-V_o e_x^a\hat{x}$ in the slot, we have, on the surface S_a,

$$\hat{n}\times\vec{E}=\hat{n}\times(-V_o e_x^a\,\hat{x})$$

$$=V_o e_x^a\,\hat{y}$$

$$=M_y\,\hat{y} \tag{3-12}$$

where V_o is the unknown amplitude of the aperture field and $M_y = V_o e_x^a$ is the equivalent magnetic current in the slot. Therefore (3-7) becomes

$$\iint_{S_o}\vec{E}\times\vec{H}^{+}\cdot d\vec{S}+\iint_{S_a}\vec{E}\times\vec{H}^{+}\cdot d\vec{S}=\iint_{S_o}\vec{E}^{+}\times\vec{H}\cdot d\vec{S} \tag{3-13}$$

Consider the first integral on the left hand side of (3-13). As shown in Fig. 3-3, S_o consists of two surfaces, namely S_1 and S_2, and one can write

$$\iint_{S_o} \vec{E} \times \vec{H}^{+} \cdot d\vec{S} = \iint_{S_1} \vec{E} \times \vec{H}^{+} \cdot d\vec{S} + \iint_{S_2} \vec{E} \times \vec{H}^{+} \cdot d\vec{S}$$

$$= \iint_{S_1} (T\vec{E}^{+}) \times \vec{H}^{+} \cdot d\vec{S} + \iint_{S_2} (\vec{E}^{+} + R\vec{E}^{-}) \times \vec{H}^{+} \cdot d\vec{S} \qquad (3\text{-}14)$$

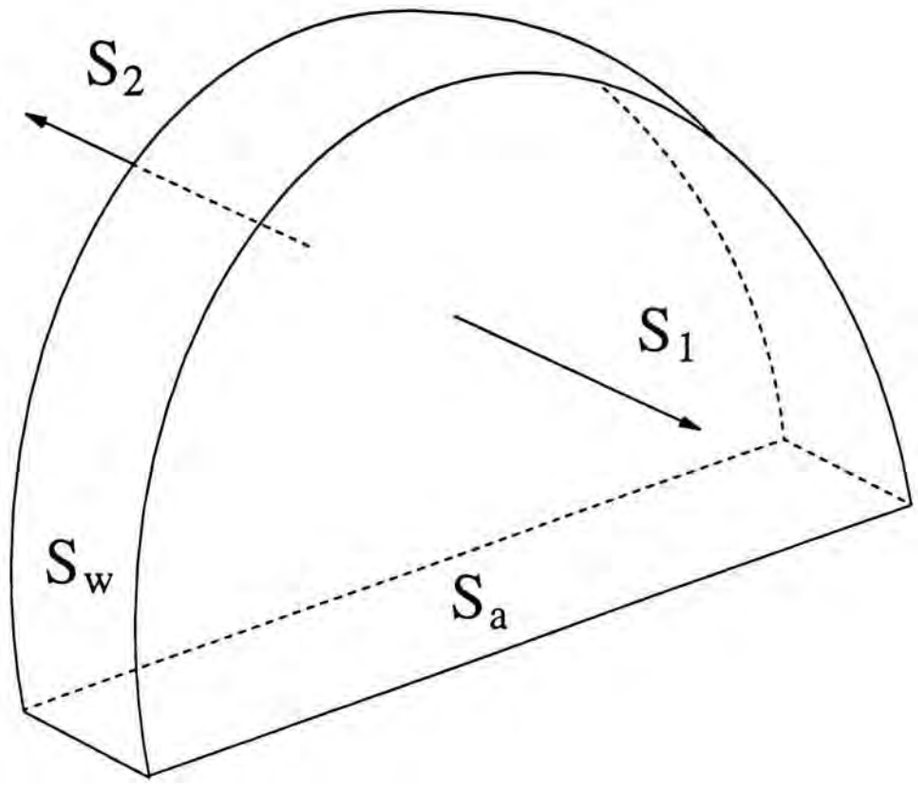

Fig. 3-3 The surface S_o composes of the two surfaces S_1 and S_2.

Insertion of (3-3) into (3-14) gives

$$\iint_{S_o} \vec{E} \times \vec{H}^{+} \cdot d\vec{S} = \iint_{S_1} (T\,\vec{e}\,e^{-j\beta x}) \times \vec{h}\,e^{-j\beta x} \cdot d\vec{S} + \iint_{S_2} (\vec{e}\,e^{-j\beta x} + R\,\vec{e}\,e^{j\beta x}) \times \vec{h}\,e^{-j\beta x} \cdot d\vec{S}$$

(3-15)

By using (3-2) for the fields normalization and noting that $d\vec{S}_2 = -d\vec{S}_1 = -\hat{x}dS_1$, one obtains

$$\iint_{S_o} \vec{E} \times \vec{H}^{+} \cdot d\vec{S} = T \iint_{S_1} \vec{e} \times \vec{h} e^{-j2\beta x} \cdot d\vec{S} + \iint_{S_2} \vec{e} \times \vec{h} e^{-j2\beta x} \cdot d\vec{S} - R \qquad (3\text{-}16)$$

Next we consider the second integral on the left hand side of (3-13). By using the vector identity

$$(\vec{E} \times \vec{H}^{+}) \cdot \hat{n} = (\hat{n} \times \vec{E}) \cdot \vec{H}^{+} \qquad (3\text{-}17)$$

the integral becomes:

$$\begin{aligned} \iint_{S_a} \vec{E} \times \vec{H}^{+} \cdot d\vec{S} &= \iint_{S_a} (\hat{n} \times \vec{E}) \cdot \vec{H}^{+} dS \\ &= \iint_{S_a} (M_y \hat{y}) \cdot \vec{h} e^{-j\beta x} dS \\ &= \iint_{S_a} (M_y \hat{y}) \cdot (h_y \hat{y} + h_z \hat{z}) e^{-j\beta x} dS \\ &= \iint_{S_a} M_y h_y e^{-j\beta x} dS \end{aligned} \qquad (3\text{-}18)$$

For narrow slots, the $e^{-j\beta x}$ term could be neglected because the phase shift across the width of the slot is small, and therefore

$$\iint_{S_a} \vec{E} \times \vec{H}^{+} \cdot d\vec{S} = \iint_{S_a} M_y h_y dS \qquad (3\text{-}19)$$

Finally we consider the integral on the right hand side of (3-13):

$$\iint_{S_o} \vec{E}^+ \times \vec{H} \cdot d\vec{S} = \iint_{S_1} \vec{E}^+ \times \vec{H} \cdot d\vec{S} + \iint_{S_2} \vec{E}^+ \times \vec{H} \cdot d\vec{S}$$

$$= \iint_{S_1} \vec{E}^+ \times (T\vec{H}^+) \cdot d\vec{S} + \iint_{S_2} \vec{E}^+ \times (\vec{H}^+ + R\vec{H}^-) \cdot d\vec{S}$$

$$= T \iint_{S_1} \vec{e} e^{-j\beta x} \times \vec{h} e^{-j\beta x} \cdot d\vec{S} + \iint_{S_2} \vec{e} e^{-j\beta x} \times \vec{h} e^{-j\beta x} \cdot d\vec{S}$$

$$-R \iint_{S_2} \vec{e} e^{-j\beta x} \times \vec{h} e^{j\beta x} \cdot d\vec{S} \qquad (3\text{-}20)$$

Using (3-2) for the normalization of fields and noting that $d\vec{S}_2 = -\hat{x} dS_2$, one obtains:

$$\iint_{S_o} \vec{E}^+ \times \vec{H} \cdot d\vec{S} = T \iint_{S_1} \vec{e} \times \vec{h} e^{-j2\beta x} \cdot d\vec{S} + \iint_{S_2} \vec{e} \times \vec{h} e^{-j2\beta x} \cdot d\vec{S} + R \qquad (3\text{-}21)$$

Substituting (3-16), (3-19) and (3-21) into (3-13) and after simplification, the following equation is obtained:

$$R = \frac{1}{2} \iint_{S_a} M_y(x,y) h_y(x,y) dS \qquad (3\text{-}22)$$

Next we apply the reciprocity theorem to the total fields $\vec{E}, \vec{H}$ and the negative travelling wave fields $\vec{E}^-, \vec{H}^-$ on the closed surface S :

$$\iint_S \vec{E} \times \vec{H}^- \cdot d\vec{S} = \iint_S \vec{E}^- \times \vec{H} \cdot d\vec{S} \qquad (3\text{-}23)$$

or equivalently

$$\iint_{S_w} \vec{E} \times \vec{H}^- \cdot d\vec{S} + \iint_{S_o} \vec{E} \times \vec{H}^- \cdot d\vec{S} + \iint_{S_a} \vec{E} \times \vec{H}^- \cdot d\vec{S}$$

$$= \iint_{S_w} \vec{E}^- \times \vec{H} \cdot d\vec{S} + \iint_{S_o} \vec{E}^- \times \vec{H} \cdot d\vec{S} + \iint_{S_a} \vec{E}^- \times \vec{H} \cdot d\vec{S} \qquad (3\text{-}24)$$

From (3-11) one can deduce that

$$\int\int_{S_w} \vec{E} \times \vec{H}^{-} \cdot dS - \int\int_{S_w} \vec{E}^{-} \times \vec{H} \cdot dS = 0 \tag{3-25}$$

In addition to the fact that $\hat{n} \times \vec{E}^{-} = 0$ on the surface S_a, equation (3-24) becomes

$$\int\int_{S_o} \vec{E} \times \vec{H}^{-} \cdot d\vec{S} + \int\int_{S_a} \vec{E} \times \vec{H}^{-} \cdot d\vec{S} = \int\int_{S_o} \vec{E}^{-} \times \vec{H} \cdot d\vec{S} \tag{3-26}$$

Using the technique used in deriving (3-16), (3-19) and (3-21), one can easily prove that

$$\int\int_{S_o} \vec{E} \times \vec{H}^{-} \cdot d\vec{S} = -T + 1 - R \int\int_{S_2} \vec{e} \times \vec{h} e^{j2\beta x} \cdot d\vec{S} \tag{3-27}$$

$$\int\int_{S_a} \vec{E} \times \vec{H}^{-} \cdot d\vec{S} = -V_o \int\int_{S_a} e_x^a(x,y) h_y(x,y) dS \tag{3-28}$$

$$\int\int_{S_o} \vec{E}^{-} \times \vec{H} \cdot d\vec{S} = T - 1 - R \int\int_{S_2} \vec{e} \times \vec{h} e^{j2\beta x} \cdot d\vec{S} \tag{3-29}$$

Substitution of (3-27)-(3-29) into (3-26) gives

$$T = 1 - \frac{V_o}{2} \int\int_{S_a} e_x^a(x,y) h_y(x,y) dS$$

$$= 1 - \frac{1}{2} \int\int_{S_a} M_y(x,y) h_y(x,y) dS$$

or

$$= 1 - R \tag{3-30}$$

Now two equations ((3-22) and (3-30)) are derived for the three unknowns (R, T, and M_y). The required third equation comes from enforcing the continuity of the magnetic field H_y across the aperture:

$$H_y^e = H_y^f + H_y^i \tag{3-31}$$

where

H_y^e = exterior field ($z < 0$) due to M_y

H_y^i = interior field ($z > 0$) due to M_y

and H_y^f = interior field ($z > 0$) due to the feed line modes

At $x = 0^-$ (or $x = 0^+$, since $1 - R = T$),

$$H_y^f = (1 - R)h_y \tag{3-32}$$

and therefore

$$H_y^e - H_y^i = (1 - R)h_y \tag{3-33}$$

Define two Green's function $G_{M_y}^{H_y}$ and G_{yy}^{HM}. The former represents H_y at (x, y, 0) inside an isolated spherical DR antenna due to a unit M_y at (x', y', 0), whereas the latter represents H_y at (x, y, 0) inside the grounded dielectric slab due to a unit M_y at (x', y', 0). Then (3-33) becomes

$$\iint_{S_a} G_{M_y}^{H_y}(x, y; x', y')[-2M_y(x', y')]\,dS' - \iint_{S_a} G_{yy}^{HM}(x, y; x', y')M_y(x', y')\,dS'$$

$$= (1 - R) \cdot \frac{1}{\sqrt{Z_c}} H_y(x, y) \tag{3-34}$$

On the other hand, equation (3-22) can be written as

$$R = \frac{1}{2\sqrt{Z_c}} \iint_{S_a} M_y(x, y)H_y(x, y)\,dS \tag{3-35}$$

where in (3-34) and (3-35)

$$H_y(x,y) = \sqrt{Z_c}\, h_y(x,y) \tag{3-36}$$

is the actual magnetic field due to the microstripline current, and the factor $\sqrt{Z_c}$ is the ratio of the actual magnetic field to the normalized field [28]. Z_c is the characteristic impedance of the microstripline. Note that in the first integral of (3-34), a factor of "-2" is added to the magnetic current M_y. The factor of two accounts for the presence of the ground plane, whereas the minus sign ensures that the tangential electric field is equal on each side of the aperture region. From (3-34) and (3-35), the unknown magnetic current M_y and the reflection coefficient R can be found. Once the reflection coefficient R is found, the equivalent series impedance Z_e of the slot can be obtained from the equivalent circuit as shown in Fig. 3-4.

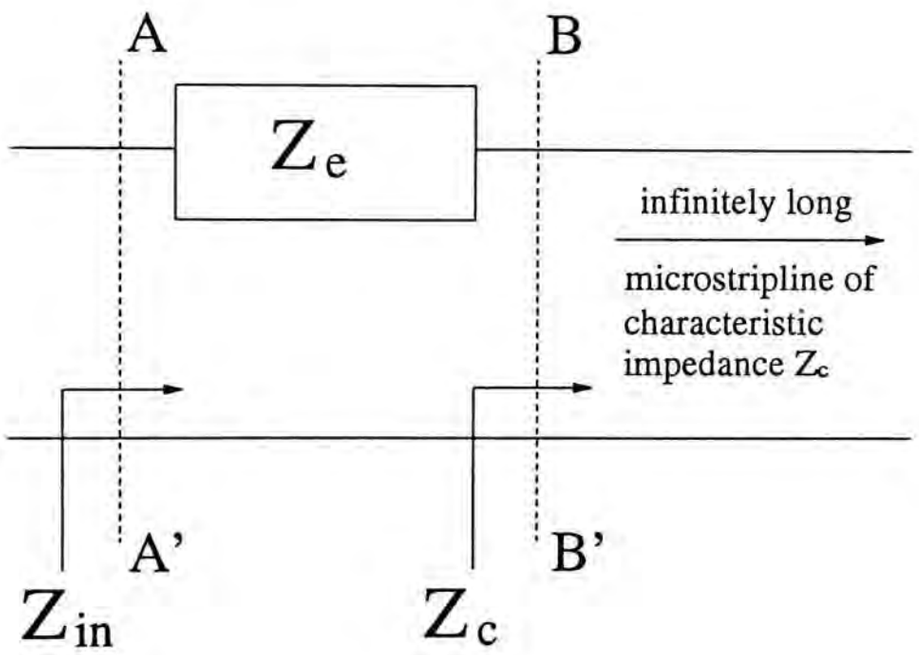

Fig. 3-4 Equivalent series impedance Z_e of the slot.

From the figure, the input impedance at the reference plane AA' is given by:

$$Z_{in} = Z_e + Z_c \tag{3-37}$$

Now consider the reflection coefficient R at the reference plane AA':

$$\begin{aligned} R &= \frac{Z_{in} - Z_c}{Z_{in} + Z_c} \\ &= \frac{(Z_e + Z_c) - Z_c}{(Z_e + Z_c) + Z_c} \end{aligned} \tag{3-38}$$

From (3-38), the equivalent series impedance Z_e is obtained as follows:

$$Z_e = Z_c \frac{2R}{1 - R} \tag{3-39}$$

In actual applications, the slot is usually terminated by an open-circuited stub of approximately $\lambda_g/4$ long as shown in Fig 3-5.

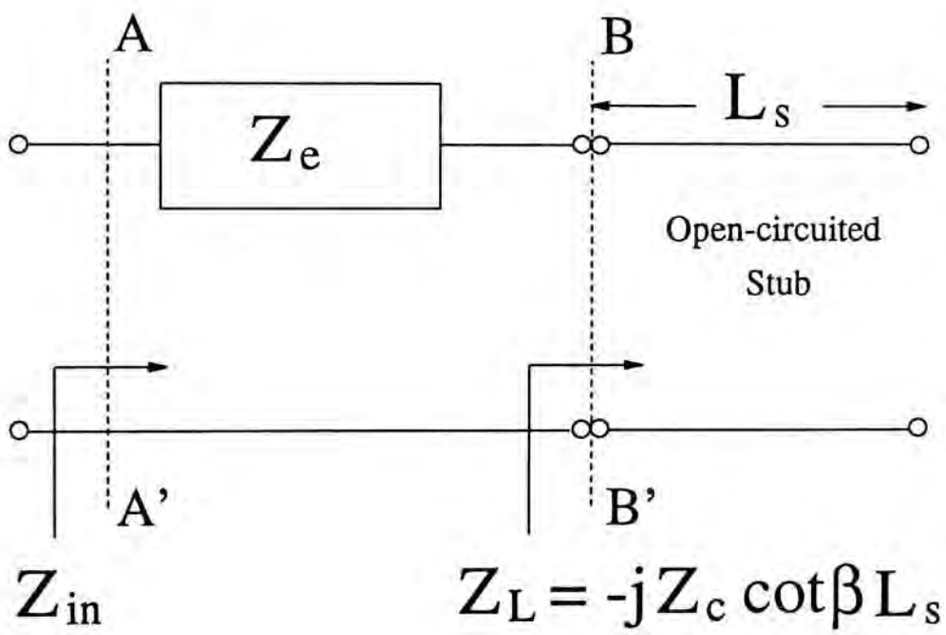

Fig. 3-5 Equivalent circuit of the antenna configuration.

From the figure, the input impedance of the actual configuration (Fig. 3-1) at the reference plane $x = 0$ is given by:

$$Z_{in} = Z_e - jZ_c \cot \beta L_s$$

or from (3-39)

$$Z_{in} = Z_c \frac{2R}{1-R} - jZ_c \cot \beta L_s \tag{3-40}$$

where L_s is the length of the open-circuited stub.

To slightly improve the results, the stub length L_s should be replaced by $(L_s + L_e)$ where L_e is the end correction of the open stub accounting for fringing fields at the end of the stub. The expression of L_e is given by [53]:

$$L_e = 0.412\left(\frac{\varepsilon_{eff} + 0.3}{\varepsilon_{eff} - 0.258}\right)\left(\frac{W_f/d + 0.262}{W_f/d + 0.813}\right) \tag{3-41}$$

where ε_{eff} is the effective permittivity of the substrate.

In the next section, the unknowns R and M_y are solved using Moment Method.

3.3 Moment Method Solution

Using moment method, the unknown magnetic current is first expanded in a set of basis function $f_n(x,y)$:

$$M_y(x,y) = \sum_{n=1}^{N} V_n f_n(x,y) \tag{3-42}$$

where V_n's are unknowns to be determined.

Since the width of the slot is electrically thin and is small as compared to the slot length, we assume that M_y has no variation in the $\hat{x}$-direction. On choosing PWS modes for the $\hat{y}$-directed current, one has:

$$f_n(x,y) = f_u(x) f_p(y - y_n) \tag{3-43}$$

where

$$f_u(x) = \begin{cases} \dfrac{1}{W} & |x| < W/2 \\ 0 & |x| > W/2 \end{cases} \tag{3-44}$$

$$f_p(y) = \begin{cases} \dfrac{\sin k_e(h - |y|)}{\sin k_e h} & |y| < h \\ 0 & |y| > h \end{cases} \tag{3-45}$$

$$h = \frac{L}{N+1} \tag{3-46a}$$

$$y_n = \frac{-L}{2} + nh \tag{3-46b}$$

and $k_e = k_o\sqrt{(\varepsilon_r + 1)/2}$ is the effective wavenumber of the PWS mode.

Substitution of (3-42) into (3-34) gives

$$-2\sum_{n=1}^{N} V_n \int\int_{S_o} G_{M_y}^{H_y}(x,y;x',y')\, f_n(x,y)\,dS' - \sum_{n=1}^{N} V_n \int\int_{S_o} G_{yy}^{HM}(x,y;x',y')\, f_n(x,y)\,dS'$$

$$=\frac{1-R}{\sqrt{Z_c}} H_y(x,y) \tag{3-47}$$

Using the Galerkin's procedure, the following equation is obtained:

$$\sum_{n=1}^{N} V_n (Y_{mn}^a - Y_{mn}^s) = (1-R)\sum_{n=1}^{N} \Delta v_m \tag{3-48}$$

where

$$Y_{mn}^a = -2\int\int_{S_o}\int\int_{S_o} f_m(x,y) G_{M_y}^{H_y}(x,y;x',y') f_n(x',y')\, dS'\, dS \tag{3-49}$$

$$Y_{mn}^s = \int\int_{S_o}\int\int_{S_o} f_m(x,y) G_{yy}^{HM}(x,y;x',y') f_n(x',y')\, dS'\, dS \tag{3-50}$$

$$\Delta v_m = \frac{1}{\sqrt{Z_c}} \int\int_{S_o} f_m(x,y) H_y(x,y)\, dS \tag{3-51}$$

In the matrix form, equation (3-48) is given by:

$$[Y_{mn}^e]\,[V_n] = (1-R)\,[\Delta v_m] \tag{3-52}$$

where

$$Y_{mn}^e = Y_{mn}^a - Y_{mn}^s \tag{3-53}$$

On the other hand, insertion of (3-42) into (3-35) gives

$$R = \frac{1}{2}\sum_{n=1}^{N} V_n \frac{1}{\sqrt{Z_c}} \int_{S_o}\int f_n(x,y) H_y(x,y)\, dS$$

$$= \frac{1}{2}\sum_{n=1}^{N} V_n \Delta v_n$$

or
$$R = \frac{1}{2}[\Delta v_n]^t [V_n] \tag{3-54}$$

where the superscript t denotes the transpose of a matrix. Substitution of (3-54) into (3-52) gives

$$[Y^e_{mn}]\,[V_n] = [\Delta v_m] - \frac{1}{2}[\Delta v_m]\,[\Delta v_n]^t [V_n] \tag{3-55}$$

which can readily give the solution of V_n:

$$[V_n] = \left\{[Y^e_{mn}] + \frac{1}{2}[\Delta v_m]\,[\Delta v_n]^t\right\}^{-1} [\Delta v_m] \tag{3-56}$$

The evaluations of Y^s_{mn} and Δv_m are performed in spectral domain [28]:

$$Y^s_{mn} = \frac{1}{4\pi^2}\int_{-\infty}^{\infty}\int F_u^2(k_x) F_p^2(k_y) \tilde{G}^{HM}_{yy}(k_x,k_y) \cos k_y(y_m - y_n)\, dk_x dk_y \tag{3-57}$$

and
$$\Delta v_m = \frac{1}{2\pi\sqrt{Z_c}}\int_{-\infty}^{\infty} \tilde{G}^{HJ}_{yx}(-\beta_f, k_y) F_u(k_y) F_p(k_y) \cos(k_y y_m)\, dk_y \tag{3-58}$$

where

$$\tilde{G}^{HM}_{yy}(k_x,k_y) = \frac{-j}{k_o\eta_o}\left[\frac{-j(k_1\cos k_1 d + jk_2\varepsilon_{rs}\sin k_1 d)(\varepsilon_{rs}k_o^2 - k_y^2)}{k_1 T_m} + \frac{jk_y^2 k_1(\varepsilon_{rs}-1)}{T_e T_m}\right] \tag{3-59a}$$

$$\tilde{G}^{HJ}_{yx}(k_x,k_y) = \frac{\varepsilon_{rs}k_1k_2\cos k_1 d + j[k_1^2 - k_x^2(\varepsilon_{rs}-1)]\sin k_1 d}{T_e T_m} \tag{3-59b}$$

$$F_u(k_x) = \int_{-\infty}^{\infty} f_u(x) e^{-jk_x x} dx = \frac{\sin(k_x W/2)}{k_x W/2} \tag{3-59c}$$

$$F_p(k_y) = \int_{-\infty}^{\infty} f_p(y) e^{-jk_y y} dy = \frac{2k_e(\cos k_y h - \cos k_e h)}{(k_e^2 - k_y^2)\sin k_e h} \tag{3-59d}$$

$$F_u(k_y) = \int_{-\infty}^{\infty} f_u(y) e^{-jk_y y} dy = \frac{\sin(k_y W_f/2)}{k_y W_f/2} \tag{3-59e}$$

$$T_e = k_1 \cos k_1 d + jk_2 \sin k_1 d \tag{3-59f}$$

$$T_m = \varepsilon_{rs} k_2 \cos k_1 d + jk_1 \sin k_1 d \tag{3-59g}$$

$$k_1^2 = \varepsilon_{rs} k_o^2 - \beta^2 \qquad \mathrm{Im}(k_1) < 0 \tag{3-59h}$$

$$k_2^2 = k_o^2 - \beta^2 \qquad \mathrm{Im}(k_2) < 0 \tag{3-59i}$$

$$\beta^2 = k_x^2 + k_y^2 \tag{3-59j}$$

$$k_o^2 = \omega^2 \mu_o \varepsilon_o \tag{3-59k}$$

$$\eta_o = \sqrt{\mu_o/\varepsilon_o} \tag{3-59l}$$

where β_f is now used to denote the propagation constant of the microstrip fields as β is redefined in (3-59j). Note that in (3-59e), W_f (the width of the feed line) is used in $f_u(y)$ instead of W (the width of the slot).

Note that special care must be taken in calculating Y_{mn}^s due to the surface wave poles of the Green's function $\tilde{G}_{yy}^{HM}$. The surface wave poles will give rise to sigularities of the integrand, and therefore the integration cannot be performed directly. The numerical technique for such integration is discussed in Appendix E.

For the evaluation of Y^a_{mn}, the expression of $G^{H_y}_{M_y}$ is required and it will be derived in the next section. Once $G^{H_y}_{M_y}$ is known, the voltage vector $[V_n]$ and hence the reflection coefficient R can be obtained from (3-56) and (3-54), respectively.

3.4 Magnetic Field Green's Function of DR Antenna

In this section, the Green's function $G_{M_y}^{H_y}$ denoting a $\hat{y}$-directed magnetic field H_y inside the DR antenna due to a $\hat{y}$-directed magnetic current M_y is derived rigorously. Note that the computation of $[V_n]$ as given by (3-56) is coordinate-independent; hence, for convenience, the geometry of the DR antenna configuration is re-defined in Fig. 3-6. To begin with, consider a $\hat{y}$-directed magnetic current inside an isolated spherical DR antenna. In general, a $\hat{y}$-directed current can be decomposed into the three components of spherical coordinates:

$$M_y = M_r \sin\theta\cos\phi + M_\theta \cos\theta\sin\phi + M_\phi \cos\phi \tag{3-60}$$

where

$$M_r = M_x \cos\phi\sin\theta + M_y \sin\phi\sin\theta + M_z \cos\theta \tag{3-61a}$$

$$M_\theta = M_x \cos\phi\cos\theta + M_y \sin\phi\cos\theta - M_z \sin\theta \tag{3-61b}$$

$$M_\phi = -M_x \sin\phi + M_y \cos\phi \tag{3-61c}$$

Since the current under consideration lies on the x-y plane ($\theta=\pi/2$) and has no other components ($M_x=M_z=0$), we have:

$$M_y = M_r \sin\phi + M_\phi \cos\phi \tag{3-62}$$

where $M_r = M_y \sin\phi$, and $M_\phi = M_y \cos\phi$.

We will consider the current components independently and then combine the results to give the required Green's function $G_{M_y}^{H_y}$. It should be mentioned that an $\hat{r}$-directed magnetic current can only excite TE to r modes, whereas a $\hat{\phi}$-directed one can, in general, excite both TE to r and TM to r modes. Therefore one potential function $G_{M_r}^{F_r}$ alone is adequate to represent all possible fields excited by an $\hat{r}$-directed current, but two potential functions $G_{M_\phi}^{F_r}$ and $G_{M_\phi}^{A_r}$ are required for a

$\hat{\phi}$-directed one. The Green's function $G_{M_r}^{F_r}$ denotes the electric potential due to an $\hat{r}$-directed magnetic point current, while the Green's functions $G_{M_\phi}^{F_r}$ and $G_{M_\phi}^{A_r}$ denote, respectively, the electric potential and the magnetic potential due to a $\hat{\phi}$-directed one. The derivation procedure of the Green's function is similar to that in the probe fed case, where the potentials are represented as the sums of a particular and a homogeneous solutions. Again, the subscripts p and h are used to denote, respectively, the particular solution and the homogeneous solution.

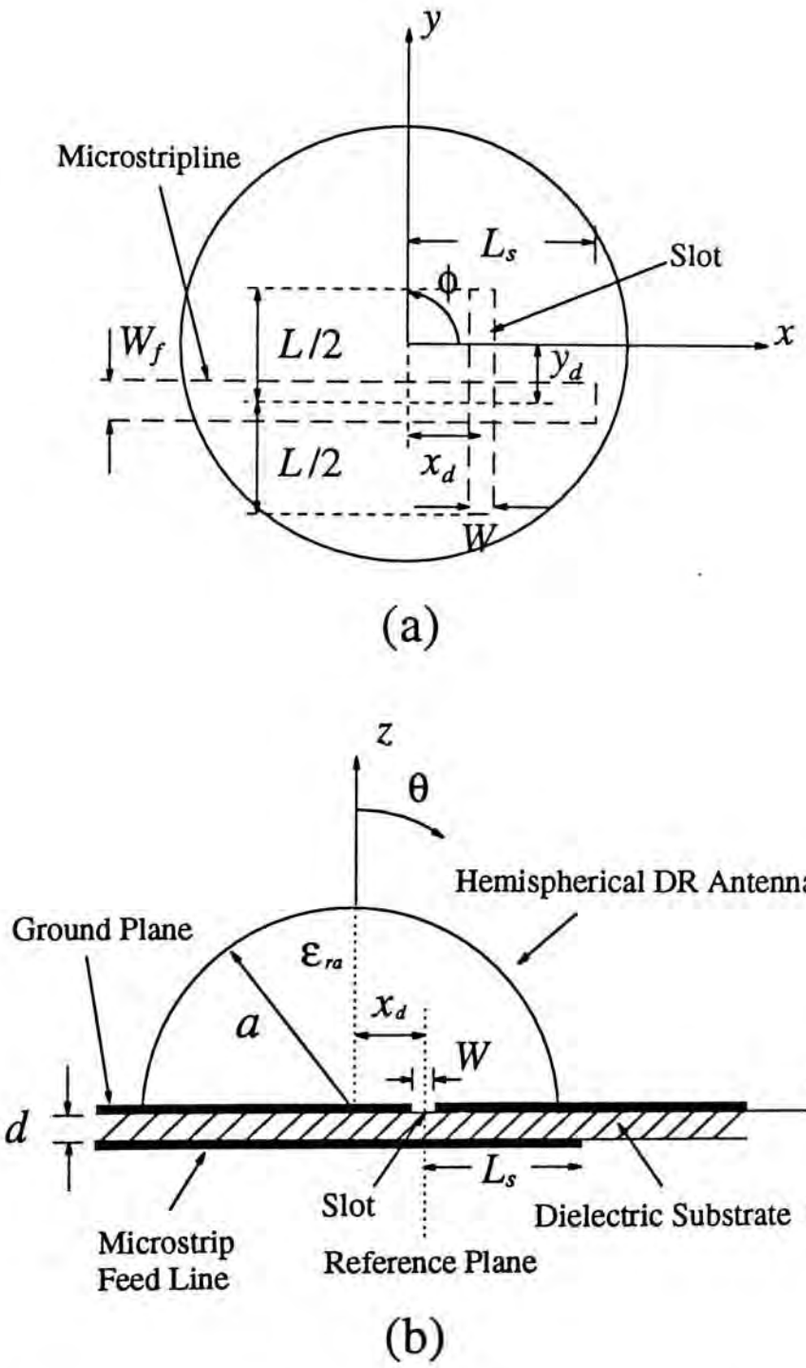

Fig. 3-6 The new geometry of the antenna configuration (a) Top View (b) Side View

(A) Derivation of $G_{M_\phi}^{F_r}$ and $G_{M_\phi}^{A_r}$

For $G_{M_\phi}^{F_r}$, we write :

Particular solution

$$G_{M_\phi}^{F_{rp}} = \sum_{n=0}^{\infty} \sum_{m=-n}^{n} A_{nm} P_n^m(\cos\theta) e^{jm\phi} \cdot \begin{cases} \hat{J}_n'(kr') \hat{H}_n^{(2)}(kr) & r > r' \\ \hat{H}_n^{(2)\prime}(kr') \hat{J}_n(kr) & r < r' \end{cases} \quad \text{(3-63a)}$$

Homogeneous solution

$$G_{M_\phi}^{F_{rh}} = \sum_{n=0}^{\infty} \sum_{m=-n}^{n} P_n^m(\cos\theta) e^{jm\phi} \cdot \begin{cases} B_{nm} \hat{J}_n(kr) & r \le a \\ C_{nm} \hat{H}_n^{(2)}(k_o r) & r \ge a \end{cases} \quad \text{(3-63b)}$$

For $G_{M_\phi}^{A_r}$, we write :

Particular solution

$$G_{M_\phi}^{A_{rp}} = \sum_{n=0}^{\infty} \sum_{m=-n}^{n} D_{nm} P_n^m(\cos\theta) e^{jm\phi} \cdot \begin{cases} \hat{J}_n(kr') \hat{H}_n^{(2)}(kr) & r > r' \\ \hat{H}_n^{(2)}(kr') \hat{J}_n(kr) & r < r' \end{cases} \quad \text{(3-63c)}$$

Homogeneous solution

$$G_{M_\phi}^{A_{rh}} = \sum_{n=0}^{\infty} \sum_{m=-n}^{n} P_n^m(\cos\theta) e^{jm\phi} \cdot \begin{cases} E_{nm} \hat{J}_n(kr) & r \le a \\ F_{nm} \hat{H}_n^{(2)}(k_o r) & r \ge a \end{cases} \quad \text{(3-63d)}$$

where k_o, k, and ε denotes, respectively, the vacuum wavenumber, the dielectric wavenumber and the dielectric permittivity, which are given in (2-5e)-(2-5g). The unknown coefficients A_{nm} , B_{nm} , C_{nm} , D_{nm} , E_{nm} and F_{nm} are constants to be determined. $P_n^m(x)$ is the associated Legendre function of the first kind with order

m and degree n, and $\hat{J}_n(x)$ and $\hat{H}_n^{(2)}(x)$ are, respectively, spherical Bessel function of the first kind (Schelkunoff type) and spherical Hankel function (Schelkunoff type) of the second kind, both of order n. All other symbols have the usual meanings.

(a) Particular Solutions

The particular solutions are considered first. The coefficients A_{nm} and D_{nm} are solved by matching the boundary conditions at the source point:

$$E_\theta^+ - E_\theta^- = -M_{\phi s} \tag{3-64a}$$

$$E_\phi^+ - E_\phi^- = 0 \tag{3-64b}$$

$$H_\theta^+ - H_\theta^- = 0 \tag{3-64c}$$

$$H_\phi^+ - H_\phi^- = 0 \tag{3-64d}$$

where the superscripts '+' and '–' correspond to, respectively, the fields at $r = r' + \delta$ and $r = r' - \delta$, and δ is positive and vanishingly small. The boundary conditions for the magnetic fields (3-64c) and (3-64d) have already been satisfied by the modal expansions (3-63). The boundary conditions for the electric fields (3-64a)-(3-64b) are now enforced.

(i) Boundary Condition for E_θ at $r = r'$

From (3-64a) and using (2-4), one obtains, after simplification,

$$\frac{k}{\omega\mu_o\varepsilon r'} \sum_{n=1}^{\infty} \sum_{m=-n}^{n} D_{nm} \frac{d}{d\theta} P_n^m(\cos\theta)\, e^{jm\phi} - \frac{1}{\varepsilon r' \sin\theta} \sum_{n=1}^{\infty} \sum_{m=-n}^{n} m\, A_{nm}\, P_n^m(\cos\theta)\, e^{jm\phi} = M_{\phi s} \tag{3-65}$$

In deriving (3-65), the Wronskian of the spherical Bessel's equation (2-8) has been used to simplify the expression.

Summation over the index m is first eliminated by using the orthogonal relationship for $e^{jm\phi}$ (equation (2-9)). Then (3-65) becomes:

$$\frac{k}{\omega\mu_o}\sum_{n=1}^{\infty} D_{nm}\frac{d}{d\theta}P_n^m(\cos\theta)-\frac{m}{\sin\theta}\sum_{n=1}^{\infty} A_{nm}P_n^m(\cos\theta)=\frac{\varepsilon r'}{2\pi}\int_0^{2\pi} M_{\phi s}\,e^{-jm\phi}d\phi \quad (3\text{-}66)$$

(ii) Boundary Condition for E_ϕ at $r=r'$

From (3-64b) and using (2-4), one obtains, after simplification,

$$\frac{k}{\omega\varepsilon\mu_o r'\sin\theta}\sum_{n=1}^{\infty}\sum_{m=-n}^{n} m\,D_{nm}P_n^m(\cos\theta)\,e^{jm\phi}-\frac{1}{\varepsilon r'}\sum_{n=1}^{\infty}\sum_{m=-n}^{n} A_{nm}\frac{d}{d\theta}P_n^m(\cos\theta)\,e^{jm\phi}=0 \quad (3\text{-}67)$$

Eliminating the summation over the index m (using (2-9)), we obtain :

$$\frac{k}{\omega\mu_o}\cdot\frac{m}{\sin\theta}\sum_{n=1}^{\infty} D_{nm}P_n^m(\cos\theta)-\sum_{n=1}^{\infty} A_{nm}\frac{d}{d\theta}P_n^m(\cos\theta)=0 \quad (3\text{-}68)$$

From the two coupled equations (3-66) and (3-68), the coefficients A_{nm} and D_{nm} can be solved. To find the unknown coefficient A_{nm}, we first multiply (3-66) by $(mP_r^m(\cos\theta)/\sin\theta)$ and (3-68) by $(dP_r^m(\cos\theta)/d\theta)$ and then add the two equations together. This gives the following equation:

$$\frac{k}{\omega\mu_o}\cdot\frac{m}{\sin\theta}\sum_{n=1}^{\infty} D_{nm}\left[P_r^m\frac{d}{d\theta}P_n^m+P_n^m\frac{d}{d\theta}P_r^m\right]-\sum_{n=1}^{\infty} A_{nm}\left[\frac{d}{d\theta}P_n^m\frac{d}{d\theta}P_r^m+\frac{m^2}{\sin^2\theta}P_n^m P_r^m\right]$$

$$=\frac{\varepsilon r'}{2\pi}\cdot\frac{m}{\sin\theta}\cdot P_r^m\int_0^{2\pi} M_{\phi s}e^{-jm\phi}d\phi \quad (3\text{-}69)$$

where $P_n^m=P_n^m(\cos\theta)$.

Finally by using the orthogonal relationship for the associated Legendre functions (2-15) and the mathematical identity (2-16), we obtain the coefficient A_{nm} as follows:

$$A_{nm}=\frac{-\varepsilon r'}{4\pi}\cdot\frac{2n+1}{n(n+1)}\cdot\frac{(n-m)!}{(n+m)!}\cdot m\int_{\theta=0}^{\pi}\int_{\phi=0}^{2\pi}M_{\phi s}\,P_n^m(\cos\theta)e^{-jm\phi}\,d\phi d\theta \qquad (3\text{-}70)$$

The coefficient D_{nm} is solved similarly by first multiply (3-66) by $(dP_r^m(\cos\theta)/d\theta)$ and (3-68) by $(mP_r^m(\cos\theta)/\sin\theta)$ and then add the results together. This results in the following equation:

$$\frac{-m}{\sin\theta}\sum_{n=1}^{\infty}A_{nm}\left[P_r^m\frac{d}{d\theta}P_n^m+P_n^m\frac{d}{d\theta}P_r^m\right]+\frac{k}{\omega\mu_o}\sum_{n=1}^{\infty}D_{nm}\left[\frac{d}{d\theta}P_n^m\frac{d}{d\theta}P_r^m+\frac{m^2}{\sin^2\theta}P_n^m\,P_r^m\right]$$
$$=\frac{\varepsilon r'}{2\pi}\cdot\frac{d}{d\theta}P_r^m\int_0^{2\pi}M_{\phi s}e^{-jm\phi}d\phi \qquad (3\text{-}71)$$

Using the orthogonal relationship for the associated Legendre functions (2-15) and the mathematical identity (2-16), we obtain D_{nm} as below:

$$D_{nm}=\frac{\omega\mu_o\varepsilon r'}{4\pi k}\cdot\frac{2n+1}{n(n+1)}\cdot\frac{(n-m)!}{(n+m)!}\int_{\theta=0}^{\pi}\int_{\phi=0}^{2\pi}M_{\phi s}\sin\theta\frac{d}{d\theta}P_n^m(\cos\theta)e^{-jm\phi}\,d\phi d\theta \qquad (3\text{-}72)$$

For a (surface) point current $M_{\phi s}$ located at (r', θ', ϕ'), we write :

$$M_{\phi s}=\frac{\delta(\theta-\theta')\,\delta(\phi-\phi')}{r'^2\sin\theta} \qquad (3\text{-}73)$$

Substituting (3-70), (3-72) and (3-73) into (3-63), we have the following particular solutions for the potential Green's functions:

$$G_{M_\phi}^{F_{rp}}=\frac{1}{r'\sin\theta'}\sum_{n=1}^{\infty}\sum_{m=1}^{n}a_{nm}P_n^m(\cos\theta')P_n^m(\cos\theta)\sin m(\phi-\phi')\cdot\begin{cases}\hat{J}_n'(kr')\hat{H}_n^{(2)}(kr) & r>r'\\ \hat{H}_n^{(2)\prime}(kr')\hat{J}_n(kr) & r<r'\end{cases}$$

(3-74a)

$$G_{M_\phi}^{A_{rp}}=\frac{1}{r'}\sum_{n=1}^{\infty}\sum_{m=0}^{n}d_{nm}\frac{d}{d\theta'}P_n^m(\cos\theta')P_n^m(\cos\theta)\cos m(\phi-\phi')\cdot\begin{cases}\hat{J}_n(kr')\hat{H}_n^{(2)}(kr) & r>r'\\ \hat{H}_n^{(2)}(kr')\hat{J}_n(kr) & r<r'\end{cases}$$

(3-74b)

where

$$a_{nm} = \frac{-j\varepsilon}{2\pi} \cdot \frac{2n+1}{n(n+1)} \cdot \frac{(n-m)!}{(n+m)!} \cdot m \tag{3-74c}$$

$$d_{nm} = \frac{\omega\mu_o\varepsilon}{\Delta_m 2\pi k} \cdot \frac{2n+1}{n(n+1)} \cdot \frac{(n-m)!}{(n+m)!} \tag{3-74d}$$

and Δ_m is defined in (2-21e).

(b) Homogeneous Solutions

The homogeneous solutions for the potential Green's functions are obtained by enforcing the boundary conditions at the spherical surface of the DR:

$$E_\theta^+ - E_\theta^- = 0 \tag{3-75a}$$

$$E_\phi^+ - E_\phi^- = 0 \tag{3-75b}$$

$$H_\theta^+ - H_\theta^- = 0 \tag{3-75c}$$

$$H_\phi^+ - H_\phi^- = 0 \tag{3-75d}$$

Since the boundary conditions on the surface of the DR (3-75) are exactly the same as that in the probe fed case, the results derived from the probe fed case can be modified to give the required homogeneous solutions. Comparing (2-5) to (3-63), one can see that the two sets of the modal expressions are basically the same, only that $A_{nm}\hat{J}_n(kr')$ $(r' < r < a)$ in (2-5a) is replaced by $A_{nm}\hat{J}_n'(kr')$ $(r' < r < a)$ in (3-63a), and $D_{nm}\hat{J}_n'(kr')$ $(r' < r < a)$ in (2-5c) replaced by $D_{nm}\hat{J}_n(kr')$ $(r' < r < a)$ in (3-63c). Then from (2-41), the required homogeneous solutions are obtained as follows:

$$G_{M_\phi}^{F_{rh}} = \frac{1}{r' \sin\theta'} \sum_{n=1}^{\infty} \sum_{m=1}^{n} P_n^m(\cos\theta') P_n^m(\cos\theta) \sin m(\phi - \phi') \hat{J}_n'(kr') \cdot \begin{cases} b_{nm} \hat{J}_n(kr) & r \le a \\ c_{nm} \hat{H}_n^{(2)}(k_o r) & r \ge a \end{cases} \tag{3-76a}$$

$$G_{M_\phi}^{A_{rh}} = \frac{1}{r'} \sum_{n=1}^{\infty} \sum_{m=0}^{n} \frac{d}{d\theta'} P_n^m(\cos\theta') P_n^m(\cos\theta) \cos m(\phi - \phi') \hat{J}_n(kr') \cdot \begin{cases} e_{nm} \hat{J}_n(kr) & r \le a \\ f_{nm} \hat{H}_n^{(2)}(k_o r) & r \ge a \end{cases} \tag{3-76b}$$

where

$$b_{nm} = \frac{-a_{nm}}{\Delta_n^{TE}} \left[\hat{H}_n^{(2)}(ka) \hat{H}_n^{(2)\prime}(k_o a) - \frac{k}{k_o} \hat{H}_n^{(2)\prime}(ka) \hat{H}_n^{(2)}(k_o a) \right] \tag{3-76c}$$

$$c_{nm} = -j \frac{k_o}{k} \cdot \frac{a_{nm}}{\Delta_n^{TE}} \tag{3-76d}$$

$$e_{nm} = \frac{-d_{nm}}{\Delta_n^{TM}} \left[\hat{H}_n^{(2)\prime}(ka) \hat{H}_n^{(2)}(k_o a) - \frac{k}{k_o} \hat{H}_n^{(2)}(ka) \hat{H}_n^{(2)\prime}(k_o a) \right] \tag{3-76e}$$

$$f_{nm} = j \frac{d_{nm}}{\Delta_n^{TM}} \tag{3-76f}$$

and a_{nm} and d_{nm} are now given in (3-74c) and (3-74d), respectively. In (3-76), Δ_n^{TE} and Δ_n^{TM} are given, respectively, by (2-40e) and (2-40f).

Finally, the Green's functions $G_{M_\phi}^{F_r}$ and $G_{M_\phi}^{A_r}$ are given by :

$$G_{M_\phi}^{F_r} = G_{M_\phi}^{F_{rp}} + G_{M_\phi}^{F_{rh}} \tag{3-77a}$$

$$G_{M_\phi}^{A_r} = G_{M_\phi}^{A_{rp}} + G_{M_\phi}^{A_{rh}} \tag{3-77b}$$

(B) Derivation of $G_{M_r}^{F_r}$

From (2-43), one can obtain the following equation using the concept of duality [32, pp.98-100]:

$$(\nabla^2 + k^2)\frac{G_{M_r}^{F_{rp}}}{r} = \frac{-\varepsilon}{r}\,\frac{\delta(r-r')\delta(\theta-\theta')\delta(\phi-\phi')}{r^2\sin\theta} \tag{3-78}$$

Equation (3-78) was solved (Appendix C, with μ_o replaced by ε) and the result for the particular solution $G_{M_r}^{F_{rp}}$ is given by:

$$G_{M_r}^{F_{rp}} = \frac{1}{r'^2}\sum_{n=0}^{\infty}\sum_{m=0}^{n} g_{nm} P_n^m(\cos\theta')P_n^m(\cos\theta)\cos m(\phi-\phi')\cdot\begin{cases}\hat{J}_n(kr')\hat{H}_n^{(2)}(kr) & r>r' \\ \hat{H}_n^{(2)}(kr')\hat{J}_n(kr) & r<r'\end{cases} \tag{3-79a}$$

where

$$g_{nm} = \frac{-j\varepsilon}{2\pi\Delta_m k}\frac{(n-m)!}{(n+m)!}(2n+1) \tag{3-79b}$$

By matching the boundary conditions at the spherical surface of the DR, the homogeneous solution is obtained as follows :

$$G_{M_r}^{A_{rh}} = \frac{1}{r'^2}\sum_{n=0}^{\infty}\sum_{m=0}^{n} P_n^m(\cos\theta')P_n^m(\cos\theta)\cos m(\phi-\phi')\hat{J}_n(kr')\cdot\begin{cases}h_{nm}\hat{J}_n(kr) & r\le a \\ i_{nm}\hat{H}_n^{(2)}(k_o r) & r\ge a\end{cases} \tag{3-80}$$

where

$$h_{nm} = \frac{-g_{nm}}{\Delta_n^{TE}}\left[\hat{H}_n^{(2)}(ka)\hat{H}_n^{(2)\prime}(k_o a) - \frac{k}{k_o}\hat{H}_n^{(2)\prime}(ka)\hat{H}_n^{(2)}(k_o a)\right] \tag{3-81a}$$

$$i_{nm} = -j\frac{k_o}{k}\cdot\frac{g_{nm}}{\Delta_n^{TE}} \tag{3-81b}$$

and g_{nm} is given in (3-79b).

The Green's function $G_{M_r}^{F_r}$ is then given by :

$$G_{M_r}^{F_r} = G_{M_r}^{F_{rp}} + G_{M_r}^{F_{rh}} \tag{3-82}$$

(C) Derivation of $G_{M_y}^{H_y}$

Define two dyadic Green's functions :

$$\overline{\overline{G}}_{M_r}^{\vec{H}} = G_{M_r}^{H_r}\hat{r}\hat{r} + G_{M_r}^{H_\theta}\hat{\theta}\hat{r} + G_{M_r}^{H_\phi}\hat{\phi}\hat{r} \tag{3-83a}$$

$$\overline{\overline{G}}_{M_\phi}^{\vec{H}} = G_{M_\phi}^{H_r}\hat{r}\hat{\phi} + G_{M_\theta}^{H_\phi}\hat{\theta}\hat{\phi} + G_{M_\phi}^{H_\phi}\hat{\phi}\hat{\phi} \tag{3-83b}$$

where $G_{M_\alpha}^{H_\beta}$ ($\alpha = r, \phi$ and $\beta = r, \theta, \phi$) is the magnetic field Green's function derived from $G_{M_r}^{F_r}$, $G_{M_\phi}^{F_r}$ and $G_{M_\phi}^{A_r}$ using (2-4). The total magnetic field excited by the $\hat{y}$-directed current is then given by :

$$\vec{H} = \int_{S_o}\int \left[\overline{\overline{G}}_{M_r}^{\vec{H}} \cdot (M_r'\hat{r}) + \overline{\overline{G}}_{M_\phi}^{\vec{H}} \cdot (M_\phi'\hat{\phi})\right] dS' \tag{3-84}$$

where S_o is now re-defined as the surface of the slot in which the $\hat{y}$-directed magnetic current is flowing.

Substitute (3-83) into (3-84), we have:

$$\begin{aligned}\vec{H} &= \int_{S_o}\int \left(G_{M_r}^{H_r} M_r'\,\hat{r} + G_{M_r}^{H_\theta} M_r'\,\hat{\theta} + G_{M_r}^{H_\phi} M_r'\,\hat{\phi}\right) + \left(G_{M_\phi}^{H_r} M_\phi'\,\hat{r} + G_{M_\phi}^{H_\theta} M_\phi'\,\hat{\theta} + G_{M_\phi}^{H_\phi} M_\phi'\,\hat{\phi}\right) dS' \\ &= \int_{S_o}\int \left(G_{M_r}^{H_r} M_r' + G_{M_\phi}^{H_r} M_\phi'\right)\hat{r} + \left(G_{M_r}^{H_\theta} M_r' + G_{M_\phi}^{H_\theta} M_\phi'\right)\hat{\theta} + \left(G_{M_r}^{H_\phi} M_r' + G_{M_\phi}^{H_\phi} M_\phi'\right)\hat{\phi}\; dS'\end{aligned} \tag{3-85}$$

Using the fact that ($\theta=\theta'=\pi/2$):

$$H_y = H_r \sin\phi + H_\phi \cos\phi \tag{2-86a}$$

$$M_r' = M_y' \sin\phi' \tag{2-86b}$$

and

$$M_\phi' = M_y' \cos\phi' \tag{2-86c}$$

the y-directed magnetic field is obtained:

$$H_y = \int_{S_o}\int \left[\left(G_{M_r}^{H_r} \sin\phi' + G_{M_\phi}^{H_r} \cos\phi' \right) \sin\phi + \left(G_{M_r}^{H_\phi} \sin\phi' + G_{M_\phi}^{H_\phi} \cos\phi' \right) \cos\phi \right] M_y' \, dS'$$

$$= \int_{S_o}\int G_{M_y}^{H_y} M_y' dS' \tag{3-87}$$

where

$$G_{M_y}^{H_y} = \left(G_{M_r}^{H_r} \sin\phi' + G_{M_\phi}^{H_r} \cos\phi' \right) \sin\phi + \left(G_{M_r}^{H_\phi} \sin\phi' + G_{M_\phi}^{H_\phi} \cos\phi' \right) \cos\phi \tag{3-88}$$

is the required Green's function. After simplification, we get ($r \le a$, and $\theta=\theta'=\pi/2$):

$$G_{M_y}^{H_y} = G_P + G_H \tag{2-89}$$

where

$$G_P = \frac{1}{j\omega\mu_o\varepsilon} \cdot \frac{\sin\phi' \sin\phi}{r^2 r'^2} \sum_{n=1}^{\infty} \sum_{m=0}^{n} n(n+1)\, g_{nm}\, P_n^m(\cos\theta') P_n^m(\cos\theta) \cos m(\phi-\phi') \Phi_n(kr') \Psi_n(kr)$$

$$+ \frac{1}{j\omega\mu_o\varepsilon} \cdot \frac{\cos\phi' \sin\phi}{r^2 r'} \sum_{n=1}^{\infty} \sum_{m=0}^{n} n(n+1) a_{nm}\, P_n^m(\cos\theta') P_n^m(\cos\theta) \sin m(\phi-\phi') \Phi_n'(kr') \Psi_n(kr)$$

$$- \frac{k}{j\omega\mu_o\varepsilon} \cdot \frac{\sin\phi' \cos\phi}{r r'^2} \sum_{n=1}^{\infty} \sum_{m=0}^{n} m\, g_{nm}\, P_n^m(\cos\theta') P_n^m(\cos\theta) \sin m(\phi-\phi') \Phi_n(kr') \Psi_n'(kr)$$

$$- \frac{1}{\mu_o} \cdot \frac{\cos\phi' \cos\phi}{r r'} \sum_{n=1}^{\infty} \sum_{m=1}^{n} d_{nm} \frac{d}{d\theta'} P_n^m(\cos\theta') \frac{d}{d\theta} P_n^m(\cos\theta) \cos m(\phi-\phi') \Phi_n(kr') \Psi_n(kr)$$

$$+ \frac{k}{j\omega\mu_o\varepsilon} \cdot \frac{\cos\phi' \cos\phi}{r r'} \sum_{n=1}^{\infty} \sum_{m=0}^{n} m\, a_{nm} P_n^m(\cos\theta') P_n^m(\cos\theta) \cos m(\phi-\phi') \Phi_n'(kr') \Psi_n'(kr)$$

(3-90)

$$G_H = \frac{1}{j\omega\mu_o\varepsilon}\cdot\frac{\sin\phi'\sin\phi}{r^2r'^2}\sum_{n=1}^{\infty}\sum_{m=0}^{n} n(n+1)\,h_{nm}\,P_n^m(\cos\theta')P_n^m(\cos\theta)\cos m(\phi-\phi')\hat{J}_n(kr')\hat{J}_n(kr)$$

$$+\frac{1}{j\omega\mu_o\varepsilon}\cdot\frac{\cos\phi'\sin\phi}{r^2r'}\sum_{n=1}^{\infty}\sum_{m=0}^{n} n(n+1)b_{nm}\,P_n^m(\cos\theta')P_n^m(\cos\theta)\sin m(\phi-\phi')\hat{J}_n'(kr')\hat{J}_n(kr)$$

$$-\frac{k}{j\omega\mu_o\varepsilon}\cdot\frac{\sin\phi'\cos\phi}{rr'^2}\sum_{n=1}^{\infty}\sum_{m=0}^{n} m\,h_{nm}\,P_n^m(\cos\theta')P_n^m(\cos\theta)\sin m(\phi-\phi')\hat{J}_n(kr')\hat{J}_n'(kr)$$

$$-\frac{1}{\mu_o}\cdot\frac{\cos\phi'\cos\phi}{rr'}\sum_{n=1}^{\infty}\sum_{m=1}^{n} e_{nm}\frac{d}{d\theta'}P_n^m(\cos\theta')\frac{d}{d\theta}P_n^m(\cos\theta)\cos m(\phi-\phi')\hat{J}_n(kr')\hat{J}_n(kr)$$

$$+\frac{k}{j\omega\mu_o\varepsilon}\cdot\frac{\cos\phi'\cos\phi}{rr'}\sum_{n=1}^{\infty}\sum_{m=0}^{n} m\,b_{nm}P_n^m(\cos\theta')P_n^m(\cos\theta)\cos m(\phi-\phi')\hat{J}_n'(kr')\hat{J}_n'(kr)$$

(3-91)

and $\Phi_n(kr')$ and $\Psi_n(kr)$ are given, respectively, in (2-54d) and (2-54e), whereas the constants a_{nm}, b_{nm}, d_{nm}, e_{nm}, g_{nm} and h_{nm} are given in (3-74), (3-76), (3-79) and (3-81). To this end, the reciprocity of $G_{M_y}^{H_y}$ in $\vec{r}$ and $\vec{r}'$ is not obvious. A form which shows this property explicitly will be shown in the next section.

3.5 Efficient Evaluations of Antenna Green's Function and Y_{mn}^{a}

In this section, the numerical difficulties in calculating the antenna Green's function $G_{M_y}^{H_y}$ and Y_{mn}^{a} are discussed, and the methods to tackle them are presented.

3.5.1 Modal Green's Function of DR Antenna

Like the convergence problem of the particular solution occurred in the probe-fed case, the Green's function $G_{M_y}^{H_y}$ cannot be evaluated using (3-102) directly because of the slowly convergent particular solution G_P. Before solving the problem, the double-summation of the Green's function in (3-89) is reduced to a single-summation using the addition theorem for Legendre polynomials (equation (2-62)) so that the computational efficiency is enhanced. The results are shown as belows:

$$G_{M_y}^{H_y} = G_P + G_H \tag{3-92a}$$

where

$$\begin{aligned}
G_P =& \frac{-1}{4\pi\omega\mu_o k}\cdot\frac{\sin\phi'\sin\phi}{r^2 r'^2}\sum_{n=1}^{\infty} n(n+1)(2n+1)\,P_n(\cos(\phi-\phi'))\Phi_n(kr')\Psi_n(kr) \\
&-\frac{1}{4\pi\omega\mu_o}\cdot\frac{\cos\phi'\sin\phi}{r^2 r'}\sum_{n=1}^{\infty}(2n+1)\frac{\partial}{\partial\phi'}P_n(\cos(\phi-\phi'))\Phi_n'(kr')\Psi_n(kr) \\
&-\frac{1}{4\pi\omega\mu_o}\cdot\frac{\sin\phi'\cos\phi}{r r'^2}\sum_{n=1}^{\infty}(2n+1)\frac{\partial}{\partial\phi}P_n(\cos(\phi-\phi'))\Phi_n(kr')\Psi_n'(kr) \\
&-\frac{\omega\varepsilon}{4\pi k}\cdot\frac{\cos\phi'\cos\phi}{r r'}\sum_{n=1}^{\infty}\frac{2n+1}{n(n+1)}P_n'(\cos(\phi-\phi'))\Phi_n(kr')\Psi_n(kr) \\
&-\frac{k}{4\pi\omega\mu_o}\cdot\frac{\cos\phi'\cos\phi}{r r'}\sum_{n=1}^{\infty}\frac{2n+1}{n(n+1)}\frac{\partial^2}{\partial\phi\partial\phi'}P_n(\cos(\phi-\phi'))\Phi_n'(kr')\Psi_n'(kr)
\end{aligned} \tag{3-92b}$$

$$G_H = \frac{-1}{4\pi\omega\mu_o k}\cdot\frac{\sin\phi'\sin\phi}{r^2 r'^2}\sum_{n=1}^{\infty} b_n\, n(n+1)(2n+1)\, P_n(\cos(\phi-\phi'))\hat{J}_n(kr')\hat{J}_n(kr)$$

$$-\frac{1}{4\pi\omega\mu_o}\cdot\frac{\cos\phi'\sin\phi}{r^2 r'}\sum_{n=1}^{\infty} b_n\,(2n+1)\frac{\partial}{\partial\phi'}P_n(\cos(\phi-\phi'))\hat{J}_n'(kr')\hat{J}_n(kr)$$

$$-\frac{1}{4\pi\omega\mu_o}\cdot\frac{\sin\phi'\cos\phi}{r r'^2}\sum_{n=1}^{\infty} b_n\,(2n+1)\frac{\partial}{\partial\phi}P_n(\cos(\phi-\phi'))\hat{J}_n(kr')\hat{J}_n'(kr)$$

$$-\frac{\omega\varepsilon}{4\pi k}\cdot\frac{\cos\phi'\cos\phi}{r r'}\sum_{n=1}^{\infty} e_n\frac{2n+1}{n(n+1)}P_n'(\cos(\phi-\phi'))\hat{J}_n(kr')\hat{J}_n(kr)$$

$$-\frac{k}{4\pi\omega\mu_o}\cdot\frac{\cos\phi'\cos\phi}{r r'}\sum_{n=1}^{\infty} b_n\frac{2n+1}{n(n+1)}\frac{\partial^2}{\partial\phi\partial\phi'}P_n(\cos(\phi-\phi'))\hat{J}_n'(kr')\hat{J}_n'(kr) \qquad \text{(3-92c)}$$

$$b_n = \frac{-1}{\Delta_n^{TE}}\left[\hat{H}_n^{(2)}(ka)\hat{H}_n^{(2)\prime}(k_o a) - \frac{k}{k_o}\hat{H}_n^{(2)\prime}(ka)\hat{H}_n^{(2)}(k_o a)\right] \qquad \text{(3-92d)}$$

$$e_n = \frac{-1}{\Delta_n^{TM}}\left[\hat{H}_n^{(2)\prime}(ka)\hat{H}_n^{(2)}(k_o a) - \frac{k}{k_o}\hat{H}_n^{(2)}(ka)\hat{H}_n^{(2)\prime}(k_o a)\right] \qquad \text{(3-92e)}$$

and Δ_n^{TE} and Δ_n^{TM} are given by (2-40e) and (2-40f), respectively. A prime denotes derivative of a function. In deriving (3-92) from (3-90), we have used the fact that $\theta = \theta' = \pi/2$. From (3-92), it is clearly seen that the Green's function $G_{M_y}^{H_y}$ is reciprocal in $\vec{r}$ and $\vec{r}'$ as expected.

To solve the convergence problem, the technique used in the previous chapter is employed again to give a simple form for the particular solution. Recall that G_P simply represents a $\hat{y}$-directed magnetic field on the x-y plane due to a $\hat{y}$-directed magnetic current on the same plane in an unbounded dielectric medium; thus the Green's function can be alternatively given by ($z = z' = 0$):

$$G_P = \frac{-j}{\omega\mu_o}\left(\frac{\partial^2}{\partial y^2} + k^2\right)\frac{e^{-jkR}}{4\pi R} \qquad \text{(3-93)}$$

where $R=\sqrt{(x-x')^2+(y-y')^2}$ is the distance between the source and the field points on the x-y plane. Hence a new mathematical identity can be established:

$$\frac{-j}{\omega\mu_o}\left(\frac{\partial^2}{\partial y^2}+k^2\right)\frac{e^{-jkR}}{4\pi R}$$

$$=\frac{-1}{4\pi\omega\mu_o k}\cdot\frac{\sin\phi'\sin\phi}{r^2r'^2}\sum_{n=1}^{\infty}n(n+1)(2n+1)P_n(\cos(\phi-\phi'))\Phi_n(kr')\Psi_n(kr)$$

$$-\frac{1}{4\pi\omega\mu_o}\cdot\frac{\cos\phi'\sin\phi}{r^2r'}\sum_{n=1}^{\infty}(2n+1)\frac{\partial}{\partial\phi'}P_n(\cos(\phi-\phi'))\Phi_n'(kr')\Psi_n(kr)$$

$$-\frac{1}{4\pi\omega\mu_o}\cdot\frac{\sin\phi'\cos\phi}{rr'^2}\sum_{n=1}^{\infty}(2n+1)\frac{\partial}{\partial\phi}P_n(\cos(\phi-\phi'))\Phi_n(kr')\Psi_n'(kr)$$

$$-\frac{\omega\varepsilon}{4\pi k}\cdot\frac{\cos\phi'\cos\phi}{rr'}\sum_{n=1}^{\infty}\frac{2n+1}{n(n+1)}P_n'(\cos(\phi-\phi'))\Phi_n(kr')\Psi_n(kr)$$

$$-\frac{k}{4\pi\omega\mu_o}\cdot\frac{\cos\phi'\cos\phi}{rr'}\sum_{n=1}^{\infty}\frac{2n+1}{n(n+1)}\frac{\partial^2}{\partial\phi\partial\phi'}P_n(\cos(\phi-\phi'))\Phi_n'(kr')\Psi_n'(kr) \qquad (3\text{-}94)$$

where
$$R=\sqrt{(r\cos\phi-r'\cos\phi')^2+(y-r'\sin\phi')^2} \qquad (3\text{-}95)$$

Finally the Green's function $G_{M_y}^{H_y}$ is given by ($r<a$, $\theta=\theta'=\pi/2$) :

$$G_{M_y}^{H_y}=\frac{-j}{\omega\mu_o}\left(\frac{\partial^2}{\partial y^2}+k^2\right)\frac{e^{-jkR}}{4\pi R}$$

$$-\frac{1}{4\pi\omega\mu_o k}\cdot\frac{\sin\phi'\sin\phi}{r^2r'^2}\sum_{n=1}^{\infty}b_n n(n+1)(2n+1)P_n(\cos(\phi-\phi'))\hat{J}_n(kr')\hat{J}_n(kr)$$

$$-\frac{1}{4\pi\omega\mu_o}\cdot\frac{\cos\phi'\sin\phi}{r^2r'}\sum_{n=1}^{\infty}b_n(2n+1)\frac{\partial}{\partial\phi'}P_n(\cos(\phi-\phi'))\hat{J}_n'(kr')\hat{J}_n(kr)$$

$$-\frac{1}{4\pi\omega\mu_o}\cdot\frac{\sin\phi'\cos\phi}{rr'^2}\sum_{n=1}^{\infty}b_n(2n+1)\frac{\partial}{\partial\phi}P_n(\cos(\phi-\phi'))\hat{J}_n(kr')\hat{J}_n'(kr)$$

$$-\frac{\omega\varepsilon}{4\pi k}\cdot\frac{\cos\phi'\cos\phi}{rr'}\sum_{n=1}^{\infty}e_n\frac{2n+1}{n(n+1)}P_n'(\cos(\phi-\phi'))\hat{J}_n(kr')\hat{J}_n(kr)$$

$$-\frac{k}{4\pi\omega\mu_o}\cdot\frac{\cos\phi'\cos\phi}{rr'}\sum_{n=1}^{\infty}b_n\frac{2n+1}{n(n+1)}\frac{\partial^2}{\partial\phi\partial\phi'}P_n(\cos(\phi-\phi'))\hat{J}_n'(kr')\hat{J}_n'(kr) \qquad (3\text{-}96)$$

It was found that the homogeneous G_H converges very quickly. Together with the simple form for the particular solution G_P, the Green's function $G_{M_y}^{H_y}$ can be evaluated very efficiently.

3.5.2 Evaluation of Y_{mn}^a

The evaluation of Y_{mn}^a in (3-49) is now discussed. Note that $G_{M_y}^{H_y}$ has a singularity at $\vec{r} = \vec{r}'$, and therefore the integration cannot be done directly. To begin with, Y_{mn}^a is written as:

$$Y_{mn}^a = Y_{mn}^P + Y_{mn}^H \tag{3-97a}$$

where

$$Y_{mn}^P = -2 \int_{S_o}\int \int_{S_o}\int f_m(x,y)\, G_P\, f_n(x',y')dS'dS \tag{3-97b}$$

$$Y_{mn}^H = -2 \int_{S_o}\int \int_{S_o}\int f_m(x,y)\, G_H\, f_n(x',y')dS'dS \tag{3-97c}$$

in which G_P and G_H are given in (3-93) and (3-92), respectively.

The evaluation of Y_{mn}^H can be done in a straightforward manner as G_H is a smooth and slowly varying function. For Y_{mn}^P, however, special consideration is needed due to the singularity of G_P occurring at $\vec{r} = \vec{r}'$. Since Y_{mn}^P represents the slot admittance in an unbounded dielectric medium, we can treat the slot as if it were located along the $\hat{y}$-axis. Moreover, for a slender slot ($k_o W \ll 1$, $W \ll L$), one can compute the slot admittance using the concept of equivalent radius a_e [50] so that the theory developed in cylindrical dipole can be utilized. The equivalent radius a_e is given by:

$$a_e = \frac{W}{4} \tag{3-98}$$

Therefore we have:

$$Y_{mn}^P = \frac{-2}{\eta^2} \int_{-\frac{L}{2}}^{\frac{L}{2}} \int_{-\frac{L}{2}}^{\frac{L}{2}} f_p(y - y_m) \left[\frac{-j}{\omega\varepsilon} \left(\frac{\partial^2}{\partial y^2} + k^2 \right) \frac{e^{-jk\zeta_e}}{4\pi\zeta_e} \right] f_p(y' - y_n)\, dy'dy \tag{3-99}$$

where

$$\zeta_e = \sqrt{(y - y')^2 + a_e^2} \tag{3-100}$$

and $\eta = \sqrt{\mu_o/\varepsilon}$ is the dielectric wave impedance. Note that by considering the (magnetic) cylindrical dipole, one can make use of the knowledge developed in electric cylindrical dipoles. Expressing (3-99) in the "Richmond form", one obtains:

$$Y_{mn}^P = \frac{-2}{\eta^2} \cdot \frac{-j\eta}{4\pi k} \int_{\frac{-L}{2}}^{\frac{L}{2}} \int_{\frac{-L}{2}}^{\frac{L}{2}} f_p(y - y_m) \frac{e^{-jk\zeta_e}}{\zeta_e^5} [(1 + jk\zeta_e)(2\zeta_e^2 - 3a_e^2) + a_e^2 k^2 \zeta_e^2]\, f_p(y' - y_n)\, dy'dy \tag{3-101}$$

Since PWS modes are now used for the current expansion modes as well as the testing current modes, the simple formula (2-88) can be used so that Y_{mn}^P can be evaluated very efficiently.

3.6 Single Cavity Mode Approximation

3.6.1 Evaluation of Input Impedance

This section will investigate the use of single mode approximations of the Green's function $G_{M_y}^{H_y}$ for the broadside TE_{111} mode and the end-fire TE_{221} mode so as to simplify the expression of the Green's function. The single mode Green's function for the broadside TE_{111} mode, G_{111}^{TE}, and that for the end-fire TE_{221} mode, G_{221}^{TE}, are given as follows ($r \le a$, $r' \le a$ and $\theta = \theta' = \pi/2$) :

$$
\begin{aligned}
G_{111}^{TE} = & \frac{-j}{\omega\mu_o}\left(\frac{\partial^2}{\partial y^2}+k^2\right)\frac{e^{-jkR}}{4\pi R} \\
& -\frac{3b_1}{2\pi\omega\mu_o k}\cdot\frac{\sin\phi\sin\phi'\cos(\phi-\phi')}{r^2r'^2}\cdot\hat{J}_1(kr')\hat{J}_1(kr) \\
& -\frac{3b_1}{4\pi\omega\mu_o}\cdot\frac{\sin\phi\cos\phi'\sin(\phi-\phi')}{r^2r'}\cdot\hat{J}_1'(kr')\hat{J}_1(kr) \\
& +\frac{3b_1}{4\pi\omega\mu_o}\cdot\frac{\sin\phi'\cos\phi\sin(\phi-\phi')}{rr'^2}\cdot\hat{J}_1(kr')\hat{J}_1'(kr) \\
& -\frac{3kb_1}{8\pi\omega\mu_o}\cdot\frac{\cos\phi'\cos\phi\cos(\phi-\phi')}{rr'}\cdot\hat{J}_1'(kr')\hat{J}_1'(kr)
\end{aligned}
\qquad (3\text{-}102)
$$

$$
\begin{aligned}
G_{221}^{TE} = & \frac{-j}{\omega\mu_o}\left(\frac{\partial^2}{\partial y^2}+k^2\right)\frac{e^{-jkR}}{4\pi R} \\
& -\frac{45b_2}{8\pi\omega\mu_o k}\cdot\frac{\sin\phi\sin\phi'\cos 2(\phi-\phi')}{r^2r'^2}\cdot\hat{J}_2(kr')\hat{J}_2(kr) \\
& -\frac{15b_2}{8\pi\omega\mu_o}\cdot\frac{\sin\phi\cos\phi'\sin 2(\phi-\phi')}{r^2r'}\cdot\hat{J}_2'(kr')\hat{J}_2(kr) \\
& +\frac{15b_2}{8\pi\omega\mu_o}\cdot\frac{\sin\phi'\cos\phi\sin 2(\phi-\phi')}{rr'^2}\cdot\hat{J}_2(kr')\hat{J}_2'(kr) \\
& -\frac{5kb_2}{8\pi\omega\mu_o}\cdot\frac{\cos\phi'\cos\phi\cos 2(\phi-\phi')}{rr'}\cdot\hat{J}_2'(kr')\hat{J}_2'(kr)
\end{aligned}
\qquad (3\text{-}103)
$$

where

$$R = \sqrt{(x-x')^2 + (y-y')^2} \tag{3-104}$$

$$b_1 = \frac{-1}{\Delta_1^{TE}} [\hat{H}_1'(k_o a)\, \hat{H}_1(ka) - \sqrt{\varepsilon_r}\, \hat{H}_1(k_o) \hat{H}_1'(ka)] \tag{3-105}$$

$$b_2 = \frac{-1}{\Delta_2^{TE}} [\hat{H}_2'(k_o a)\, \hat{H}_2(ka) - \sqrt{\varepsilon_r}\, \hat{H}_2(k_o) \hat{H}_2'(ka)] \tag{3-106}$$

$$\Delta_1^{TE} = \hat{J}_1(ka) \hat{H}_1^{(2)\prime}(k_o a) - \frac{k}{k_o} \hat{J}_1'(ka) \hat{H}_1^{(2)}(k_o a) \tag{3-107}$$

$$\Delta_2^{TE} = \hat{J}_2(ka) \hat{H}_2^{(2)\prime}(k_o a) - \frac{k}{k_o} \hat{J}_2'(ka) \hat{H}_2^{(2)}(k_o a) \tag{3-108}$$

To further simplify the problem, the magnetic current of the slot is modelled by a single PWS mode:

$$M_y(x,y) = V_o \frac{\sin k_e (L/2 - |y|)}{W \sin k_e L/2} \tag{3-109}$$

where V_o is the unknown amplitude of the aperture field. With this approximation, the reflection coefficient in (3-54) is now simply reduced to

$$R = \frac{\Delta v^2}{\Delta v^2 + 2(Y^a + Y^s)} \tag{3-110}$$

where

$$Y^a = -2 \int_{S_o}\int \int_{S_o}\int M_y(x,y) G(x,y;x',y') M_y(x',y') dS' dS \tag{3-111}$$

$$Y^s = \frac{1}{4\pi^2} \int_{-\infty}^{\infty}\int F_u^2(k_x) F_p^2(k_y) \tilde{G}_{yy}^{HM}(k_x,k_y) dk_x dk_y \tag{3-112}$$

$$\Delta v = \frac{1}{2\pi\sqrt{Z_c}} \int_{-\infty}^{\infty} \tilde{G}_{yx}^{HJ}(-\beta_f, k_y) F_u(k_y) F_p(k_y) \cos(k_y L/2) dk_y \tag{3-113}$$

in which $G = G_{111}^{TE}$ or G_{221}^{TE}. All other symbols are defined in (3-59). Once the reflection coefficient R is obtained, the input impedance at the reference plane is obtained using (3-40).

3.6.2 Measured and Computed Results

(A) Experimental Set-up

To verify the validity of the theory, measurements have been done and the experimental set-up is shown in Appendix G. A dielectric hemisphere of radius 8.2 mm and dielectric constant ε_{ra}=9.5, fed by a slot coupled to a microstripline, was measured for the broadside TE_{111} mode. For the end-fire TE_{221} mode verification, another dielectric hemisphere of radius 12.5mm and dielectric constant ε_{ra}=9.5 was measured instead. In the experiment, the PCB's used are ROGERS RT/DUROID 6002 with substrate dielectric constant ε_r=2.96 and height d=0.635 mm. The measurements were taken using an HP8510C network analyzer, and the reference plane is taken at the center of the slot.

(B) The Broadside TE_{111} *Mode*

Theoretical prediction and measured value of the normalized input impedance are shown in Fig. 3-7. From the theory, the resonant frequency (where Z_{in} is real) is found to be 5.49 GHz, which is very close to the measured value of 5.50 GHz. Moreover, this is consistent with the predicted value of 5.61 GHz as obtained by solving the characteristic equation Δ_1^{TE}=0. Due to the effects of the slot and the open-circuited stub L_s, the calculated resonant frequency (5.49 GHz) is expected to be slightly different from the predicted value (5.61 GHz). From the figure, it is seen that the theory agrees reasonably well with the experiment. Fig. 3-8 compares the return loss between theory and experiment for different slot lengths. It is seen that the theory, again, agrees reasonably well with the experiment. Moreover, the longer the slot, the larger the return loss. For L = 8.5 mm, the dip of the measured

data is not as sharp as that of the theory, which is probably due to experimental limitations. Fig. 3-9 shows the variation of the computed normalized input impedance for different slot lengths on the smith chart. It is seen that the coupling factor (defined by the radius of the impedance circle [27]) increases with the slot length.

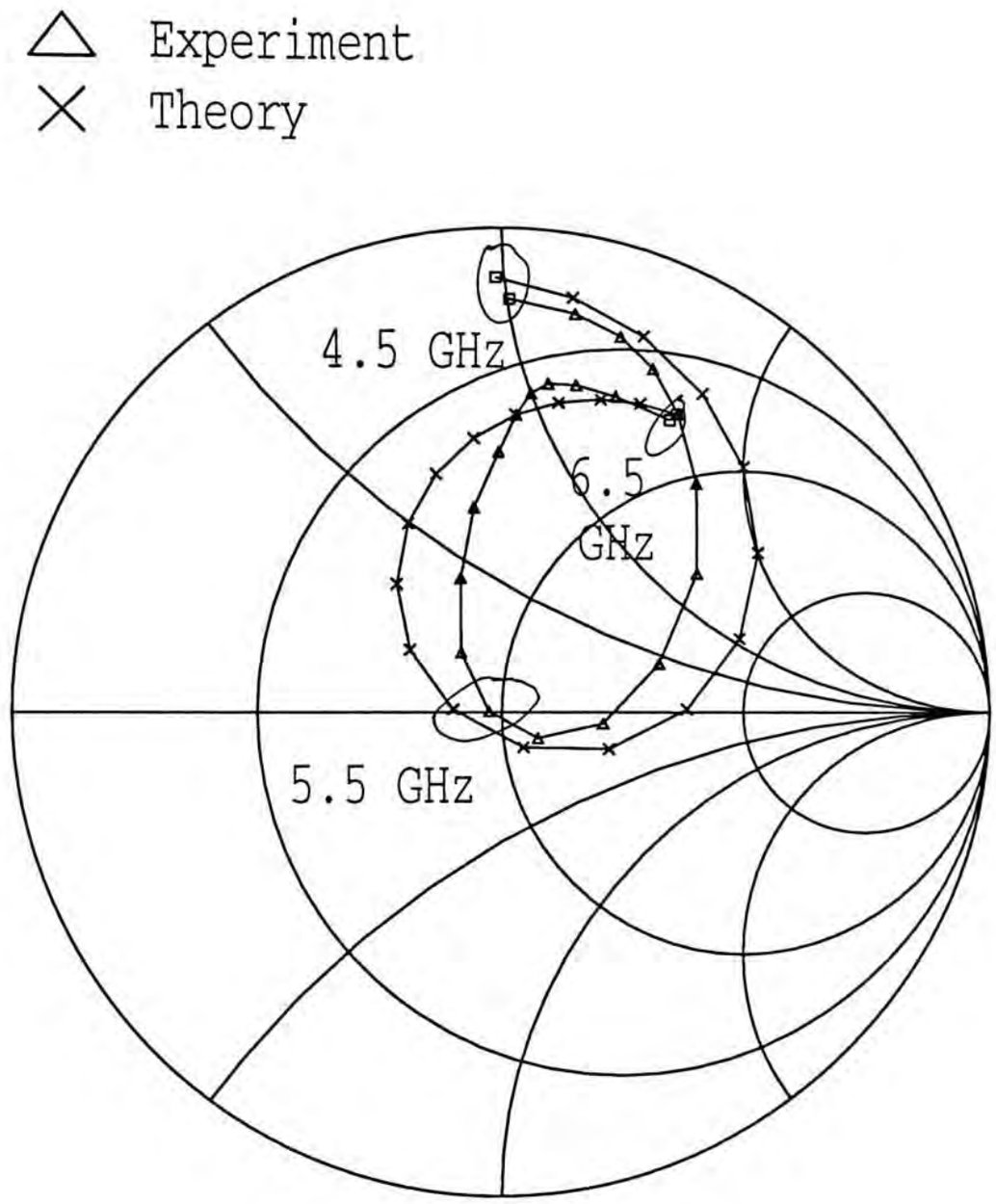

Fig. 3-7 Computed and measured normalized input impedance at the reference plane : a=8.2 mm, ε_{ra}=9.5, L=8.5 mm, x_d=0.0mm, y_d=0.0mm, W=0.863 mm, W_f=1.6 mm, d=0.635 mm, ε_{rs}=2.96, L_s=8.63 mm.

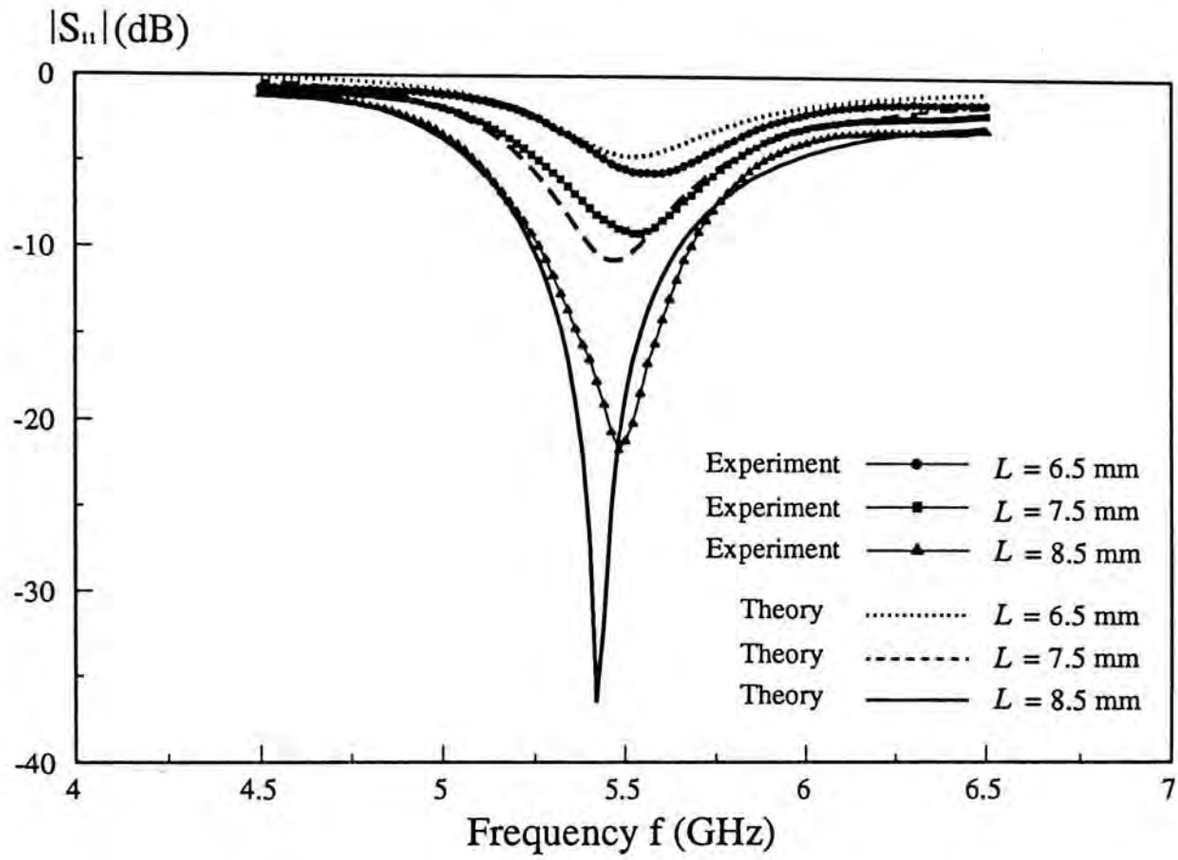

Fig. 3-8 Computed and measured return loss at the reference plane for different slot lengths : a=8.2 mm, ε_{ra}=9.5, x_d=0.0mm, y_d=0.0mm, W=0.5 mm, W_f=1.6 mm, d=0.635 mm, ε_{rs}=2.96, L_s=8.63 mm.

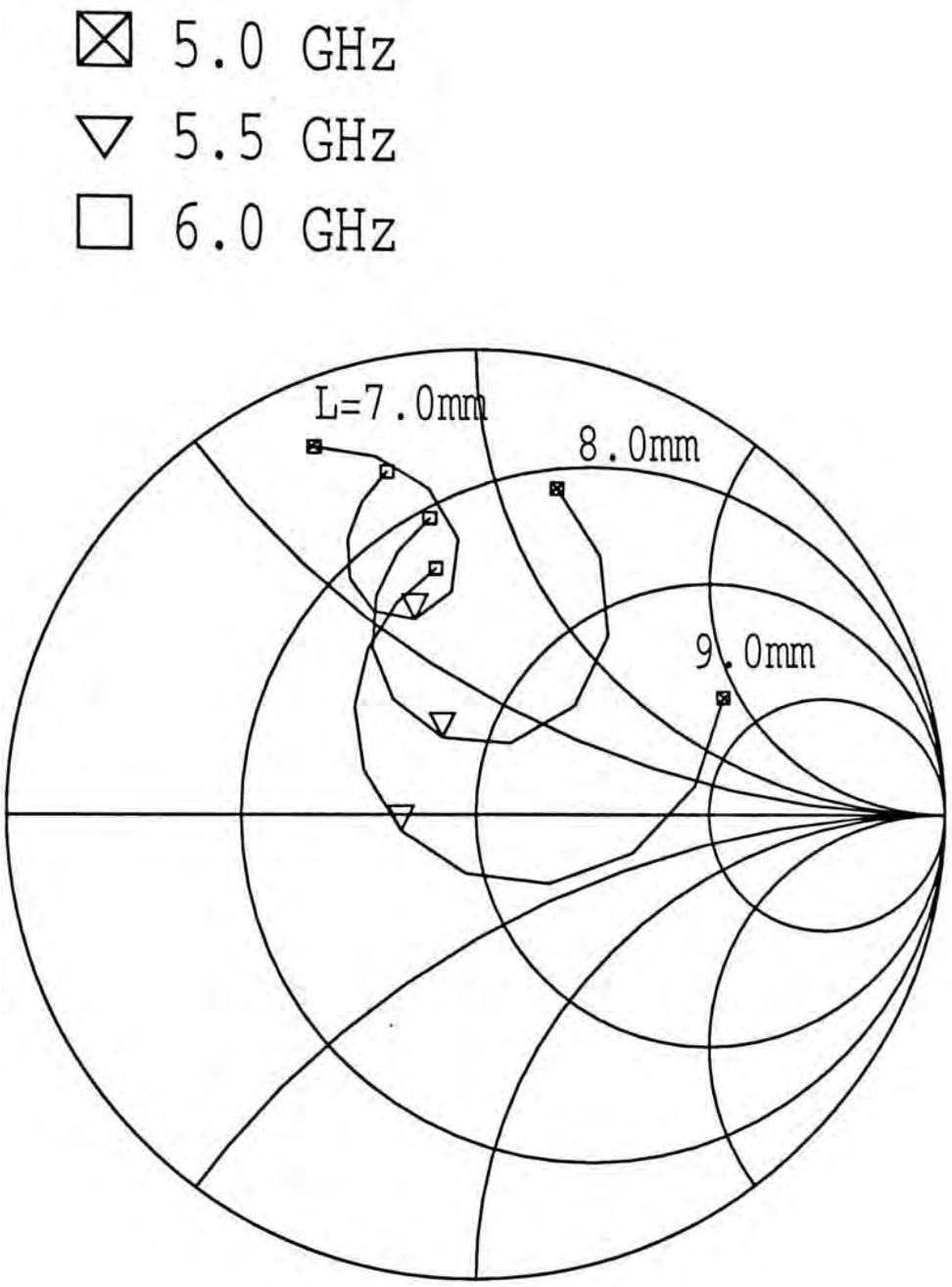

Fig. 3-9 Computed normalized input impedance at the reference plane for different slot lengths : a=8.2 mm, ε_{ra}=9.5, x_d=0.0mm, y_d=0.0mm, W=0.5 mm, W_f=1.6 mm, d=0.635 mm, ε_{rs}=2.96, L_s=8.63 mm.

(C) The End-fire TE_{221} Mode

Theoretical prediction and measured value of the return loss as a function of frequency for different slot displacements are shown in Fig. 3-10. The measured resonant frequency (the frequency at which the return loss is minimum) is 5.40 GHz, which is very close to the calculated value of 5.30 GHz (1.89 % error). Furthermore, from the figure, it is seen that the theory agrees reasonably well with the experiment for y_d = 8.0 mm and y_d = 4.0 mm. For the case of y_d = 0.0 mm, the TE_{221} mode cannot be excited properly. In this case, the fields inside the DR are strongly influenced by other resonant modes, which are neglected in the present theory. This explains the relatively large discrepancy between theory and experiment for y_d = 0.0 mm. It is also seen that the return loss increases with the slot displacement y_d. This trend will continue until the input impedance at the reference plane is matched with the characteristic impedance Z_c of the microstripline. Fig. 3-11 shows the computed and the measured return loss as a function of frequency for different slot lengths. Again, reasonable agreement between theory and experiment is obtained. Moreover, the longer the slot, the larger the return loss.

(D) Error Discussions

The difference between theory and experiment is caused by the imperfect hemispherical DR where it has slight dips on various parts of its surface. In addition, the tolerance of ε_r is not given for the DR so that the uncertainty in the permittivity is a source of error. Moreover, the use of the single mode approximation has also introduced another error.

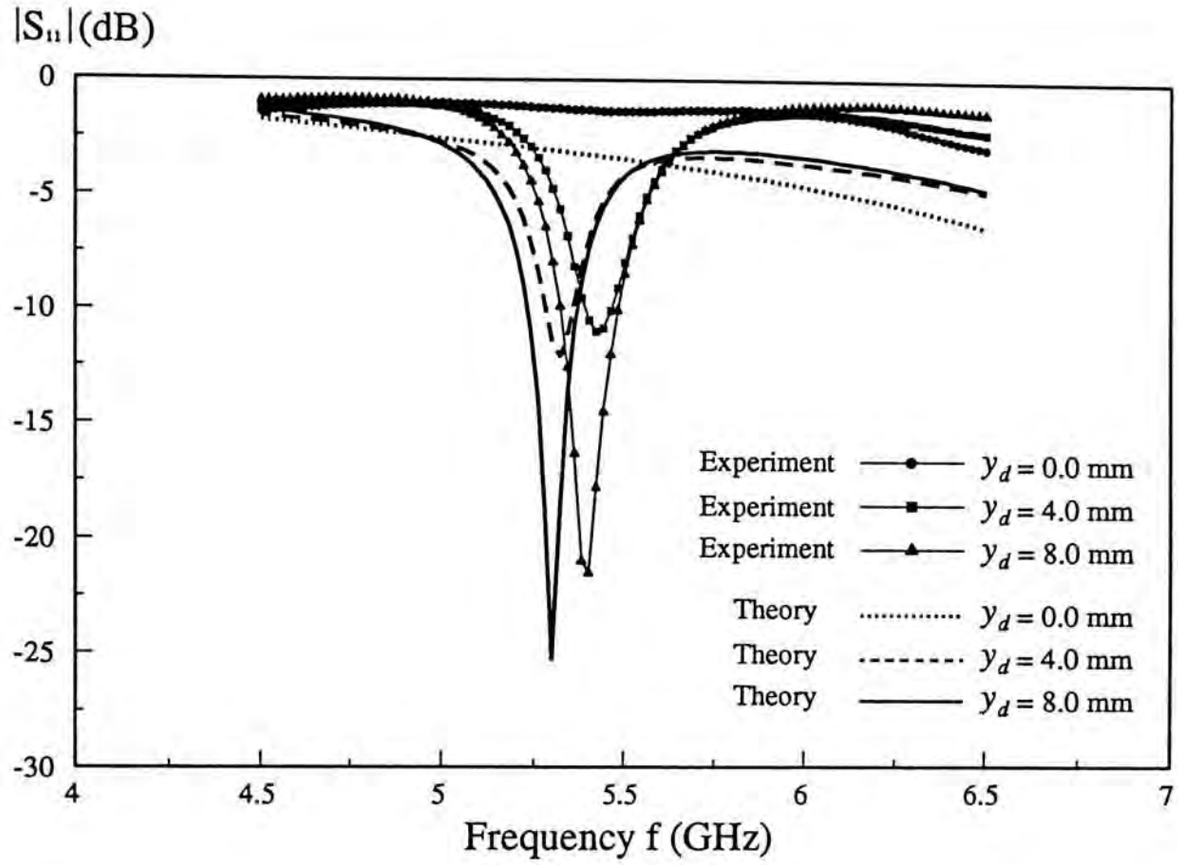

Fig. 3-10 Computed and measured return loss at the reference plane for different slot positions : a=12.5 mm, ε_{ra}=9.5, L=8.5 mm, x_d=0.0 mm, W=0.863 mm, W_f=1.6 mm, d=0.635 mm, ε_{rs}=2.96, L_s=8.63 mm.

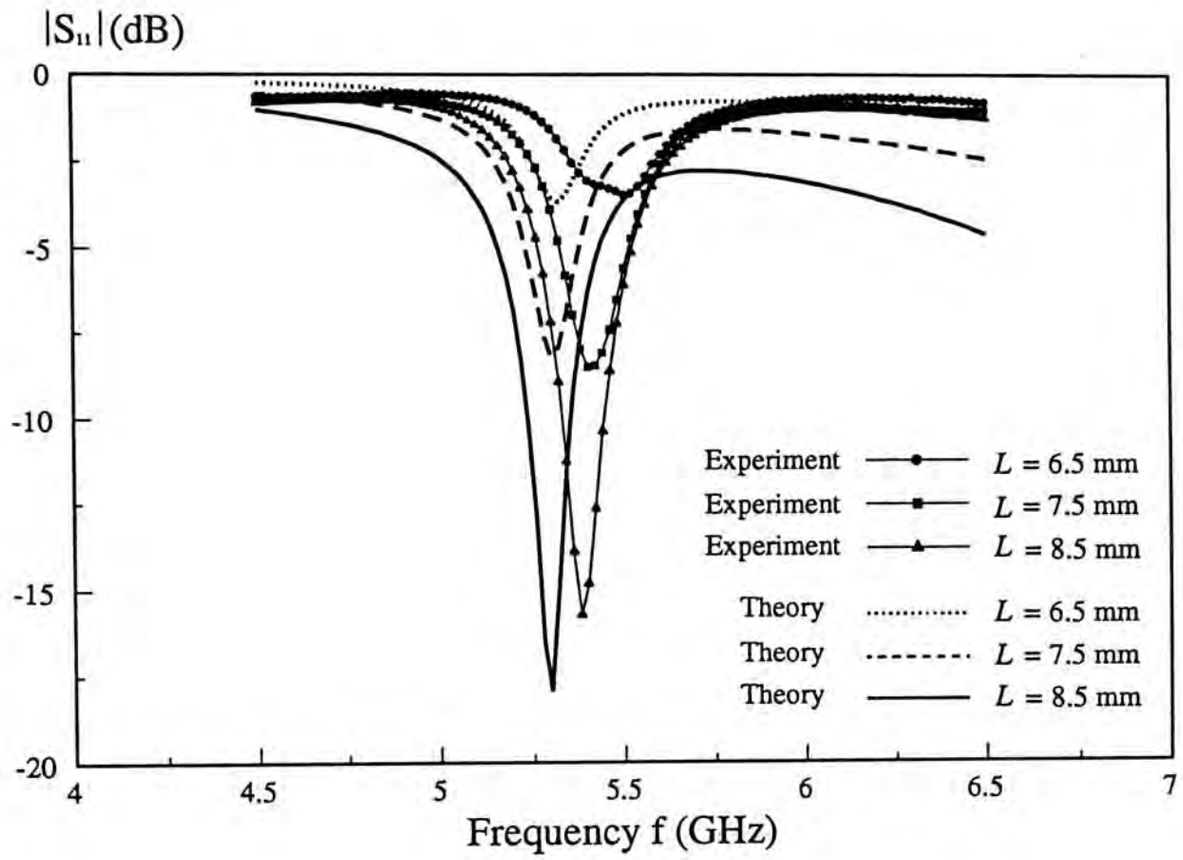

Fig. 3-11 Computed and measured return loss at the reference plane for different slot lengths : a=12.5 mm, ε_{ra}=9.5, x_d=0.0 mm, y_d=8.0mm, W=0.5 mm, W_f=1.6 mm, d=0.635 mm, ε_{rs}=2.96, L_s=8.63 mm.

3.6.3 Conclusion

The input impedance and the return loss of the aperture-coupled DR antenna has been studied using the single mode approximations for the antenna Green's function $G_{M_y}^{H_y}$. Reasonable agreement between theory and experiment has been obtained. It is found that impedance matching is possible by simply varying the slot length for both the broadside TE_{111} mode and the end-fire TE_{221} mode, making his antenna feasible in circuit designs.

Although the present theory gives reasonable agreement with the measurements, the solution so obtained is not general. For example, the result for the end-fire TE_{221} mode is less satisfactory for $y_d = 0$ due to the fact that other resonant modes have been neglected. Moreover, for the TE_{221} mode ,the theory is valid only when the slot is aligned with the y-axis ($x_d = 0$), otherwise the end-fire TM_{101} mode which has been neglected will also be excited. In the next section, the general MM solution using the exact modal Green's function given by (3-96) will be presented, and such solution will eliminate these problems.

3.7 Exact Modal Solution

3.7.1 Convergence Checks

Before comparing the theory with the measurements, convergence tests for the MM solution are performed for the theoretical results. Fig. 3-12 shows the convergence check for the broadside TE_{111} mode. The convergence is quite stable for increasing N, the number of the current expansion mode used. Moreover, when $N = 1$, a quite good result is obtained. The convergence check for the end-fire TE_{221} mode is shown in Fig. 3-13. Again, the convergence is quite stable for increasing N. Moreover, a satisfactory result is obtained even for $N = 1$. Therefore in the following calculations, we will use $N = 3$ as a compromise between the accuracy and the computation time.

3.7.2 Measured and Computed Results

(A) Experimental Set-up

The experimental set-up is shown in Appendix G. A dielectric hemisphere of radius 12.5 mm was used for both the TE_{111} mode and the TE_{221} mode verifications. The PCB's used are ROGERS RT/DUROID 6002 with substrate dielectric constant ε_r=2.96 and height d=0.635 mm. Measurements were taken using the HP8510C network analyzer with the reference plane taken at the center of the slot.

(B) The Broadside TE_{111} *Mode*

The comparison between theory and experiment for the normalized input impedance is shown in Fig. 3-14. The slot has length 13.5 mm and is fed at the center of the DR antenna. The measured resonant frequency is 3.61 GHz, which is very close to the calculated value of 3.56 GHz (1.38 % error). Moreover, it is consistent with the predicted value of 3.68 GHz obtained by solving the characteristic equation $\Delta_1^{TE} = 0$. It is seen that the theory agrees reasonably well

with the measurement. To study the effect of the slot length on the input impedance, two slots of length 11.0 mm and 16.3 mm are used and the results are shown in Figs. 3-15 and 3-16, respectively. Again, reasonable agreements between theory and experiment are obtained. It is found that the coupling factor (defined as the radius of the impedance circle [27]) increases with the slot length. Hence one can achieve impedance matching by simply varying the slot length. The result of using a slightly wider slot is shown in Fig. 3-17. It is seen that by using the larger slot, the coupling is increased. Therefore one may also adjust the slot width to help achieve impedance matching. Of course the slot width cannot be too wide, otherwise the assumption that the $\hat{x}$-directed magnetic current is constant across the width of the slot is no longer valid.

The variation of the input impedance using different x_d 's are shown in Figs. 3-18 through 3-19. Reasonable agreement between theory and experiment is obtained. It is seen that the larger the offset x_d, the weaker the TE_{111} mode excitation. This is in contrast to the probe-fed case where a displacement from the center of the DR is required to excite the TE_{111} properly. Fig. 3-20 shows the reflection coefficient $|S_{11}|$ for different slot-offset x_d's. By changing x_d, one can also perform impedance matching.

The input impedance for different y_d 's is shown in Fig. 3-21. Again, the larger the slot-offset y_d, the weaker the coupling between the DR antenna and the slot. Fig. 3-22 shows the corresponding $|S_{11}|$, and it is observed that the trend is similar to that for the case of varying x_d.

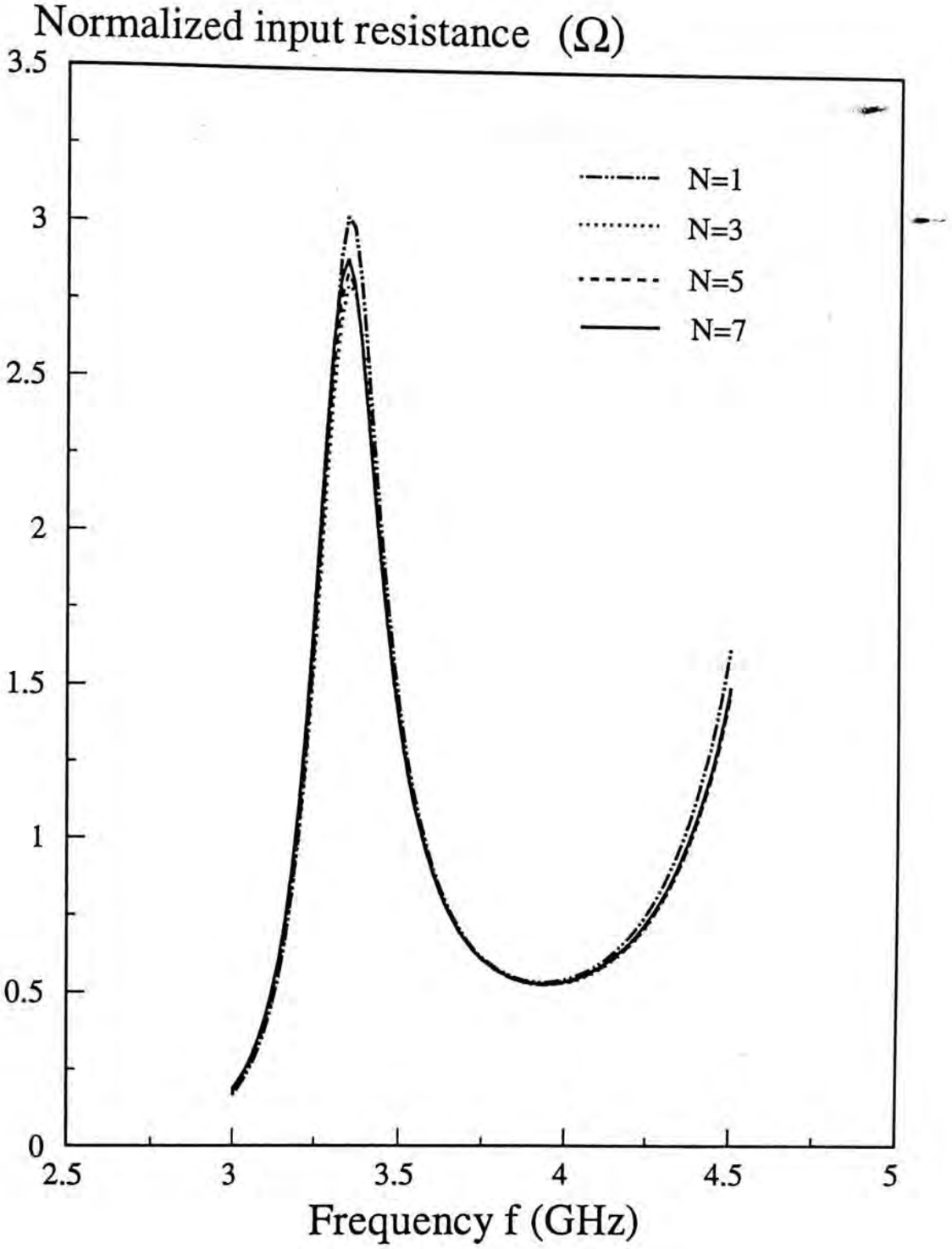

Fig. 3-12(a): Convergence check for the input resistance against frequency for the TE_{111} mode: a=12.5mm, ε_{ra}=9.5, L=13.5 mm, W=0.87 mm, x_d=0.0 mm, y_d=0.0 mm, W_f=1.45 mm, d=0.635 mm, ε_{rs}=2.96, L_s=13.6 mm.

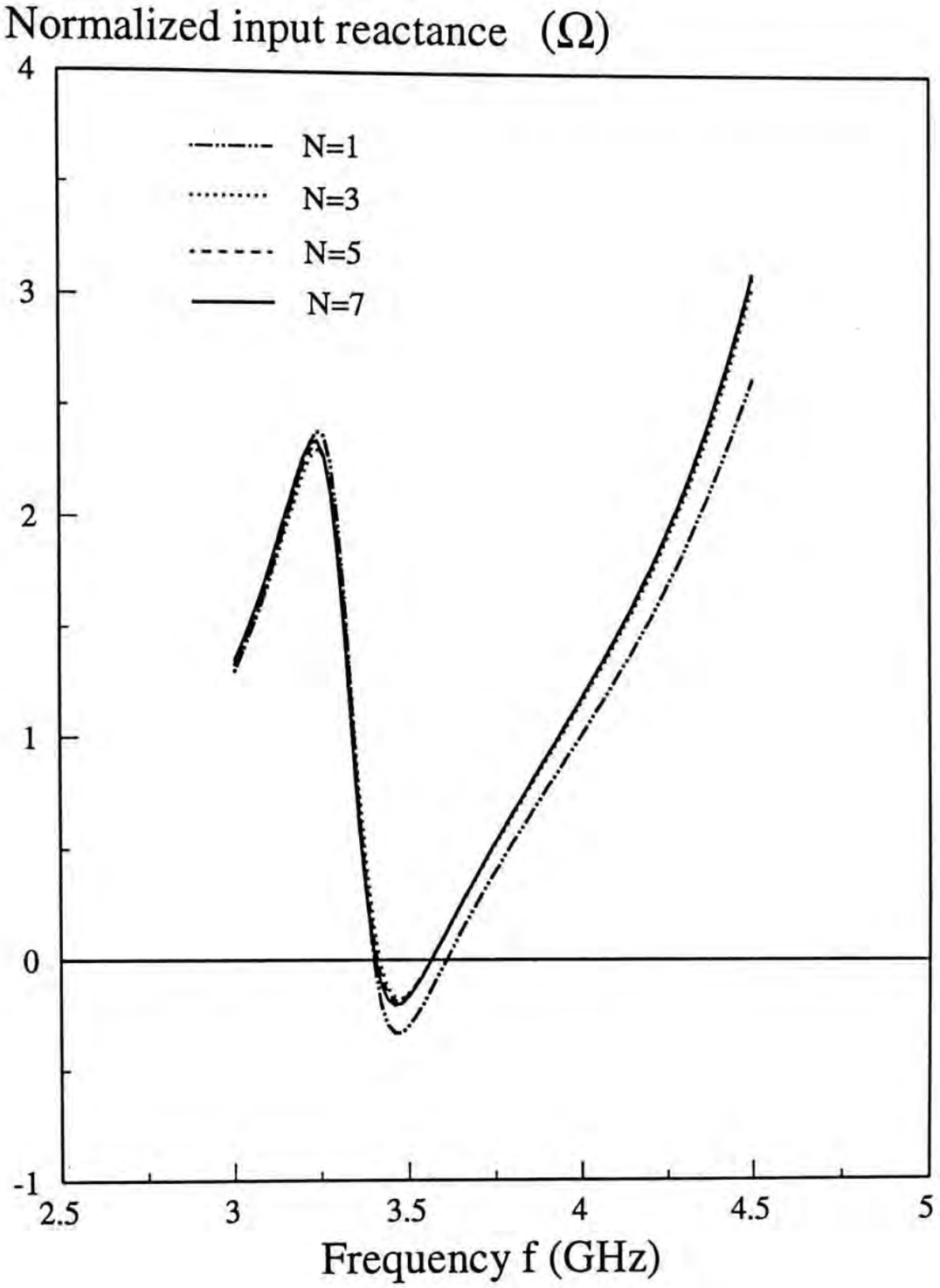

Fig. 3-12(b): Convergence check for the input reactance against frequency for the TE_{111} mode: a=12.5mm, ε_{ra}=9.5, L=13.5 mm, W=0.87 mm, x_d=0.0 mm, y_d=0.0 mm, W_f=1.45 mm, d=0.635 mm, ε_{rs}=2.96, L_s=13.6 mm.

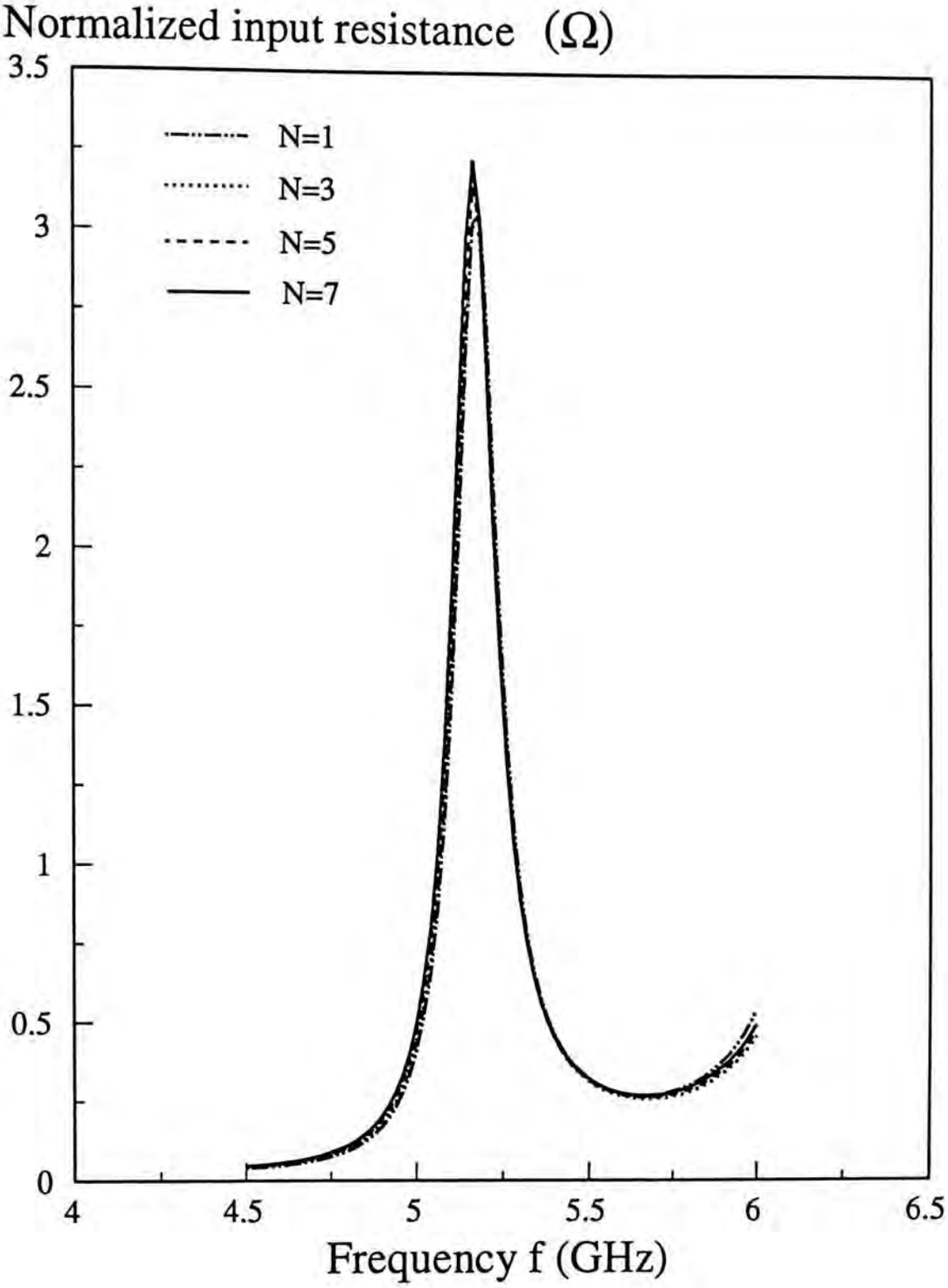

Fig. 3-13(a): Convergence check for the input resistance against frequency for the TE_{221} mode: a=12.5 mm, ε_{ra}=9.5, L=8.5 mm, W=0.863 mm, x_d=0.0 mm, y_d=8.0 mm, W_f=1.6 mm, d=0.635 mm, ε_{rs}=2.96, L_s=8.63 mm.

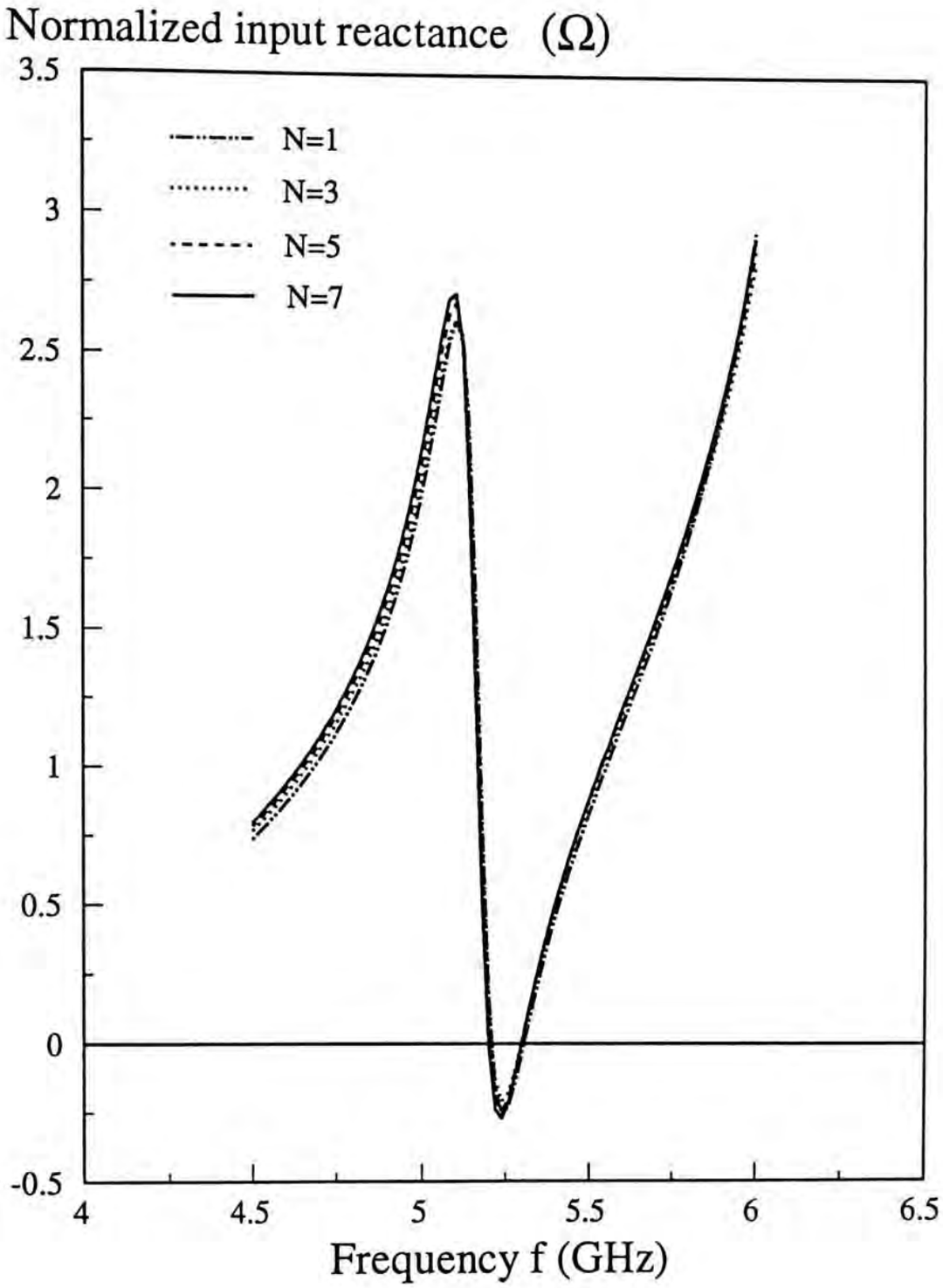

Fig. 3-13(b): Convergence check for the input reactance against frequency for the TE_{221} mode: a=12.5 mm, ε_{rd}=9.5, L=8.5 mm, W=0.863 mm, x_d=0.0 mm, y_d=8.0 mm, W_f=1.6 mm, d=0.635 mm, ε_{rs}=2.96, L_s=8.63 mm.

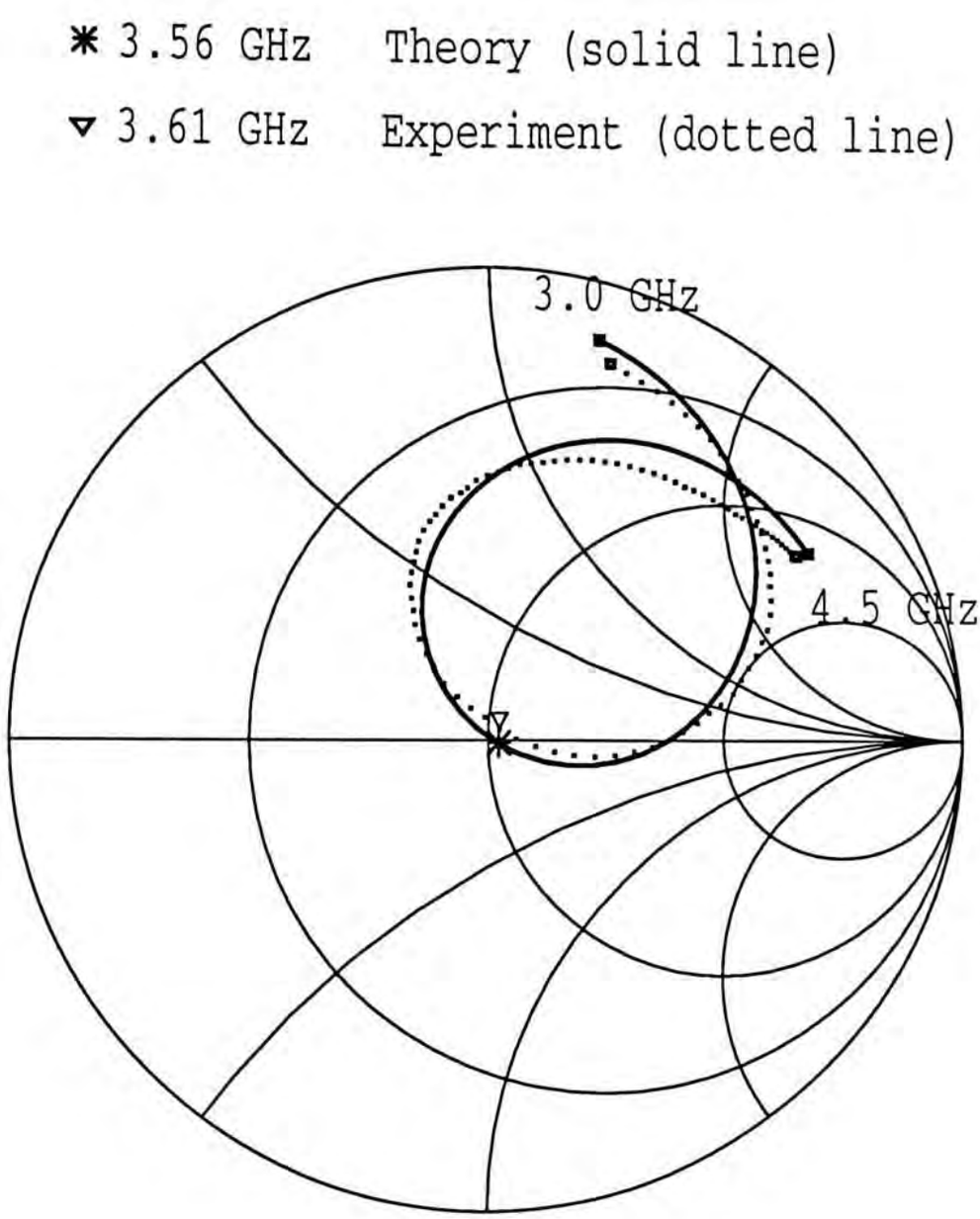

Fig. 3-14: Computed and measured normalized TE_{111} mode input impedance: a=12.5mm, ε_{ra}=9.5, L=13.5 mm, W=0.87 mm, x_d=0.0 mm, y_d=0.0 mm, W_f=1.45 mm, d=0.635 mm, ε_{rs}=2.96, L_s=13.6 mm.

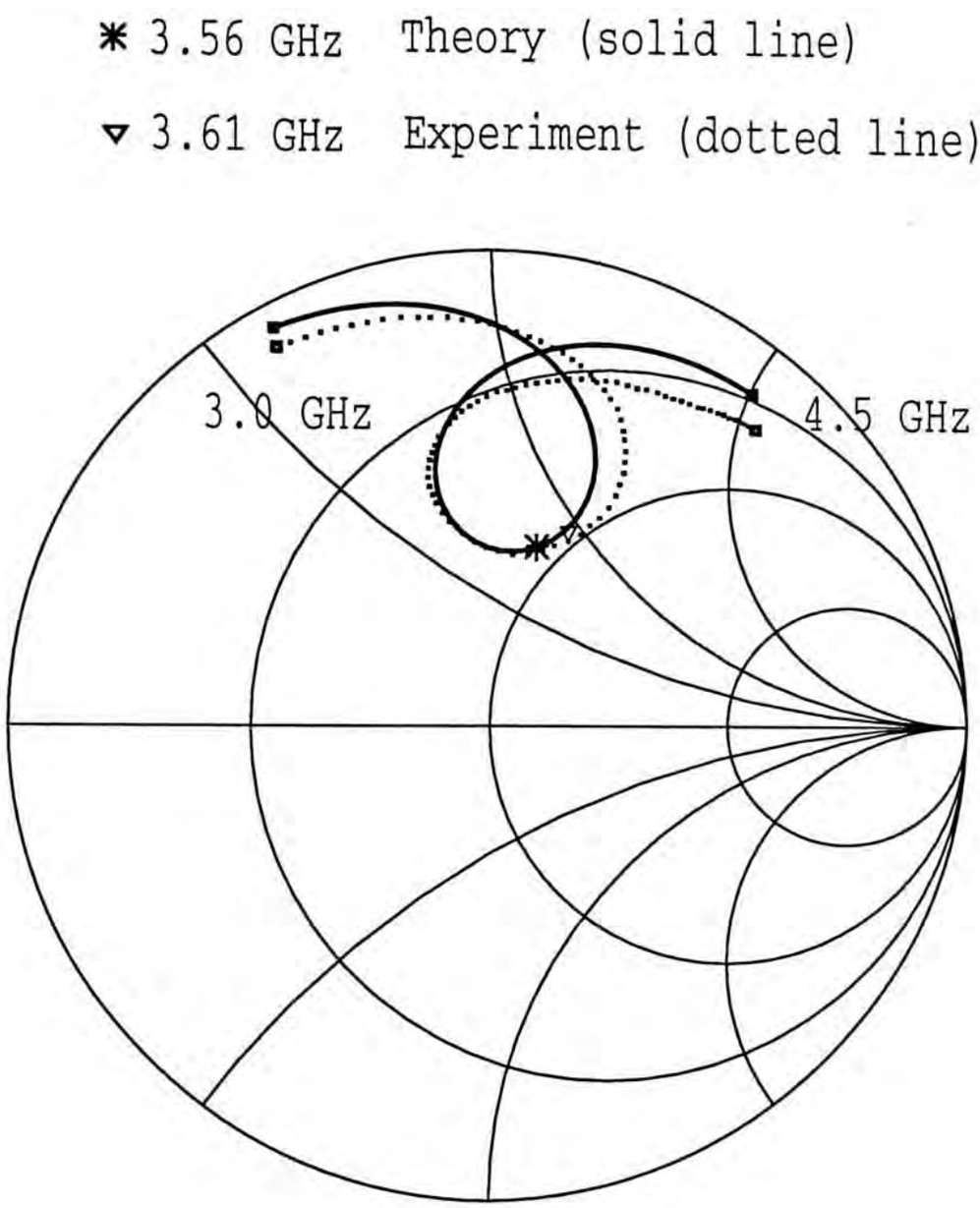

Fig. 3-15: Computed and measured normalized TE_{111} mode input impedance: a=12.5 mm, ε_{ra}=9.5, L=11.0 mm, W=0.88 mm, x_d=0.0 mm, y_d=0.0 mm, W_f=1.45 mm, d=0.635 mm, ε_{rs}=2.96, L_s=13.6 mm.

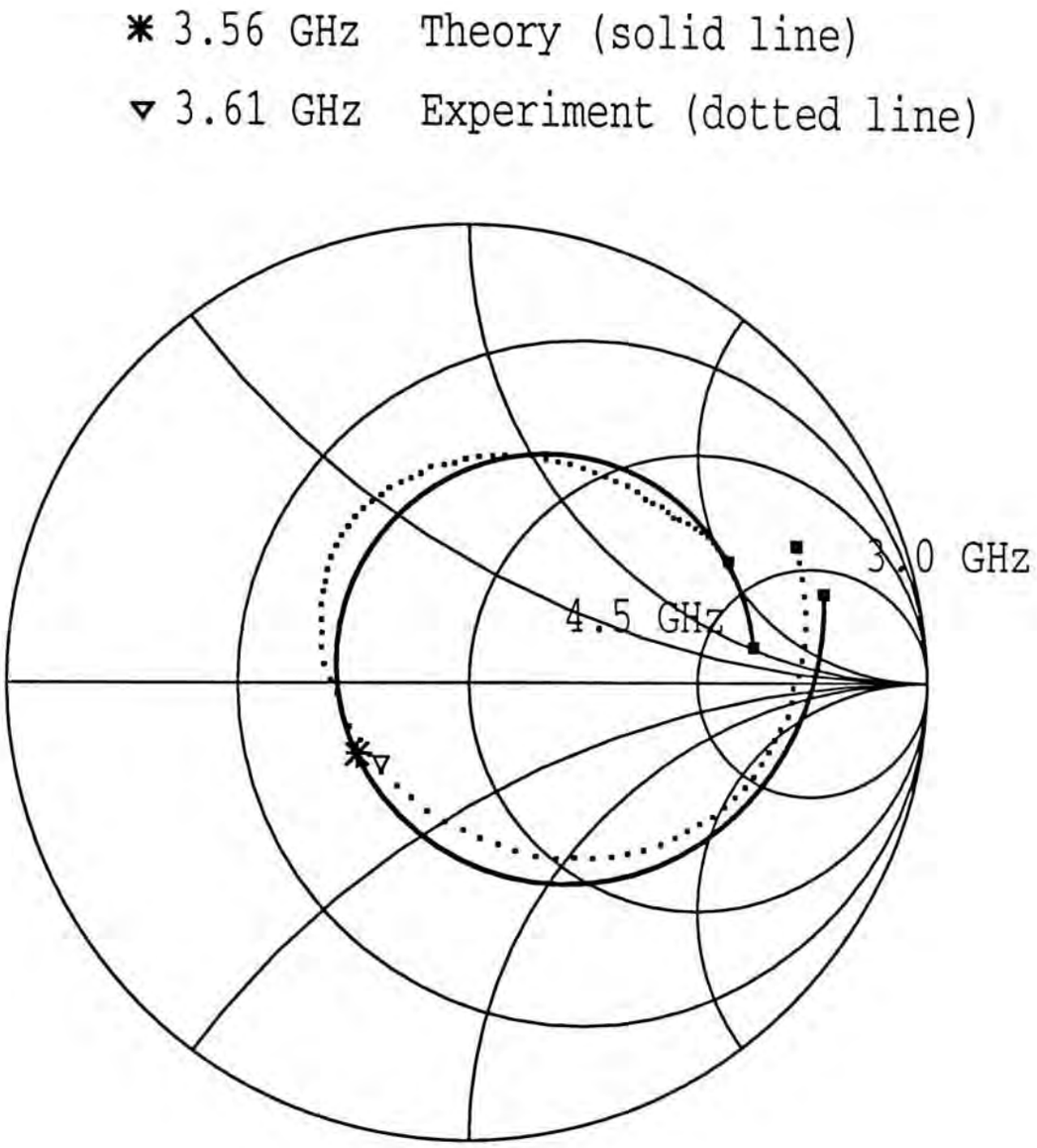

Fig. 3-16: Computed and measured normalized TE_{111} mode input impedance: a=12.5mm, ε_{ra}=9.5, L=16.3 mm, W=0.92 mm, x_d=0.0 mm, y_d=0.0 mm, W_f=1.45 mm, d=0.635 mm, ε_{rs}=2.96, L_s=13.6 mm.

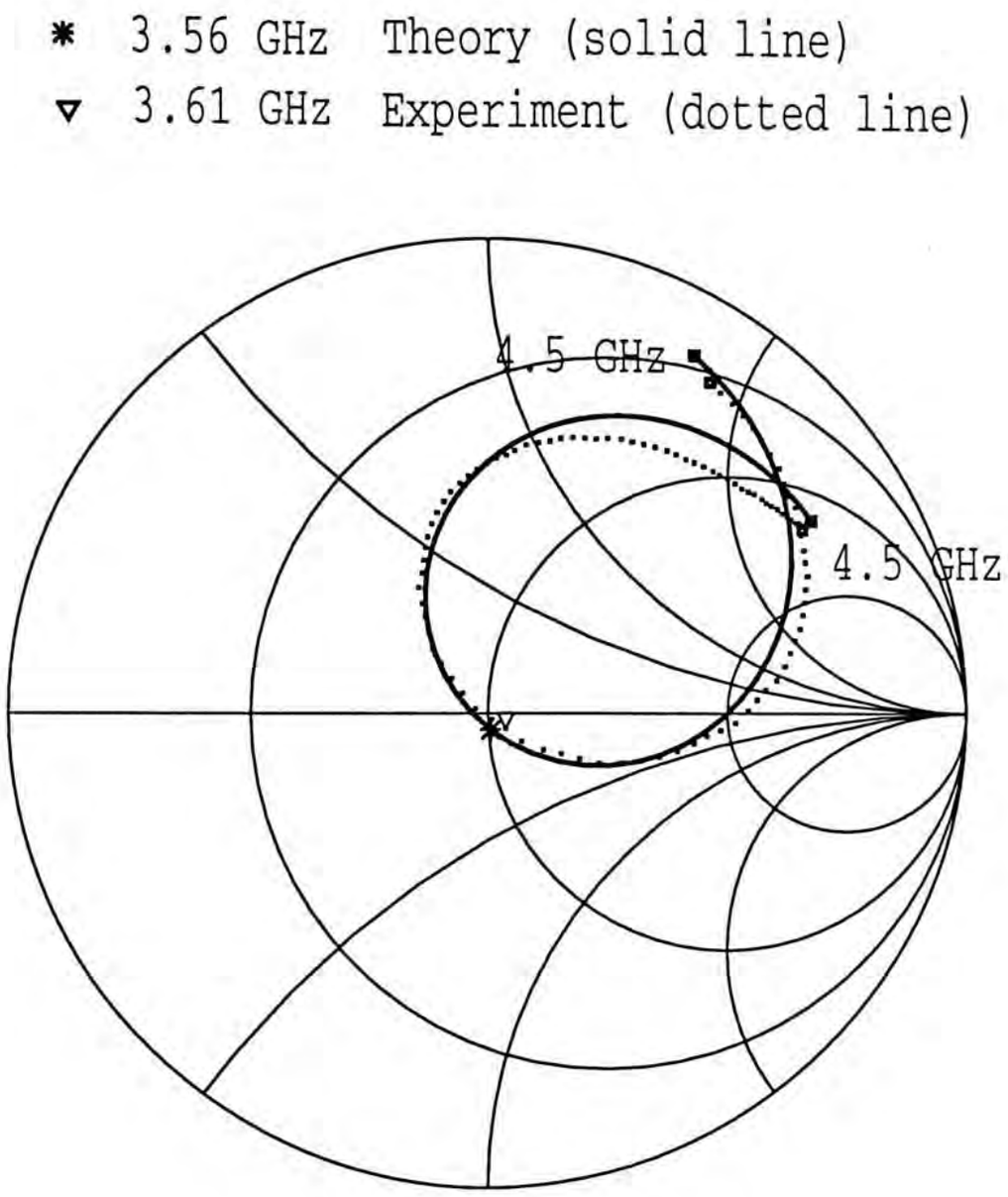

Fig. 3-17: Computed and measured normalized TE_{111} mode input impedance: a=12.5 mm, ε_{ra}=9.5, L=13.5 mm, W=1.33 mm, x_d=0.0 mm, y_d=0.0 mm, W_f=1.45 mm, d=0.635 mm, ε_{rs}=2.96, L_s=13.6 mm.

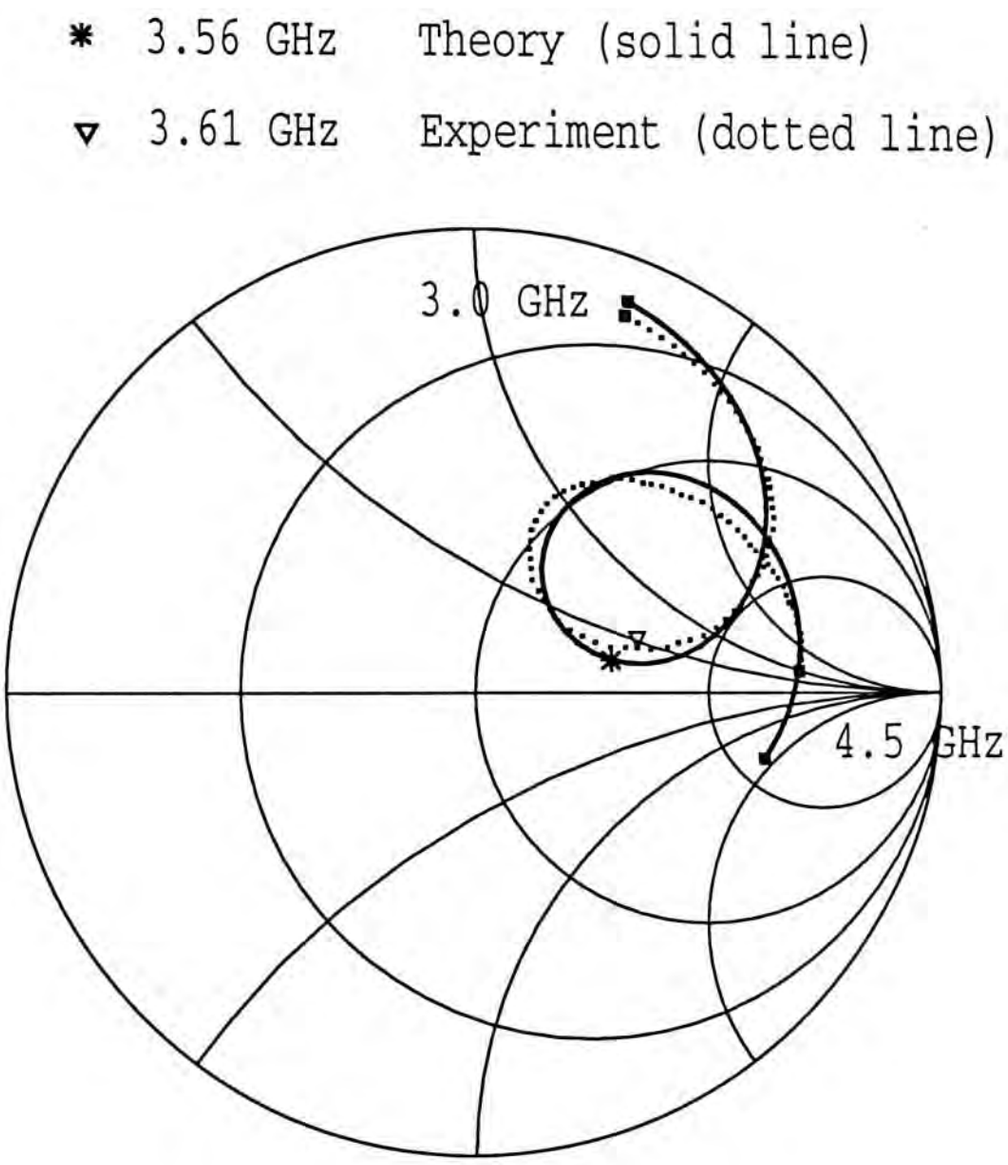

Fig. 3-18: Computed and measured normalized TE_{111} mode input impedance: a=12.5 mm, ε_{ra}=9.5, L=13.5 mm, W=1.33 mm, x_d=5.0 mm, y_d=0.0 mm, W_f=1.45 mm, d=0.635 mm, ε_{rs}=2.96, L_s=13.6 mm.

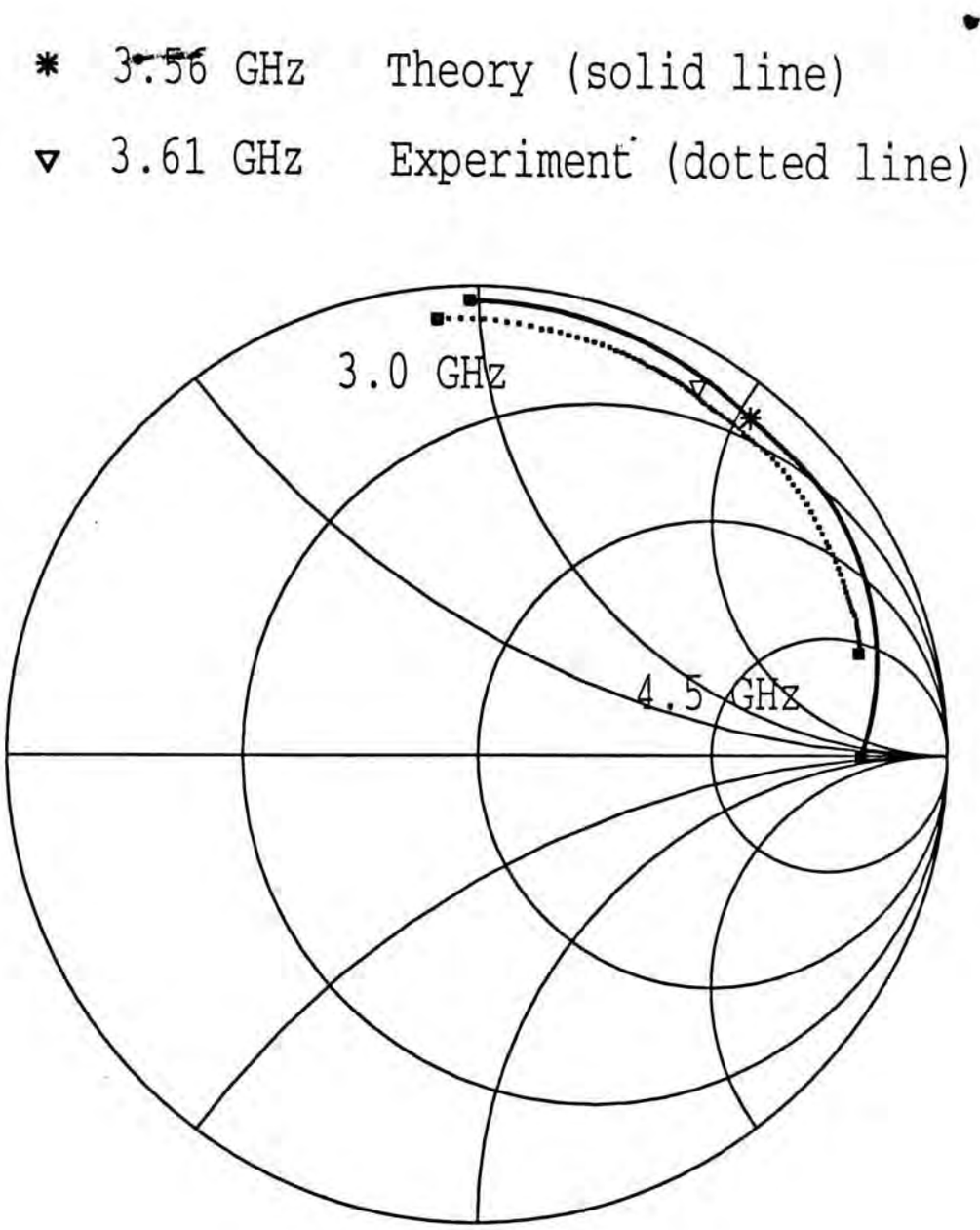

Fig. 3-19: Computed and measured normalized TE_{111} mode input impedance: a=12.5 mm, ε_{ra}=9.5, L=13.5 mm, W=1.33 mm, x_d=10.5 mm, y_d=0.0 mm, W_f=1.45 mm, d=0.635 mm, ε_{rs}=2.96, L_s=13.6 mm.

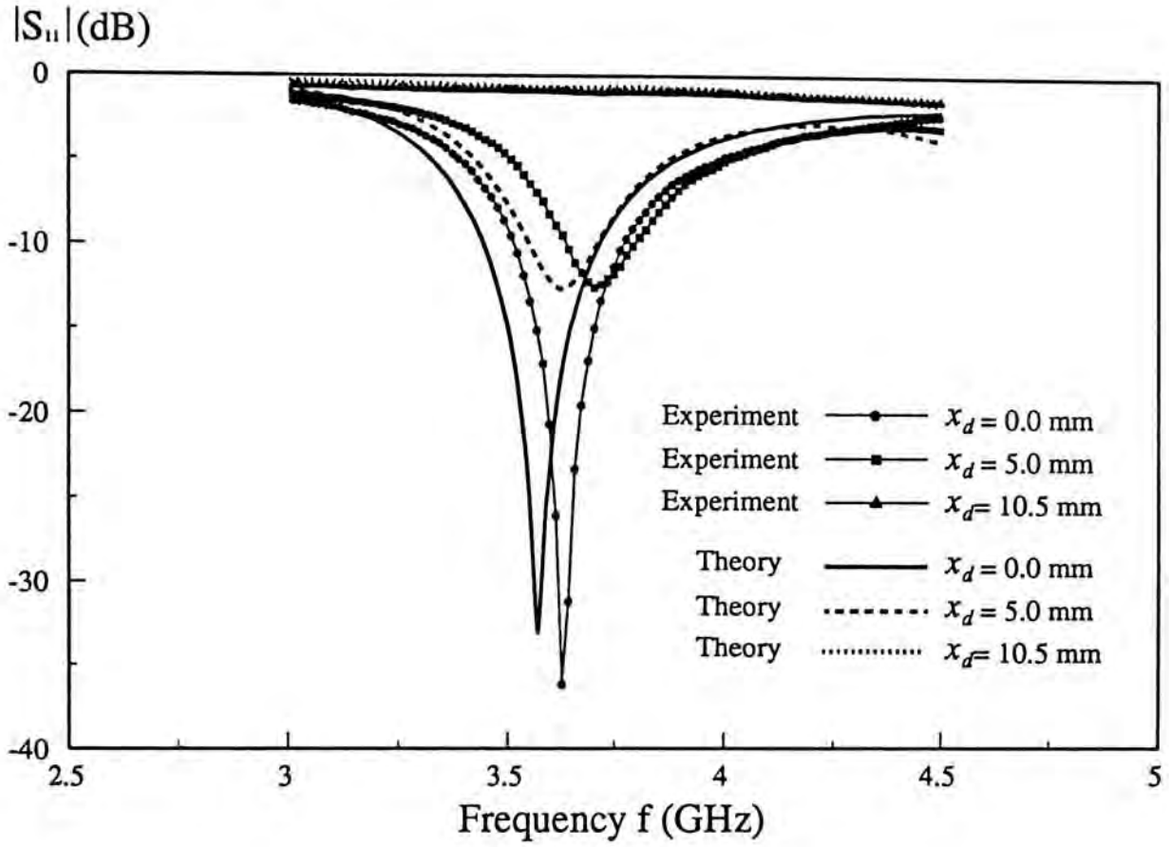

Fig. 3-20: Computed and measured TE_{111} mode reflection coefficient for different x_d : a=12.5 mm, ε_{ra}=9.5, L=13.5 mm, W=1.33 mm, y_d=0.0 mm, W_f=1.45 mm, d=0.635 mm, ε_{rs}=2.96, L_s=13.6 mm.

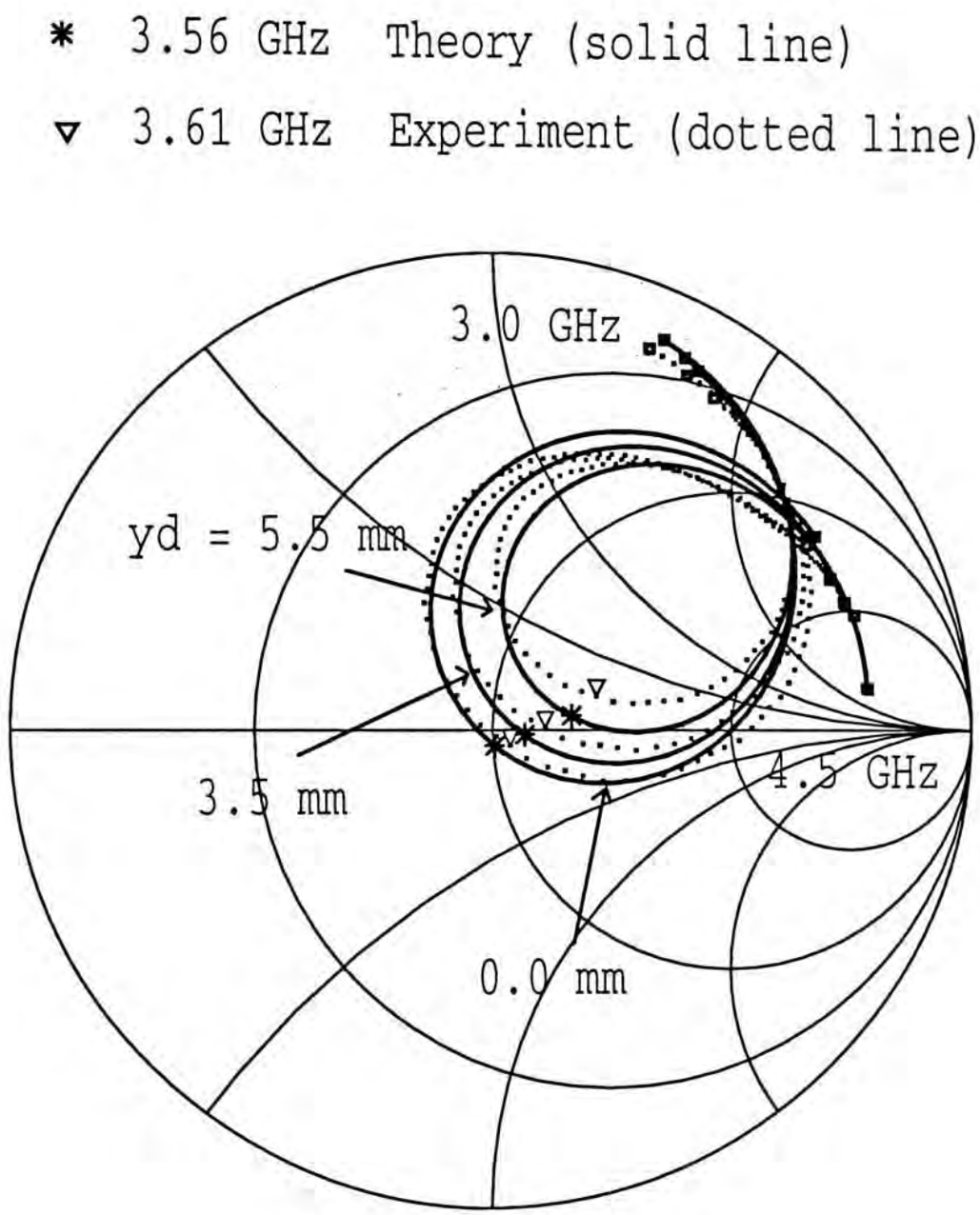

Fig. 3-21: Computed and measured normalized TE_{111} mode input impedance for different y_d : a=12.5 mm, ε_{ra}=9.5, L=13.5 mm, W=1.33 mm, x_d=0.0 mm, W_f=1.45 mm, d=0.635 mm, ε_{rs}=2.96, L_s=13.6 mm.

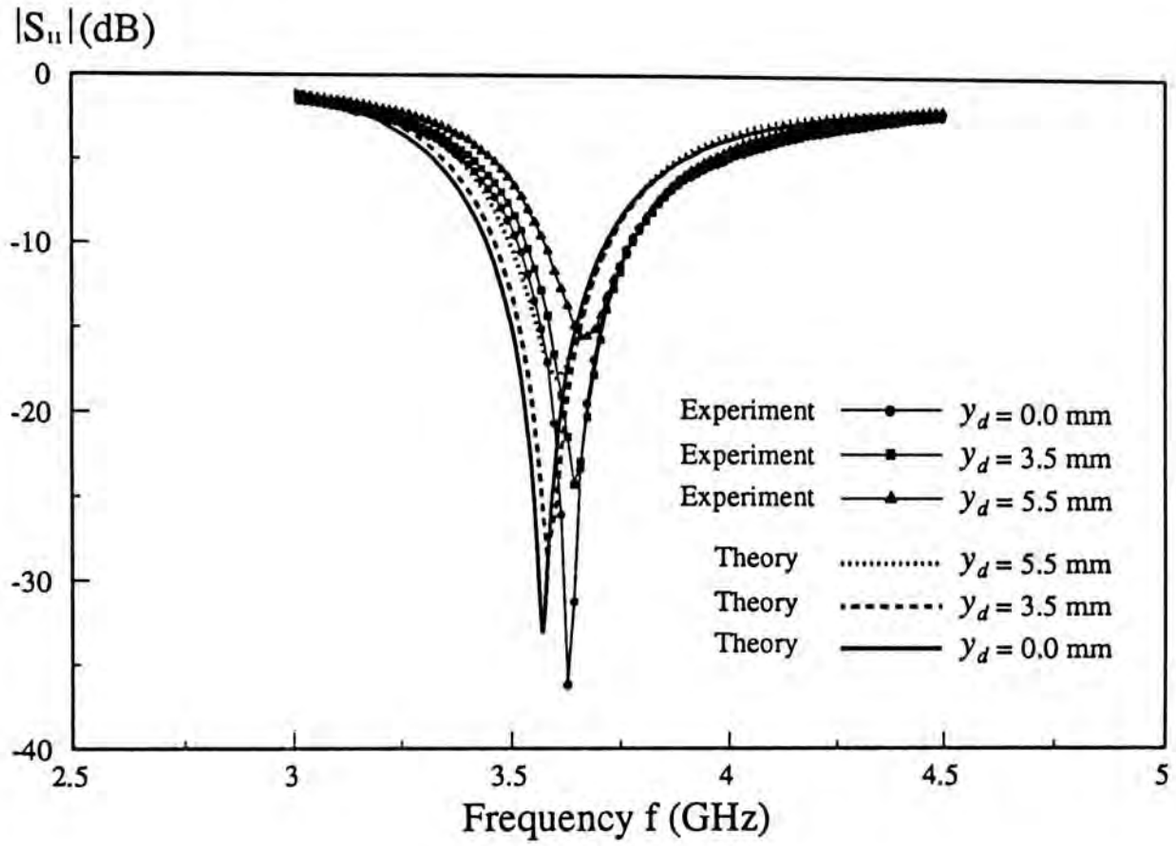

Fig. 3-22: Computed and measured TE_{111} mode reflection coefficient for different y_d: a=12.5 mm, ε_{ra}=9.5, L=13.5 mm, W=1.33 mm, x_d=0.0 mm, W_f=1.45 mm, d=0.635 mm, ε_{rs}=2.96, L_s=13.6 mm.

(C) End-fire TE_{221} *Mode*

Fig. 3-23 shows the measured and computed TE_{221} mode input impedance. The slot is aligned with the y-axis and has an offset y_d = 8.0 mm. It is seen that the calculations and the measurements are in reasonable agreement. From the figure, it is seen that the measured resonant frequency is 5.40 GHz, which is very close to the calculated value of 5.30 GHz (1.89% error) as well as the predicted value of 5.34 GHz obtained by solving the characteristic equation $\Delta_2^{TE} = 0$. Figs. 3-24 and 3-25 show the input impedance for different y_d's, whereas Fig. 3-26 shows the corresponding $|S_{11}|$. Unlike the TE_{111} mode excitation in which a center-fed slot results in the strongest coupling, the TE_{221} cannot be excited when the slot is near the center of the DR.

The reflection coefficient $|S_{11}|$ for different slot lengths is shown in Fig. 3-27. Again, the longer the slot length, the larger the coupling.

(D) Error Discussions

The discrepancy between theory and experiment is mainly caused by the imperfect hemispherical DRs where they have slight dips on various parts of its surface. In addition, the tolerance of ε_r is not given for the DRs so that the uncertainty in the permittivity is also a source of error.

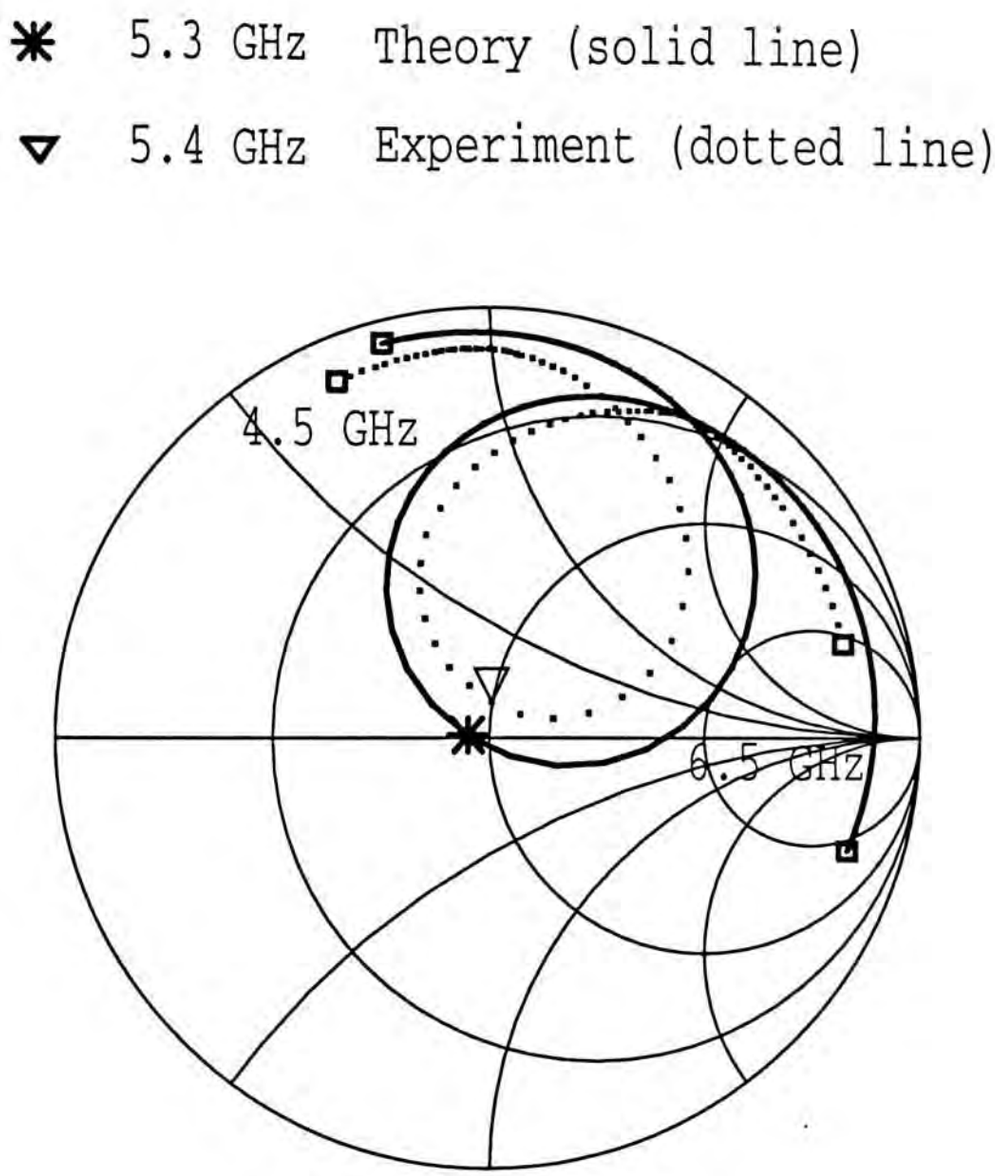

Fig. 3-23: Computed and measured normalized TE_{221} mode input impedance: a=12.5 mm, ε_{rs}=9.5, L=8.5 mm, W=0.863 mm, x_d=0.0 mm, y_d=8.0 mm, W_f=1.6 mm, d=0.635 mm, ε_{rs}=2.96, L_s=8.63 mm.

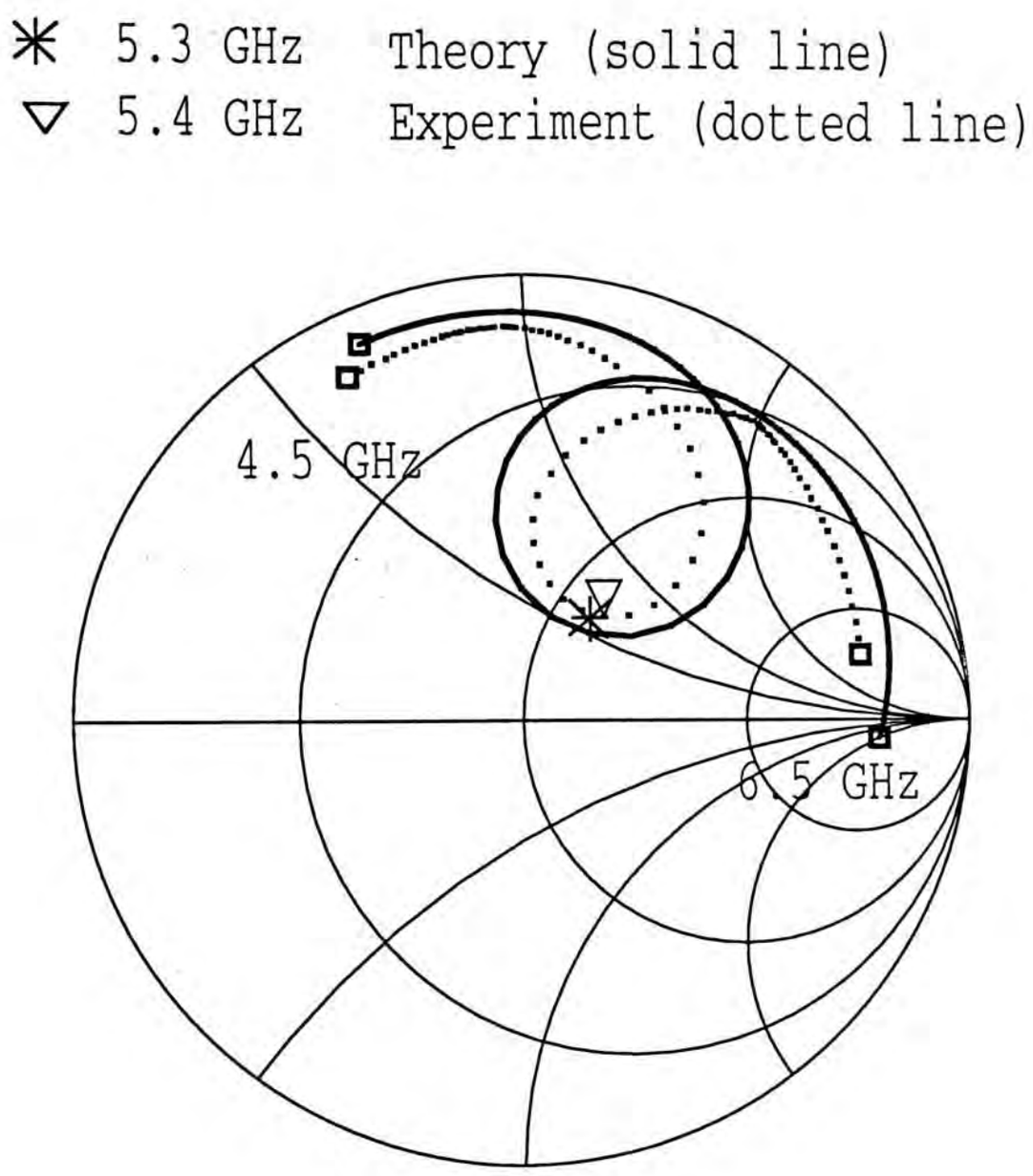

Fig. 3-24: Computed and measured normalized TE_{221} mode input impedance: a=12.5 mm, ε_{ra}=9.5, L=8.5 mm, W=0.863 mm, x_d=0.0 mm, y_d=4.0 mm, W_f=1.6 mm, d=0.635 mm, ε_{rs}=2.96, L_s=8.63 mm.

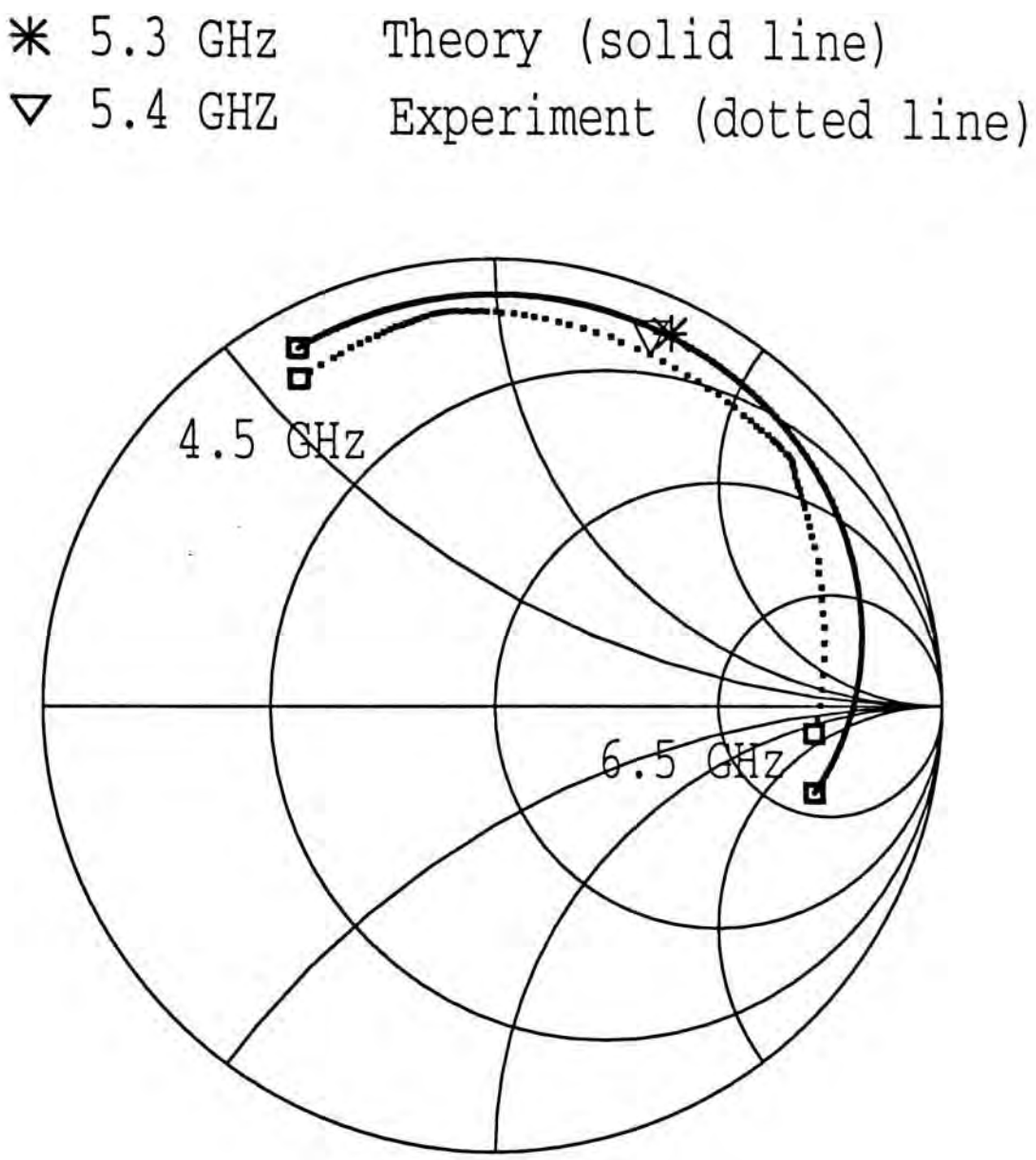

Fig. 3-25: Computed and measured normalized TE_{221} mode input impedance: a=12.5 mm, ε_{ra}=9.5, L=8.5 mm, W=0.863 mm, x_d=0.0 mm, y_d=0.0 mm, W_f=1.6 mm, d=0.635 mm, ε_{rs}=2.96, L_s=8.63 mm.

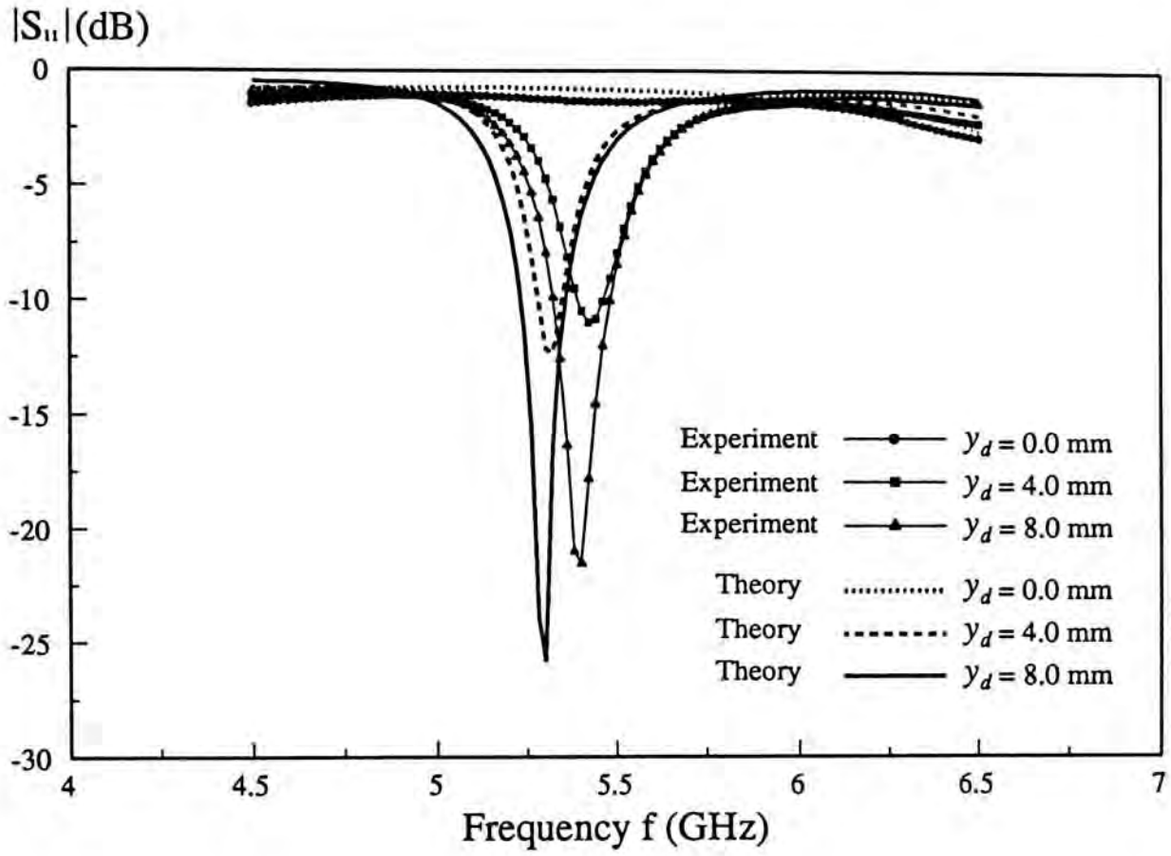

Fig. 3-26: Computed and measured TE_{221} mode reflection coefficient for different y_d: a=12.5 mm, ε_{ra}=9.5, L=8.5 mm, W=0.863 mm, x_d=0.0 mm, y_d=0.0 mm, W_f=1.6 mm, d=0.635 mm, ε_{rs}=2.96, L_s=8.63 mm.

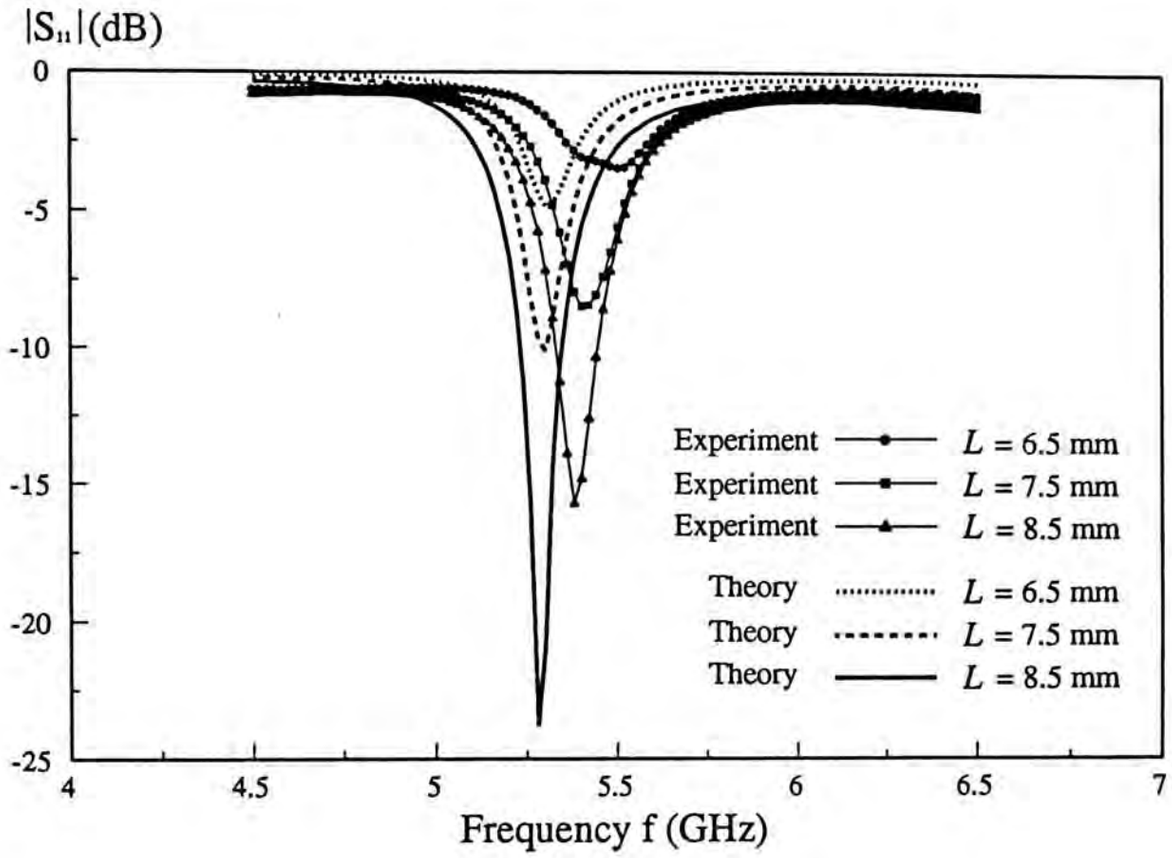

Fig. 3-27: Computed and measured TE_{221} mode reflection coefficient for different slot lengths: a=12.5 mm, ε_{ra}=9.5, W=0.5 mm, x_d=0.0 mm, y_d=8.0 mm, W_f=1.6 mm, d=0.635 mm, ε_{rs}=2.96, L_s=8.63 mm.

3.7.3 Conclusion

The exact modal Green's function of the DR is used to obtain the input impedance at the reference plane. The equivalent magnetic current is solved by moment method with the Galerkin's procedure. The effect of the slot's offsets x_d and y_d on the input impedance has been studied. Measurements have been carried out to verify the theory, and reasonable agreement between theory and experiment is obtained.

3.8 Conclusion

An aperture-coupled hemispherical DR antenna has been studied both theoretically and experimentally. The exact Green's function for the magnetic field inside the DR antenna due to the equivalent magnetic current in the slot is derived. For the microstrip line excitation, the reciprocity method has been employed to obtain the expression of the equivalent series impedance of the slot. This method provides a simple problem formulation, and, on the other hand, the expressions are computationally efficient. The single mode approximation as well as the exact modal Green's function are used to evaluate the input impedance at the reference plane. In using the exact modal Green's function, the Green's function is presented in a form which can be implemented numerically very easily. The concept of equivalent radius of a cylindrical (magnetic) dipole is used so that the knowledge developed in cylindrical dipole can be utilized to simplify the computation. Both the broadside TE_{111} mode as well as the end-fire TE_{221} mode are studied. Experiment has been carried out to verify the theory, and reasonably agreement between them has been obtained. The effects of the slot-length, the slot position and the slot width on the input impedance have been studied. By varying these parameters, one can perform impedance matching in practical circuit designs, showing potential applications of DR antennas in MMIC's.

CHAPTER 4

CONCLUSION

This dissertation has been devoted to the analysis of a hemispherical DR antenna, which has potential applications in the millimeter wave band. This new antenna offers several advantages such as no conductor loss, small size and low cost.

Two excitation methods have been considered for the DR antenna, namely the coaxial probe-feed and the aperture-coupling. In the former, the exact Green's function of the electric field inside the DR antenna due to an electric point current is derived using mode matching method. The probe current and hence the input impedance of the antenna are then found using moment method with the Galerkin's procedure. In the calculation of Z-matrix elements, the electric field is reacted with the source on the probe surface and this causes a convergence problem. To handle this difficulty, the modal solution is first expressed as the sum of a particular and a homogeneous solutions. Using the physical argument, the slowly convergent particular solution is then replaced by a simple expression which can be evaluated very efficiently. While the singularity of the Green's function is absorbed in the particular solution, the homogeneous solution is a smooth and slowly varying function. Moreover, it converges very quickly, and therefore the evaluation of the Green's function is very computationally efficient. Using this technique, the numerical difficulties in evaluating the Green's function are avoided and, besides, a new mathematical identity is established.

In considering the energy radiated from the coaxial probe to the DR, the problem of a cylindrical monopole antenna is encountered. The results using various dipole kernels (traditional reduced kernel, reduced kernel with correction term, and exact kernel) and different source models (delta gap source and magnetic frill source) have been discussed and compared. Furthermore, both PWS and EB basis functions have been used in obtaining the MM solution. Convergence check has been performed and it is found that the result using the exact kernel together with the magnetic frill source and EB basis function gives the best convergence behaviour.

The lowest order TE mode, the broadside TE_{111}, and the lowest order TM mode, the end-fire TM_{101}, have been studied. Experiment has been carried out to verify the results, and reasonable agreement between theory and experiment is obtained. The effects of the probe position, the probe length and the dielectric constant on the input impedance have been studied. By varying the probe length and the probe position, one can perform impedance matching in circuit designs. Moreover, by exciting different resonant modes, either a broadside or an end-fire radiation pattern can be obtained.

The aperture-coupled excitation is studied as it offers several advantages over the probe-fed one such as the feasibility of integration with MMIC's and the avoidance of large probe self reactances at millimeter wave frequencies. Moreover, drilling holes in DR antenna for probe penetration is no longer necessary. To analyze the configuration, the reciprocity method has been used to formulate the problem, and the expression of the equivalent series impedance of the slot is obtained. The analysis consists of two parts: the DR antenna above the ground plane and the microstrip line excitation below the ground plane. In the former, modal method is used to obtain the exact magnetic field Green's function inside the DR due to the equivalent magnetic current in the slot. Again, the Green's function is expressed as

the sum of a particular and a homogeneous solutions so as to avoid numerical difficulties. In replacing the particular solution by a simple expression, another mathematical identity is established. The concept of equivalent radius of a cylindrical (magnetic) dipole is used so that the knowledge developed in the cylindrical dipole can be utilized to simplify computations. For the analysis of the microstrip part, the expressions are evaluated in spectral domain. Such calculations are well developed and computationally efficient.

The broadside TE_{111} mode and the end-fire TE_{221} mode are studied, and the results are verified by measurements. The effects of the slot length, slot position and the slot width on the input impedance are studied. It has been shown that impedance matching can be achieved by varying these parameters, and the feasibility of this new configuration is thus confirmed.

While the single DR antenna has been studied successfully, the mutual coupling between two DRs is a potential topic for further DR study. Results of the mutual coupling can be used in array designs, which are necessary in some applications where a high antenna gain is required.

APPENDIX A

PROOF OF EQUATION (2-16)

A proof of (2-16) is given in this appendix. Using integration by parts, one obtains

$$m\int_0^{\pi} P_n^m \frac{d}{d\theta}P_r^m \, d\theta = m[P_n^m \, P_r^m]_0^{\pi} - m\int_0^{\pi} P_r^m \frac{d}{d\theta}P_n^m \, d\theta \qquad \text{(A-1)}$$

which can be rearranged to give

$$m\left[\int_0^{\pi} P_n^m \frac{d}{d\theta}P_r^m \, d\theta + \int_0^{\pi} P_r^m \frac{d}{d\theta}P_n^m \, d\theta\right] = m\,[P_n^m \, P_r^m]_0^{\pi}$$

$$= m\,[P_n^m(-1)P_r^m(-1) - P_n^m(1)P_r^m(1)] \qquad \text{(A-2)}$$

Using the fact that

$$P_n^m(-1) = (-1)^{n+m} P_n^m(1) \qquad \text{(A-3)}$$

and

$$P_n^m(1) = \begin{cases} 1 & \text{for} \quad m = 0 \\ 0 & \text{for} \quad m > 0 \end{cases} \qquad \text{(A-4)}$$

equation (2-16) can be established.

APPENDIX B

DERIVATION OF EQUATION (2-43)

In this appendix, equation (2-43) is derived. To begin with, the Maxwell's equation in phasor form are written below

$$\nabla \times \vec{H} = j\omega\varepsilon\vec{E} + \vec{J} \tag{B-1}$$

$$\nabla \times \vec{E} = -j\omega\mu_o\vec{H} \tag{B-2}$$

$$\nabla \cdot \vec{H} = \frac{\rho}{\varepsilon} \tag{B-3}$$

$$\nabla \cdot \vec{H} = 0 \tag{B-4}$$

where $\vec{J}$ and ρ are the source current density and the source charge density, respectively.

Note that (B-4) is satisfied if $\vec{H}$ is represented as the curl of some vector. Define a vector potential $\vec{A}$ such that

$$\mu_o\vec{H} = \nabla \times \vec{A} \tag{B-5}$$

then substitution of (B-5) into (B-2) gives

$$\nabla \times (\vec{E} + j\omega\vec{A}) = 0 \tag{B-6}$$

Equation (B-6) is satisfied if $(\vec{E} + j\omega\vec{A})$ is represented as the gradient of some arbitrary scalar Φ. This leads to the following equation:

$$\vec{E} + j\omega\vec{A} = -\nabla\Phi \tag{B-7}$$

Insertion of (B-5) and (B-7) into (B-1) gives

$$\nabla\times\nabla\times\vec{A}-k^2\vec{A}=-j\omega\mu_o\varepsilon\nabla\Phi+\mu_o\vec{J} \tag{B-8}$$

where $k^2=\omega\mu_o\varepsilon$.

Now consider a vector potential $\vec{A}=A_r\hat{r}$ and a current vector $\vec{J}=J_r\hat{r}$. Expansion of $\nabla\times\nabla\times\vec{A}$ in spherical coordinates then gives

$$\begin{aligned}\nabla\times\nabla\times\vec{A}=&\frac{\hat{r}}{r^2\sin\theta}\left[-\frac{\partial}{\partial\theta}\left(\sin\theta\frac{\partial A_r}{\partial\theta}\right)-\frac{1}{\sin\theta}\frac{\partial^2A_r}{\partial\phi^2}\right]\\&+\frac{\hat{\theta}}{r}\frac{\partial^2A_r}{\partial\theta\partial r}\\&+\frac{\hat{\phi}}{r\sin\theta}\frac{\partial^2A_r}{\partial r\partial\phi}\end{aligned} \tag{B-9}$$

On the other hand, expansion of $\nabla\Phi$ in spherical coordinates gives

$$\nabla\Phi=\hat{r}\frac{\partial\Phi}{\partial r}+\hat{\theta}\frac{1}{r}\frac{\partial\Phi}{\partial\theta}+\hat{\phi}\frac{1}{r\sin\theta}\frac{\partial\Phi}{\partial\phi} \tag{B-10}$$

By equating the components of $\hat{r}$, $\hat{\theta}$ and $\hat{\phi}$ on both sides of (B-8), one obtains the following three equations:

$$\frac{-1}{r^2\sin\theta}\left[\frac{\partial}{\partial\theta}\left(\sin\theta\frac{\partial A_r}{\partial\theta}\right)+\frac{1}{\sin\theta}\frac{\partial^2A_r}{\partial\phi^2}\right]-k^2A_r=-j\omega\mu_o\varepsilon\frac{\partial\Phi}{\partial r}+\mu_oJ_r \tag{B-11}$$

$$\frac{1}{r}\frac{\partial^2A_r}{\partial\theta\partial r}=-\frac{j\omega\mu_o\varepsilon}{r}\frac{\partial\Phi}{\partial\theta} \tag{B-12}$$

$$\frac{1}{r\sin\theta}\frac{\partial^2A_r}{\partial r\partial\phi}=-j\omega\mu_o\varepsilon\frac{\partial\Phi}{\partial\phi} \tag{B-13}$$

By choosing

$$\frac{\partial A_r}{\partial r} = -j\omega\mu_o\varepsilon\Phi \tag{B-14}$$

equations (B-12) and (B-13) are satisfied identically, while (B-11) becomes

$$\frac{1}{r}\frac{\partial^2 A_r}{\partial r^2} + \frac{1}{r^2\sin\theta}\frac{\partial}{\partial\theta}\left(\sin\theta\frac{\partial}{\partial\theta}\frac{A_r}{r}\right) + \frac{1}{r^2\sin^2\theta}\frac{\partial^2}{\partial\phi^2}\frac{A_r}{r} + k^2\frac{A_r}{r} = -\mu_o\frac{J_r}{r} \tag{B-15}$$

Noting that

$$\frac{1}{r}\frac{\partial^2 A_r}{\partial r} = \frac{1}{r^2}\frac{\partial}{\partial r}\left(r^2\frac{\partial}{\partial r}\frac{A_r}{r}\right) \tag{B-16}$$

and

$$\nabla^2 = \frac{1}{r^2}\frac{\partial}{\partial r}\left(r^2\frac{\partial}{\partial r}\right) + \frac{1}{r^2\sin\theta}\frac{\partial}{\partial\theta}\left(\sin\theta\frac{\partial}{\partial\theta}\right) + \frac{1}{r^2\sin^2\theta}\frac{\partial^2}{\partial\phi^2} \tag{B-17}$$

the following equation results:

$$(\nabla^2 + k^2)\frac{A_r}{r} = -\mu_o\frac{J_r}{r} \tag{B-18}$$

For a point current J_r located at $\vec{r}'(r', \theta', \phi')$, one has

$$J_r = \frac{\delta(r-r')\delta(\theta-\theta')\delta(\phi-\phi')}{r^2\sin\theta} \tag{B-19}$$

Replacing the function A_r by the Green's function $G_{J_r}^{A_{rp}}$, one obtains

$$(\nabla^2 + k^2)\frac{G_{J_r}^{A_{rp}}}{r} = \frac{-\mu_o}{r}\frac{\delta(r-r')\delta(\theta-\theta')\delta(\phi-\phi')}{r^2\sin\theta}$$

which is (2-43).

APPENDIX C

DERIVATION OF EQUATION (2-44)

In this Appendix, the procedure of solving the following equation is shown:

$$(\nabla^2 + k^2)\frac{G_{J_r}^{A_{rp}}}{r} = \frac{-\mu_o}{r}\frac{\delta(r-r')\delta(\theta-\theta')\delta(\phi-\phi')}{r^2\sin\theta} \tag{C-1}$$

To begin with, we first construct

$$A_p = \sum_{n=0}^{\infty}\sum_{m=-n}^{n}\alpha_{nm}P_n^m(\cos\theta)e^{jm\phi}\cdot\begin{cases} j_n(kr')h_n^{(2)}(kr) & r>r' \\ h_n^{(2)}(kr')j_n(kr) & r<r' \end{cases} \tag{C-2a}$$

where

$$A_p = \frac{A_{rp}}{r} \tag{C-2b}$$

and α_{nm} is the coefficient to be determined. In (C-2), $j_n(x) = \hat{J}_n(x)/x$ and $h_n^{(2)}(x) = \hat{H}_n^{(2)}(x)/x$ are spherical Bessel of the first kind and spherical Hankel function of the second kind, respectively. To solve for α_{nm}, we integrate both sides of (C-1) with respect to r over a vanishing interval including the point r'. The following equation is obtained :

$$\left[\frac{\partial A_p}{\partial r}\right]_{r_-'}^{r_+'} = -\frac{\mu_o\delta(\theta-\theta')\delta(\phi-\phi')}{r'^3\sin\theta} \tag{C-3}$$

Next, the following transformation is defined :

$$\tilde{A}_p = \int_{\theta=0}^{\pi}\int_{\phi=0}^{2\pi} A_p\ P_n^m(\cos\theta)\sin\theta\, e^{-jm\phi}\, d\phi d\theta \tag{C-4}$$

so that (C-3) can be transformed to

$$\left[\frac{\partial \tilde{A}_p}{\partial r}\right]_{r_-'}^{r_+'} = -\frac{\mu_o P_n^m(\cos\theta')e^{-jm\phi'}}{r'^3} \tag{C-5}$$

Using the orthogonal relationship for $e^{jm\phi}$ (equation (2-9)) together with the following orthogonal relationship for the associated Legendre functions [33, p.403]:

$$\int_0^{\pi} P_n^m(\cos\theta)\, P_r^m(\cos\theta)\sin\theta\ d\theta = \begin{cases} \dfrac{2}{2n+1}\cdot\dfrac{(n+m)!}{(n-m)!} & \text{for } n=r \\ 0 & \text{for } n\neq r \end{cases} \tag{C-6}$$

equation (C-2a) can also be transformed to

$$\tilde{A}_p = \alpha_{nm}\cdot\frac{4\pi}{2n+1}\cdot\frac{(n+m)!}{(n-m)!}\cdot\begin{cases} j_n(kr')h_n^{(2)}(kr) & , \quad r>r' \\ h_n^{(2)}(kr')j_n(kr) & , \quad r<r' \end{cases} \tag{C-7}$$

Differentiating (C-7) with respect to r at $r=r_+'$ and $r=r_-'$ and comparing with (C-5), one obtains the coefficient :

$$\alpha_{nm} = \frac{-j\mu_o k}{r'}\cdot\frac{2n+1}{4\pi}\cdot\frac{(n-m)!}{(n+m)!}\cdot P_n^m(\cos\theta')e^{-jm\phi'} \tag{C-8}$$

From (C-2) and (C-8), equation (2-44) is obtained.

APPENDIX D

PROPAGATION CONSTANT OF FIELDS INSIDE MICROSTRIPLINE

This appendix gives some formulae to compute the propagation constant β of fields inside a microstripline. Given a dielectric substrate of dielectric constant ε_r and height d, and a microstripline of width W_f, the effective dielectric constant ε_{eff} using the static approximation is given by

(a) $\frac{W_f}{d} \leq 1$

$$\varepsilon_{eff} = \frac{1}{2}(\varepsilon_r + 1) + \frac{1}{2}(\varepsilon_r - 1)\left[\left(1 + 12\frac{d}{W_f}\right)^{-\frac{1}{2}} + 0.04\left(1 - \frac{W_f}{d}\right)^2\right] \qquad \text{(D-1)}$$

where k_o is the vacuum wave number.

(b) $\frac{W_f}{d} \geq 1$

$$\varepsilon_{eff} = \frac{1}{2}(\varepsilon_r + 1) + \frac{1}{2}(\varepsilon_r - 1)\left(1 + 12\frac{d}{W_f}\right)^{-\frac{1}{2}} \qquad \text{(D-2)}$$

The propagation constant β is then given by:

$$\beta = \sqrt{\varepsilon_{eff}}\, k_o \qquad \text{(D-3)}$$

The formula given above is valid only for low frequencies. At high frequencies where the dispersion effect is significant, the propagation constant β can be obtained using the full wave analysis [54], in which β is obtained by searching the root of the following equation:

$$\int_0^{\infty} \tilde{G}_{yx}^{HJ}(-\beta, k_y) F_u^2(k_y)\, dk_y = 0 \tag{D-4}$$

where

$$\tilde{G}_{xx}^{EJ}(k_x, k_y) = \frac{-j\eta_o}{k_o} \sin k_1 d \left[\frac{(\varepsilon_r k_o^2 - k_x^2) k_2 \cos k_1 d + j k_1 (k_o^2 - k_x^2) \sin k_1 d}{T_e T_m} \right] \tag{D-5}$$

$$F_u(k_y) = \frac{\sin(k_y W_f/2)}{k_y W_f/2} \tag{D-6}$$

and all other symbols are defined in (3-59).

APPENDIX E

NUMERICAL TECHNIQUE OF SPECTRAL DOMAIN INTEGRAL

In this appendix, the treatment of the surface wave pole in the evaluation of Y^s_{mn} as given by (3-57) is discussed. To begin with, the evaluation of the integral is facilitated by changing the rectangular coordinates k_x, k_y to polar coordinates β, α [20] where

$$k_x = \beta \cos\alpha \tag{E-1a}$$

$$k_y = \beta \sin\alpha \tag{E-1b}$$

The new integration ranges are $\beta = 0 \rightarrow \infty$ and $\alpha = 0 \rightarrow 2\pi$. The problem in evaluating the spectral domain integral Y^s_{mn} is due to singularities introduced by the surface wave poles, whose locations can be determined by searching the roots of the following characteristic equations:

TM surface wave poles

$$T_m(\beta) = \varepsilon_{rs} k_2 \cos k_1 d + j k_1 \sin k_1 d = 0 \tag{E-2}$$

TE surface wave poles

$$T_e(\beta) = k_1 \cos k_1 d + j k_2 \sin k_1 d = 0 \tag{E-3}$$

where the symbols are defined in (3-59).

For lossless dielectric slab, the poles (occurring at $\beta = \beta_o$) are real numbers which lie between $k_o < \beta_o < \sqrt{\varepsilon_{rs}}\, k_o$. If dielectric loss is present, the poles move off

the real β axis to $\beta = \beta_o - j\gamma$, $\gamma > 0$. Given the dielectric constant ε_{rs}, the substrate thickness d and the operating wavenumber k_o, the number of surface wave poles can be predicted as follows [52]:

$$N_e = \begin{cases} 0 & a < \dfrac{\pi}{2} \\ n & \left(n - \dfrac{1}{2}\right)\pi < a < \left(n + \dfrac{1}{2}\right)\pi, \qquad n = 1, 2, .. \end{cases} \tag{E-4}$$

$$N_m = n + 1 \qquad n\pi < a < (n+1)\pi, \qquad n = 1, 2, .. \tag{E-5}$$

where

$$a = k_o \sqrt{\varepsilon_{rs} - 1}\, d$$

N_e =number of TE surface wave poles

N_m =number of TM surface wave poles

Note that N_m is always greater than zero, which implies that TM surface wave has a zero cutoff frequency.

Suppose only one surface wave mode is present. To avoid numerical difficulties caused by the surface wave pole β_o, the integration in the vicinity of β_o is done analytically [20]. The procedure is given below:

$$\int_0^{2\pi} \int_0^{\infty} (\qquad)\, d\beta d\alpha$$

$$= \int_0^{2\pi} \left\{ \int_0^{\beta_o - \delta} (\qquad)\, d\beta + \int_{\beta_o - \delta}^{\beta_o + \delta} (\qquad)\, d\beta + \int_{\beta_o + \delta}^{\infty} (\qquad)\, d\beta \right\} d\alpha \tag{E-6}$$

where δ is chosen to be about $0.001 k_o$. The surface wave is only contributed from the second integral which is evaluated analytically. To begin with, we write:

$$I_\delta = \int_{\beta_o - \delta}^{\beta_o + \delta} (\qquad)\, d\beta = \int_{\beta_o - \delta}^{\beta_o + \delta} \frac{f(\beta)}{T_m(\beta)} d\beta \tag{E-7}$$

where $T_m(\beta)$ has a zero at $\beta = \beta_o - j\gamma$ and $f(\beta)$ represents the remaining non-singular portion of the integrand. To evaluate I_δ, the function $T_m(\beta)$ is first expanded into a Taylor series. By truncating the first two terms, we have:

$$\begin{aligned} T_m(\beta) &= T_m(\beta_o - j\gamma) + T_m'(\beta_o - j\gamma)[\beta - (\beta_o - j\gamma)] \\ &= T_m'(\beta_o - j\gamma)[\beta - (\beta_o - j\gamma)] \end{aligned} \tag{E-8}$$

Substituting (E-8) into (E-7), we get:

$$\begin{aligned} I_\delta &\approx \int_{\beta_o-\delta}^{\beta_o+\delta} \frac{f(\beta)}{T_m'(\beta_o - j\gamma)[\beta - (\beta_o - j\gamma)]} d\beta \\ &\approx \frac{f(\beta_o)}{T_m'(\beta_o - j\gamma)} \int_{\beta_o-\delta}^{\beta_o+\delta} \frac{d\beta}{\beta - (\beta_o - j\gamma)} \\ &= \frac{f(\beta_o)}{T_m'(\beta_o - j\gamma)} \int_{\beta_o-\delta}^{\beta_o+\delta} \frac{d\beta}{\beta + j\gamma} \\ &= \frac{-jf(\beta_o)}{T_m'(\beta_o - j\gamma)} \left(2\tan^{-1}\frac{\delta}{\gamma}\right) \end{aligned} \tag{E-9}$$

For lossless dielectric, we have $\gamma \to 0^+$ and therefore

$$I_\delta = -j\pi \frac{f(\beta_o)}{T_m'(\beta_o)} \tag{E-10}$$

Since the integrations of the first and the third integrals can be done directly, Y_{mn}^s can now be evaluated without difficulties. Note that the infinite integration can generally be terminated at $\beta \approx 150k_o$.

APPENDIX F

EXPERIMENTAL SET-UP FOR PROBE -FED DR ANTENNA MEASUREMENT

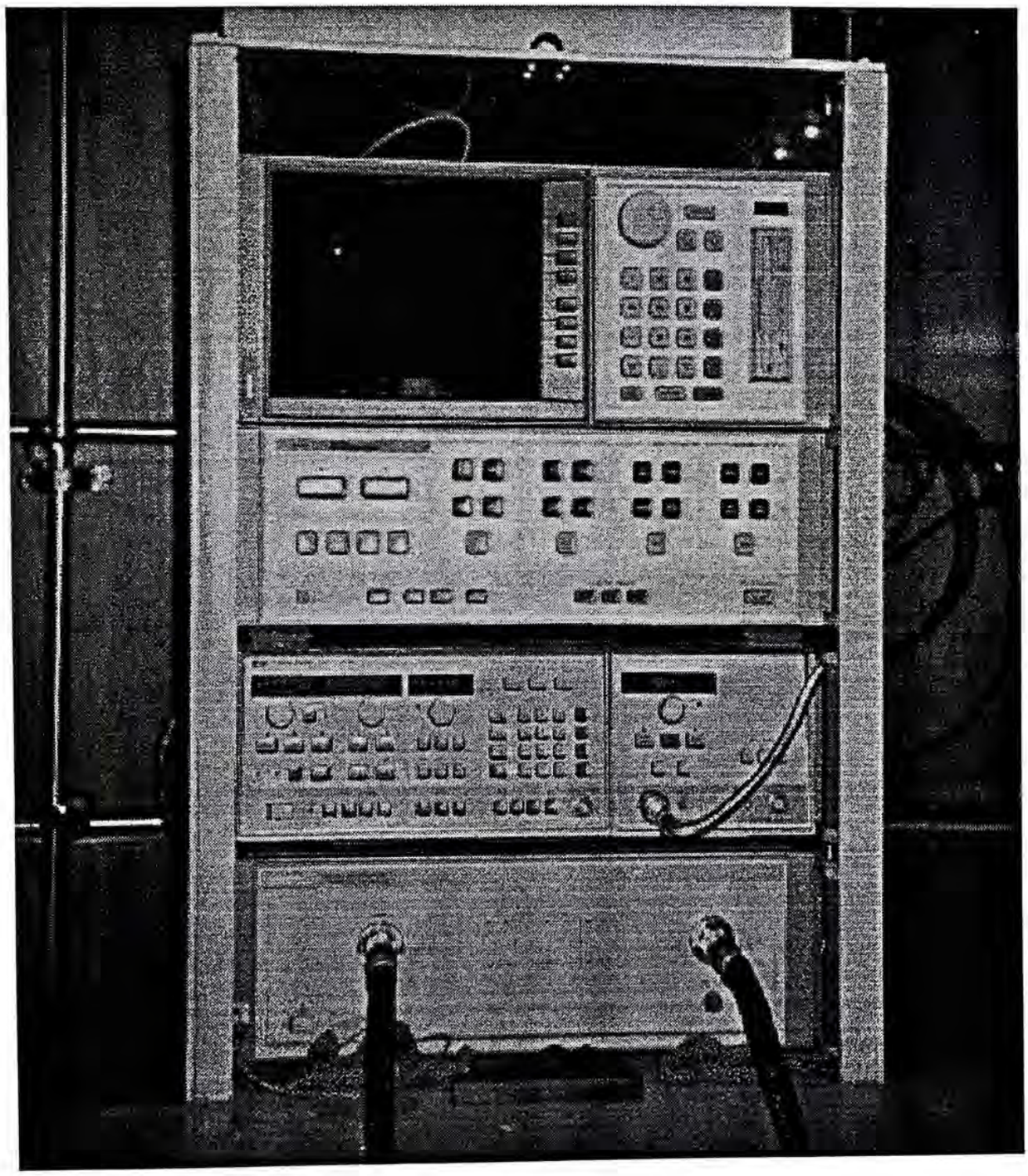

Fig. F-1 HP8510C Network Analyzer

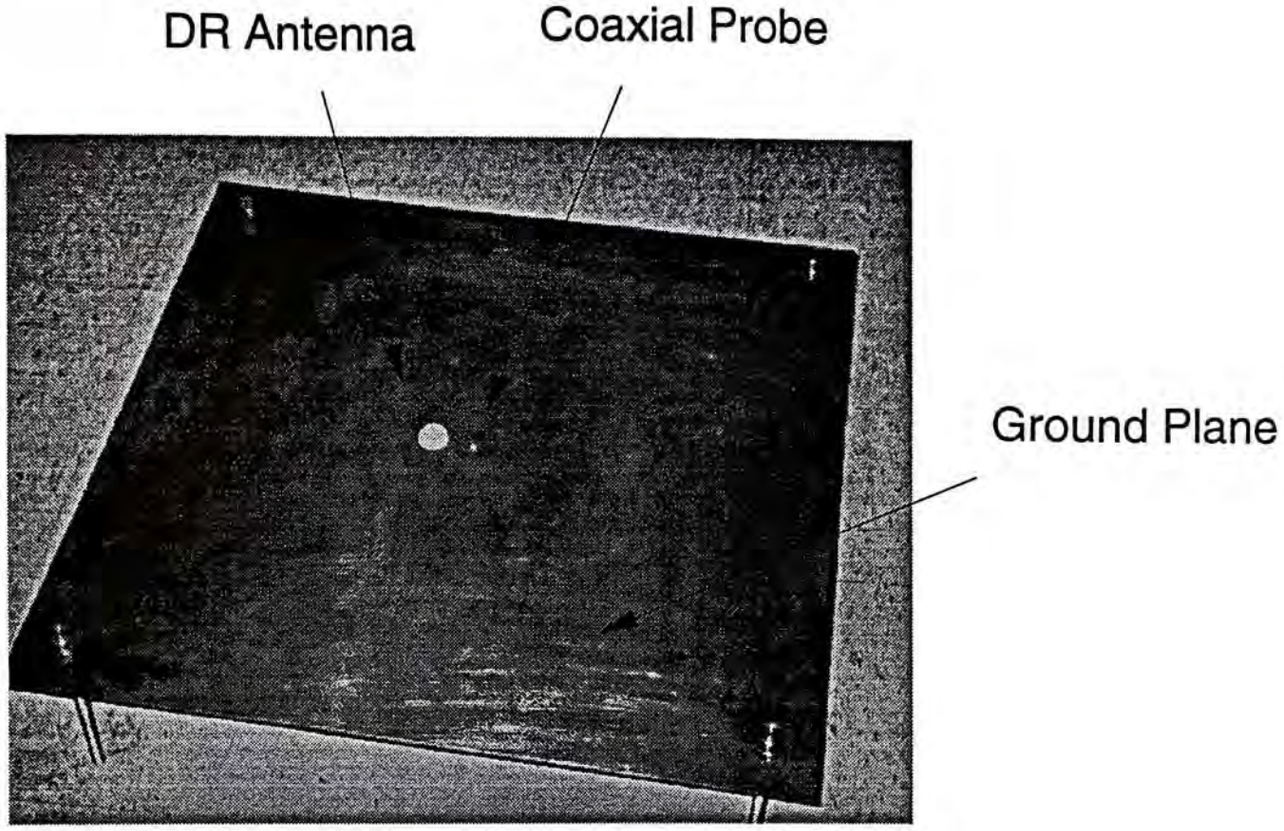

(a)

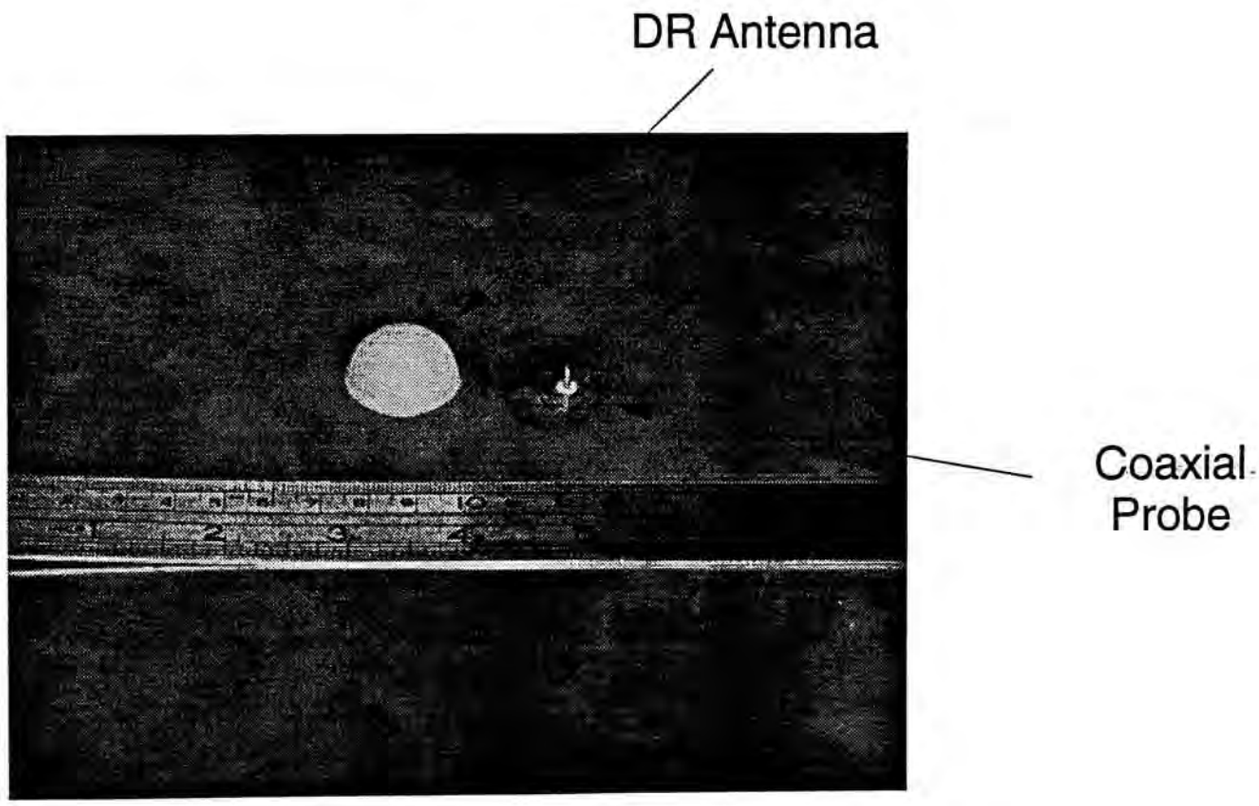

(b)

Fig. F-2 DR antenna, coaxial probe, and ground plane :
(a) Top view (b) Close view

APPENDIX G

EXPERIMENTAL SET-UP FOR APERTURE-COUPLED DR ANTENNA MEASUREMENT

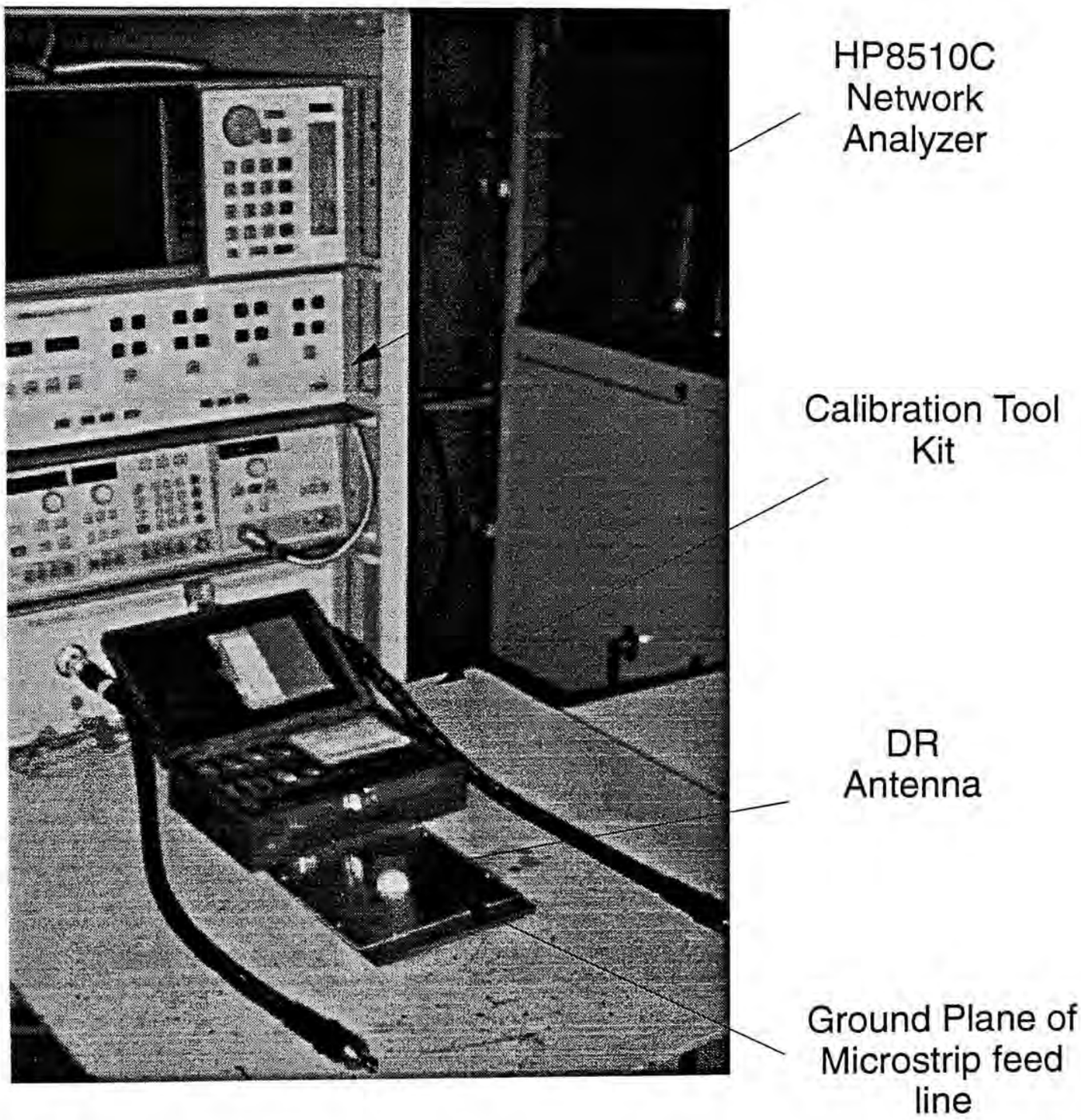

Fig G-1 Experimental set-up for aperture-coupled DR antenna

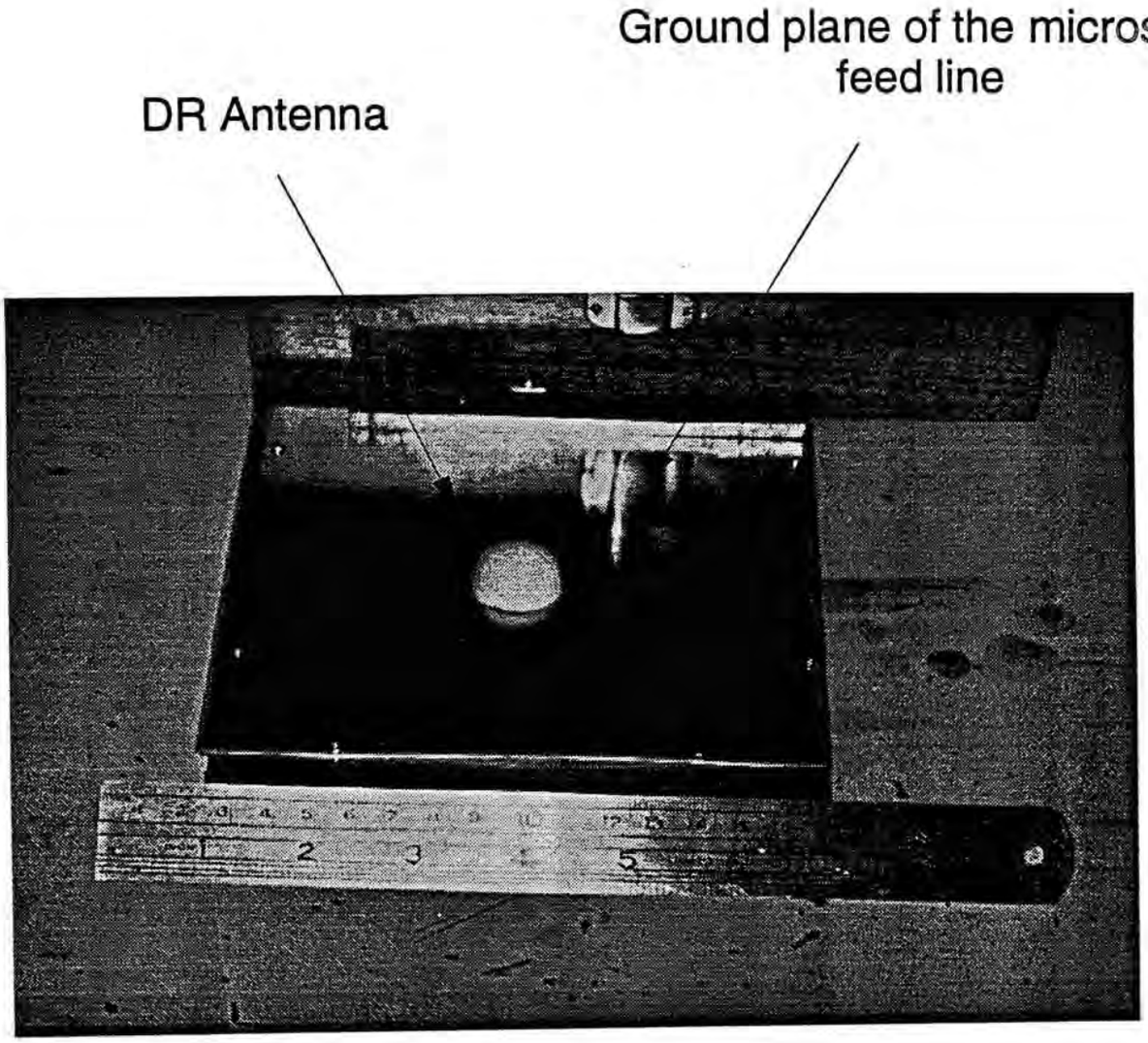

Fig. G-2 Close view of the DR antenna resting on the ground plane

REFERENCES

[1] D. Kajfez and P. Guillon, Eds., *Dielectric Resonators.* Norwood, MA: Artech House, 1986.

[2] S. A. Long, M. W. McAllister and L. C. Shen , 'The resonant cylindrical Dielectric Cavity Antenna,' *IEEE Trans. Antennas Propagat.*, vol. AP-31, pp.406-412, 1983, May 1983.

[3] M. W. McAllister, S. A. Long and G. L. Conway, 'Rectangular dielectric resonator antenna,' *Electron. Lett.*, vol. 19, pp.218-219, 1983.

[4] M. W. McAllister and S. A. Long, 'Resonant hemispherical dielectric antenna,' *Electron. Lett.*, vol. 20, pp.657-659, 1984.

[5] R. A. Kranenburg, and S. A. Long, 'Microstrip transmission line excitation of dielectric resonator antennas,' *Electron. Lett.*, vol. 24, pp. 1156-1157, 1988.

[6] J. T . H. St. Martin, Y. M. M. Antar, A. A. Kishk, A. Ittipiboon, and M. Cuhaci, 'Dielectric resonator antenna using apeture coupling,' *Electron Lett.*, vol. 26, pp. 2015-2016, Nov. 1990.

[7] R. K. Mongia, A. Ittipiboon, Y. M. M. Antar, P. Bhartia, and M. Cuhaci, 'A half-split cylindrica dielectric resonator antenna using slot-coupling,' *IEEE Microwave Guided Wave Lett.*, vol. 3, pp.38-39, Feb. 1993.

[8] A. A. Kishk, H. A. Auda, and B. C. Ahn, 'Radiation characteristics of cylindrical dielectric resonator antennas with new applications,' *IEEE Antennas Propag. Soc. News Lett.*, vol. 31 pp.7-16, 1989.

[9] J. Van Bladel, 'On the resonances of a dielectric resonator of very high permittivity,' *IEEE Trans. Microwave Theory Tech.*, vol. MTT-23, pp.199-208, 1975.

[10] M. Verplanken and J. Van Bladel, 'The electric-dipole resonances of ring resonators of very high permittivity,' *IEEE Trans. Microwave Theory Tech.*, vol. MTT-24, pp. 108-112, 1976.

[11] M. Verplanken and J. Van Bladel, 'The magnetic-dipole resonances of ring resonators of very high permittivity,' *IEEE Trans. Microwave Theory Tech.*, vol. MTT-27, pp. 328-333, 1979.

[12] A. W. Glisson, D. Kajfez, and J. James, 'Evaluation of modes in dielectric resonators using a surface integral equation formulation,' *IEEE Trans. Microwave Theory Tech.*, vol. MTT-31, pp.1023-1029, Dec. 1983.

[13] D. Kajfez, A. W. Glisson, and J. James, 'Computed modal field distributions for isolatd dielectric resonators,' *IEEE Trans. Microwave Theory Tech.*, vol. MTT-32, pp.1609-1616, Dec. 1984.

[14] E. C. Jordan and K. G. Balmain, *Electromagnetic Waves and Radiating Systems.* (Second Edition) New Delhi : Prentice-Hall, 1968, pp.485-496.

[15] A. H. Ghods and Y. Rahmat-Samii, 'Electromagnetic properties of an insulated dipole antenna immersed in an arbitrary medium,' *IEE proc. H*, vol 138, no.6, pp.497-503, Dec. 1991.

[16] H. Y. Yee, 'Natural resonant frequencies of microwave dielectric resonators,' *IEEE Trans. Microwave Theory Tech.*, vol. MTT-13, p.256, March 1965.

[17] M. Gastine, L. Courtois and J. L. Dormann, 'Electromagnetic resonances of free dielectric spheres,' *IEEE Trans. Microwave Theory Tech.*, vol. MTT-15, pp.694-700, Dec. 1967.

[18] K. W. Leung, K. M. Luk, K. Y. A. Lai, and D. Lin, 'Input impedance of hemispherical dielectric resonator antenna,' *Electron. Lett.*, vol. 27, pp.2259-2260, 1991.

[19] R. F. Harrington, *Field Computation by the Method of Moments.* New York : Macmillan, 1968.

[20] D. M. Pozar, 'Input impedance and mutual coupling of rectangular microstrip antennas,' *IEEE Trans. Antennas Propagat.*, vol. AP-30, pp.1191-1196, Nov. 1982.

[21] D. C. Chang, 'On the electrically thick cylindrical antenna,' *Radio Science*, vol. 2 (New Series), No.9, Sept. 1967, pp.1043-1060.

[22] G. Zhou and G. S. Smith, 'An accurate theoretical model for the thin-wire circular half-loop antenna,' *IEEE Trans. Antennas Propagat.*, vol. AP-39, pp.1167-1177, Aug. 1991.

[23] J. D. Kraus, *Antennas.*(Second Edition) McGraw-Hill, 1988, pp.391-392.

[24] R. S. Elliott, *Antenna Theory and Design.* Prentice-Hall, 1981, pp.569-572.

[25] W. A. Imbriale and P. G. Ingerson, 'On numerical convergence of moment solutions of moderately thick wire antennas using sinusoidal basis functions,' *IEEE Trans. Antennas Propagat.*, vol. AP-21, pp.363-366, May 1973.

[26] D. M. Pozar, 'Mircrostrip antenna aperture-coupled to a microstripline,' *Electron. Lett.*, vol. 21, no.2 , pp.49-50, 1985.

[27] P. L. Sullivan and D. H. Schaubert, 'Analysis of an aperture coupled microstrip antenna,' *IEEE Trans. Antennas Propagat.*, vol. Ap-34, pp.977-984, Aug. 1986.

[28] D. M. Pozar, 'A reciprocity method of analysis for printed slot and slot-coupled microstrip antennas,' *IEEE Tans. Antennas and Progagat.*, vol. AP-34, pp.1439-1446, 1986.

[29] R. D. Nevels, 'The annular aperture antenna with a hemispherical center conductor extension,' *IEEE Trans. Antennas Propagat.*, vol. AP-35, pp. 41-45, Jan. 1987.

[30] R. D. Nevels and J. E. Wheeler, 'Radiation from a dielectric coated hemispherical conductor fed by a coaxial transmission line,' *IEEE Trans. Electromagn, Compat.*, vol. 31, pp.16-20, Feb. 1989.

[31] J. E. Wheeler and R. D. Nevels, 'Reflection and transmission properties of annular slot covered by dielectric hemisphere,' *IEE Proc. H*, vol. 136, pp.59-63, Feb, 1989.

[32] R. F. Harrington, *Time Harmonic Electromagnetic Fields.* McGraw-Hill, 1961.

[33] J. A. Stratton, *Electromagnetic Theory.* New York : McGraw-Hill, 1941, p.417.

[34] R. E. Collin, *Field Theory of Guided Waves.* New York : McGraw Hill, 1960.

[35] T. K. Sarkar, A. R. Djordjevic, and E. Arvas, 'On the choice of expansion and weighting functions in the numerical solution of operator equations,' *IEEE Trans. Antennas Propagat.*, vol. AP-33, pp.988-996, Sept. 1985.

[36] J. D. Kraus, *Antennas.*(Second Edition) McGraw-Hill, 1988, pp.391-392.

[37] R. S. Elliott, *Antenna Theory and Design.* Prentice-Hall, 1981, pp.569-572.

[38] R. C. Hansen, 'Formulation of echelon dipole mutual impedance for computer,' *IEEE Trans. Antennas and Propagat.*, vol. AP-20, pp.780-781, Nov. 1972.

[39] D. M. Pozar, *Antenna Design Using Personal Computers.* Dedham, MA : Artech House, 1985, pp.35-43.

[40] M. Abramowitz and I. A. Stegun, *Handbook of Mathematical Functions.* National Bureau of Standards, AMS No.55, June 1964.

[41] S. A. Schelkunoff, *Advanced Antenna Theory.* New York : Wiley, 1952, pp.140-142.

[42] D. R. Wilton and C. M. Butler, 'Effective methods for solving integral and integro-differential equations,' *Electromagnetics,* vol. 1, pp.289-308, 1981.

[43] F. M. Tesche, 'Evaluation of the surface integral occurring in the E-field integral equations for wire antennas,' *IEEE Trans. Electromagn. Compat.*, pp.209-210, Nov. 1974.

[44] C. M. Butler, 'Evaluation of potential integral at singularity of exact kernel in thin-wire calculations,' *IEEE Trans. Antennas Propagat.*, pp.293-295, March 1975.

[45] L. W. Pearson, 'A Separation of the logarithmic singularity in the exact kernel of the cylindrical antenna integral equation,' *IEEE Trans. Antennas Propagat.*, pp.256-261, March 1975.

[46] W. X. Wang, 'The exact kernel for cylindrical antenna,' *IEEE Trans. Antennas Propagat.*, vol. AP-39, pp.434-435, April 1991.

[47] A. Jeffrey, I. Ruzhik, I. Gradshteyn, Yu. Geronimus, and M. Tseytlin, *Tables of integrals*, Series and Products, Academic Press, 1980, pp.905.

[48] R. E. Collin, *Field Theory of Guided Waves.*(Second Edition) IEEE Press, 1991, pp.479-481.

[49] T. K. Sarkar, 'A study of the various methods for computing electromagnetic field utilizing thin wire integral equations,' *Radio Science*, vol. 18, pp.29-38, 1983.

[50] R. W. P. King, *Theory of Linear Antennas.* Cambridge, Mass : Harvard University Press, 1956, pp.16-20.

[51] R. E. Collin and F. J. Zucker, *Antenna Theory.* (Part 1). New York : McGraw-Hill, 1969, p.72.

[52] B. W. Kwan and E. H. Newman, Mutual coupling analysis for conformal microstrip antennas. Technical Report 712692-4, ElectroScience Laboratory, The Ohio State University.

[53] T. C Edwards, *Foundations for Microstrip Circuit Design.* New York : John Wiley & Sons, 1981, p.103.

[54] R. W. Jackson and D. M. Pozar, 'Full analysis of microstrip open-end and gap discontinuities,' *IEEE Trans. Microwave Theory and Tech.*, vol. MTT-33, pp.1036-1042, Oct. 1985.

LIST OF PUBLICATIONS PRODUCED DURING THE STUDY

[1] K.W. Leung, K.M. Luk, K.Y.A. Lai, and D. Lin, 'Input impedance of dielectric resonator antenna,' *Electron. Letters*, vol. 27, pp.2259-2260, Nov. 1991.

[2] K.W. Leung, K.M. Luk, K.Y.A. Lai, and D. Lin, 'On the TM_{101} mode of dielectric resonator antenna,' *Microwave and Optical Technology Letters*, vol. 6, pp.626-629, Sept. 1993.

[3] K.W. Leung, K.M. Luk, K.Y.A. Lai, and D. Lin, 'Theory and experiment of probe fed dielectric resonator antenna,' *IEEE Trans. Antennas Propagat.* (to appear in Oct. 1993).

[4] K.M. Luk, K.W. Leung, K.Y.A. Lai, and D. Lin, 'Analysis of dielectric resonator antenna', *Radio Sci.* (invited paper, to appear).

[5] K.W. Leung, K.Y.A. Lai, K. M. Luk, and D. Lin, 'End-fire TE_{221} mode of aperture coupled hemispherical dielectric resonator antenna,' *Electron. Lett.*, vol. 29, pp.981-982, May 1993.

[6] K.W. Leung, K.Y.A. Lai, K.M. Luk, and D. Lin, 'Input impedance of aperture coupled hemispherical DR antenna,' *Electron. Lett.*, vol. 29, pp.1165-1167, June 1993.

[7] K.W. Leung, K.Y.A. Lai, K.M. Luk, and D. Lin, 'Theory and experiment on aperture-coupled hemispherical dielectric resonator antenna,' *IEEE Trans. Antennas Propagat.* (submitted).

[8] K.M. Luk, K.W. Leung, K.Y.A. Lai, and D. Lin, 'Analysis of dielectric resonator antenna,' *Proceedings of URSI Electromagnetic Theory Symposium*, pp.382-384, August 1992, Sydney, Australia.

[9] K.W. Leung, K. M. Luk, K.Y.A. Lai, and D. Lin, "A slot-coupled heimspherical dielectric resonator antenna," *Proceedings of 1993 Asia-Pacific Microwave Conference,* Hsinchu, Taiwan China, pp.2.23-2.26, October 1993.

[10] K.W. Leung, K. M. Luk, K.Y.A. Lai, and D. Lin, "Analysis of aperture coupled dielectric resonator antenna," *Proceedings of the XXIVth General Assembly of the International Union of Radio Science,* Kyoto, Japan, p.80, August 1993.

INTERNATIONAL AWARD OBTAINED DURING THE STUDY

URSI Young Scientists Award offered by XXIVth General Assembly of the International Union of Radio Science, August 1993, Kyoto, Japan.